

¹

©Copyright 2021

²

Sean Gasiorowski

$HH \rightarrow b\bar{b}b\bar{b}$ or How I Learned to Stop Worrying and Love the QCD Background

Sean Gasiorowski

A dissertation
submitted in partial fulfillment of the
requirements for the degree of

Doctor of Philosophy

University of Washington

2021

Reading Committee:

Anna Goussiou, Chair

Jason Detwiler

Shih-Chieh Hsu

David Kaplan

Henry Lubatti

Thomas Quinn

Gordon Watts

Programme Structure in CSE - I

Physics

22

University of Washington

23

Abstract

24

$HH \rightarrow b\bar{b}b\bar{b}$ or How I Learned to Stop Worrying and Love the QCD Background

25

Sean Gasiorowski

26

Chair of the Supervisory Committee:

27

Professor Anna Goussiou

28

Physics

29

Insert abstract here

TABLE OF CONTENTS

	Page
31 List of Figures	iii
32 Glossary	xv
33 Preface	xviii
34 Chapter 1: The Standard Model of Particle Physics	1
35 1.1 Introduction: Particles and Fields	1
36 1.2 Quantum Electrodynamics	4
37 1.3 An Aside on Group Theory	9
38 1.4 Quantum Chromodynamics	11
39 1.5 The Weak Interaction	14
40 1.6 The Higgs Potential and the SM	20
41 1.7 The Standard Model: A Summary	26
42 Chapter 2: Di-Higgs Phenomenology and Physics Beyond the Standard Model	30
43 2.1 Intro to Di-Higgs	30
44 2.2 Resonant HH Searches	31
45 2.3 Non-resonant HH Searches	33
46 Chapter 3: Experimental Apparatus	37
47 3.1 The Large Hadron Collider	37
48 3.2 The ATLAS Experiment	40
49 Chapter 4: Simulation	49
50 4.1 Event Generation	49
51 4.2 Detector Simulation	52
52 4.3 Correlated Fluctuations in FastCaloSim	54

53	4.4 Outlook	62
54	Chapter 5: Reconstruction	64
55	5.1 Jets	64
56	5.2 Flavor Tagging	66
57	Chapter 6: The Anatomy of an LHC Search	76
58	6.1 Object Selection and Identification	76
59	6.2 Defining a Signal Region	76
60	6.3 Background Estimation	76
61	6.4 Uncertainty Estimation	76
62	6.5 Hypothesis Testing	76
63	Chapter 7: Search for pair production of Higgs bosons in the $b\bar{b}b\bar{b}$ final state	77
64	7.1 Data and Monte Carlo Simulation	79
65	7.2 Triggers and Object Definitions	81
66	7.3 Analysis Selection	83
67	7.4 Background Reduction and Top Veto	89
68	7.5 Kinematic Region Definition	90
69	7.6 Background Estimation	96
70	7.7 Uncertainties	157
71	7.8 Background Validation	167
72	7.9 Overview of Other $b\bar{b}b\bar{b}$ Channels	170
73	7.10 m_{HH} Distributions	172
74	7.11 Statistical Analysis	183
75	7.12 Results	184
76	Chapter 8: Future Ideas for $HH \rightarrow b\bar{b}b\bar{b}$	189
77	8.1 pairAGraph: A New Method for Jet Pairing	189
78	8.2 Background Estimation with Mass Plane Interpolation	194
79	Chapter 9: Conclusions	209

LIST OF FIGURES

Figure Number		Page
81	1.1 Diagram of the elementary particles described by the Standard Model [4].	3
82	2.1 Representative diagrams for the gluon-gluon fusion production of spin-0 (X) and spin-2 (G_{KK}^*) resonances which decay to two Standard Model Higgs bosons. The spin-0 resonance considered for this thesis is a generic narrow width resonance which may be interpreted in the context of two Higgs doublet models [21], whereas the spin-2 resonance is considered as a Kaluza-Klein graviton within the bulk Randall-Sundrum (RS) model [22, 23].	31
88	2.2 Dominant contributing diagrams for non-resonant gluon-gluon fusion production of HH . κ_λ and κ_t represent ratios of the Higgs self-coupling and coupling to top quarks respectively, relative to the values predicted by the Standard Model.	32
92	2.3 Illustration of dominant HH branching ratios. $HH \rightarrow b\bar{b}b\bar{b}$ is the most common decay mode, representing 34 % of all HH events produced at the LHC.	33
94	2.4 Monte Carlo generator level m_{HH} distributions for various values of κ_λ , demonstrating the impact of the interference between the two diagrams of Figure 2.2 on the resulting m_{HH} distribution. For $\kappa_\lambda = 0$ there is no triangle diagram contribution, demonstrating the shape of the box diagram contribution, whereas for $\kappa_\lambda = 10$, the triangle diagram dominates, with a strong low mass peak. The interplay between the two is quite evident for other values, resulting in, e.g., the double peaked structure present for $\kappa_\lambda = 2$ (near maximal destructive interference) and $\kappa_\lambda = -5$. At $\kappa_\lambda = 5$, the interference leads to a deficit at high m_{HH} , resulting in a narrower distribution (and thus a more pronounced low mass peak) than the $\kappa_\lambda = 10$ case. [24]	35
104	3.1 Diagram of the ATLAS detector [44]	40
105	3.2 Cross section of the ATLAS detector showing how particles interact with various detector components [46]	42
107	3.3 2D projections of the ATLAS coordinate system	43

108	4.1	Schematic diagram of the Monte Carlo simulation of a hadron-hadron collision. The incoming hadrons are the green blobs with the arrows on the left and right, with the red blob in the center representing the hard scatter event, and the purple representing a secondary hard scatter. Radiation from both incoming and outgoing particles is shown, and the light green blobs represent hadronization, with the outermost dark green circles corresponding to the final state hadrons. Yellow lines are radiated photons. [60]	51
115	4.2	The projected ATLAS computational requirements for Run 3 and the HL-LHC relative to the projected computing budget. Aggressive R&D is required to keep resources within budget [63].	53
118	4.3	Energy and variable weta2, defined as the energy weighted lateral width of a shower in the second electromagnetic calorimeter layer, for 16 GeV photons with full simulation (G4) and FastCaloSimV2 (FCSV2) [65].	55
121	4.4	Example of photon and pion average shapes in 5×5 calorimeter cells. The left column shows the average shape over a sample of 10000 events, while the right column shows the energy ratio, in each cell, of single GEANT4 events with respect to this average. The photon ratios are all close to 1, while the pion ratios show significant deviation from the average.	57
126	4.5	Distribution of the ratio of voxel energy in single events to the corresponding voxel energy in the average shape, with GEANT4 events in blue and Gaussian model events in orange, for 65 GeV central pions in EMB2. Moving top to bottom corresponds to increasing α , left to right corresponds to increasing R , with core voxels numbered 1, 10, 19, Agreement is quite good across all voxels. Results are similar for the VAE method.	58
132	4.6	Correlation coefficient of ratios of voxel energy in single events to the corresponding voxel energy in the average shape, examined between the core bin from $\alpha = 0$ to $2\pi/8$ and each of the other voxels. The periodic structure represents the binning in α , and the increasing numbers in each of these periods correspond to increasing R , where the eight points with correlation coefficient 1 are the eight core bins. Both the Gaussian and VAE generated toy events are able to reproduce the major correlation structures for 65 GeV central pions in EMB2.	59
140	4.7	Comparison of the RMS fluctuations about the average shape with the Gaussian fluctuation model (red), the VAE fluctuation model (green), and without correlated fluctuations (blue) for a range of pion energies, η points, and layers.	60

143	4.8 Comparison of the Gaussian fluctuation model to the default FCSV2 version	61
144	and to G4 simulation, using pions of 65 GeV energy and $0.2 < \eta < 0.25$.	
145	Variables shown relate to calorimeter clusters, three-dimensional spatial group-	
146	ings of cells [71] which provide powerful insight on the structure of energy	
147	deposits in the calorimeter. Variables considered include number and energy	
148	of clusters, the 2nd moment in lambda, ($\langle \lambda^2 \rangle$), which describes the square	
149	of the longitudinal extension of a cluster, where λ is the distance of a cell from	
150	the shower center along the shower axis, and a cluster moment is defined as	
151	$\langle x^n \rangle = \frac{\sum E_i x_i}{\sum E_i}$, and the distance ΔR , between the cluster and the true pion.	
152	With the correlated fluctuations, variables demonstrate improved modeling	
153	relative to default FastCaloSimV2.	
154	5.1 Illustration of an interaction producing two light jets and one b -jet in the	69
155	transverse plane. While the light jets decay “promptly”, coinciding with	
156	the primary vertex of the proton-proton interaction, the longer lifetime of B	
157	hadrons leads to a secondary decay vertex, displaced from the primary vertex	
158	by length L_{xy} . This is typically a few mm, and therefore is not directly visible	
159	in the detector, but leads to a large transverse impact parameter, d_0 , for the	
160	resulting tracks. [79]	
161	5.2 Performance of the various low and high level flavor tagging algorithms in	73
162	$t\bar{t}$ simulation, demonstrating the tradeoff between b -jet efficiency and light	
163	and c -jet rejection. The high level taggers demonstrate significantly better	
164	performance than any of the individual low level taggers, with DL1 offering	
165	slight improvements over MV2 due to the inclusion of additional input variables.	
166	5.3 Performance of the MV2, DL1, and DL1r algorithms in $t\bar{t}$ simulation, demon-	74
167	strating the tradeoff between b -jet efficiency and light and c -jet rejection. f_c	
168	controls the importance of c -jet rejection in the discriminating variable, and	
169	values shown have been optimized separately for each DL1 configuration. DL1r	
170	demonstrates a significant improvement in both light and c jet rejection over	
171	MV2 and DL1. [84]	
172	7.1 Comparison of m_{H1} vs m_{H2} planes for the full Run 2 2 b dataset with different	87
173	pairings. As evidenced, this choice significantly impacts where events fall in	
174	this plane, and therefore which events fall into the various kinematic regions	
175	defined in this plane (see Section 7.5). The signal regions for the resonant/early	
176	Run 2 analysis are shown for reference for the BDT and D_{HH} pairings, while	
177	the the min ΔR signal region shifted is shifted slightly up and to the right to	
178	match the non-resonant selection. Note that the band structure around 80 GeV	
179	in both m_{H1} and m_{H2} is introduced by the top veto described in Section 7.4.	

180	7.2	Comparison of signal distributions in the respective signal regions for the min ΔR and D_{HH} pairing for various values of the Higgs trilinear coupling in the respective signal regions. The distributions are quite similar at the Standard Model point, but for other variations, min ΔR does not pick up the low mass features.	88
185	7.3	Regions used for the resonant search, shown on the $2b$ data mass plane. The outermost region (the “control region”) is used for derivation of the nominal background estimate. The innermost region is the signal region, where the signal extraction fit is performed. The region in between (the “validation region”) is used for the assessment of an uncertainty.	91
190	7.4	Regions used for the non-resonant search. The “top” and “bottom” quadrants together comprise the control region, in which the nominal background estimate is derived. The “left” and “right” quadrants together comprise the validation region, which is used to assess an uncertainty. The signal region, in the center, is where the signal extraction fit is performed.	93
195	7.5	Impact of the m_{HH} correction on a range of spin-0 resonant signals. The corrected m_{HH} distributions (solid lines) are much sharper and more centered on the corresponding resonance masses than the uncorrected m_{HH} distributions (dashed).	94
200	7.6	Resonant Search: Distributions of ΔR between the closest Higgs Candidate jets, ΔR between the other two, and average absolute value of HC jet η before (left) and after (right) CR derived reweighting for the 2018 Control Region.	103
205	7.7	Resonant Search: Distributions of p_T of the 2nd and 4th leading Higgs Candidate jets and the p_T of the di-Higgs system before (left) and after (right) CR derived reweighting for the 2018 Control Region.	104
210	7.8	Resonant Search: Distributions of the number of jets before (left) and after (right) CR derived reweighting for the 2018 Control Region. A minimum of 4 jets is required in each event in order to form Higgs candidates.	105
215	7.9	Resonant Search: Distributions of p_T of the 1st and 3rd leading Higgs Candidate jets and ΔR between Higgs candidates before (left) and after (right) CR derived reweighting for the 2018 Control Region.	106
220	7.10	Resonant Search: Distributions of η of the 1st, 2nd, and 3rd leading Higgs Candidate jets before (left) and after (right) CR derived reweighting for the 2018 Control Region.	107
225	7.11	Resonant Search: Distributions of η of the 4th leading Higgs Candidate jet and the p_T of the leading and subleading Higgs candidates before (left) and after (right) CR derived reweighting for the 2018 Control Region.	108

217	7.12 Resonant Search: Distributions of mass of the leading and subleading Higgs candidates and of the di-Higgs system before (left) and after (right) CR derived reweighting for the 2018 Control Region.	109
220	7.13 Resonant Search: Distributions of $\Delta\phi$ between jets in the leading and sub-leading Higgs candidates before (left) and after (right) CR derived reweighting for the 2018 Control Region.	110
223	7.14 Resonant Search: Distributions of the top veto variable, X_{Wt} , before (left) and after (right) CR derived reweighting for the 2018 Control Region. Reweighting is done after the cut on this variable is applied	111
226	7.15 Resonant Search: Distributions of ΔR between the closest Higgs Candidate jets, ΔR between the other two, and average absolute value of HC jet η before (left) and after (right) CR derived reweighting for the 2018 Validation Region.	112
229	7.16 Resonant Search: Distributions of p_T of the 2nd and 4th leading Higgs Candidate jets and the p_T of the di-Higgs system before (left) and after (right) CR derived reweighting for the 2018 Validation Region.	113
232	7.17 Resonant Search: Distributions of the number of jets before (left) and after (right) CR derived reweighting for the 2018 Validation Region. A minimum of 4 jets is required in each event in order to form Higgs candidates.	114
235	7.18 Resonant Search: Distributions of p_T of the 1st and 3rd leading Higgs Candidate jets and ΔR between Higgs candidates before (left) and after (right) CR derived reweighting for the 2018 Validation Region.	115
238	7.19 Resonant Search: Distributions of η of the 1st, 2nd, and 3rd leading Higgs Candidate jets before (left) and after (right) CR derived reweighting for the 2018 Validation Region.	116
241	7.20 Resonant Search: Distributions of η of the 4th leading Higgs Candidate jet and the p_T of the leading and subleading Higgs candidates before (left) and after (right) CR derived reweighting for the 2018 Validation Region.	117
244	7.21 Resonant Search: Distributions of mass of the leading and subleading Higgs candidates and of the di-Higgs system before (left) and after (right) CR derived reweighting for the 2018 Validation Region.	118
247	7.22 Resonant Search: Distributions of $\Delta\phi$ between jets in the leading and sub-leading Higgs candidates before (left) and after (right) CR derived reweighting for the 2018 Validation Region.	119
250	7.23 Resonant Search: Distributions of the top veto variable, X_{Wt} , before (left) and after (right) CR derived reweighting for the 2018 Validation Region. Reweighting is done after the cut on this variable is applied	120

253	7.24 Non-resonant Search (4b): Distributions of ΔR between the closest Higgs Candidate jets, ΔR between the other two, and average absolute value of HC jet η before (left) and after (right) CR derived reweighting for the 2018 4b Control Region.	121
254		
255		
256		
257	7.25 Non-resonant Search (4b): Distributions of p_T of the 2nd and 4th leading Higgs Candidate jets and the p_T of the di-Higgs system before (left) and after (right) CR derived reweighting for the 2018 4b Control Region.	122
258		
259		
260	7.26 Non-resonant Search (4b): Distributions of the number of jets before (left) and after (right) CR derived reweighting for the 2018 4b Control Region. A minimum of 4 jets is required in each event in order to form Higgs candidates.	123
261		
262		
263	7.27 Non-resonant Search (4b): Distributions of p_T of the 1st and 3rd leading Higgs Candidate jets and ΔR between Higgs candidates before (left) and after (right) CR derived reweighting for the 2018 4b Control Region.	124
264		
265		
266	7.28 Non-resonant Search (4b): Distributions of η of the 1st, 2nd, and 3rd leading Higgs Candidate jets before (left) and after (right) CR derived reweighting for the 2018 4b Control Region.	125
267		
268		
269	7.29 Non-resonant Search (4b): Distributions of η of the 4th leading Higgs Candidate jet and the p_T of the leading and subleading Higgs candidates before (left) and after (right) CR derived reweighting for the 2018 4b Control Region.	126
270		
271		
272		
273	7.30 Non-resonant Search (4b): Distributions of mass of the leading and subleading Higgs candidates and of the di-Higgs system before (left) and after (right) CR derived reweighting for the 2018 4b Control Region.	127
274		
275		
276	7.31 Non-resonant Search (4b): Distributions of $\Delta\phi$ between jets in the leading and subleading Higgs candidates before (left) and after (right) CR derived reweighting for the 2018 4b Control Region.	128
277		
278		
279	7.32 Non-resonant Search (4b): Distributions of the top veto variable, X_{Wt} , before (left) and after (right) CR derived reweighting for the 2018 4b Control Region. Reweighting is done after the cut on this variable is applied.	129
280		
281		
282	7.33 Non-resonant Search (4b): Distributions of ΔR between the closest Higgs Candidate jets, ΔR between the other two, and average absolute value of HC jet η before (left) and after (right) CR derived reweighting for the 2018 4b Validation Region.	130
283		
284		
285		
286	7.34 Non-resonant Search (4b): Distributions of p_T of the 2nd and 4th leading Higgs Candidate jets and the p_T of the di-Higgs system before (left) and after (right) CR derived reweighting for the 2018 4b Validation Region.	131
287		
288		

289	7.35 Non-resonant Search (4b): Distributions of the number of jets before (left)	
290	and after (right) CR derived reweighting for the 2018 4b Validation Region. A	
291	minimum of 4 jets is required in each event in order to form Higgs candidates.	132
292	7.36 Non-resonant Search (4b): Distributions of p_T of the 1st and 3rd leading	
293	Higgs Candidate jets and ΔR between Higgs candidates before (left) and after	
294	(right) CR derived reweighting for the 2018 4b Validation Region.	133
295	7.37 Non-resonant Search (4b): Distributions of η of the 1st, 2nd, and 3rd lead-	
296	ing Higgs Candidate jets before (left) and after (right) CR derived reweighting	
297	for the 2018 4b Validation Region.	134
298	7.38 Non-resonant Search (4b): Distributions of η of the 4th leading Higgs	
299	Candidate jet and the p_T of the leading and subleading Higgs candidates before	
300	(left) and after (right) CR derived reweighting for the 2018 4b Validation Region.	135
301	7.39 Non-resonant Search (4b): Distributions of mass of the leading and sub-	
302	leading Higgs candidates and of the di-Higgs system before (left) and after	
303	(right) CR derived reweighting for the 2018 4b Validation Region.	136
304	7.40 Non-resonant Search (4b): Distributions of $\Delta\phi$ between jets in the leading	
305	and subleading Higgs candidates before (left) and after (right) CR derived	
306	reweighting for the 2018 4b Validation Region.	137
307	7.41 Non-resonant Search (4b): Distributions of the top veto variable, X_{Wt} ,	
308	before (left) and after (right) CR derived reweighting for the 2018 4b Validation	
309	Region. Reweighting is done after the cut on this variable is applied.	138
310	7.42 Non-resonant Search (3b1l): Distributions of ΔR between the closest	
311	Higgs Candidate jets, ΔR between the other two, and average absolute value	
312	of HC jet η before (left) and after (right) CR derived reweighting for the 2018	
313	3b1l Control Region.	139
314	7.43 Non-resonant Search (3b1l): Distributions of p_T of the 2nd and 4th leading	
315	Higgs Candidate jets and the p_T of the di-Higgs system before (left) and after	
316	(right) CR derived reweighting for the 2018 3b1l Control Region.	140
317	7.44 Non-resonant Search (3b1l): Distributions of the number of jets before	
318	(left) and after (right) CR derived reweighting for the 2018 3b1l Control Region.	
319	A minimum of 4 jets is required in each event in order to form Higgs candidates.	141
320	7.45 Non-resonant Search (3b1l): Distributions of p_T of the 1st and 3rd leading	
321	Higgs Candidate jets and ΔR between Higgs candidates before (left) and after	
322	(right) CR derived reweighting for the 2018 3b1l Control Region.	142
323	7.46 Non-resonant Search (3b1l): Distributions of η of the 1st, 2nd, and 3rd	
324	leading Higgs Candidate jets before (left) and after (right) CR derived reweight-	
325	ing for the 2018 3b1l Control Region.	143

326	7.47 Non-resonant Search (3b1l): Distributions of η of the 4th leading Higgs Candidate jet and the p_T of the leading and subleading Higgs candidates before (left) and after (right) CR derived reweighting for the 2018 3b1l Control Region.	144
329	7.48 Non-resonant Search (3b1l): Distributions of mass of the leading and subleading Higgs candidates and of the di-Higgs system before (left) and after (right) CR derived reweighting for the 2018 3b1l Control Region.	145
332	7.49 Non-resonant Search (3b1l): Distributions of $\Delta\phi$ between jets in the leading and subleading Higgs candidates before (left) and after (right) CR derived reweighting for the 2018 3b1l Control Region.	146
335	7.50 Non-resonant Search (3b1l): Distributions of the top veto variable, X_{Wt} , before (left) and after (right) CR derived reweighting for the 2018 3b1l Control Region. Reweighting is done after the cut on this variable is applied.	147
338	7.51 Non-resonant Search (3b1l): Distributions of ΔR between the closest Higgs Candidate jets, ΔR between the other two, and average absolute value of HC jet η before (left) and after (right) CR derived reweighting for the 2018 3b1l Validation Region.	148
342	7.52 Non-resonant Search (3b1l): Distributions of p_T of the 2nd and 4th leading Higgs Candidate jets and the p_T of the di-Higgs system before (left) and after (right) CR derived reweighting for the 2018 3b1l Validation Region.	149
345	7.53 Non-resonant Search (3b1l): Distributions of the number of jets before (left) and after (right) CR derived reweighting for the 2018 3b1l Validation Region. A minimum of 4 jets is required in each event in order to form Higgs candidates.	150
349	7.54 Non-resonant Search (3b1l): Distributions of p_T of the 1st and 3rd leading Higgs Candidate jets and ΔR between Higgs candidates before (left) and after (right) CR derived reweighting for the 2018 3b1l Validation Region.	151
352	7.55 Non-resonant Search (3b1l): Distributions of η of the 1st, 2nd, and 3rd leading Higgs Candidate jets before (left) and after (right) CR derived reweighting for the 2018 3b1l Validation Region.	152
355	7.56 Non-resonant Search (3b1l): Distributions of η of the 4th leading Higgs Candidate jet and the p_T of the leading and subleading Higgs candidates before (left) and after (right) CR derived reweighting for the 2018 3b1l Validation Region.	153
359	7.57 Non-resonant Search (3b1l): Distributions of mass of the leading and subleading Higgs candidates and of the di-Higgs system before (left) and after (right) CR derived reweighting for the 2018 3b1l Validation Region.	154

362	7.58 Non-resonant Search (3b1l): Distributions of $\Delta\phi$ between jets in the leading and subleading Higgs candidates before (left) and after (right) CR derived reweighting for the 2018 3b1l Validation Region.	155
363		
364		
365	7.59 Non-resonant Search (3b1l): Distributions of the top veto variable, X_{Wt} , before (left) and after (right) CR derived reweighting for the 2018 3b1l Validation Region. Reweighting is done after the cut on this variable is applied.	156
366		
367		
368		
369	7.60 Illustration of the approximate bootstrap band procedure, shown as a ratio to the nominal estimate for the 2017 non-resonant background estimate. Each grey line is from the m_{HH} prediction for a single bootstrap training. Figure 7.60(a) shows the variation histograms constructed from median weight \pm the IQR of the replica weights. It can be seen that this captures the rough shape of the bootstrap envelope, but is not good estimate for the overall magnitude of the variation. Figure 7.60(b) demonstrates the applied normalization correction, and Figure 7.60(c) shows the final band (normalized Figure 7.60(a) + Figure 7.60(b)). Comparing this with the IQR variation for the prediction from each bootstrap in each bin in Figure 7.60(d), the approximate envelope describes a very similar variation.	161
370		
371		
372		
373		
374		
375		
376		
377		
378		
379		
380	7.61 Resonant Search: Example of CR vs VR variation in each H_T region for 2018. The variation nicely factorizes into low and high mass components.	163
381		
382		
383		
384		
385		
386	7.62 Non-resonant Search (4b): Example of CR vs VR variation in each signal region quadrant for 2018. Significantly different behavior is seen between quadrants, with the largest variation in quadrant 1 and the smallest in quadrant 4.	164
387		
388		
389		
390		
391		
392		
393	7.63 Resonant Search: Performance of the background estimation method in the resonant analysis reversed $\Delta\eta_{HH}$ kinematic signal region. A new background estimate is trained following nominal procedures entirely within the reversed $\Delta\eta_{HH}$ region, and the resulting model, including uncertainties, is compared with 4b data in the corresponding signal region. Good agreement is shown. The quoted p -value uses the χ^2 test statistic, and demonstrates no evidence that the data differs from the assessed background.	168
394		
395		
396		
397		
398	7.64 Non-resonant Search: Performance of the background estimation method in the 3b + 1 fail validation region. A new background estimate is trained following nominal procedures but with a reweighting from 2b to 3b + 1 fail events. Generally good agreement is seen, though there is some deviation at very low masses in the low $\Delta\eta_{HH}$ low X_{HH} category.	169
399		

398	7.65 Resonant Search: Demonstration of the performance of the nominal reweighting in the control region on corrected m_{HH} , with Figure 7.65(a) showing 2b events normalized to the total 4b yield and Figure 7.65(b) applying the reweighting procedure. Agreement is much improved with the reweighting. Note that overall reweighted 2b yield agrees with 4b yield in the control region by construction.	173
404	7.66 Resonant Search: Demonstration of the performance of the control region derived reweighting in the validation region on corrected m_{HH} . Agreement is generally good for this extrapolated estimate. Note that the uncertainty band includes the extrapolation systematic, which is defined by a reweighting trained in the validation region.	174
409	7.67 Resonant Search: Signal region agreement of the background estimate and observed data after a background-only profile likelihood fit. The closure is generally quite good, though there is an evident deficit in the background estimate relative to the data for higher values of corrected m_{HH}	175
413	7.68 Non-resonant Search (4b): Demonstration of the performance of the nominal reweighting in the control region on m_{HH} , split into the two $\Delta\eta_{HH}$ regions. Closure is generally good, with some residual mis-modeling in the low $\Delta\eta_{HH}$ region near 600 GeV.	177
417	7.69 Non-resonant Search (3b1l): Demonstration of the performance of the nominal reweighting in the control region on m_{HH} , split into the two $\Delta\eta_{HH}$ regions. Closure is generally good, with similar conclusions as for the 4b region.	178
420	7.70 Non-resonant Search (4b): Demonstration of the performance of the nominal reweighting in the validation region on m_{HH} , split into the two $\Delta\eta_{HH}$ regions. The low $\Delta\eta_{HH}$ region is consistently overestimated, but, systematic uncertainties are defined via the difference between VR and CR estimates.	179
424	7.71 Non-resonant Search (3b1l): Demonstration of the performance of the nominal reweighting in the validation region on m_{HH} , split into the two $\Delta\eta_{HH}$ regions. A deficit is present near 600 GeV, but agreement is fairly good otherwise.	180
427	7.72 Non-resonant Search (4b): Signal region agreement of the background estimate and observed data after a background-only profile likelihood fit for the 4b channels, with Standard Model and $\kappa_\lambda = 6$ signal overlaid for reference. Modeling is generally quite good near the Standard Model peak, but disagreements are seen at very low and high masses. A deficit is present in low $\Delta\eta_{HH}$ bins near 600 GeV.	181

433	7.73 Non-resonant Search (3b1l): Signal region agreement of the background estimate and observed data after a background-only profile likelihood fit for the 3b1l channels, with Standard Model and $\kappa_\lambda = 6$ signal overlaid for reference. Conclusions are very similar to the 4b channels, with generally good modeling near the Standard Model peak, but disagreements at very low and high masses. A deficit is present near 600 GeV.	182
439	7.74 Expected (dashed black) and observed (solid black) 95% CL upper limits on the cross-section times branching ratio of resonant production for spin-0 ($X \rightarrow HH$) and spin-2 $G_{KK}^* \rightarrow HH$. The $\pm 1\sigma$ and $\pm 2\sigma$ ranges for the expected limits are shown in the colored bands. The resolved channel expected limit is shown in dashed pink and covers the range from 251 and 1500 GeV. It is combined with the boosted channel (dashed blue) between 900 and 1500 GeV. The theoretical prediction for the bulk RS model with $k/\bar{M}_{\text{Pl}} = 1$ [23] (solid red line) is shown, with the decrease below 350 GeV due to a sharp reduction in the $G_{KK}^* \rightarrow HH$ branching ratio. The nominal $H \rightarrow b\bar{b}$ branching ratio is taken as 0.582.	186
449	7.75 Expected (dashed black) and observed (solid black) 95% CL upper limits on the cross-section times branching ratio of non-resonant production for a range of values of the Higgs self-coupling, with the Standard Model value ($\kappa_\lambda = 1$) illustrated with a star. The $\pm 1\sigma$ and $\pm 2\sigma$ ranges for the expected limits are shown in the colored bands. The cross section limit for HH production is set at 140 fb (180 fb) observed (expected), corresponding to an observed (expected) limit of 4.4 (5.9) times the Standard Model prediction. κ_λ is constrained to be within the range $-4.9 \leq \kappa_\lambda \leq 14.4$ observed ($-3.9 \leq \kappa_\lambda \leq 10.9$ expected). The nominal $H \rightarrow b\bar{b}$ branching ratio is taken as 0.582. We note that the excess present for $\kappa_\lambda \geq 5$ is thought to be due to a low mass background mis-modeling, present due to the optimization of this analysis for the Standard Model point, and is not present in more sensitive channels in this same region (e.g. $HH \rightarrow bb\gamma\gamma$).	187
462	7.76 Comparison of the limits in Figure 7.75 with an equivalent set of limits that drop the m_{HH} bins below 381 GeV, with the value of 381 GeV determined by the optimized variable width binning. The expected limit band with this mass cut is shown in dashed blue, and the observed is shown in solid blue. The excess at and above $\kappa_\lambda = 5$ is significantly reduced, demonstrating that this is driven by low mass. Notably, there is minimal impact on the expected sensitivity with this m_{HH} cut.	188

469	8.1 Comparison of distributions of $HH p_T$ in the 2018 resonant validation region before reweighting for BDT pairing (left) and pairAGraph (right). $HH p_T$ is a variable with a large difference between $2b$ and $4b$, but the relative shapes seem to be more similar for pairAGraph than for BDT paring, corresponding to the hypothesis that pairAGraph chooses more “ $4b$ -like” jets.	194
470		
471		
472		
473		
474	8.2 Comparison of distributions of $HH p_T$ in the 2018 resonant validation region after reweighting for BDT pairing (left) and pairAGraph (right). $HH p_T$ is a variable with a large difference between $2b$ and $4b$, and the reweighted agreement in the high p_T tail is significantly improved with pairAGraph, with a corresponding reduction in the assigned bootstrap uncertainty in that region.	195
475		
476		
477		
478		
479	8.3 Gaussian process sampling prediction of marginals m_{H1} and m_{H2} for $2b$ signal region events compared to real $2b$ signal region events for the 2018 dataset. Good agreement is seen. Only a small fraction (0.01) of the $2b$ dataset is used for both training and this final comparison to mimic $4b$ statistics.	202
480		
481		
482		
483	8.4 Gaussian process sampling prediction for the mass plane compared to the real $2b$ dataset for 2018. Only a small fraction (0.01) of the $2b$ dataset is used for both training and this final comparison to mimic $4b$ statistics. Good agreement is seen.	204
484		
485		
486		
487	8.5 Gaussian process sampling prediction of marginals m_{H1} and m_{H2} for $4b$ signal region events compared to both control and validation reweighting predictions. While there are some differences, the estimates are compatible.	205
488		
489		
490	8.6 Gaussian process sampling prediction for the $4b$ mass plane compared to the reweighted $2b$ estimate in the signal region. Both estimates are compatible. .	206
491		
492	8.7 Comparison of the interpolation background estimate with real $2b$ data in the signal region. Only 1 % of $2b$ data is used in order to mimic $4b$ statistics, and results are presented here summed across years. The “Flow Only” prediction uses samples of actual $2b$ signal region data for the input values of m_{H1} and m_{H2} , whereas the “Flow + GP” prediction uses samples following the Gaussian process procedure above, more closely mimicking a the full background estima- tion procedure. The two predictions are quite comparable, demonstrating the closure of the Gaussian process estimate, and the predicted m_{HH} shape agrees well with $2b$ data. Only $2b$ statistical uncertainty is shown.	207
493		
494		
495		
496		
497		
498		
499		
500		
501	8.8 Comparison of the interpolation background estimate in the $4b$ signal region with the control region derived reweighted $2b$ estimate, shown for each year individually. Results are generally similar, within around 10 %.	208
502		
503		

GLOSSARY

505 ARGUMENT: replacement text which customizes a L^AT_EX macro for each particular usage.

ACKNOWLEDGMENTS

507 Five years is both a short time and a long time – many things have happened and many
508 have stayed the same. I certainly know much more physics than I did at the outset, but also
509 have learned to ski, discovered a love for hiking, eaten large amounts of cheese, and survived
510 a pandemic by making sourdough and cinnamon rolls. Of course, the most important part of
511 any journey is the friends we made along the way – the utmost gratitude and appreciation
512 goes to the Seattle friends, for the many nights both hard at work and at College Inn, to
513 the CERN friends, for adventures around Europe and days by the lake, the Chicago friends,
514 for my position as European correspondent for the Dum Dum Donut Intellectuals, and the
515 friends from home, for New Years Eve parties and visits in between. Though we’re scattered
516 across the world, I hope to see you all soon.

517 A thank you, of course, to my family for their continued and constant support, for trying
518 their best to learn physics along with me, and going along on this Ph.D. adventure every
519 step of the way.

520 I am only writing this thesis because of the incredible support of my research group, so a
521 massive thank you to Anna, for your guidance and compassion, for advising me as both a
522 physicist and a person, and for always being available, and Jana, for shaping who I am as a
523 physicist and providing feedback on almost literally every talk that I’ve written – I knew I
524 was getting ready to graduate when you started running out of comments.

525 A special set of thank yous to the SLAC group, namely Nicole, Michael, and Rafael, for
526 being an excellent set of collaborators with an excellent set of ideas to push the analysis
527 forward, many of which are in this thesis, and for being my second research family.

528 And last but not least, a thank you to the entire $HH \rightarrow 4b$ group, of course to Max

529 and Rafael for their guidance and direction, Bejan for being an excellent collaborator and
530 co-editor for the resonant search, Dale and Alex for excelling on the boosted side of things,
531 Lucas, for great work on triggers and for diving headfirst into all of my code, the ggF push
532 squad, for a huge amount of hard work on the non-resonant, and of course the $HH \rightarrow 4\text{beers}$
533 team, many of whom have already been mentioned, but who deserve an extra shout out for
534 keeping things fun even during stressful times.

535 The physics is done, the rest is paperwork. Let us begin.

PREFACE

537 This thesis focuses primarily on searches for pair production of Higgs bosons in the $b\bar{b}b\bar{b}$
538 final state. In Chapter 1, I provide an overview of the Standard Model of particle physics,
539 with discussion of the theoretical and experimental development of such a model. Chapter
540 2 dives more into the details of Higgs boson pair production, as well as the physics beyond
541 the Standard Model relevant for this thesis. Chapter 3 then provides an introduction to the
542 experimental apparatus used for the presented searches, with an outline of the Large Hadron
543 Collider and the ATLAS detector.

544 Chapter 4 details the procedure to simulate the physics processes discussed in Chapters 1
545 and 2, including simulation of the detector discussed Chapter 3. A review of the procedures
546 to reconstruct objects used for physics analysis is provided in Chapter 5, with a focus on jets
547 and flavor-tagging. To conclude the introductory material of the thesis, a discussion of the
548 general procedures behind a physics search at the LHC is provided in Chapter 6.

549 While this thesis provides a review of the necessary background information, it also presents
550 a significant body of original research. Chapter 4 includes my work on the development
551 of methods to improve the modeling of hadronic showers within a parametrized simulation
552 of the ATLAS calorimeter. I entirely developed both the method and the software for the
553 Gaussian method discussed in Chapter 4, including all of the validations presented there.
554 The development of the Variational Autoencoder method was done in conjunction with Dalila
555 Salamani, but also contains significant contribution from me.

556 The content presented in Chapters 7 and 8 is almost entirely original research. Chapter 7
557 details searches for resonant and non-resonant pair production of Higgs bosons in the $b\bar{b}b\bar{b}$ final
558 state. I was one of the main analyzers for both of these searches, but my dominant contribution

559 was the development of the background estimation procedure and the associated uncertainties,
560 which I spearheaded both conceptually and practically. This is quite a significant contribution
561 for both the resonant and non-resonant – to paraphrase Georges Aad during the resonant
562 review process, “This is the analysis.”

563 This was not my only contribution – for the resonant search, I contributed to the
564 development of the analysis selection and limit setting, as well as many many cross checks,
565 and was the co-editor of the ATLAS internal documentation, along with Bejan Stanislaus,
566 who developed the BDT pairing and much of the analysis software. Credit goes as well to
567 Lucas Borgna, for much of the work behind the development of the trigger strategy.

568 The resonant search follows many of the procedures of the early Run 2 analysis [1],
569 with the pairing method and background estimation method constituting the two biggest
570 analysis-level differences from that work. However, the non-resonant analysis has several
571 additional changes, including various kinematic variable and region definitions and a different
572 pairing method than both the early Run 2 search and the resonant search. I was responsible
573 for a large majority of the studies behind each of these decisions, literally improving the
574 Standard Model sensitivity by a factor of three relative to the resonant analysis strategy
575 baseline. I am also responsible for the development of much of the modern $4b$ software
576 infrastructure, including, of course, the background estimation framework, a new limit setting
577 framework, and a new centralized plotting framework, the latter of which greatly facilitates
578 both studies and documentation for the more complicated non-resonant analysis strategy.

579 Chapter 8 is also entirely original research, done in collaboration primarily with Nicole
580 Hartman, presenting two novel methods for the future of the $4b$ channel. While these
581 represent promising directions for the $4b$ analysis, they are also methodologically interesting,
582 and conceptually related results were published concurrently with the development of the
583 work presented in this thesis in [2] and [3].

584

DEDICATION

585

To family, both given and found

586

Chapter 1

587

THE STANDARD MODEL OF PARTICLE PHYSICS

588

The Standard Model of Particle Physics (SM) is a monumental historical achievement, providing a formalism with which one may describe everything from the physics of everyday experience to the physics that is studied at very high energies at the Large Hadron Collider (Chapter 3). In this chapter, we will provide a brief overview of the pieces that go into the construction of such a model. The primary focus of this thesis is searches for pair production of Higgs bosons decaying to four b -quarks. Consequently, we will pay particular attention to the relevant pieces of the Higgs Mechanism, as well as the theory behind searches at a hadronic collider.

596

1.1 *Introduction: Particles and Fields*

597

What is a particle? The Standard Model describes a set of fundamental, point-like, objects shown in Figure 1.1. These objects have distinguishing characteristics (e.g., mass and spin). These objects interact in very specific ways. The set of objects and their interactions result in a set of observable effects, and these effects are the basis of a field of experimental physics.

601

The effects of these objects and their interactions are familiar as fundamental forces: electromagnetism (photons, electrons), the strong interaction (quarks, gluons), the weak interaction (neutrinos, W and Z bosons). Gravity is not described in this model, as the weakest, with effects most relevant on much larger distance scales than the rest. However, the description of these other three is powerful – verifying and searching for cracks in this description is a large effort, and the topic of this thesis.

607

The formalism for describing these particles and their interactions is that of quantum field theory. Classical field theory is most familiar in the context of, e.g., electromagnetism – an

609 electric field exists in some region of space, and a charged point-particle experiences a force
610 characterized by the charge of the point-particle and the magnitude of the field at the location
611 of the point-particle in spacetime. The same language translates to quantum field theory.
612 Here, particles are described in terms of quantum fields in some region of spacetime. These
613 fields have associated charges which describe the forces they experience when interacting
614 with other quantum fields. Most familiar is electric charge – however this applies to e.g., the
615 strong interaction as well, where quantum fields have an associated *color charge* describing
616 behavior under the strong force.

617 Particles are observed to behave in different ways under different forces. These behaviors
618 respect certain *symmetries*, which are most naturally described in the language of group
619 theory. The respective fields, charges, and generators of these symmetry groups are the basic
620 pieces of the SM Lagrangian, which describes the full dynamics of the theory. In the following,
621 we will build up the basic components of this Lagrangian. The treatment presented here relies
622 heavily on Jackson's Classical Electrodynamics [5] for the build-up, and Thomson's Modern
623 Particle Physics [6] for the rest, with reference to Srednicki's Quantum Field Theory [7], and
624 some personal biases and interjections.

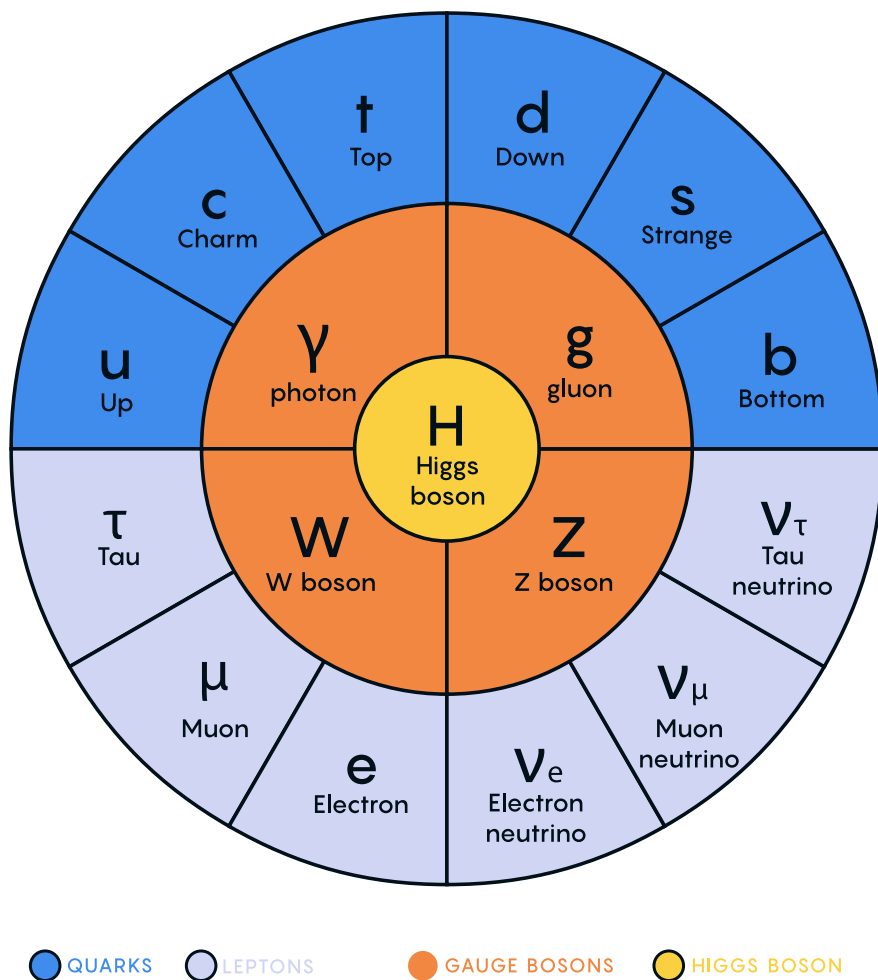


Figure 1.1: Diagram of the elementary particles described by the Standard Model [4].

625 **1.2 Quantum Electrodynamics**

Classical electrodynamics is familiar to the general physics audience: electric (\vec{E}) and magnetic (\vec{B}) fields are used to describe behavior of particles with charge q moving with velocity \vec{v} , with forces described as $\vec{F} = q\vec{E} + q\vec{v} \times \vec{B}$. Hints at some more fundamental properties of electric and magnetic fields come via a simple thought experiment: in a frame of reference moving along with the particle at velocity \vec{v} , the particle would appear to be standing still, and therefore have no magnetic force exerted. Therefore a *relativistic* formulation of the theory is required. This is most easily accomplished with a repackaging: the fundamental objects are no longer classical fields but the electric and magnetic *potentials*: ϕ and \vec{A} respectively, with

$$\vec{E} = -\nabla\phi - \frac{\partial\vec{A}}{\partial t} \quad (1.1)$$

$$\vec{B} = \nabla \times \vec{A} \quad (1.2)$$

It is then natural to fully repackage into a relativistic *four-vector*: $A^\mu = (\phi, \vec{A})$. Considering $\partial^\mu = (\frac{\partial}{\partial t}, \nabla)$, the x components of these above two equations become:

$$E_x = -\frac{\partial\phi}{\partial x} - \frac{\partial A_x}{\partial t} = -(\partial^0 A^1 - \partial^1 A^0) \quad (1.3)$$

$$B_x = \frac{\partial A_z}{\partial y} - \frac{\partial A_y}{\partial z} = -(\partial^2 A^3 - \partial^3 A^2) \quad (1.4)$$

626 where we have used the sign convention $(+, -, -, -)$, such that $\partial^\mu = (\frac{\partial}{\partial x_0}, -\nabla)$.

This is naturally suggestive of a second rank, antisymmetric tensor to describe both the electric and magnetic fields (the *field strength tensor*), defined as:

$$F^{\alpha\beta} = \partial^\alpha A^\beta - \partial^\beta A^\alpha \quad (1.5)$$

Defining a four-current as $J_\mu = (q, \vec{J})$, with q standard electric charge, \vec{J} standard electric current, conservation of charge may be expressed via the continuity equation

$$\partial_\mu J^\mu = 0 \quad (1.6)$$

and all of classical electromagnetism may be packaged into the Lagrangian density:

$$\mathcal{L} = -\frac{1}{4} F_{\mu\nu} F^{\mu\nu} - J^\mu A_\mu. \quad (1.7)$$

627 This gets us partway to our goal, but is entirely classical - the description is of classical
 628 fields and point charges, not of quantum fields and particles. To reframe this, let us go back
 629 to the zoomed out view of the particles of the Standard Model. Two of the most familiar
 630 objects associated with electromagnetism are electrons: spin-1/2 particles with charge e , mass
 631 m , and photons: massless spin-1 particles which are the "pieces" of electromagnetic radiation.

632 We know that electrons experience electromagnetic interactions with other objects. Given
 633 this, and the fact that such interactions must be transmitted *somewhat* between e.g. two
 634 electrons, it seems natural that these interactions are facilitated by electromagnetic radiation.
 635 More specifically, we may think of photons as *mediators* of the electromagnetic force. It
 636 follows, then, that a description of electromagnetism on the level of particles must involve a
 637 description of both the "source" particles (e.g. electrons), the mediators (photons), and their
 638 interactions. Further, this description must be (1) relativistic and (2) consistent with the
 639 classically derived dynamics described above.

The beginnings of a relativistic description of spin-1/2 particles is due to Paul Dirac, with the famous Dirac equation:

$$(i\gamma^\mu \partial_\mu - m)\psi = 0 \quad (1.8)$$

where ∂_μ is as defined above, ψ is a Dirac *spinor*, i.e. a four-component wavefunction, m is the mass of the particle, and γ^μ are the Dirac gamma matrices, which define the algebraic structure of the theory. For the following, we also define a conjugate spinor,

$$\bar{\psi} = \psi^\dagger \gamma^0 \quad (1.9)$$

which satisfies the conjugate Dirac equation

$$\bar{\psi}(i\gamma^\mu \partial_\mu - m) = 0 \quad (1.10)$$

640 where the derivative acts to the left.

The Dirac equation is the dynamical equation for spin-1/2, but we'd like to express these dynamics via a Lagrangian density. Further, to have a relativistic description, we'd like to

have this be density be Lorentz invariant. These constraints lead to a Lagrangian of the form

$$\mathcal{L} = \bar{\psi}(i\gamma^\mu \partial_\mu - m)\psi \quad (1.11)$$

641 where the Euler-Lagrange equation exactly recovers the Dirac equation.

The question now becomes how to marry the two Lagrangian descriptions that we have developed. Returning for a moment to classical electrodynamics, we know that the Hamiltonian for a charged particle in an electromagnetic field is described by

$$H = \frac{1}{2m}(\vec{p} - q\vec{A})^2 + q\phi. \quad (1.12)$$

Comparing this to the Hamiltonian for a free particle, we see that the modifications required are $\vec{p} \rightarrow \vec{p} - q\vec{A}$ and $E \rightarrow E - q\phi$. Using the canonical quantization trick of identifying \vec{p} with operator $-i\nabla$ and E with operator $i\frac{\partial}{\partial t}$, this identification becomes

$$i\partial_\mu \rightarrow i\partial_\mu - qA_\mu \quad (1.13)$$

Allowing for the naive substitution in the Dirac Lagrangian:

$$\mathcal{L} = \bar{\psi}(i\gamma^\mu(\partial_\mu + iqA_\mu) - m)\psi - \frac{1}{4}F_{\mu\nu}F^{\mu\nu}. \quad (1.14)$$

642 where the source term may be interpreted as coming from the Dirac fields themselves, namely,

643 $-q\bar{\psi}\gamma^\mu\psi A_\mu$.

Setting $q = e$ here (as appropriate for the case of an electron), and defining $D_\mu \equiv \partial_\mu + ieA_\mu$, this may then be written in the form

$$\mathcal{L} = \bar{\psi}(i\gamma^\mu D_\mu - m)\psi - \frac{1}{4}F_{\mu\nu}F^{\mu\nu}. \quad (1.15)$$

644 which is exactly the quantum electrodynamics Lagrangian.

645 We have swept a few things under the rug here, however. Recall that the general form
646 of a Lagrangian is conventionally $\mathcal{L} = T - V$, where T is the kinetic term, and thus ought
647 to contain a derivative with respect to time (c.f. the standard $\frac{1}{2}m\frac{\partial x}{\partial t}$ familiar from basic
648 kinematics). More particularly, given the definition of conjugate momentum as $\partial\mathcal{L}/\partial\dot{q}$ for

649 $\mathcal{L}(q, \dot{q}, t)$ and $\dot{q} = \frac{\partial q}{\partial t}$, any field q which has no time derivative in the Lagrangian has 0
650 conjugate momentum, and thus no dynamics.

651 Looking at this final form, there is an easily identifiable kinetic term for the spinor fields
652 (just applying the D_μ operator). However trying to identify something similar for the A fields,
653 one comes up short – the antisymmetric nature of $F^{\mu\nu}$ term means that there is no time
654 derivative applied to A^0 .

655 What does this mean? A^μ is a four component object, but it would appear that only three
656 of the components have dynamics: we have too many degrees of freedom in the theory. This
657 is the principle behind *gauge symmetry* – an extra constraint on A^μ (a *gauge condition*) must
658 be defined such that a unique A^μ defines the theory and satisfies the condition. However,
659 we are free to choose this extra condition – the physics content of the theory should be
660 independent of this choice (that is, it should be *gauge invariant*).

To ground this a bit, let us return to basic electric and magnetic fields. These are physical quantities that can be measured, and are defined in terms of potentials as

$$\vec{E} = -\nabla\phi - \frac{\partial\vec{A}}{\partial t} \quad (1.16)$$

$$\vec{B} = \nabla \times \vec{A}. \quad (1.17)$$

661 It is easy to show, for any scalar function λ , that $\nabla \times \nabla\lambda = 0$. This implies that the physical
662 \vec{B} field is invariant under the transformation $\vec{A} \rightarrow \vec{A} + \nabla\lambda$ for any scalar function λ .

663 Under the same transformation of \vec{A} , the electric field \vec{E} becomes $-\nabla\phi - \frac{\partial\vec{A}}{\partial t} - \frac{\partial\nabla\lambda}{\partial t} =$
664 $-\nabla(\phi + \frac{\partial\lambda}{\partial t}) - \frac{\partial\vec{A}}{\partial t}$, such that, for the \vec{E} field to be unchanged, we must additionally apply
665 the transformation $\phi \rightarrow \phi - \frac{\partial\lambda}{\partial t}$.

This set of transformations to the potentials that leave the physical degrees of freedom invariant is expressed in our four vector notation naturally as

$$A_\mu \rightarrow A_\mu - \partial_\mu \lambda \quad (1.18)$$

666 where $A_\mu = (\phi, -\vec{A})$ with our sign convention. It should be noted that this function λ is an
667 arbitrary function of *local* spacetime, and thus expresses invariance of the physics content

668 under a local transformation.

Let us return to the Lagrangian for QED. In particular, focusing on the free Dirac piece

$$\mathcal{L} = \bar{\psi}(i\gamma^\mu \partial_\mu - m)\psi \quad (1.19)$$

we note that if we apply a local transformation of the form $\psi \rightarrow e^{iq\lambda(x)}\psi$ (and correspondingly $\bar{\psi} \rightarrow \bar{\psi}e^{-iq\lambda(x)}$, by definition), the Lagrangian becomes

$$\bar{\psi}e^{-iq\lambda(x)}(i\gamma^\mu \partial_\mu - m)e^{iq\lambda(x)}\psi = \bar{\psi}e^{-iq\lambda(x)}(i\gamma^\mu \partial_\mu)e^{iq\lambda(x)}\psi - m\bar{\psi}\psi. \quad (1.20)$$

As $\partial_\mu(e^{iq\lambda(x)}\psi) = iq e^{iq\lambda(x)}(\partial_\mu \lambda(x))\psi + e^{iq\lambda(x)}\partial_\mu \psi$, this becomes

$$\bar{\psi}(i\gamma^\mu(\partial_\mu + iq\partial_\mu \lambda(x)) - m)\psi. \quad (1.21)$$

Thus, the free Dirac Lagrangian on its own is not invariant under this transformation. We may note, however, that on interaction with an electromagnetic field, as described above, this transformed Lagrangian may be packaged as:

$$\bar{\psi}(i\gamma^\mu(\partial_\mu + iq\partial_\mu \lambda(x) + iqA_\mu) - m)\psi = \bar{\psi}(i\gamma^\mu(\partial_\mu + iq(A_\mu + \partial_\mu \lambda(x))) - m)\psi. \quad (1.22)$$

669 since by the arguments above, the physics content of the Lagrangian is invariant under the
670 transformation $A_\mu \rightarrow A_\mu - \partial_\mu \lambda$, we may directly make this transformation, and remove this
671 extra $\partial_\mu \lambda(x)$ term. It is straightforward to verify that the $\frac{1}{4}F_{\mu\nu}F^{\mu\nu}$ term is invariant under
672 this same transformation of A_μ , so we may say that the QED Lagrangian is invariant under
673 local transformations of the form $\psi \rightarrow e^{iq\lambda(x)}\psi$.

674 These arguments illuminate some important concepts which will serve us well going forward.
675 First, while we have remained grounded in the “familiar” physics of electromagnetism for the
676 above, arguments of the “top down” variety would lead us to the exact same conclusions.
677 That is, suppose we wanted to construct a theory of spin-1/2 particles that was invariant
678 under local transformations of the form $\psi \rightarrow e^{iq\lambda(x)}\psi$. More broadly, we could say that we
679 desire this theory to be invariant under local $U(1)$ transformations, where $U(1)$ is exactly
680 this group, under multiplication, of complex numbers with absolute value 1. By very similar

681 arguments as above, we would see that, to achieve invariance, this theory would necessitate
682 an additional degree of freedom, A_μ , with the exact properties that are familiar to us from
683 electrodynamics. These arguments based on symmetries are extremely powerful in building
684 theories with a less familiar grounding, as we will see in the following.

Second, we defined this quantity $D_\mu \equiv \partial_\mu + ieA_\mu$ above, seemingly as a matter of notational convenience. However, from the latter set of arguments, such a packaging takes on a new power: by explicitly including this gauge field A_μ which transforms in such a way as to keep invariance under a given transformation, the invariance is immediately more manifest. That is, to pose the $U(1)$ invariance in a more zoomed out way, under the transformation $\psi \rightarrow e^{iq\lambda(x)}\psi$, while

$$\bar{\psi}\partial_\mu\psi \rightarrow \bar{\psi}(\partial_\mu + iq\partial_\mu\lambda(x))\psi \quad (1.23)$$

with the extra term that gets canceled out by the gauge transformation of A_μ ,

$$\bar{\psi}D_\mu\psi \rightarrow \bar{\psi}D_\mu\psi \quad (1.24)$$

685 where this transformation is already folded in. This repackaging, called a *gauge covariant*
686 *derivative* is much more immediately expressive of the symmetries of the theory.

687 Finally, to emphasize how fundamental these gauge symmetries are to the corresponding
688 theory, let us examine the additional term needed for $U(1)$ invariance, $q\bar{\psi}\gamma^\mu A_\mu\psi$. While a
689 first principles examination of Feynman rules is beyond the scope of this thesis, it is powerful
690 to note that this is expressive of a QED vertex: the $U(1)$ invariance of the theory and the
691 interaction between photons and electrons are inextricably tied together.

692 1.3 An Aside on Group Theory

693 Quantum electrodynamics is very familiar and well covered, and provides (both historically
694 and in this thesis) a nice bridge between “standard” physics and the language of symmetries
695 and quantum field theory. However, now that we are acquainted with the language, we
696 may set up to dive a bit deeper. To begin, let us look again at the $U(1)$ group that is so
697 fundamental to QED. We have expressed this via a set of transformations on our Dirac spinor

698 objects, ψ , of the form $e^{iq\lambda(x)}$. Note that such transformations, though they are local (i.e. a
 699 function of spacetime) are purely *phase* transformations. Relatedly, $U(1)$ is an Abelian group,
 700 meaning that group elements commute.

701 To set up language to generalize beyond $U(1)$, note that we may equivalently write $U(1)$
 702 elements as $e^{ig\vec{\alpha}(x)\cdot\vec{T}}$, $\vec{\alpha}(x)$ and \vec{T} and are vectors in the space of *generators* of the group,
 703 with each $\alpha^a(x)$ an associated scalar function to generator t^a , and g is some scalar strength
 704 parameter. Of course this is a bit silly for $U(1)$, which has a single generator, and thus
 705 reduces to the transformation we discussed above. However, this becomes much more useful
 706 for groups of higher degree, with more generators and degrees of freedom.

707 To discuss these groups in a bit more detail, note that $U(n)$ is the unitary group of degree
 708 n , and corresponds to the group of $n \times n$ unitary matrices (that is, $U^\dagger U = UU^\dagger = 1$). Given
 709 that group elements are $n \times n$, this means that there are n^2 degrees of freedom: n^2 generators
 710 are needed to characterize the group.

711 For $U(1)$, this is all consistent with what we have said above – the group of 1×1 unitary
 712 matrices have a single generator, and the phases we identify above clearly satisfy unitarity.
 713 Note that these degrees of freedom for the gauge group also characterize the number of gauge
 714 bosons we need to satisfy the local symmetry: for $U(1)$, we need one gauge boson, the photon.

715 Of relevance for the Standard Model are also the special unitary groups $SU(n)$. These
 716 are defined similarly to the unitary groups, with the additional requirement that group
 717 elements have determinant 1. This extra constraint removes 1 degree of freedom: groups are
 718 characterized by $n^2 - 1$ generators.

719 In particular, we will examine the groups $SU(2)$ in the context of the weak interaction,
 720 with an associated $2^2 - 1 = 3$ gauge bosons (cf. the W^\pm and Z bosons), and $SU(3)$, with an
 721 associated $3^2 - 1 = 8$ gauge bosons (cf. gluons of different flavors). Note that these groups
 722 are non-Abelian (2×2 or 3×3 matrices do not, in general, commute), leading to a variety of
 723 complications. However, both of these theories feature interactions with spin-1/2 particles,
 724 with transformations of a very similar form: $\psi \rightarrow e^{ig\vec{\alpha}(x)\cdot\vec{T}}\psi$, and the general framing of the
 725 arguments for QED will serve us well in the following.

726 **1.4 Quantum Chromodynamics**

727 In some sense, the simplest extension the development of QED is quantum chromodynamics
728 (QCD). QCD is a theory in which, once the basic dynamics are framed (a non-trivial task!)
729 the group structure becomes apparent. The quark model, developed by Murray Gell-Mann [8]
730 and George Zweig [9], provided the fundamental particles involved in the theory, and had
731 great success in explaining the expanding zoo of experimentally observed hadronic states.

732 Some puzzles were still apparent – the Δ^{++} baryon, e.g., is composed of three up quarks,
733 u , with aligned spins. As quarks are fermions, such a state should not be allowed by the
734 Pauli exclusion principle. The existence of such a state in nature implies the existence
735 of another quantum number, and a triplet of values, called *color charge* was proposed by
736 Oscar Greenberg [10]. With these pieces in place, the structure becomes more apparent, as
737 elucidated by Han and Nambu [11].

738 Let us reason our way to the symmetries using color charge. Experimentally, we know
739 that there is this triplet of color charge values r, g, b (the “plus” values, cf. electric charge)
740 and correspondingly anti-color charge $\bar{r}, \bar{g}, \bar{b}$ (the “minus” values). Supposing that the force
741 behind QCD (the *strong force*) is, similar to QED, interactions between fermions mediated
742 by gauge bosons (quarks and gluons respectively), we can start to line up the pieces.

743 What color charge does a gluon have? Similarly to electric charge, we may associate
744 particles with color charge, anti-particles with anti-color charge. Notably, free particles
745 observed experimentally are colorless (have no color charge). Thus, in order for charge to
746 be conserved throughout such processes, this already implies that there are charged gluons.
747 Further, examining color flow diagrams such as *TODO: insert*, it is apparent first that a
748 gluon has not one but two associated color charges and second that these two must be one
749 color charge and one anti-color charge.

750 Counting up the available types of gluons, then, we come up with nine. Six of mixed
751 color type: $r\bar{b}, r\bar{g}, b\bar{r}, b\bar{g}, g\bar{b}$, and $g\bar{r}$, and three of same color type: $r\bar{r}, g\bar{g}$, and $b\bar{b}$. In practice,
752 however, these latter three are a bit redundant: all express a colorless gluon, which, if we

could observe this as a free particle, would be indistinguishable from each other. The *color singlet* state is then a mix of these, $\frac{1}{\sqrt{3}}(r\bar{r} + g\bar{g} + b\bar{b})$, leaving two unclaimed degrees of freedom, which may be satisfied by the linearly independent combinations $\frac{1}{\sqrt{2}}(r\bar{r} - g\bar{g})$ and $\frac{1}{\sqrt{6}}(r\bar{r} + g\bar{g} - 2b\bar{b})$.

We thus have an octet of color states plus a colorless singlet state. If this colorless singlet state existed, however, we would be able to observe it, not only via interactions with quarks, but as a free particle. Since do not observe this in nature, this restricts us to 8 gluons. The simplest group with a corresponding 8 generators is $SU(3)$. Under the assumption that $SU(3)$ is the local gauge symmetry of the strong interaction, we may proceed in a similar way as we did for QED. The gauge transformation is $\psi \rightarrow e^{ig_S \vec{\alpha}(x) \cdot \vec{T}} \psi$, where \vec{T} is an eight component vector of the generators of $SU(3)$, often expressed via the Gell-Mann matrices, λ^a , as $t^a = \frac{1}{2}\lambda^a$, and the spinor ψ represents the fields corresponding to quarks.

This $SU(3)$ symmetry exactly expresses the color structure elucidated above – the Gell-Mann matrices are an equivalent presentation of the color combinations described above. Proceeding by analogy to QED, gauge invariance is achieved by introducing eight new degrees of freedom, G_μ^a , which are the gauge fields corresponding to the gluons, with the gauge covariant derivative then analogously taking the form $D_\mu \equiv \partial_\mu + ig_S G_\mu^a t^a$.

Recall from the QED derivation that the field strength tensor, $F^{\mu\nu}$ is a rank two antisymmetric tensor which is manifestly gauge invariant and which describes the physical dynamics of the A_μ field. We would like to analogously define a term for the gluon fields. Repackaging this QED tensor, it is apparent that

$$[D_\mu, D_\nu] = D_\mu D_\nu - D_\nu D_\mu \quad (1.25)$$

$$= (\partial_\mu + iqA_\mu)(\partial_\nu + iqA_\nu) - (\partial_\nu + iqA_\nu)(\partial_\mu + iqA_\mu) \quad (1.26)$$

$$= \partial_\mu \partial_\nu + iq\partial_\mu A_\nu + iqA_\mu \partial_\nu + (iq)^2 A_\mu A_\nu - (\partial_\nu \partial_\mu + iq\partial_\nu A_\mu + iqA_\nu \partial_\mu + (iq)^2 A_\nu A_\mu) \quad (1.27)$$

$$= iq(\partial_\mu A_\nu - \partial_\nu A_\mu) + (iq)^2 (A_\mu A_\nu - A_\nu A_\mu) \quad (1.28)$$

$$= iq(\partial_\mu A_\nu - \partial_\nu A_\mu) + (iq)^2 [A_\mu, A_\nu]. \quad (1.29)$$

We proceed through this derivation to highlight that, in the specific case of QED, with its Abelian $U(1)$ gauge symmetry, the field commutator vanishes, leaving exactly the definition of $F_{\mu\nu}$ as described above, i.e.,

$$F_{\mu\nu} = \frac{1}{iq}[D_\mu, D_\nu]. \quad (1.30)$$

We may proceed to define an analogous field strength term for G_μ^a in a similar way:

$$G_{\mu\nu} = \frac{1}{ig_S}[D_\mu, D_\nu] \quad (1.31)$$

This has an extremely nice correspondence, but is complicated by the non-Abelian nature of $SU(3)$, with

$$G_{\mu\nu} = \partial_\mu(G_\nu^a t^a) - \partial_\nu(G_\mu^a t^a) + ig_s[G_\mu^a t^a, G_\nu^a t^a]. \quad (1.32)$$

in which the field commutator term is non-zero. In particular (since each term is summing over a , so we may relabel) as

$$[G_\mu^a t^a, G_\nu^b t^b] = [t^a, t^b]G_\mu^a G_\nu^b \quad (1.33)$$

and as $[t^a, t^b] = if^{abc}t^c$ for the Gell-Mann matrices, where f^{abc} are the structure constants of $SU(3)$, we have

$$G_{\mu\nu} = \partial_\mu(G_\nu^a t^a) - \partial_\nu(G_\mu^a t^a) - g_s f^{abc} t^c G_\mu^a G_\nu^b \quad (1.34)$$

$$= t^a(\partial_\mu G_\nu^a - \partial_\nu G_\mu^a - f^{bca} G_\mu^b G_\nu^c) \quad (1.35)$$

$$= t^a G_{\mu\nu}^a \quad (1.36)$$

⁷⁷⁰ for $G_{\mu\nu}^a = \partial_\mu G_\nu^a - \partial_\nu G_\mu^a - f^{abc} G_\mu^b G_\nu^c$.

⁷⁷¹ This gives the component of the field strength corresponding to a particular gauge field a ,
⁷⁷² where the first two terms have the familiar form of the QED field strength, while the last
⁷⁷³ term is new, and explicitly related to the group structure via the f^{abc} constants. In terms
⁷⁷⁴ of the physics content of the theory, this latter term gives rise to a gluon *self-interaction*, a
⁷⁷⁵ distinguishing feature of QCD.

⁷⁷⁶ Similarly as in QED, a Lorentz invariant combination of field strength tensors may be made
⁷⁷⁷ as $G_{\mu\nu} G^{\mu\nu}$. However, this is not manifestly gauge invariant. Under a gauge transformation

778 U , the covariant derivative behaves as $D^\mu \rightarrow UD^\mu U^{-1}$, corresponding to $G^{\mu\nu} \rightarrow UG^{\mu\nu}U^{-1}$.
779 The cyclic property of the trace thus ensures the gauge invariance of $\text{tr}(G_{\mu\nu}G^{\mu\nu})$, which we
780 will write as $G_{\mu\nu}^a G_a^{\mu\nu}$ with the implied sum over generators a .

Packaging up the theory, it is tempting to copy the form of the QED Lagrangian, with the identifications we have made above:

$$\mathcal{L} = \bar{\psi}(i\gamma^\mu D_\mu - m)\psi - \frac{1}{4}G_{\mu\nu}^a G_a^{\mu\nu}. \quad (1.37)$$

However this is not quite correct due to the $SU(3)$ nature of the theory. In terms of the physics, the Dirac fields ψ have associated color charge, which must interact appropriately with the G_μ fields. Mathematically, the generators t^a are 3×3 matrices, while the ψ are four component spinors. Adding a color index to the Dirac fields, i.e., ψ_i where i runs over the three color charges, and similarly indexing the generators t_{ij}^a , we may then express the $SU(3)$ gauge covariant derivative component-wise as

$$(D_\mu)_{ij} = \partial_\mu \delta_{ij} + ig_S G_\mu^a t_{ij}^a \quad (1.38)$$

781 where δ_{ij} is the Kronecker delta, as ∂_μ does not participate in the $SU(3)$ structure.

The Lagrangian then becomes

$$\mathcal{L} = \bar{\psi}_i(i(\gamma^\mu D_\mu)_{ij} - m\delta_{ij})\psi_j - \frac{1}{4}G_{\mu\nu}^a G_a^{\mu\nu}. \quad (1.39)$$

782 and we have constructed QCD.

783 1.5 The Weak Interaction

784 One of the first theories of the weak interaction was from Enrico Fermi [12], in an effort to
785 explain beta decay, a process in which an electron or positron is emitted from an atomic
786 nucleus, resulting in the conversion of a neutron to a proton or proton to a neutron respectively.
787 Fermi's hypothesis was of a direct interaction between four fermions. However, in the advent of
788 QED, it is natural to wonder if a theory based on mediator particles and gauge symmetries
789 applies to the weak force as well. The modern formulation of such a theory is due to Sheldon

790 Glashow, Steven Weinberg, and Abdus Salam [13], and is what we will describe in the
791 following.

792 Considering emission of an electron, Fermi's theory involves an initial state neutron that
793 transitions to a proton with the emission of an electron and a neutrino. This transition
794 gives a hint that something slightly more complicated is happening than in QED: there is an
795 apparent mixing between particle types.

796 Now, with the assumption there are mediators for such an interaction, we further know
797 from beta decay and charge conservation that there must be at least two such degrees of
798 freedom: e.g. one that decays to an electron and neutrino (W^-) and one that decays to a
799 positron and neutrino (W^+). From consideration of the process $e^+e^- \rightarrow W^+W^-$, it turns
800 out that with just these two degrees of freedom, the cross section for this process increases
801 without limit as a function of center-of-mass energy, ultimately violating unitarity (more
802 W^+W^- pairs come out than e^+e^- pairs go in). This is resolved with a third, neutral degree
803 of freedom, the Z boson, whose contribution interferes negatively, regulating this process.

804 This leads to three degrees of freedom for the gauge symmetry of the weak interactions, so
805 we thus need a theory which is locally invariant under transformations of a group with three
806 generators. The simplest such choice is $SU(2)$. We may follow a very similar prescription as
807 for QED and QCD: $SU(2)$ has three generators, which implies the existence of three gauge
808 bosons, call them W_μ^k . The gauge transformation may be expressed as $\psi \rightarrow e^{ig_W \vec{\alpha}(x) \cdot \vec{T}} \psi$, where
809 in this case the generators are for $SU(2)$, which may be written in terms of the familiar Pauli
810 matrices: $\vec{T} = \frac{1}{2}\vec{\sigma}$. The structure constants for $SU(2)$ are the antisymmetric Levi-Civita
811 tensor, so the corresponding gauge covariant derivative is $D_\mu \equiv \partial_\mu + ig_W W_\mu^k t^k$, and the field
812 strength tensor is $W_{\mu\nu}^k = \partial_\mu W_\nu^k - \partial_\nu W_\mu^k - \epsilon^{ijk} W_\mu^k W_\nu^k$.

The corresponding Lagrangian would thus be

$$\mathcal{L} = \bar{\psi}_i (i(\gamma^\mu D_\mu)_{ij} - m\delta_{ij}) \psi_j - \frac{1}{4} W_{\mu\nu}^k W_k^{\mu\nu} \quad (1.40)$$

813 where indices i and j run over $SU(2)$ charges.

814 On considering some of the details, the universe unfortunately turns out to be a bit

more complicated. However, this still provides a useful starting place for elucidating the theory of weak interactions. First off, let us consider the particle content, namely, what do the Dirac fields correspond to? This is still a theory of fermionic interactions with gauge bosons. However, we might notice that the fermion content of this theory is both a) broader than QCD, as we know experimentally (cf. beta decay) that both quarks and leptons (e.g. electrons) participate in the weak interaction and b) this fermion content seemingly has a large overlap with QED. In terms of the gauge bosons, we know that at both W^+ and W^- are electrically charged – this means that we expect some interaction of the weak theory with electromagnetism.

However, before diving deeper into this apparent connection between the weak interaction and QED, let us focus on the gauge symmetry. In QCD, the $SU(3)$ content of the theory is expressed via a contraction of color indices – the theory allows for transitions between quarks of one color and quarks of another. Thinking similarly in terms of $SU(2)$ transitions, the beta decay example is already fruitful – there is a transition between an electron and its corresponding neutrino, as well as between two types of quark. In particular, for the case of neutron (with quark content udd) and proton (with quark content udu), the weak interaction provides for a transition from down to up quark.

Such $SU(2)$ dynamics are described via a quantity called *weak isospin*, denoted I_W with third component $I_W^{(3)}$, and can be thought of in a very similar way as color charge in QCD (i.e. as the charge corresponding to the weak interaction). Since $SU(2)$ is 2×2 , there are two such charge states for the fermions, denoted as $I_W^{(3)} = \pm\frac{1}{2}$. This means that the bosons must have $I_W = 1$ such that, by sign convention corresponding to electric charge, the W^+ boson has $I_W^{(3)} = +1$, the Z boson has $I_W^{(3)} = 0$, and the W^- boson has $I_W^{(3)} = -1$.

From conservation of electric charge, this means that transitions involving a W^\pm are between particles that differ by ± 1 in both weak isospin $I_W^{(3)}$ and electric charge. We may thus line up all such doublets as:

$$\begin{pmatrix} \nu_e \\ e^- \end{pmatrix}, \begin{pmatrix} \nu_\mu \\ \mu^- \end{pmatrix}, \begin{pmatrix} \nu_\tau \\ \tau^- \end{pmatrix}, \begin{pmatrix} u \\ d' \end{pmatrix}, \begin{pmatrix} c \\ s' \end{pmatrix}, \begin{pmatrix} t \\ b' \end{pmatrix} \quad (1.41)$$

838 with the top corresponding to the lower weak isospin and electric charge particles, and the
839 lower quark entries (d' , etc) corresponding to the weak quark eigenstates (which are related
840 to the mass eigenstates by the CKM matrix *TODO: more detail*). Similar doublets may be
841 constructed for the corresponding anti-particles.

The fundamental structuring of these transitions around both electric and weak charge is again indicative of a natural connection. However, nature is again a bit more complicated than we have described. This is because the weak interaction is a *chiral* theory. For massless particles, chirality is the same as the perhaps more intuitive *helicity*. This describes the relationship between a particle's spin and momentum: if the spin vector points in the same direction as the momentum vector, helicity is positive (the particle is “right-handed”), and if the two point in opposite directions, the helicity is negative (the particle is “left-handed”). More concretely:

$$H = \frac{\vec{s} \cdot \vec{p}}{|\vec{s} \cdot \vec{p}|}. \quad (1.42)$$

For massive particles, this generalizes a bit – in the language of Dirac fermions that we have developed, we define projection operators

$$P_R = \frac{1}{2}(1 + \gamma^5) \quad \text{and} \quad P_L = \frac{1}{2}(1 - \gamma^5) \quad (1.43)$$

842 for right and left-handed chiralities respectively – acting on a Dirac field with such operators
843 projects the field onto the corresponding chiral state.

Experimentally, this pops up via parity violation and the famous $V - A$ theory. For the scope of this thesis, it is sufficient to say that the weak interaction is only observed to take place for left-handed particles (and correspondingly, right-handed anti-particles). We therefore modify the theory stated above by projecting all fermions participating in the weak interaction onto respective chiral states – in particular, the $SU(2)$ gauge symmetry only acts on left-handed particles and right-handed anti-particles. We therefore modify the theory appropriately, denoting the chiral projected gauge symmetry as $SU(2)_L$, and similarly for the

Dirac fields. In particular, the weak isospin doublets listed above must now be left-handed:

$$\begin{pmatrix} \nu_e \\ e^- \end{pmatrix}_L, \begin{pmatrix} \nu_\mu \\ \mu^- \end{pmatrix}_L, \begin{pmatrix} \nu_\tau \\ \tau^- \end{pmatrix}_L, \begin{pmatrix} u \\ d' \end{pmatrix}_L, \begin{pmatrix} c \\ s' \end{pmatrix}_L, \begin{pmatrix} t \\ b' \end{pmatrix}_L \quad (1.44)$$

⁸⁴⁴ and right-handed particle states are placed in singlets and assigned 0 charge under $SU(2)_L$
⁸⁴⁵ ($I_W = I_W^{(3)} = 0$).

With all of these assignments, let us revisit our guess at the form of the weak interaction Lagrangian. First, dwelling on the kinetic term $\bar{\psi}_i(i(\gamma^\mu D_\mu)_{ij}\psi_j)$, we note that the assigning of left-handed fermions to isospin doublets and right-handed fermions to isospin singlets allows us to remove explicit $SU(2)$ indices by treating these as the fundamental objects, that is, for a single *generation* of fermions, we may write:

$$\bar{Q}i\gamma^\mu D_\mu Q + \bar{u}i\gamma^\mu D_\mu u + \bar{d}i\gamma^\mu D_\mu d + \bar{L}i\gamma^\mu D_\mu L + \bar{e}i\gamma^\mu D_\mu e \quad (1.45)$$

⁸⁴⁶ for left-handed doublets Q and L for quarks and electron fields respectively and right handed
⁸⁴⁷ singlets u and d for up and down quark fields and e for electrons.

More concisely, and summing over the three generations of fermions, we may write

$$\sum_f \bar{f}i\gamma^\mu D_\mu f \quad (1.46)$$

⁸⁴⁸ where the f are understood to run over the fermion chiral doublets and singlets as above.

This then leaves our Lagrangian as

$$\mathcal{L} = \sum_f \bar{f}i\gamma^\mu D_\mu f - \frac{1}{4}W_{\mu\nu}^k W_k^{\mu\nu} \quad (1.47)$$

$$= \sum_f \bar{f}\gamma^\mu(i\partial_\mu - \frac{1}{2}g_W W_\mu^k \sigma_k)f - \frac{1}{4}W_{\mu\nu}^k W_k^{\mu\nu}, \quad (1.48)$$

⁸⁴⁹ where we have expanded the covariant derivative for clarity. You may note that we have
⁸⁵⁰ dropped the mass term in the equation above – we will discuss this in detail in just a moment.

First, however, we return to the above comment about fermion content – we neglected to include the sum over fermions in our QED derivation for simplicity. However, all of the

fermions considered in the discussion of the weak interaction have an electric charge (except for the neutrinos). It would be nice to repackage the theory into a coherent *electroweak* theory. This is fairly straightforward when considering the gauge approach – from the discussion above we should expect the electroweak gauge group to be something like $SU(2) \times U(1)$, with four corresponding gauge bosons. Consider a gauge theory with group $SU(2)_L \times U(1)_Y$ – that is, the same weak interaction as discussed previously, but a new $U(1)_Y$ gauge group for electromagnetism, with transformations defined as

$$\psi \rightarrow e^{ig' \frac{Y}{2} \lambda(x)} \psi \quad (1.49)$$

851 with *weak hypercharge* Y .

Similarly to our discussion of QED, we may write the $U(1)_Y$ gauge field as B_μ , and interactions with the Dirac fields take the form $g' \frac{Y}{2} \gamma^\mu B_\mu \psi$. The relationship between this hypercharge and new B_μ field and classical electrodynamics is not so obvious – however it is convenient to parametrize as

$$\begin{pmatrix} A_\mu \\ Z_\mu \end{pmatrix} = \begin{pmatrix} \cos \theta_W & \sin \theta_W \\ -\sin \theta_W & \cos \theta_W \end{pmatrix} \begin{pmatrix} B_\mu \\ W_\mu^3 \end{pmatrix} \quad (1.50)$$

852 where A_μ and Z_μ are the physical fields, and we pick W_μ^3 as the neutral weak boson.

853 Note that in the $SU(2)_L \times U(1)_Y$ theory, the Lagrangian must be invariant under all of
854 the local gauge transformations. In particular, this means that the hypercharge must be the
855 same for fermion fields in each weak doublet to preserve $U(1)_Y$ invariance. This gives insight
856 into the relation between the charges of $SU(2)_L \times U(1)_Y$ and electric charge. In particular
857 we know that the hypercharge, Y , of e^- ($I_W^{(3)} = -\frac{1}{2}$) and ν_e ($I_W^{(3)} = +\frac{1}{2}$) is the same.

Supposing that $Y = \alpha I_W^{(3)} + \beta Q$, we must have $-\alpha \frac{1}{2} - \beta = \alpha \frac{1}{2} \implies \beta = -\alpha$. Therefore, choosing an overall scaling from convention,

$$Y = 2(Q - I_W^{(3)}). \quad (1.51)$$

858 Some of these particular forms are best understood in the context of the Higgs mechanism
859 – we will return to this discussion below.

860 **1.6 The Higgs Potential and the SM**

861 In the above, we have neglected a discussion of masses. However there are several things to
862 sort out here. In the first place, we know experimentally that the weak interactions occur
863 over very short ranges at low energies (e.g., why Fermi's effective four fermion interaction was
864 such a good description). This is consistent with massive W^\pm and Z bosons (and indeed, this
865 is seen experimentally). However, requiring local gauge invariance forbids mass terms in the
866 Lagrangian. In the simple $U(1)$ QED example, such a term would have the form $\frac{1}{2}m_\gamma^2 A_\mu A^\mu$,
867 which is not invariant under the transformation $A_\mu \rightarrow A_\mu - \partial_\mu \lambda$, and similar arguments hold
868 for gauge bosons in the electroweak theory and QCD.

Similar issues are encountered with fermions – in the electroweak theory above, the gauge symmetries are separated into left and right handed chirality via doublet and singlet states. This means that a mass term would need to be separated as well. Such a term would have the form:

$$m\bar{f}f = m(\bar{f}_L + \bar{f}_R)(f_L + f_R) \quad (1.52)$$

$$= m(\bar{f}_L f_L + \bar{f}_L f_R + \bar{f}_R f_L + \bar{f}_R f_R) \quad (1.53)$$

$$= m(\bar{f}_L f_R + \bar{f}_R f_L) \quad (1.54)$$

869 where we have used that $f_{L,R} = P_{L,R}f$, $\bar{f}_{L,R} = \bar{f}P_{R,L}$, and $P_R P_L = P_L P_R = 0$. As left
870 and right-handed particles transform differently under $SU(2)_L$, this is manifestly not gauge
871 invariant.

872 The question then becomes: how do we include particle masses while preserving the
873 gauge properties of our theory? The answer, due to Robert Brout and François Englert [14],
874 Peter Higgs [15], and Gerald Guralnik, Richard Hagen, and Tom Kibble [16] comes via the
875 Higgs mechanism, which we will describe in the following. Importantly for this thesis, this
876 mechanism predicts the existence of a physical particle, the Higgs boson, and a particle
877 consistent with the Higgs boson was seen by both ATLAS [17] and CMS [18] in 2012.

To explain the Higgs, we focus first on generating masses for the electroweak gauge bosons.

Consider adding two complex scalar fields ϕ^+ and ϕ^0 to the Standard Model embedded in a weak isospin doublet ϕ . We may write the doublet as

$$\phi = \begin{pmatrix} \phi^+ \\ \phi^0 \end{pmatrix} = \frac{1}{\sqrt{2}} \begin{pmatrix} \phi_1 + i\phi_2 \\ \phi_3 + i\phi_4 \end{pmatrix} \quad (1.55)$$

⁸⁷⁸ where we explicitly note the four available degrees of freedom.

The Lagrangian for such a doublet takes the form

$$\mathcal{L} = (\partial_\mu \phi)^\dagger (\partial^\mu \phi) - V(\phi) \quad (1.56)$$

where V is the corresponding potential. Considering the particular form

$$V(\phi) = \mu^2 \phi^\dagger \phi + \lambda (\phi^\dagger \phi)^2 \quad (1.57)$$

⁸⁷⁹ we may notice that this has some interesting properties. Considering, as illustration, a similar
⁸⁸⁰ potential for a real scalar field, $\mu^2 \chi^2 + \lambda \chi^4$, taking the derivative and setting it equal to 0
⁸⁸¹ yields extrema when $\chi = 0$ and $(\mu^2 + 2\lambda\chi^2) = 0 \implies \chi^2 = -\frac{\mu^2}{2\lambda}$. For $\mu^2 > 0$, there is a
⁸⁸² unique minimum at $\chi = 0$, and for $\mu^2 < 0$ there are degenerate minima at $\chi = \pm\sqrt{-\frac{\mu^2}{2\lambda}}$.
⁸⁸³ Note that we take $\lambda > 0$, otherwise the only minima in the theory are trivial.

The same simple calculus for the complex Higgs doublet above yields degenerate minima for $\mu^2 < 0$ at

$$\phi^\dagger \phi = \frac{1}{2}(\phi_1^2 + \phi_2^2 + \phi_3^2 + \phi_4^2) = \frac{v}{2} = -\frac{\mu^2}{2\lambda} \quad (1.58)$$

However, though there is this degenerate set of minima, there can only be a single *physical* vacuum state (we say that the symmetry is *spontaneously broken*). Without loss of generality, we may align our axes such that the physical vacuum state is at

$$\langle 0 | \phi | 0 \rangle = \frac{1}{\sqrt{2}} \begin{pmatrix} 0 \\ v \end{pmatrix} \quad (1.59)$$

⁸⁸⁴ where we have explicitly chosen a real, non-zero vacuum expectation value for the neutral
⁸⁸⁵ component of the Higgs doublet to maintain a massless photon, as we shall see. Physically,
⁸⁸⁶ however, this makes sense - the vacuum is not electrically charged.

The vacuum is a classical state – we want a quantum one. We may express fluctuations about this nonzero expectation value via an expansion as $v + \eta(x) + i\xi(x)$. However, renaming of fields is only meaningful for the non-zero vacuum component - we thus have:

$$\phi = \frac{1}{\sqrt{2}} \begin{pmatrix} \phi_1 + i\phi_2 \\ v + \eta(x) + i\phi_4 \end{pmatrix}. \quad (1.60)$$

where we may expand the Lagrangian listed above:

$$\mathcal{L} = (\partial_\mu \phi)^\dagger (\partial^\mu \phi) - \mu^2 \phi^\dagger \phi - \lambda(\phi^\dagger \phi)^2. \quad (1.61)$$

It is an exercise in algebra to plug in the expansion about v into this Lagrangian: first expanding the potential

$$V(\phi) = \mu^2 \phi^\dagger \phi + \lambda(\phi^\dagger \phi)^2 \quad (1.62)$$

$$= \mu^2 \left(\sum_i \phi_i(x)^2 + (v + \eta(x))^2 \right) + \lambda \left(\sum_i \phi_i(x)^2 + (v + \eta(x))^2 \right) \quad (1.63)$$

$$= -\frac{1}{4} \lambda v^4 + \lambda v^2 \eta^2 + \lambda v \eta^3 + \frac{1}{4} \lambda \eta^4 \quad (1.64)$$

$$+ \frac{1}{2} \lambda \sum_{i \neq j} \phi_i^2 \phi_j^2 + \lambda v \eta \sum_i \phi_i(x)^2 + \frac{1}{2} \lambda \eta^2 \sum_i \phi_i(x)^2 + \frac{1}{4} \sum_i \phi_i(x)^4 \quad (1.65)$$

where the sums are over the $i \in 1, 2, 4$, that is, the fields with 0 vacuum expectation, and we have used the definition $\mu^2 = -\lambda v^2$.

Within this potential, we note a quadratic term in $\eta(x)$ which we may identify with a mass, namely $m_\eta = \sqrt{2\lambda v^2}$, whereas the ϕ_i are massless. These ϕ_i are known as *Goldstone bosons*, and correspond to quantum fluctuations along the minimum of the potential. Of particular note for this thesis are the interaction terms $\lambda v \eta^3$ and $\frac{1}{4} \lambda \eta^4$, expressing trilinear and quartic self-interactions of the η field.

Expanding the kinetic term

$$(\partial_\mu \phi)^\dagger (\partial^\mu \phi) = \frac{1}{2} \sum_i (\partial_\mu \phi_i)(\partial^\mu \phi_i) + \frac{1}{2} (\partial_\mu(v + \eta(x)))(\partial^\mu(v + \eta(x))) \quad (1.66)$$

$$= \frac{1}{2} \sum_i (\partial_\mu \phi_i)(\partial^\mu \phi_i) + \frac{1}{2} (\partial_\mu \eta)(\partial^\mu \eta) \quad (1.67)$$

⁸⁹⁴ in a similar way, completing the story of three massless degrees of freedom (Goldstone bosons)
⁸⁹⁵ and one massive one.

Now, this doublet is embedded in an $SU(2)_L \times U(1)$ theory, so we would like to preserve that gauge invariance. This is achieved in the same way as for the Dirac fields, with the introduction of the electroweak gauge covariant derivative such that the Lagrangian for the Higgs doublet and the electroweak bosons is just

$$\mathcal{L} = (D_\mu \phi)^\dagger (D^\mu \phi) - \mu^2 \phi^\dagger \phi - \lambda (\phi^\dagger \phi)^2 - \frac{1}{4} W_{\mu\nu}^k W_k^{\mu\nu} - \frac{1}{4} F_{\mu\nu} F^{\mu\nu} \quad (1.68)$$

⁸⁹⁶ with $D_\mu = \partial_\mu + ig_W W_\mu^k t^k + ig' \frac{Y}{2} B_\mu$.

We note that it is convenient to pick a gauge such that the Goldstone fields do not appear in the Lagrangian, upon which we may identify the field $\eta(x)$ with the physical Higgs field, $h(x)$. The field mass terms then very apparently come via the covariant derivative, namely, as

$$W_\mu^k \sigma^k + B_\mu = \begin{pmatrix} W_\mu^3 + B_\mu & W_\mu^1 - iW_\mu^2 \\ W_\mu^1 + iW_\mu^2 & -W_\mu^3 + B_\mu \end{pmatrix} \quad (1.69)$$

we may then write

$$D_\mu \phi = \frac{1}{2\sqrt{2}} \begin{pmatrix} 2\partial_\mu + ig_W W_\mu^3 + ig' Y B_\mu & ig_W W_\mu^1 + \frac{1}{2} g_W W_\mu^2 \\ ig_W W_\mu^1 - g_W W_\mu^2 & 2\partial_\mu - ig_W W_\mu^3 + ig' Y B_\mu \end{pmatrix} \begin{pmatrix} 0 \\ v + h \end{pmatrix} \quad (1.70)$$

$$= \frac{1}{2\sqrt{2}} \begin{pmatrix} ig_W (W_\mu^1 - iW_\mu^2)(v + h) \\ (2\partial_\mu - ig_W W_\mu^3 + ig' Y B_\mu)(v + h) \end{pmatrix} \quad (1.71)$$

⁸⁹⁷ As identified above, $Y = 2(Q - I_W^{(3)})$. The Higgs has 0 electric charge, and the lower doublet
⁸⁹⁸ component has $I_W^{(3)} = -\frac{1}{2}$, yielding $Y = 1$.

Computing $(D_\mu \phi)^\dagger (D^\mu \phi)$, then, yields

$$\frac{1}{8} g_W^2 (W_\mu^1 + iW_\mu^2)(W^{\mu 1} - iW^{\mu 2})(v + h)^2 + \frac{1}{8} (2\partial_\mu + ig_W W_\mu^3 - ig' B_\mu)(2\partial^\mu - ig_W W^{\mu 3} + ig' B^\mu)(v + h)^2 \quad (1.72)$$

and extracting terms quadratic in the fields gives

$$\frac{1}{8} g_W^2 v^2 (W_{\mu 1} W^{\mu 1} + W_{\mu 2} W^{\mu 2}) + \frac{1}{8} v^2 (g_W W_\mu^3 - g' B_\mu)(g_W W^{\mu 3} - g' B^\mu) \quad (1.73)$$

meaning that W_μ^1 and W_μ^2 have masses $m_W = \frac{1}{2}g_W v$. The neutral boson case is a bit more complicated. Writing the corresponding term as

$$\frac{1}{8}v^2 \begin{pmatrix} W_\mu^3 & B_\mu \end{pmatrix} \begin{pmatrix} g_W^2 & -g_W g' \\ -g_W g' & g'^2 \end{pmatrix} \begin{pmatrix} W^{\mu 3} \\ B^\mu \end{pmatrix} \quad (1.74)$$

we note that we must diagonalize this mass matrix to get the physical mass eigenstates. Doing so in the usual way yields eigenvalues 0 , $g'^2 + g_W^2$, thus corresponding to $m_\gamma = 0$ and $m_Z = \frac{1}{2}v\sqrt{g'^2 + g_W^2}$, with physical fields as the (normalized) eigenvectors

$$A_\mu = \frac{g'W_\mu^3 + g_W B_\mu}{\sqrt{g_W^2 + g'^2}} \quad (1.75)$$

$$Z_\mu = \frac{g_W W_\mu^3 - g' B_\mu}{\sqrt{g_W^2 + g'^2}} \quad (1.76)$$

From this form, the angular parametrization of the physical fields is very apparent, namely, defining

$$\tan \theta_W = \frac{g'}{g_W}, \quad (1.77)$$

these equations may be written in terms of the single parameter θ_W as

$$A_\mu = \cos \theta_W B_\mu + \sin \theta_W W_\mu^3 \quad (1.78)$$

$$Z_\mu = -\sin \theta_W B_\mu + \cos \theta_W W_\mu^3 \quad (1.79)$$

and, notably, from the above equations,

$$\frac{m_W}{m_Z} = \cos \theta_W. \quad (1.80)$$

To get the mass terms from Equation 1.72, we extracted those terms quadratic in fields, i.e., the v^2 terms within $(v + h)^2$. However there are also terms of the form VVh and $VVhh$ that arise, which describe the Higgs interactions with the corresponding vector bosons $V = W^\pm, Z$. Namely, identifying physical W bosons as

$$W^\pm = \frac{1}{\sqrt{2}}(W^1 \mp iW^2) \quad (1.81)$$

we may express the first term of Equation 1.72 as

$$\frac{1}{4}g_W^2 W_\mu^- W^{+\mu} (v + h)^2 = \frac{1}{4}g_W^2 v^2 W_\mu^- W^{+\mu} + \frac{1}{2}g_W^2 v W_\mu^- W^{+\mu} h + \frac{1}{4}g_W^2 W_\mu^- W^{+\mu} h^2 \quad (1.82)$$

with the first term corresponding to the mass term $m_W = \frac{1}{2}g_W v$, and the second two terms corresponding to hW^+W^- and hhW^+W^- vertices. Of particular note is the coupling strength

$$g_{HWW} = \frac{1}{2}g_W^2 v = g_W m_W \quad (1.83)$$

899 which is proportional to the W mass – an analysis with the form of the physical Z boson
900 finds that the coupling g_{HZZ} is also proportional to the Z mass.

The Higgs coupling to fermions (in particular to quarks) is of particular interest for this thesis. We showed above that a naive introduction of a mass term

$$m\bar{f}f = m(\bar{f}_L f_R + \bar{f}_R f_L) \quad (1.84)$$

901 is manifestly not gauge invariant because right and left handed particles transform differently
902 under $SU(2)_L$. However, because the Higgs is constructed via an $SU(2)_L$ doublet, ϕ , writing
903 a fermion doublet as L and conjugate \bar{L} , it is apparent that $\bar{L}\phi$ is invariant under $SU(2)_L$.

Combining with the right handed singlet, R , creates a term invariant under $SU(2)_L \times U(1)_Y$, $\bar{L}\phi R$ (and correspondingly $(\bar{L}\phi R)^\dagger$), such that we may include Yukawa [19] terms

$$\mathcal{L}_{Yukawa} = -g_f \left[\begin{pmatrix} \bar{f}_1 & \bar{f}_2 \end{pmatrix}_L \begin{pmatrix} \phi^+ \\ \phi^0 \end{pmatrix} f_R + \bar{f}_R \begin{pmatrix} \phi^{+*} & \phi^{0*} \end{pmatrix} \begin{pmatrix} f_1 \\ f_2 \end{pmatrix}_L \right] \quad (1.85)$$

904 where g_f is a corresponding Yukawa coupling, f_1 and f_2 have been used to denote components
905 of the left-handed doublet and f_R the corresponding right-handed singlet.

After spontaneous symmetry breaking, with the gauge as described above to remove the Goldstone fields, the Higgs doublet becomes

$$\phi(x) = \begin{pmatrix} 0 \\ v + h(x) \end{pmatrix} \quad (1.86)$$

giving rise to terms such as

$$-\frac{1}{\sqrt{2}}g_f v(\bar{f}_{2L}\bar{f}_R + \bar{f}_R f_{2L}) - \frac{1}{\sqrt{2}}g_f h(\bar{f}_{2L}\bar{f}_R + \bar{f}_R f_{2L}) \quad (1.87)$$

where we have kept the subscript f_{2L} to emphasize that these terms *only* impact the lower component of the left-handed doublet because of the 0 in the upper component of the Higgs doublet. Leaving this aside for a second, we note that the first term has the form of the desired mass term above (identifying f_{2L} to f_L) while the second term describes the coupling of the fermion to the physical Higgs field. The corresponding Yukawa coupling may be chosen to be consistent with the observed fermion mass, namely

$$g_f = \sqrt{2} \frac{m_f}{v} \quad (1.88)$$

such that

$$\mathcal{L}_f = -m_f \bar{f}f - \frac{m_f}{v} \bar{f}fh. \quad (1.89)$$

906 Notably here, the fermion coupling to the Higgs boson scales with the mass of the fermion, a
907 fact that is extremely relevant for this thesis analysis.

As we said above, these terms *only* impact the lower component of the left-handed doublet. The inclusion of terms for the upper component is accomplished via the introduction of a Higgs conjugate doublet, defined as

$$\phi_c = -i\sigma_2\phi^* = \begin{pmatrix} -\phi^{0*} \\ \phi^- \end{pmatrix}. \quad (1.90)$$

908 The argument proceeds similarly to the above, with similar results for couplings and masses
909 of upper components.

910 1.7 The Standard Model: A Summary

After all of the above, we may write the Standard Model as a theory with a local $SU(3) \times SU(2)_L \times U(1)_Y$ gauge symmetry, described by the Lagrangian

$$\mathcal{L} = \sum_f \bar{f}i\gamma^\mu D_\mu f - \frac{1}{4} \sum_{gauges} F_{\mu\nu}F^{\mu\nu} + (D_\mu\phi)^\dagger(D^\mu\phi) - \mu^2\phi^\dagger\phi - \lambda(\phi^\dagger\phi)^2 \quad (1.91)$$

where $D_\mu = \partial_\mu + ig_W W_\mu^k t^k + ig' \frac{Y}{2} B_\mu + ig_S G_\mu^a t^a$, in addition to the Yukawa terms, which we write generally as

$$\mathcal{L}_{Yukawa} = - \sum_{f,\phi=\phi,-\phi_c} y_f (\bar{f}\phi f + (\bar{f}\phi f)^\dagger) \quad (1.92)$$

with the sum running over running over appropriate chiral fermion and Higgs doublets.

The $SU(2)_L \times U(1)_Y$ subgroup is spontaneously broken to a $U(1)$ symmetry, lending mass to the associated gauge bosons and fermions. Of relevance for this thesis is the resulting physical Higgs field, with a predicted trilinear self-interaction and associated coupling λv , related to the experimentally observed Higgs boson mass by $m_H = \sqrt{2\lambda v^2}$, as well as the fact that the strength of the Higgs coupling to fermions scales proportionally with the fermion mass.

The Standard Model has been monumentally successful, with many verified predictions and many cross checks. While we have spent much time in this chapter on the theoretical components of the Standard Model, we have not discussed the corresponding experimental discoveries in detail, though this thesis itself participates in an experimental cross check of the Standard Model.

As listed in Figure [4], there are 17 particles in the Standard Model, and the history of interplay between theoretical prediction and experimental discoveries surrounding each of these is paramount to the development of the field of particle physics, and of the way we understand the universe.

Indicative of the importance and strength of electromagnetism in the everyday world, the electron and photon were foundational discoveries that began the theoretical flurry which resulted in the Standard Model. While electric charge was observed by even the ancient Greeks (and, in fact, the word electric is derived from the Greek word for amber, which picks up a charge when rubbed with fur), the connection of this charge to a subatomic particle came later, with J.J. Thompson the first (in 1897) to definitively show the existence of electrons, using cathode ray tubes to demonstrate a particle with a mass much smaller than hydrogen and with a charge to mass ratio independent the of material used in the cathode.

935 The discovery of the photon is much talked about in any introductory quantum mechanics
 936 course via the dual wave/particle nature of light. The assumption in 1900 of Max Planck that
 937 electromagnetic radiation could only be emitted or absorbed in discrete quantities (“quanta”)
 938 resolved the ultraviolet catastrophe, a classical prediction that energy emitted by a black
 939 body diverges for high frequencies. Soon after, in 1905, Einstein postulated that such quanta
 940 corresponded to physical particles, explaining, for instance, the photoelectric effect.

941 These two foundational particles led to the development of both atomic theory and
 942 quantum mechanics. In 1936, Carl D. Anderson and Seth Neddermeyer, while studying
 943 cosmic radiation, observed a particle that behaved similarly to an electron but had a shallower
 944 curvature in a magnetic field (though a sharper curvature than protons). With an assumption
 945 of the same electric charge, this difference is indicative of a particle with mass in between
 946 that of an electron and a proton, and this was the first observation of the muon.

947 In 1968, deep inelastic scattering experiments at SLAC, in which a beam of electrons is
 948 fired at atomic nuclei to probe internal structure of protons and neutrons, confirmed the
 949 existence of internal proton structure, the first observation of what would be identified as
 950 quarks. The proton contains two up quarks and a down quark – however the existence of up
 951 and down quarks, in conjunction with the observation of kaons and pions and the “eightfold
 952 way” of Gell-Mann and Zweig, indirectly confirmed the existence of the strange quark.

953 The charm quark was discovered via the observation of a charm anti-charm meson, called
 954 J/ψ , by Burton Richter and Samuel Ting in 1974, with the dual name a consequence of
 955 the shared, but independent, discovery. Richter’s group at SLAC made the discovery with
 956 SPEAR, an electron-positron collider, whereas Ting’s group utilized fixed target collisions of
 957 a proton beam. Both observed a new resonance near 3 GeV.

958 SPEAR was additionally used for the discovery of the tau by Martin Lewis Perl in
 959 experiments between 1974 and 1977, via the detection of anomalous events requiring the
 960 production and decay of a new particle pair $\tau^+\tau^-$.

961 In 1977, the bottom quark was discovered at Fermilab by Leon Lederman via the obser-
 962 vation of a resonance near 9.5 GeV produced by fixed target proton beam collisions. This

963 resonance, the Υ meson, consists of a bottom quark and an anti-bottom quark, and was
 964 observed in the di-muon decay channel.

965 The same resonance was important in the discovery of the gluon, this time in electron-
 966 positron collisions, first by the PLUTO detector at DORIS (DESY) in 1978 and then by the
 967 TASSO, MARK-J, JADE, and PLUTO experiments at PETRA (DESY) in 1979. The 1978
 968 observation demonstrated excellent consistency with a three-gluon decay topology for the
 969 $\Upsilon(9.46)$ decay, but the mass of the $\Upsilon(9.46)$ is not high enough to resolve three distinct jets.
 970 Operating at $\sqrt{s} = 27.4 \text{ GeV}$, the experiments in 1979 demonstrated a three jet topology
 971 consistent (at these higher energies) with gluon bremsstrahlung, that is $e^+e^- \rightarrow q\bar{q}g$, providing
 972 the first evidence for the existence of the gluon.

973 At CERN in 1983, proton-antiproton collisions led to the discovery of the W and Z bosons
 974 with the UA1 and UA2 experiments, for which Carlo Rubbia and Simon van der Meer received
 975 the Nobel Prize in 1984.

976 The top quark was discovered in 1995 at the Tevatron at Fermilab, a proton anti-proton
 977 collider, by the CDF and DØ experiments, offering a center of mass energy of 1.8 TeV.

978 The final piece of the puzzle was the Higgs boson, discovered by ATLAS and CMS at the
 979 Large Hadron Collider in 2012.

980 The Standard Model, for all of its power, is notably not a complete theory of the universe
 981 – there is no inclusion of gravity, for instance, though a consistent description may be provided
 982 with the introduction of a spin-2 particle. Neutrino oscillations demonstrate that neutrinos
 983 have mass, but right-handed neutrinos have not been observed, leading to questions about
 984 whether there is a different mechanism to provide neutrinos with mass than that described
 985 above. Cosmology tells us that dark matter exists, but there is no corresponding particle
 986 within the Standard Model. This thesis therefore also participates in searches for physics
 987 beyond the Standard Model. We will provide a sketch of the relevant theories in the following
 988 chapter, though a detailed theoretical discussion is beyond the scope of this work.

989

Chapter 2

990

DI-HIGGS PHENOMENOLOGY AND PHYSICS BEYOND THE STANDARD MODEL

991

992 This thesis focuses on searches for di-Higgs production in the $b\bar{b}b\bar{b}$ final state. In this
 993 chapter, we will provide a brief overview of the practical theoretical information motivating
 994 such searches. Though the searches test for physics beyond the Standard Model, particularly
 995 in the search for resonances, the goal of the experimental results is to be somewhat agnostic
 996 to particular theoretical frameworks. An in depth treatment of such models is therefore
 997 beyond the scope of this thesis, though we will attempt to provide a grounding for the models
 998 that we consider.

999 **2.1 Intro to Di-Higgs**

1000 Di-Higgs searches can be split into two major theoretical categories: *resonant searches*, in
 1001 which a physical resonance is produced that subsequently decays into two Higgs bosons,
 1002 and *non-resonant searches* in which no physical resonance is produced, but where the HH
 1003 production cross section has a contribution from an exchange of a *virtual* or *off-shell* particle.

1004 The focus of this thesis is gluon initiated processes – in the case of di-Higgs this is
 1005 termed gluon-gluon fusion (ggF). HH production may also occur via vector boson fusion [20].
 1006 However the cross section for such production is significantly smaller. Representative Feynman
 1007 diagrams are shown for gluon-gluon fusion resonant production in Figure 2.1 and for non-
 1008 resonant production in Figure 2.2.

1009 As shown in Chapter 1, the Higgs coupling to fermions scales with particle mass. As the
 1010 top quark has a mass of 173 GeV, whereas the H has a mass of 125 GeV, such that $H \rightarrow t\bar{t}$ is
 1011 kinematically disfavored, $H \rightarrow b\bar{b}$ is the dominant fermionic Higgs decay mode, and, in fact,

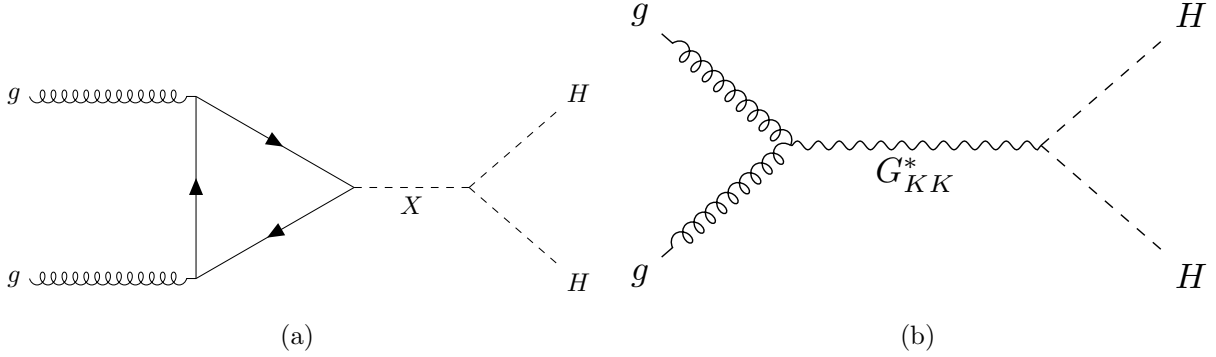


Figure 2.1: Representative diagrams for the gluon-gluon fusion production of spin-0 (X) and spin-2 (G_{KK}^*) resonances which decay to two Standard Model Higgs bosons. The spin-0 resonance considered for this thesis is a generic narrow width resonance which may be interpreted in the context of two Higgs doublet models [21], whereas the spin-2 resonance is considered as a Kaluza-Klein graviton within the bulk Randall-Sundrum (RS) model [22, 23].

the dominant overall decay mode, with a branching fraction of around 58 %. The dominant top quark Yukawa coupling to the H does play a role in H production, however – gluon-gluon fusion is dominated by processes including a top loop.

The single H properties translate to HH production, with $HH \rightarrow b\bar{b}b\bar{b}$ accounting for around 34 % of all HH decays. The H H branching fractions are shown in Figure 2.3.

2.2 Resonant HH Searches

Resonant di-Higgs production is predicted in a variety of extensions to the Standard Model. In particular, this thesis presents searches for both spin-0 and spin-2 resonances. The decay of spin-1 resonances to two identical spin-0 bosons is prohibited, as the final state must correspondingly be symmetric under particle exchange, but this process would require orbital angular momentum $\ell = 1$, and thus an anti-symmetric final state. Each model considered here is implemented in a particular theoretical context, but set up experimental results for generic searches.

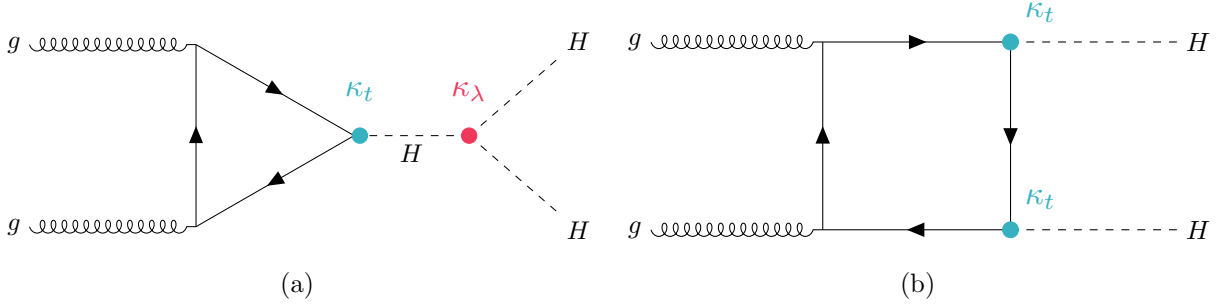


Figure 2.2: Dominant contributing diagrams for non-resonant gluon-gluon fusion production of HH . κ_λ and κ_t represent ratios of the Higgs self-coupling and coupling to top quarks respectively, relative to the values predicted by the Standard Model.

The spin-2 signal considered is implemented within the bulk Randall-Sundrum (RS) model [22, 23], which features spin-2 Kaluza-Klein gravitons, G_{KK}^* , that are produced via gluon-fusion and which may decay to a pair of Higgs bosons. The model predicts such gravitons as a consequence of warped extra dimensions, and is correspondingly parametrized by a value $c = k/\overline{M}_{\text{Pl}} = 1$, where k describes a curvature scale for the extra dimension and \overline{M}_{Pl} is the Planck mass. The model considered here has $c = 1.0$. However, this model was considered in the early Run 2 HH analyses [24], and was excluded across much of the relevant mass range.

The primary theoretical focus of this work is therefore the spin-0 result, which is implemented as a generic resonance with width below detector resolution. Scalar resonances are interesting, for instance, in the context of two Higgs doublet models [21], which posit the existence of a second Higgs doublet. This leads to the existence of five scalar particles in the Higgs sector – roughly, two complex doublets provide eight degrees of freedom, three of which are “eaten” by the electroweak bosons, leaving five degrees of freedom which may correspond to physical fields.

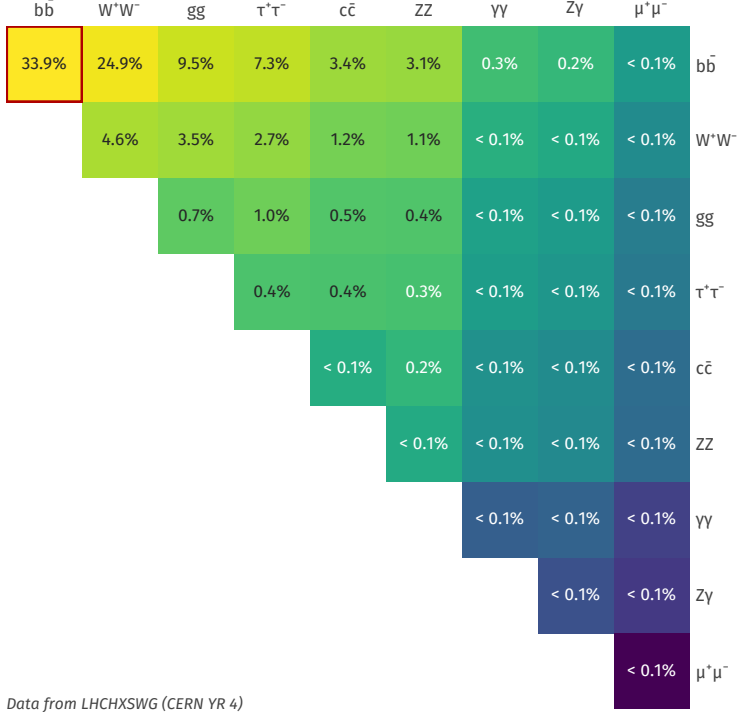


Figure 2.3: Illustration of dominant HH branching ratios. $HH \rightarrow b\bar{b}b\bar{b}$ is the most common decay mode, representing 34 % of all HH events produced at the LHC.

1040 2.3 Non-resonant HH Searches

Non-resonant HH production is predicted by the Standard Model via the trilinear coupling discussed above, as well as via production in a fermion loop. More explicitly, after electroweak symmetry breaking, we have

$$\mathcal{L}_{SM} \supset -\lambda v^2 h^2 - \lambda v h^3 - \frac{1}{4} \lambda h^4 \quad (2.1)$$

$$= -\frac{1}{2} m_H^2 - \lambda_{HHH}^{SM} v h^3 - \lambda_{HHHH}^{SM} h^4 \quad (2.2)$$

where $m_H = \sqrt{2\lambda v^2}$ so that

$$\lambda_{HHH}^{SM} = \frac{m_H^2}{2v^2}. \quad (2.3)$$

1041 The mass of the SM Higgs boson has been experimentally measured to be 125 GeV [25],
 1042 and the vacuum expectation value $v = 246$ GeV has a precise determination from the muon
 1043 lifetime [26]. This coupling is therefore precisely predicted in the Standard Model, such that
 1044 an observed deviation from this prediction would be a clear sign of new physics.

1045 The relevant diagrams for non-resonant HH production are shown in Figure 2.2. Notably,
 1046 the diagrams *interfere* with each other, which can be easily seen by counting the fermion
 1047 lines. A detailed theoretical discussion is provided by, e.g. [27].

1048 For the searches presented here, the quark couplings to the Higgs are considered to be
 1049 consistent with the Standard Model value, with measurements of the dominant top Yukawa
 1050 coupling left to more sensitive direct measurements, e.g. from $t\bar{t}$ final states [28]. Variations of
 1051 the trilinear coupling away from the Standard Model are considered, however. Such variations
 1052 are parametrized via

$$\kappa_\lambda = \frac{\lambda_{HHH}}{\lambda_{HHH}^{SM}} \quad (2.4)$$

1053 where λ_{HHH} is a varied coupling and λ_{HHH}^{SM} is the Standard Model prediction. As this
 1054 variation comes as a prefactor only with the *triangle* diagram, significant and interesting
 1055 effects are observed due to the interference. Examples of the impact of this tradeoff on the
 1056 di-Higgs invariant mass are shown in Figure 2.4. Generally speaking, the triangle diagram
 1057 contributes more at low mass, while the box diagram contributes more at high mass.

From a quick analysis of Figure 2.2, one may see that, at leading order, the box diagram, B has amplitude proportional to κ_t^2 , defined as the ratio of the top Yukawa coupling to the value predicted by the Standard Model, whereas the triangle diagram, T has amplitude proportional to $\kappa_t \kappa_\lambda$. Therefore, the cross section is proportional to

$$\sigma(\kappa_t, \kappa_\lambda) = |A(\kappa_t, \kappa_\lambda)|^2 \quad (2.5)$$

$$\sim |\kappa_t^2 B + \kappa_t \kappa_\lambda T|^2 \quad (2.6)$$

$$= \kappa_t^4 |B|^2 + \kappa_t^3 \kappa_\lambda (BT + TB) + \kappa_t^2 \kappa_\lambda^2 |T|^2, \quad (2.7)$$

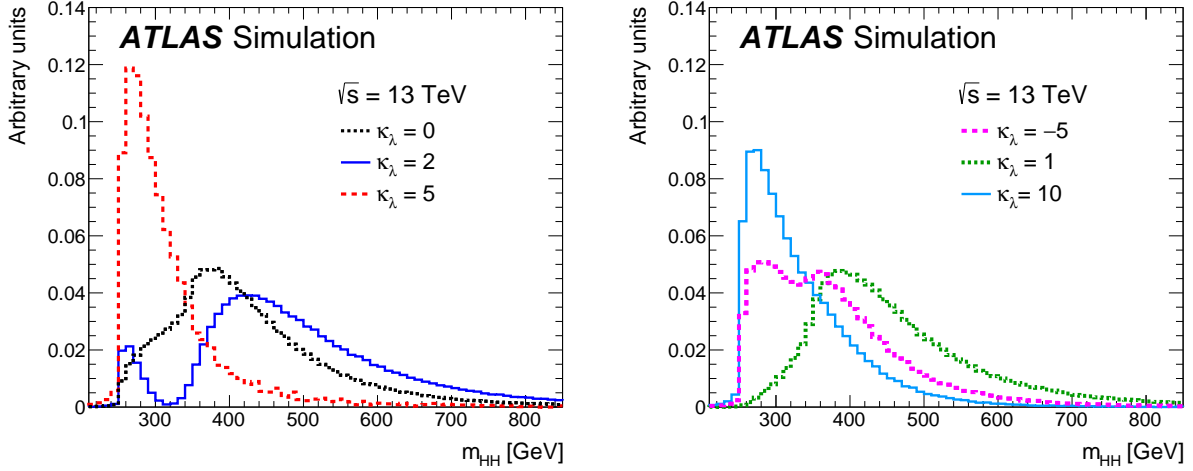


Figure 2.4: Monte Carlo generator level m_{HH} distributions for various values of κ_λ , demonstrating the impact of the interference between the two diagrams of Figure 2.2 on the resulting m_{HH} distribution. For $\kappa_\lambda = 0$ there is no triangle diagram contribution, demonstrating the shape of the box diagram contribution, whereas for $\kappa_\lambda = 10$, the triangle diagram dominates, with a strong low mass peak. The interplay between the two is quite evident for other values, resulting in, e.g., the double peaked structure present for $\kappa_\lambda = 2$ (near maximal destructive interference) and $\kappa_\lambda = -5$. At $\kappa_\lambda = 5$, the interference leads to a deficit at high m_{HH} , resulting in a narrower distribution (and thus a more pronounced low mass peak) than the $\kappa_\lambda = 10$ case. [24]

1058 and thus non-resonant HH production cross section may be parametrized as a second order
1059 polynomial in κ_λ .

1060 For positive values of κ_λ , due to the relative minus sign between the triangle and box
1061 diagrams, the interference between the two diagrams is *destructive*, with a maximum in-
1062 terference near $\kappa_\lambda = 2.3$, corresponding to the minimum cross section prediction. One
1063 may note that the Standard Model value of $\kappa_\lambda = 1$ is not far away from this minimum –
1064 correspondingly the Standard Model cross section for HH production is quite small, namely

1065 31.05 fb at $\sqrt{s} = 13 \text{ TeV}$ for production via gluon-gluon fusion [29–36] compared to, e.g.
 1066 single Higgs production, with a gluon-gluon fusion production cross section of 46.86 pb at
 1067 $\sqrt{s} = 13 \text{ TeV}$ [37] roughly 1500 times larger! For negative values of κ_λ , the interference is
 1068 constructive.

1069 ATLAS projections [38] of $b\bar{b}b\bar{b}$, $b\bar{b}\gamma\gamma$, and $b\bar{b}\tau^+\tau^-$ predict an expected signal strength
 1070 for Standard Model HH of 3.5σ with no systematic uncertainties and 3.0σ with systematic
 1071 uncertainties using the 3000 fb^{-1} of data from the HL-LHC (around $20\times$ the full Run 2
 1072 dataset considered in this thesis), constituting an *observation* of HH . As the cross section
 1073 for Standard Model HHH production, corresponding to the quartic Higgs interaction, is
 1074 much smaller (around 0.1 fb at $\sqrt{s} = 14 \text{ TeV}$ [39]), observation of triple Higgs production is
 1075 even farther in the future, and so is not considered here. However this may be interesting for
 1076 future work in a variety of Beyond the Standard Model scenarios (e.g. [40–42]).

1077

Chapter 3

1078

EXPERIMENTAL APPARATUS

1079 What machines must we build to examine the smallest pieces of the universe? The famous
 1080 equation $E = m$ provides that to create massive particles, we need to provide enough energy.
 1081 In order to give kinematic phase space to the types of processes that are examined in this
 1082 thesis (and many others besides), a system must be created in which there is enough energy
 1083 to (at bare minimum), overcome kinematic thresholds: if you want to search for HH decays,
 1084 you should have at least 250 GeV ($= 2 \times m_H$) to work with. It is not enough to simply induce
 1085 such processes, however. These processes need to be captured in some way, emitted energy
 1086 and particles must be characterized and identified, and in the end all of this information must
 1087 be put into a useful and useable form such that selections can be made, statistics can be run,
 1088 and a meaningful statement can be made about the universe. In this chapter, we describe the
 1089 machines behind the physics, namely the Large Hadron Collider and the ATLAS experiment.

1090 **3.1 The Large Hadron Collider**

1091 The Large Hadron Collider is a particle accelerator near Geneva, Switzerland. In broad scope,
 1092 it is a ring with a 27 kilometer circumference. Hadrons (usually protons or heavy ions) move
 1093 in two counter-circulating beams, which are made to collide at four collision points at various
 1094 points on the ring. These four collision points correspond to the four detectors placed around
 1095 the ring: two “general purpose” experiments: ATLAS and CMS; LHCb, focused primarily on
 1096 flavor physics; and ALICE, focused primarily on heavy ions.

1097 The focus of this thesis is proton-proton collisions at center of mass energy $\sqrt{s} = 13$ TeV.
 1098 The process to achieve such collisions proceeds as follows: first, an electric field strips hydrogen
 1099 of its electrons, creating protons. A linear accelerator, LINAC 2, accelerates protons to

1100 50 MeV. The resulting beam is injected into the Proton Synchrotron Booster (PSB), which
 1101 pushes the protons to 1.4 GeV, and then the Proton Synchrotron, which brings the beam to
 1102 25 GeV.

1103 Protons are then transferred to the Super Proton Synchrotron (SPS), which ramps up
 1104 the energy to 450 GeV. Finally, the protons enter the LHC itself, bringing the beam up to
 1105 6.5 TeV [43].

1106 While there is, of course, much that goes into the Large Hadron Collider development and
 1107 operation, perhaps two of the most fundamental ideas are (1) how are the beams directed
 1108 and manipulated and (2) what do we mean when we say “protons are accelerated”. These
 1109 questions both are directly answered by pieces of hardware, namely (1) magnets and (2)
 1110 radiofrequency (RF) cavities.

1111 One of fundamental components of the LHC is a large set of superconducting niobium-
 1112 titanium magnets. These are cooled by liquid helium to achieve superconducting temperatures,
 1113 and there are several types with very specific purposes. The obvious first question with a
 1114 circular accelerator is how to keep the particle beam moving around in that circle. This job
 1115 is done via a set of dipole magnets placed around the *beam pipes*: the tubes containing the
 1116 beam. These are designed such that the magnetic field in the center of the beam pipe runs
 1117 perpendicular to the velocity of the charged particles, providing the necessary centripetal
 1118 force for the synchrotron motion.

1119 A proton beam is not made of a single proton, however, but of many protons, grouped
 1120 into a series of *bunches*. As all of these are positively charged, if unchecked, these bunches
 1121 would become diffuse and break apart. What we want is a stable beam with tightly clustered
 1122 protons to maximize the chance of a high energy collision. Such clustering is done via a series
 1123 of quadropole magnets, with field distributed as in *TODO: grab image from General Exam*.
 1124 Alternating sets of quadropoles provide the necessary forces for a tight, stable beam. While
 1125 these are the two major components of the LHC magnet system, it is not the full story –
 1126 higher order magnets are used to correct for small imperfections in the beam.

1127 Magnetic fields do no work, however, so the magnet system is unable to do the job of the

actual acceleration. This is accomplished via a set of radiofrequency (RF) cavities. Within these cavities, an electric field is made to oscillate (switch direction) at a precise rate. This oscillation creates RF *buckets*, with bunches corresponding to groups of protons that fill a given bucket. The timing is such that protons will always experience an accelerating voltage, corresponding to the 25 ns bunch spacing used at the LHC.

A nice property of this bucket/bunch configuration is that there is some self-correction – there is some finite spread in the grouping of particles. If a particle arrives too early, it will experience some decelerating voltage; if too late, it will experience a higher accelerating voltage.

3.1.1 The LHC Schedule

The physics program at the Large Hadron Collider is split into a variety of data taking periods called *runs*. These runs correspond to various detector/accelerator configurations, and are interspersed with *long shutdowns* – periods used for detector/accelerator upgrades in preparation for the next run. The LHC timeline is as follows

1. Run 1 (2010–2013): First run of the LHC, operating at center of mass energy $\sqrt{s} = 7 \text{ TeV}$, increased to 8 TeV in 2012. ATLAS recorded 4.57 fb^{-1} and 20.3 fb^{-1} of data usable for physics at $\sqrt{s} = 7 \text{ TeV}$ and 8 TeV respectively.
2. Long Shutdown 1 (LS1; 2013–2015): Upgrades to accelerator complex, magnet system, to allow for increase in energy. Design energy was $\sqrt{s} = 14 \text{ TeV}$, delays in “training” of superconducting magnets led to decrease to $\sqrt{s} = 13 \text{ TeV}$.
3. Run 2 (2015–2018): Second run of the LHC, operating at center of mass energy $\sqrt{s} = 13 \text{ TeV}$. Data from this run is used in this thesis, with 139 fb^{-1} of data available for physics from the ATLAS experiment.
4. Long Shutdown 2 (LS2; 2019–2021): Upgrades to ATLAS muon spectrometer (New

1152 Small Wheel), liquid argon calorimeter; upgrades in preparation for the High Luminosity
1153 LHC (HL-LHC).

1154 5. Run 3 (2021–2023?): Third run of the LHC, target center of mass energy $\sqrt{s} =$
1155 $13 - 14 \text{ TeV}$, total target luminosity 300 fb^{-1} .

1156 6. Long Shutdown 3 (LS3; 2024?–2026?): Further upgrades for the HL-LHC.

1157 7. Run 4, 5, ... (2026? onward): High Luminosity LHC – goal is to achieve instantaneous
1158 luminosities by a factor of five, massively enlarging available statistics for physics.
1159 Projected 3000 to 4000 fb^{-1} , > 20 times the full Run 2 ATLAS dataset.

1160 **3.2 The ATLAS Experiment**

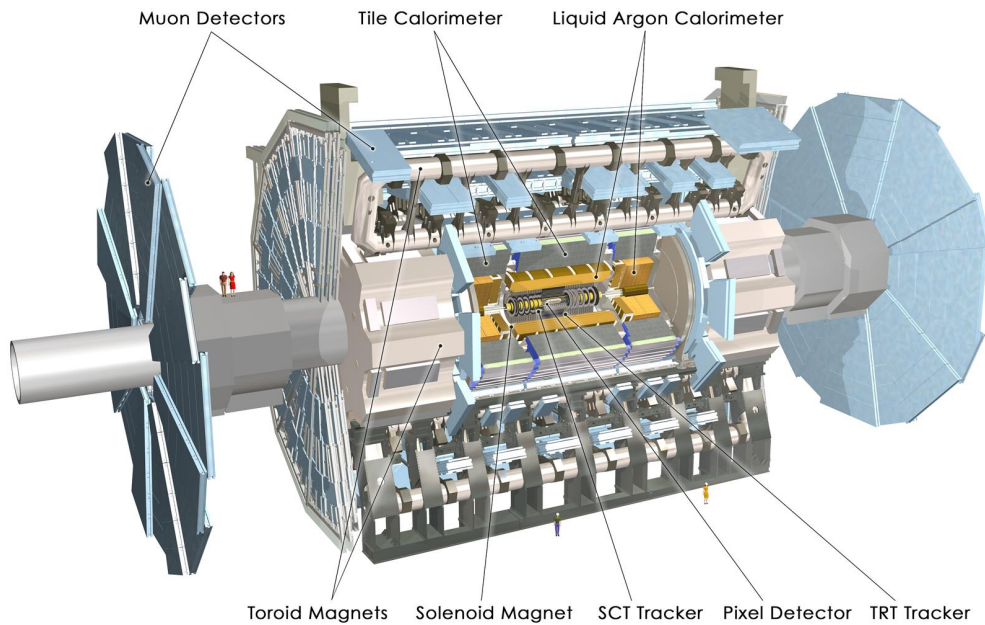


Figure 3.1: Diagram of the ATLAS detector [44]

1161 This thesis focuses on searches done with the ATLAS experiment. As mentioned, this is one

of two “general purpose” experiments at the LHC, by which we mean there is a very large and broad variety of physics done within the experimental collaboration. This broad physics focus has a direct relation to the design of the ATLAS detector [45], pictured in Figure 3.1, which is composed of a sophisticated set of subsystems designed to fully characterize the physics of a given high energy particle collision. It consists of an inner tracking detector surrounded by a thin superconducting solenoid, electromagnetic and hadronic calorimeters, and a muon spectrometer incorporating three large superconducting toroidal magnets. The ATLAS detector covers nearly the entire solid angle around the collision point, fully characterizing the “visible” components of a collision and allowing for indirect sensitivity to particles that do not interact with the detector (e.g. neutrinos) via “missing” energy (roughly momentum balance). We will go through the design and physics contribution of each of the detector components in the following. A schematic of how various particles interact with the detector is shown in Figure 3.2.

3.2.1 ATLAS Coordinate System

Of relevance for the following discussion, as well as for the analysis presented in Chapter 7, is the ATLAS coordinate system. ATLAS uses a right-handed coordinate system with its origin at the nominal interaction point (IP) in the center of the detector and the z -axis along the beam pipe. The x -axis points from the IP to the centre of the LHC ring, and the y -axis points upwards. Cylindrical coordinates (r, ϕ) are used in the transverse plane, ϕ being the azimuthal angle around the z -axis. The pseudorapidity is defined in terms of the polar angle θ as $\eta = -\ln \tan(\theta/2)$. Angular distance is measured in units of $\Delta R \equiv \sqrt{(\Delta\eta)^2 + (\Delta\phi)^2}$. These coordinates are shown in Figure 3.3.

3.2.2 Inner Detector

The purpose of the inner detector is the reconstruction of the trajectory of charged particles, called *tracking*. This is accomplished primarily through the collection of electrons displaced when a charged particle passes through a tracking detector. By setting up multiple layers of

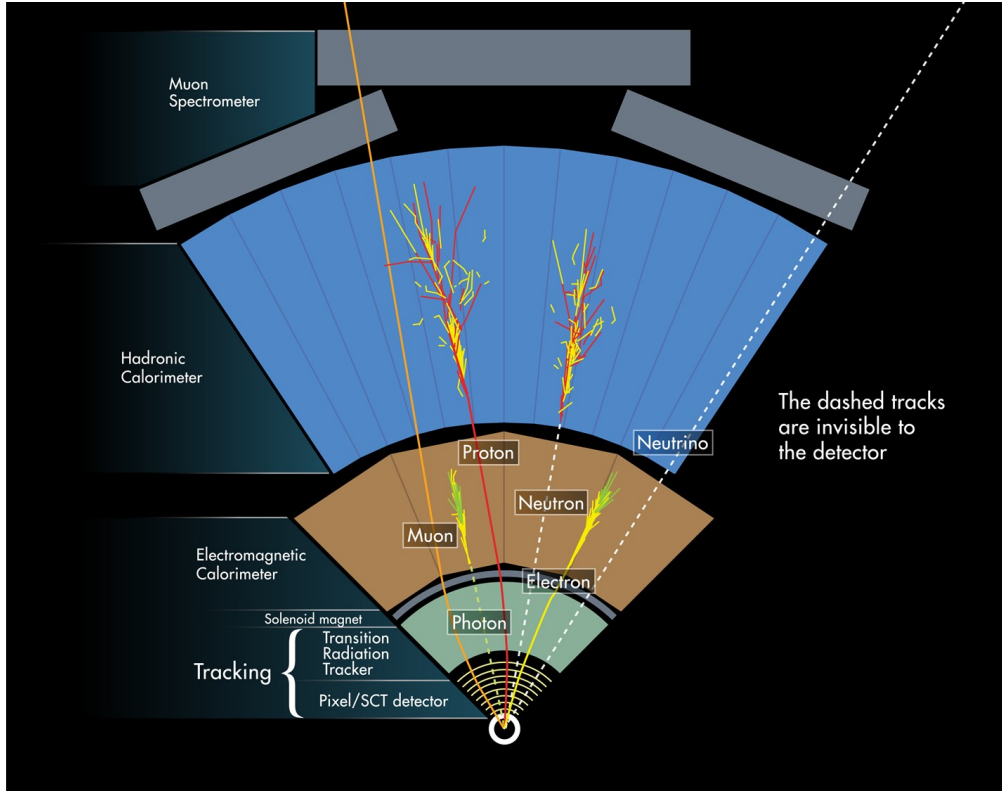


Figure 3.2: Cross section of the ATLAS detector showing how particles interact with various detector components [46]

such detectors, such that a given particle leaves a signature, known as a “hit”, in each layer, the trajectory of the particle may be inferred via “connecting the dots” between these hits.

The raw trajectory of a particle only provides positional information. However, the trajectory of a charged particle in a known magnetic field additionally provides information on particle momentum and charge via the curvature of the corresponding track (cf. $\vec{F} = q\vec{v} \times \vec{B}$). The inner detector system is therefore surrounded by a solenoid magnet, providing a 2 T magnetic field along the z -axis (yielding curvature in the transverse $x - y$ plane).

The inner detector provides charged particle tracking in the range $|\eta| < 2.5$ via a series of detector layers. The innermost of these is the high-granularity silicon pixel detector which typically provides four measurements per track, with the first hit in the insertable B-layer

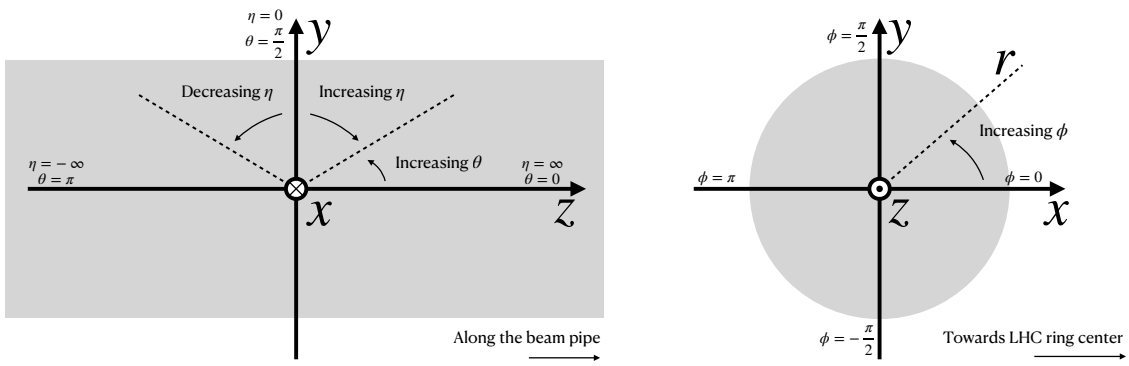


Figure 3.3: 2D projections of the ATLAS coordinate system

1198 (IBL) installed before Run 2 [47, 48]. This is very close to the interaction point with a
1199 high degree of positional information, and is therefore very important for e.g. b -tagging (see
1200 Chapter 5). It is followed by the silicon microstrip tracker (SCT), which usually provides
1201 eight measurements per track. This is lower granularity, but similar in concept to the pixel
1202 detector.

1203 Both of these silicon detectors are complemented by the transition radiation tracker
1204 (TRT), which extends the radial track reconstruction within the range $|\eta| < 2.0$. This is
1205 a different design, composed of *drift tubes*, i.e. straws filled with Xenon gas with a wire
1206 in the center, but similarly collects electrons displaced by ionizing particles. In addition,
1207 the TRT includes materials with widely varying indices of refraction, which leads to the
1208 production of transition radiation, namely radiation produced by a charged particle passing
1209 through an inhomogeneous medium. The energy loss on such a transition is proportional
1210 to the Lorentz factor $\gamma = E/m$ – correspondingly, lighter particles (e.g. electrons) tend to
1211 lose more energy and emit more photons compared to heavier particles (e.g. pions). In the
1212 detector, this corresponds to a larger fraction of hits (typically 30 in total) above a given

1213 high energy-deposit threshold for electrons, providing particle identification information.

1214 *3.2.3 Calorimeter*

1215 Surrounding the inner detector in ATLAS is the calorimeter. The principle of the calorimeter
1216 is to completely absorb the energy of a produced particle in order to measure it. However,
1217 a pure block of absorber does not provide much information about the particle interaction
1218 with the material. The ATLAS calorimeter therefore has a *sampling calorimeter* structure,
1219 namely, layers of absorber interspersed with layers of sensitive material, giving the calorimeter
1220 “stopping power” while allowing detailed measurement of the resulting particle shower and
1221 corresponding deposited energy.

1222 The ATLAS calorimetersystem covers the pseudorapidity range $|\eta| < 4.9$, and is primarily
1223 composed of two components, an electromagnetic calorimeter, designed to measure particles
1224 which primarily interact via electromagnetism (e.g. photons and electrons), and a hadronic
1225 calorimeter, designed to measure particles which interact via the strong force (e.g. pions,
1226 other hadrons). We will return to the differences between these in a moment.

1227 In ATLAS, the electromagnetic calorimeter covers the region of $|\eta| < 3.2$, and uses
1228 lead for the absorbers and liquid-argon for the sensitive material. It is high granularity
1229 and, geometrically, has two components: the “barrel”, which covers the cylindrical body of
1230 the detector volume and the “endcap”, covering the ends. An additional thin liquid-argon
1231 presampler covers $|\eta| < 1.8$ to correct for energy loss in material upstream of the calorimeters.

1232 The hadronic calorimeter is composed of alternating steel and plastic scintillator tiles,
1233 segmented into three barrel structures within $|\eta| < 1.7$, in addition to two copper/liquid-argon
1234 endcap calorimeters.

1235 The solid angle coverage is completed with forward copper/liquid-argon and tungsten/liquid-
1236 argon calorimeter modules optimized for electromagnetic and hadronic energy measurements
1237 respectively.

1238 *3.2.4 Muon Spectrometer*

1239 While muons interact electromagnetically, they are around 200 times heavier than electrons
 1240 ($m_\mu = 106 \text{ MeV}$, while $m_e = 0.510 \text{ MeV}$). Therefore, electromagnetic interactions with ab-
 1241 sorbers in the calorimeter are not sufficient to stop them, and, as they do not interact via the
 1242 strong force, hard scattering with nuclei is rare. A dedicated system for muon measurements
 1243 is therefore required.

1244 The muon spectrometer (MS) is the outermost layer of ATLAS and is designed for this
 1245 purpose. It is composed of three parts: a set of triggering chambers, which detect if there is
 1246 a muon and provide a coordinate measurement, in conjunction with high-precision tracking
 1247 chambers, which measure the deflection of muons in a magnetic field to measure muon
 1248 momentum, similar to the inner detector solenoid. The magnetic field is generated by the
 1249 superconducting air-core toroidal magnets, with a field integral between 2.0 and 6.0 T m
 1250 across most of the detector. The toroid magnetic field runs roughly in a circle in the $x - y$
 1251 plane around the beam line, leading to muon curvature along the z-axis.

1252 The precision tracking system covers the region $|\eta| < 2.7$ via three layers of monitored
 1253 drift tubes, and is complemented by cathode-strip chambers in the forward region, where the
 1254 background is highest. The muon trigger system covers the range $|\eta| < 2.4$ with resistive-plate
 1255 chambers in the barrel, and thin-gap chambers in the endcap regions.

1256 *3.2.5 Triggering*

1257 During a typical run of the LHC, there are roughly 1 billion collisions in ATLAS per second
 1258 (1 GHz), corresponding to a 40 MHz bunch crossing rate [49]. Saving the information from
 1259 all of them is not only unnecessary, but infeasible. The ATLAS trigger system provides a
 1260 sophisticated set of selections to filter the collision data and only keep those collision events
 1261 useful for downstream analysis.

1262 These events are selected by the first-level trigger system, which is implemented in custom
 1263 hardware, and accepts events at a rate below 100 kHz. Selections are then made by algorithms

1264 implemented in software in the high-level trigger [50], reducing this further, and, in the end,
1265 events are recorded to disk at much more manageable rate of about 1 kHz.

1266 An extensive set of ATLAS software [51] is open source, including the software used for
1267 real and simulated data reconstruction and analysis and that used in the trigger and data
1268 acquisition systems of the experiment.

1269 *3.2.6 Particle Showers and the Calorimeter*

1270 The design of the ATLAS detector is directly tied to the physics it is trying to detect. Of these,
1271 possibly the most non-trivial distinction is in the calorimeter design. It is therefore useful to
1272 discuss in more detail the various properties of electromagnetic and hadronic interactions
1273 with material, and how these correspond to the particle showers measured by the detector
1274 described above.

1275 Electromagnetic showers in ATLAS predominantly occur via bremsstrahlung, or “braking
1276 radiation”, and electron-positron pair production. This proceeds roughly as follows: an
1277 electron entering a material is deflected by the electromagnetic field of a heavy nucleus. This
1278 results in the radiation of a photon. That photon produces an electron-positron pair, and
1279 the process repeats, resulting in a shower structure. At each step, characterized by *radiation*
1280 *length*, X_0 , the number of particles approximately doubles and the average particle energy
1281 decreases by approximately a factor of two. *TODO: Include nice Thomson image*

Note that bremsstrahlung and pair production only dominate in specific energy regimes, with other processes taking over depending on particle energy. For electrons, bremsstrahlung only dominates for higher energies, as low energy electrons will form ions with the atoms of the material. The point where the rates for the two processes are equal is called the *critical energy*, and is roughly

$$E_c \approx \frac{800 \text{ MeV}}{Z} \quad (3.1)$$

1282 where Z is the nuclear charge. From a similar analysis of rates, we may see that the
1283 bremsstrahlung rate is inversely proportional to the square of the mass of the particle. This

¹²⁸⁴ explains why muons do not shower in a similar way, as the rate of bremsstrahlung is suppressed
¹²⁸⁵ by $(m_e/m_\mu)^2$ relative to electrons.

For lead, the absorber used for the ATLAS electromagnetic calorimeter, which has $Z = 82$, this critical energy is therefore around 10 MeV. Electrons resulting from LHC collisions are of a 1.3×10^3 GeV scale. With the approximation of a reduction in particle energy by a factor of two every radiation length, the number of radiation lengths before the critical energy is reached is

$$x = \frac{\ln(E/E_c)}{\ln 2} \quad (3.2)$$

¹²⁸⁶ such that for a 100 GeV shower in lead, $x \sim 13$. The radiation length for lead is around
¹²⁸⁷ 0.56 cm, such that an electromagnetic shower could be expected to be captured within 10 cm
¹²⁸⁸ of lead.

¹²⁸⁹ Electromagnetic showers are therefore characterized by depositing much of their energy
¹²⁹⁰ within a small region of space. As we show below (Chapter 4) though electromagnetic
¹²⁹¹ showering is not deterministic, the large number of particles and the restricted set of processes
¹²⁹² involved means that the shower development as a whole is very similar between individual
¹²⁹³ electromagnetic showers of the same energy.

¹²⁹⁴ For completeness, note as well that pair production dominates for photons of energy greater
¹²⁹⁵ than around 10 MeV, whereas for lower energies (below around 1 MeV), the photoelectric
¹²⁹⁶ effect, namely atomic photon absorption and electron emission, dominates.

¹²⁹⁷ Hadronic showers are distinguished by the fact that they interact strongly with atomic
¹²⁹⁸ nuclei. They are correspondingly more complex because (1) they involve a wider variety
¹²⁹⁹ of processes than electromagnetic showers, and (2) these processes have a wide variety of
¹³⁰⁰ associated length scales. Because these are heavier than electrons (e.g. protons and charged
¹³⁰¹ pions) bremsstrahlung is suppressed, but ionization interactions with the electrons will cause
¹³⁰² these particles to lose energy as they pass through the material. Hadronic showering occurs
¹³⁰³ on interaction with atomic nuclei. This may lead to production of, e.g. both charged (π^\pm)
¹³⁰⁴ and neutral (π^0) pions. The π^0 lifetime is much much shorter than that of the charged pions
¹³⁰⁵ (around a factor of 10^8), and immediately decays to two photons, starting an electromagnetic

1306 shower, as described above. The longer lived π^\pm travel further in the detector before
1307 experiencing another strong interaction with more particles produced, also with varying
1308 lifetimes and decay properties.

1309 It is therefore immediately apparent that hadronic showers are more complex than
1310 electromagnetic ones (electromagnetic showers can be a subset of the hadronic!), and therefore
1311 much more variable from shower to shower. The length scales involved are also significantly
1312 larger due to the reliance on nuclear interactions, characterized by length λ_I , which is around
1313 17 cm for iron (used in the ATLAS hadronic calorimeter). This motivates the calorimeter
1314 design, and results in the properties demonstrated in Figure 3.2.

1315

Chapter 4

1316

SIMULATION

1317 Simulated physics samples are a core piece of the physics output of the Large Hadron
 1318 Collider, providing a map from a physics theory into what is observed in our detector. This
 1319 is crucial for searches for new physics, where simulation is necessary to describe what a given
 1320 signal model looks like, but also extremely valuable for describing the physics of the Standard
 1321 Model, providing detailed predictions of background processes for use in everything from
 1322 designing simple cuts to training multivariate discriminators. Broadly, simulation can be split
 1323 into two stages: *event generation*, in which physics theory is used to generate a description of
 1324 particles present after a proton-proton collision, and *detector simulation*, which passes this
 1325 particle description through a simulation of the detector material, providing a view of the
 1326 physics event as it would be seen in ATLAS data. Such simulation is often called Monte Carlo
 1327 in reference to the underlying mathematical framework, which relies on random sampling.

1328 **4.1 Event Generation**

1329 A variety of tools are used to simulate various aspects of event generation. One such aspect
 1330 is generation of the “hard scatter” event, i.e., two protons collide and some desired physics
 1331 process happens. In practice, this is not quite as simple as two quarks or gluons interacting.
 1332 Protons are composed of three “valence” quarks with various momenta interacting with each
 1333 other via exchange of gluons, but also a sea of virtual gluons which may decay into other
 1334 quarks. A hard scatter event is therefore characterized by the corresponding particle level
 1335 diagrams, but additionally by a set of *parton distribution functions* (PDFs), which describe
 1336 the probability to find constituent quarks or gluons at carrying various momenta at a given
 1337 energy scale (often written Q^2). Such PDFs are measured experimentally *TODO: cite* and

1338 the selection of a “PDF set” and a given physics process characterizes the hard scatter.
 1339 Depending on the model being considered and the particular theoretical constraints, processes
 1340 are often simulated at either leading (LO) or next to leading order (NLO), corresponding to
 1341 the order of the perturbative expansion (i.e. tree level or 1 loop diagrams). Various additional
 1342 tools are developed for such NLO calculations, including POWHEG Box v2 [52–54], which is
 1343 used for this thesis. MADGRAPH [55] is used in this thesis for leading order simulation.

1344 The hard scatter is not the only component of a given collider event, however. Incoming
 1345 and outgoing particles are themselves very energetic and may radiate particles along their
 1346 trajectory. In particular, gluons, which have a self-interaction term as described in Chapter 1,
 1347 may be radiated, which subsequently themselves radiate gluons or decay to quarks which can
 1348 also radiate gluons, in a whole mess of QCD that both contributes to the particle content
 1349 of a collider event and is not directly described by the hard scatter. This cascade, called a
 1350 *parton shower*, has a dedicated set of simulation tools. For this thesis, HERWIG 7 [56][57] and
 1351 PYTHIA 8 [58] are used, which interface with tools such as MADGRAPH for simulation.

1352 Due to color confinement (Chapter 1), quarks and gluons cannot be observed free particles,
 1353 but rather undergo a process called hadronization, in which they are grouped into colorless
 1354 hadrons (e.g. *mesons*, consisting of one quark and one anti-quark). In simulation, this is also
 1355 handled with tools such as HERWIG 7 or PYTHIA 8.

1356 The physics of b -quarks is quite important for a variety of searches for new physics and
 1357 measurements of the Standard Model, including this thesis work. Correspondingly, the decay
 1358 of “heavy flavor” particles (e.g. B and D mesons, containing b and c quarks respectively)
 1359 has been very well studied, and a dedicated simulation tool, EVTGEN [59], is used for such
 1360 processes.

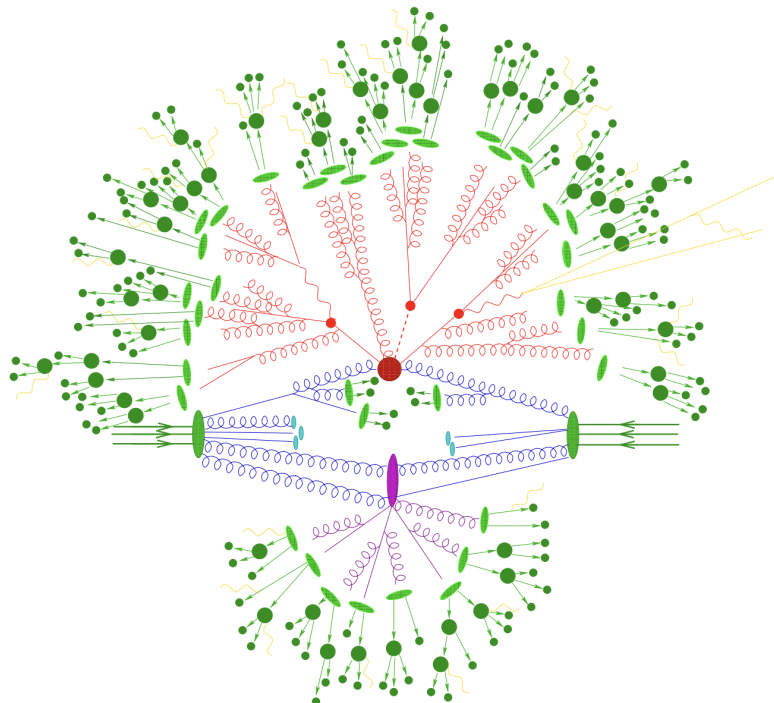


Figure 4.1: Schematic diagram of the Monte Carlo simulation of a hadron-hadron collision. The incoming hadrons are the green blobs with the arrows on the left and right, with the red blob in the center representing the hard scatter event, and the purple representing a secondary hard scatter. Radiation from both incoming and outgoing particles is shown, and the light green blobs represent hadronization, with the outermost dark green circles corresponding to the final state hadrons. Yellow lines are radiated photons. [60]

1361 **4.2 Detector Simulation**

1362 Event generation provides a full and exact description of the particle content of a given
1363 collider event. This description is useful, but is an artifact of the simulation – for real physics
1364 events, we must rely on the information collected by sophisticated detectors (Chapter 3) to
1365 make statements about the physics content of collider events. The simulation of how particles
1366 interact with the physical detector and of the corresponding information that is collected is
1367 therefore a necessary step of physics simulation at the LHC. The design and components of
1368 the ATLAS detector are described in Chapter 3. Simulation of this detector quickly becomes
1369 complicated – there are a variety of different materials and sub-detectors, each with particular
1370 configurations and resolutions. Interactions of particles with the detector materials can cause
1371 showering, and such showers must be simulated and characterized.

1372 In ATLAS, the GEANT4 [61] simulation toolkit is used for detailed simulation of the
1373 ATLAS detector, often referred to as *full simulation*. The method can be thought of as
1374 proceeding step by step as a particle moves through the detector, simulating the interaction
1375 of the material at each stage, and following each branch of each resulting shower with a
1376 similarly detailed step by step simulation.

1377 This type of simulation is very computationally intensive, especially in the calorimeter,
1378 which has a high density of material, leading to an extremely large set of material interactions
1379 to simulate. There is correspondingly a large effort within ATLAS to develop techniques to
1380 decrease the computational load – these techniques will be of increasing importance for Run
1381 3 and the HL-LHC, which will have increased computational need due to the high complexity
1382 and large volume of collected physics events, along with the corresponding set of simulated
1383 physics events [62]. The divergence of the baseline computing model from the projected
1384 computing budget is shown in Figure 4.2.

1385 The fast simulation used for this thesis, AtlFast-II [64], is one such technique, which uses
1386 a parametrized simulation of the calorimeter, called FastCaloSim, in conjunction with full
1387 simulation of the inner detector, to achieve an order of magnitude speed up in simulation

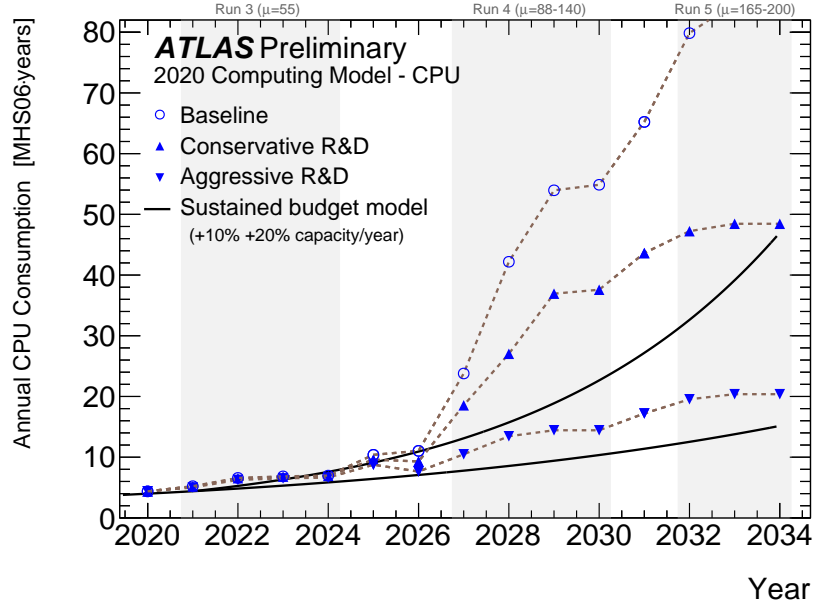


Figure 4.2: The projected ATLAS computational requirements for Run 3 and the HL-LHC relative to the projected computing budget. Aggressive R&D is required to keep resources within budget [63].

time. This parametrized simulation uses a simplified detector geometry, in conjunction with a simulation of particle shower development based on statistical sampling of distributions from fully simulated events, to massively speed up simulation time and computational load.

Such a speed up comes at a bit of a cost in performance. In particular, the modeling of jet substructure (see Chapter 5) historically has been an issue for FastCaloSim. The ATLAS authorship qualification work supporting this thesis is an effort to improve such modeling, and is part of a suite of updates being considered for a new fast simulation targeting Run 3. We briefly describe this work in the following.

1396 **4.3 Correlated Fluctuations in FastCaloSim**

1397 A variety of developments have been made to FastCaloSim, improving on the version used for
1398 AtlFast-II. This new fast calorimeter simulation [65] is largely based on two components: one
1399 which describes the *total energy* deposited in each calorimeter layer as a shower moves from
1400 the interaction point outward, and one which describes the *shape*, i.e., the pattern of energy
1401 deposits, of a shower in each respective calorimeter layer. Both methods are parametrizations
1402 of the full simulation, and therefore are considered to be performing well if they are able
1403 to reproduce corresponding full simulation distributions. Of course, directly sampling from
1404 a library of showers would identically reproduce such distributions – however a statistical
1405 sampling of various shower *properties* provides much more generality in the simulation.

1406 For the simulation of total energy in each given layer, the primary challenge is that such
1407 energy deposits are highly correlated. The new FastCaloSim thus relies on a technique called
1408 Principal Component Analysis (PCA) [66] to de-correlate the layers, aiding parametrization.

1409 The PCA chain transforms N energy inputs into N Gaussians and projects these Gaussians
1410 onto the eigenvectors of the corresponding covariance matrix. This results in N de-correlated
1411 components, as the eigenvectors are orthogonal. The component of the PCA decomposition
1412 with the largest corresponding eigenvalue is then used to define bins, in which showers
1413 demonstrate similar patterns of energy deposition across the calorimeter layers. To further
1414 de-correlate the inputs, the PCA chain is repeated on the showers within each such bin. This
1415 full process is reversed for the particle simulation. A full description of the method can be
1416 found in [65].

1417 Modeling of the lateral shower shape makes use of 2D histograms filled with GEANT4
1418 hit energies in each layer and PCA bin. Binned in polar $\alpha - R$ coordinates in a local plane
1419 tangential to the surface of the calorimeter system, these histograms represent the spatial
1420 distribution of energy deposits for a given particle shower. Such histograms are constructed
1421 for a number of GEANT4 events, and the histograms for each event are normalized to total
1422 energy deposited in the given layer. The average of these histograms is then taken (what is

1423 called here the “average shape”).

1424 In simulation, these average shape histograms are used as probability distributions, from
 1425 which a finite number of equal energy hits are drawn. This finite drawing of hits induces
 1426 a statistical fluctuation about the average shape which is tuned to match the expected
 1427 calorimeter sampling uncertainty.

1428 As an example, the intrinsic resolution of the ATLAS Liquid Argon calorimeter has a
 1429 sampling term of $\sigma_{\text{samp}} \approx 10\%/\sqrt{E}$ [67]. The number of hits to be drawn for each layer, $N_{\text{hits}}^{\text{layer}}$,
 1430 is thus taken from a Poisson distribution with mean $1/\sigma_{\text{samp}}^2$, where the energy assigned to
 1431 each hit is then just $E_{\text{hit}} = \frac{E_{\text{layer}}}{N_{\text{hits}}^{\text{layer}}}$. This induces a fluctuation of the order of $10\%/\sqrt{E_{\text{bin}}}$ for
 1432 each bin in the average shape.

1433 Figure 4.3 shows a comparison of energy and weta2 [68], defined as the energy weighted
 1434 lateral width of a shower in the second electromagnetic calorimeter layer, for 16 GeV photons
 1435 simulated with the new FastCaloSim and with full GEANT4 simulation. The agreement is
 1436 quite good, with FastCaloSim matching the GEANT4 mean to within 0.3 and 0.03 percent
 respectively. Similar results are seen for other photon energies and η points.

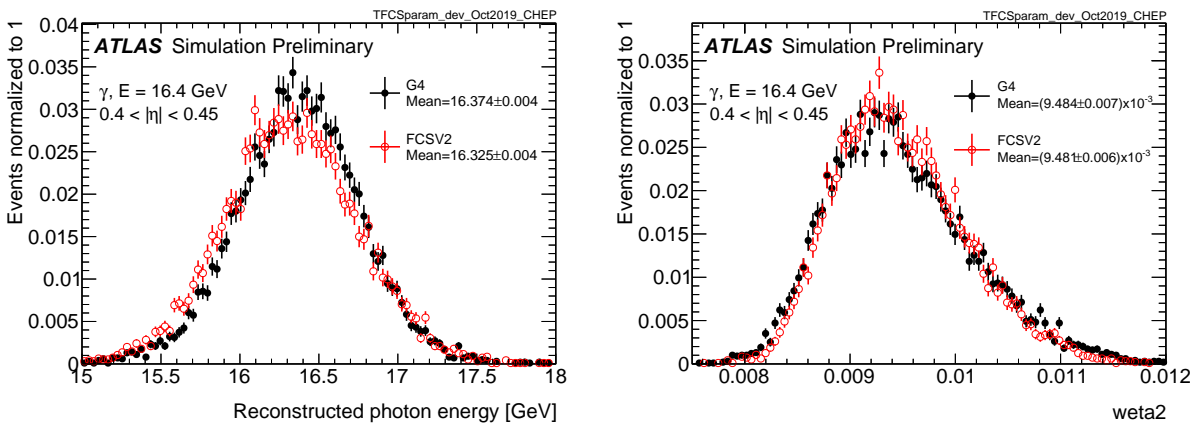


Figure 4.3: Energy and variable weta2, defined as the energy weighted lateral width of a shower in the second electromagnetic calorimeter layer, for 16 GeV photons with full simulation (G4) and FastCaloSimV2 (FCSV2) [65].

1438 4.3.1 *Fluctuation Modeling*

1439 Figure 4.4 shows the ratio of calorimeter cell energies for single GEANT4 photon and pion
 1440 events to the corresponding cell energies in their respective average shapes. While the photon
 1441 event is quite close to the corresponding average, the pion event shows a deviation from the
 1442 average which is much larger and has a non-trivial structure, reflecting the different natures
 1443 of electromagnetic and hadronic showering.

1444 While the shape parametrization described above is thus sufficient for describing electro-
 1445 magnetic showers, we will demonstrate below that it is not sufficient for describing hadronic
 1446 showers (Figures 4.7 and 4.8). We therefore present and validate methods to improve this
 1447 hadronic shower modeling. Such methods have been presented as well in [69].

1448 Two methods for modeling deviations from the average shape have been studied: (1)
 1449 a neural network based approach using a Variational Autoencoder (VAE) [70] and (2) a
 1450 map through cumulative distributions to an n -dimensional Gaussian. With both methods,
 1451 the shape simulation then proceeds as described in Section 4.3, with the drawing of hits
 1452 according to the average shape. However, these hits no longer have equal energy, but have
 1453 weights applied to increase or decrease their energy depending on their spatial position.
 1454 This application of weights is designed to mimic a realistic shower structure and to encode
 1455 correlations between energy deposits.

1456 Both methods are trained on ratios of energy in binned units called voxels. This voxelization
 1457 is performed in the same polar $\alpha - R$ coordinates as the average shape, with a 5 mm core in
 1458 R and 20 mm binning thereafter. There are a total of 8 α bins from 0 to 2π and 8 additional
 1459 R bins from 5 mm to 165 mm. The 5 mm core is filled with the average value of core voxels
 1460 across the 8 α bins when creating the parametrization. However, during simulation, each of
 1461 these 8 core bins is treated independently. The outputs of both methods mimic these energy
 1462 ratios and are used in the shape simulation as the weights described above. In contrast to
 1463 an approach based on, e.g., calorimeter cells, using voxels allows for flexibility in tuning the
 1464 binning used in creating the parametrization. Further, due to their relatively large size, using

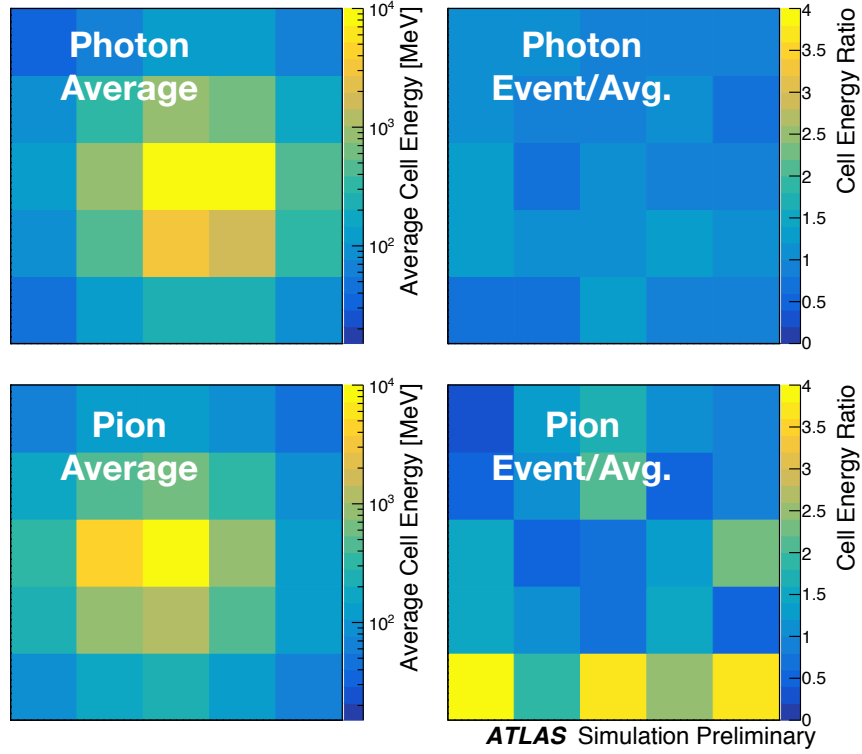


Figure 4.4: Example of photon and pion average shapes in 5×5 calorimeter cells. The left column shows the average shape over a sample of 10000 events, while the right column shows the energy ratio, in each cell, of single GEANT4 events with respect to this average. The photon ratios are all close to 1, while the pion ratios show significant deviation from the average.

1465 calorimeter cells is subject to “edge effects”, where the splitting of energy between cells has a
 1466 non-trivial effect on the observed energy ratio. The binning used here is of the order of half
 1467 of a cell size, mitigating this effect.

1468 The Gaussian method operates by using cumulative distributions to map GEANT4 energy
 1469 ratios to a multidimensional Gaussian distribution. New events are generated by randomly
 1470 sampling from this Gaussian distribution.

1471 For the VAE method, a system of two linked neural networks is trained to generate events.

1472 The first “encoder” neural network maps input GEANT4 energy ratios to a lower dimensional
 1473 latent space. A second “decoder” neural network then samples from that latent space and
 1474 tries to reproduce the inputs. In simulation, events are generated by taking random samples
 1475 from the latent space and passing them through the trained decoder.

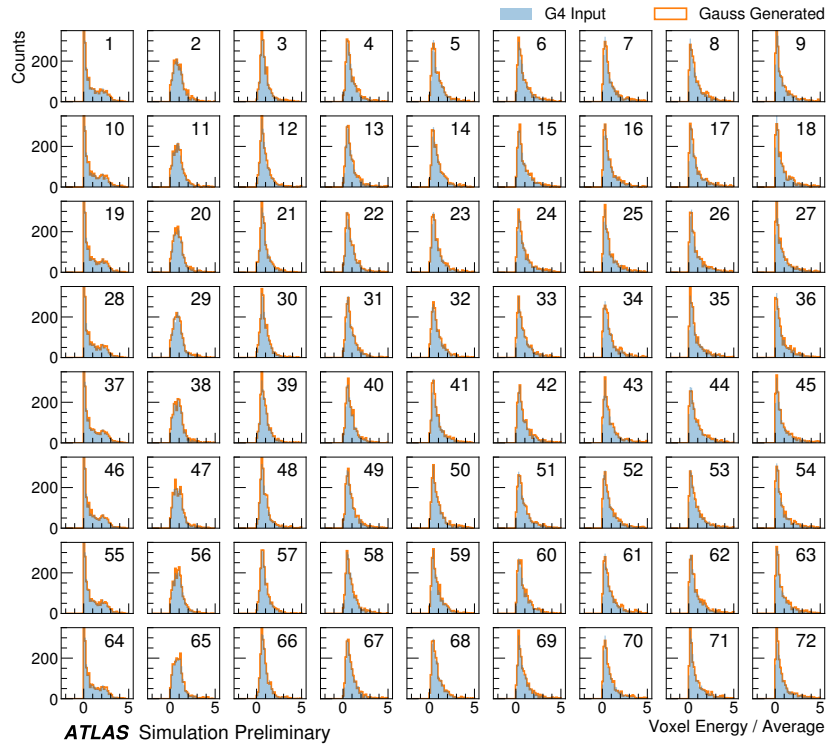


Figure 4.5: Distribution of the ratio of voxel energy in single events to the corresponding voxel energy in the average shape, with GEANT4 events in blue and Gaussian model events in orange, for 65 GeV central pions in EMB2. Moving top to bottom corresponds to increasing α , left to right corresponds to increasing R , with core voxels numbered 1, 10, 19, Agreement is quite good across all voxels. Results are similar for the VAE method.

1476 Figure 4.5 shows the distributions of input GEANT4 and Gaussian method generated
 1477 energy ratios in the grid of voxels. Figure 4.6 shows the correlation coefficient between the
 1478 center voxel from $\alpha = 0$ to $2\pi/8$ for input GEANT4 and the Gaussian and VAE fluctuation

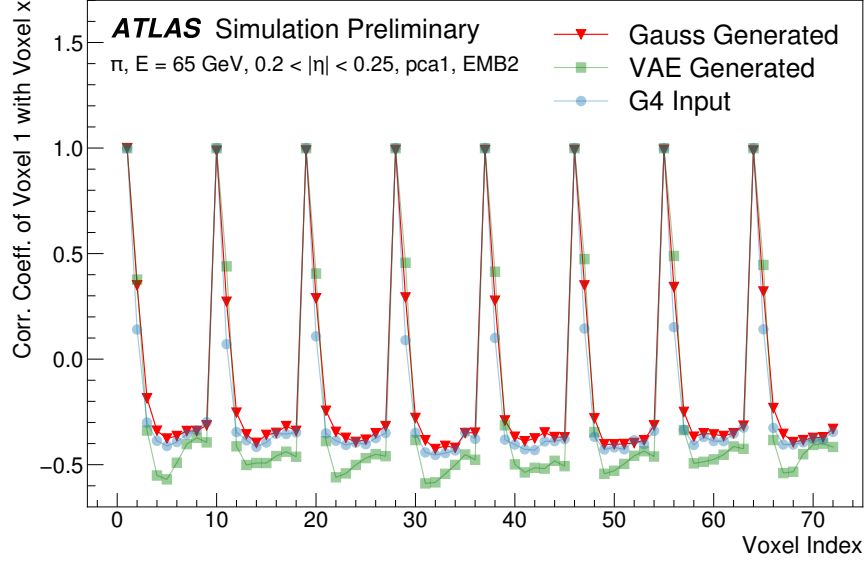


Figure 4.6: Correlation coefficient of ratios of voxel energy in single events to the corresponding voxel energy in the average shape, examined between the core bin from $\alpha = 0$ to $2\pi/8$ and each of the other voxels. The periodic structure represents the binning in α , and the increasing numbers in each of these periods correspond to increasing R , where the eight points with correlation coefficient 1 are the eight core bins. Both the Gaussian and VAE generated toy events are able to reproduce the major correlation structures for 65 GeV central pions in EMB2.

1479 methods. Agreement is good throughout.

1480 Validation of the Gaussian and VAE fluctuation methods was performed within FastCaloSimV2.
 1481 Figure 4.7 shows the energy ratio of cells for a given simulation to the corresponding cells in
 1482 the average shape as a function of the distance from the shower center. The mean for all
 1483 simulation methods is expected to be around 1, with deviation from the average (the RMS
 1484 fluctuation) shown by the error bars. The Gaussian method RMS (red) and VAE method
 1485 RMS (green) both match the GEANT4 RMS (yellow) better than the case without correlated
 1486 fluctuations (blue) for a variety of energies, η points, and layers, often reproducing 80 – 100 %

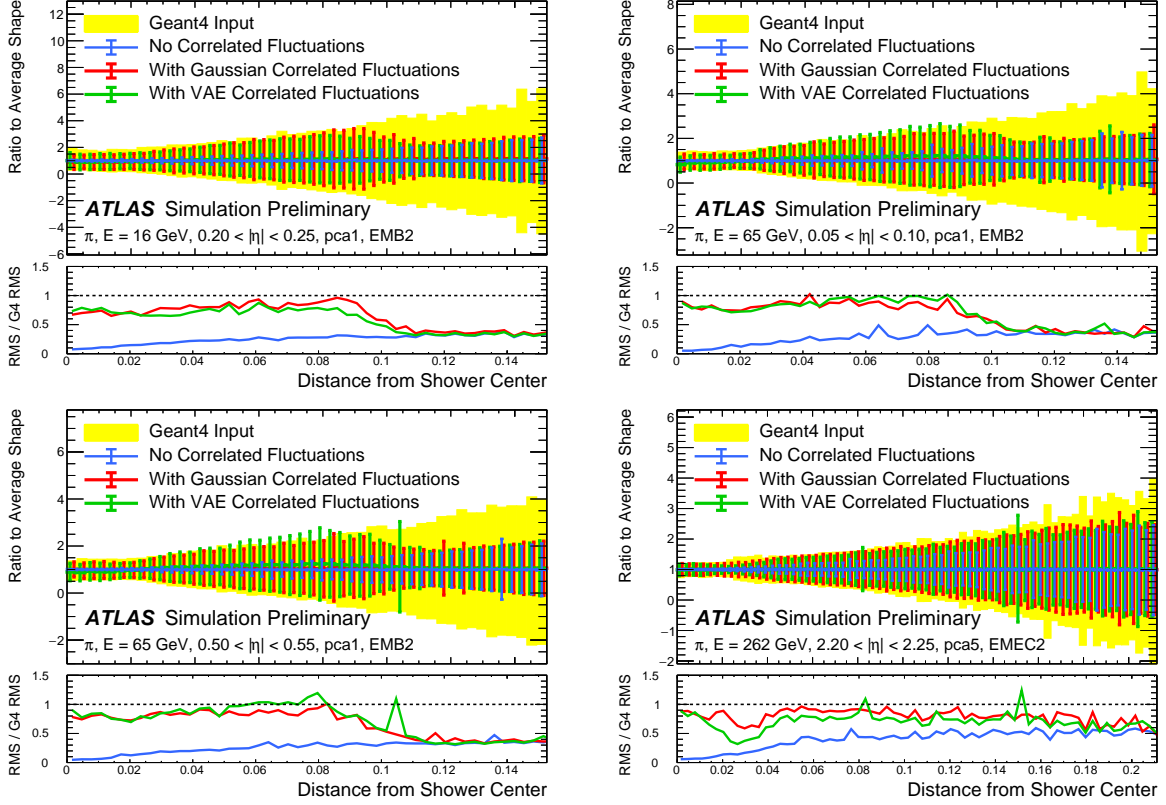


Figure 4.7: Comparison of the RMS fluctuations about the average shape with the Gaussian fluctuation model (red), the VAE fluctuation model (green), and without correlated fluctuations (blue) for a range of pion energies, η points, and layers.

1487 of the GEANT4 RMS magnitude, compared to the 5 – 30 % observed in the no correlated
1488 fluctuations case.

1489 Figure 4.8 shows the result of a simulation with full ATLAS reconstruction for 65 GeV
1490 central pions with the Gaussian fluctuation model. Here a *cluster* [71] is defined as a three-
1491 dimensional spatial grouping of calorimeter cells which are summed based on the input signals
1492 relative to their neighboring cells. The multiplicity, shape, and spatial distribution of such
1493 clusters provides a powerful insight on the structure of energy deposits in the calorimeter,
1494 and good performance in cluster variables is a promising step towards good performance

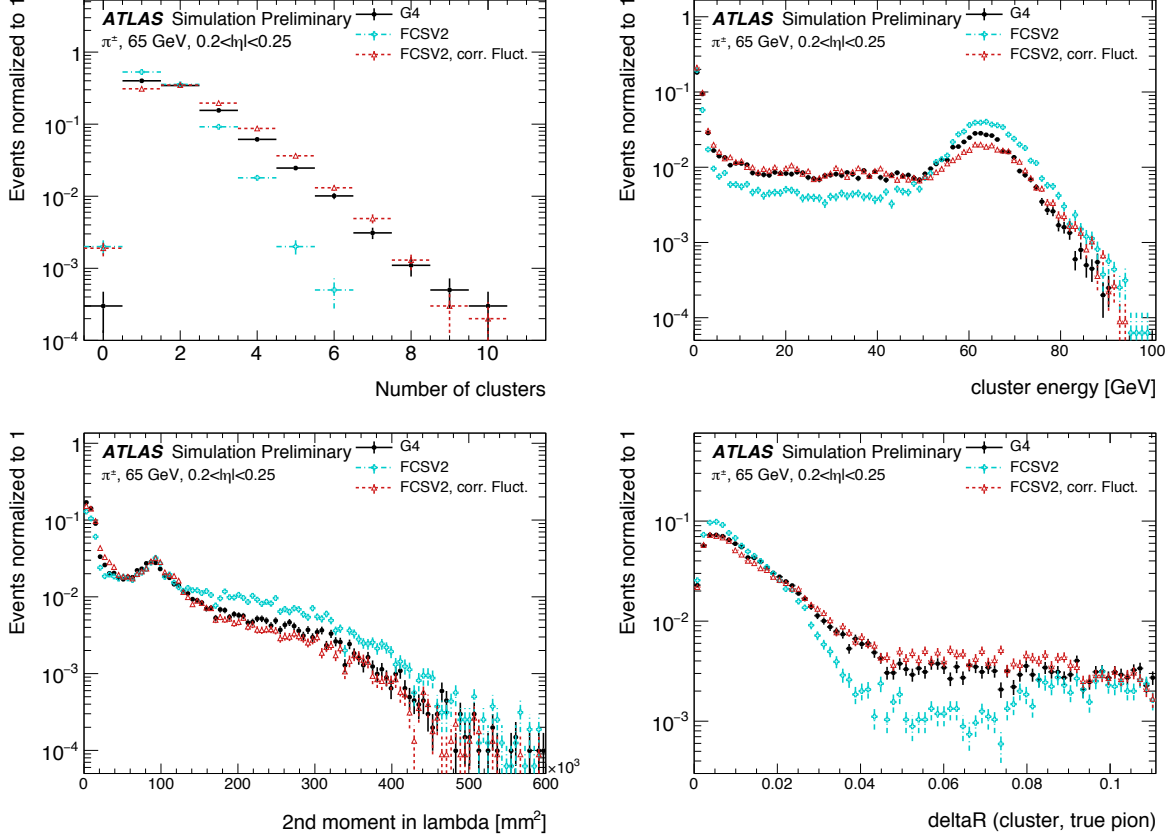


Figure 4.8: Comparison of the Gaussian fluctuation model to the default FCSV2 version and to G4 simulation, using pions of 65 GeV energy and $0.2 < |\eta| < 0.25$. Variables shown relate to calorimeter clusters, three-dimensional spatial groupings of cells [71] which provide powerful insight on the structure of energy deposits in the calorimeter. Variables considered include number and energy of clusters, the 2nd moment in lambda, ($\langle \lambda^2 \rangle$), which describes the square of the longitudinal extension of a cluster, where λ is the distance of a cell from the shower center along the shower axis, and a cluster moment is defined as $\langle x^n \rangle = \frac{\sum E_i x_i}{\sum E_i}$, and the distance ΔR , between the cluster and the true pion. With the correlated fluctuations, variables demonstrate improved modeling relative to default FastCaloSimV2.

1495 in the modeling of jet substructure, as these clusters may themselves be summed to form
 1496 jets (see Chapter 5). The simulation with the Gaussian fluctuation model demonstrates
 1497 improved modeling of several of these cluster variables relative to baseline FastCaloSimV2,
 1498 reproducing the distributions of events simulated with GEANT4. These include number and
 1499 energy of clusters, the 2nd moment in lambda, ($\langle \lambda^2 \rangle$), which describes the square of the
 1500 longitudinal extension of a cluster, where λ is the distance of a cell from the shower center
 1501 along the shower axis, and a cluster moment is defined as $\langle x^n \rangle = \frac{\sum E_i x_i}{\sum E_i}$, and the distance
 1502 ΔR , between the cluster and the true pion.

1503 The new fast calorimeter simulation is a crucial part of the future of simulation for the
 1504 ATLAS Experiment at the LHC. The per event simulation time of the full detector with
 1505 GEANT4, calculated over 100 $t\bar{t}$ events, is 228.9 s. Using FastCaloSim for the calorimeter
 1506 simulation reduces this to 26.6 s, of which FastCaloSim itself is only 0.015 s, with the majority
 1507 of the remaining simulation time due to GEANT4. Good physics modeling is achieved, and
 1508 the correlated fluctuations method shows good proof of concept improvement for the modeling
 1509 of hadronic showers.

1510 **4.4 Outlook**

1511 There has been significant effort in the community to develop a set of fast simulation tools,
 1512 with the use of machine learning methods at the forefront of such approaches (e.g. [72], [73]).
 1513 Most fast simulation approaches generally are based on parametrizations of fully simulated
 1514 events, but fall into two paradigms - a “by hand” simulation, which focuses on the modeling
 1515 of individual detector effects, or a fully parametrized simulation, in which a generative model
 1516 (e.g. a Generative Adversarial Network or Variational Autoencoder) is trained to directly
 1517 reproduce the input events. Both approaches can be extremely powerful, but each suffer from
 1518 certain drawbacks. The “by hand” approach offers the advantage of direct encoding of expert
 1519 knowledge – if an effect needs to be modeled, a new parametrization is introduced. However,
 1520 by the same token, it requires dedicated parametrizations for each effect. Fully parametrizing
 1521 the simulation with a generative model offloads this burden onto the network itself. However,

1522 by doing so, the ability to use expert knowledge is diminished – the network is required to
1523 learn all relevant effects.

1524 The method presented here represents an effort to step towards a hybrid between these two
1525 approaches, leveraging the power of machine learning techniques for individual parametriza-
1526 tions within the by hand framework. Such hybrid solutions have the potential to be extremely
1527 powerful, and further work on the development of these solutions is an interesting direction
1528 of future study.

1529

Chapter 5

1530

RECONSTRUCTION

1531 Chapter 3 discusses how a proton-proton collision may be captured by a physical detector
 1532 and turned into data that may be stored and analyzed. Chapter 4 discusses the simulation
 1533 of this same process. At this most basic level, however, the ATLAS detector is only a
 1534 machine for turning particles into a set of electrical signals, albeit in a very sophisticated,
 1535 physics motivated way. This chapter discusses the step of turning these electrical signals into
 1536 objects which may be identified with the underlying physics processes, and therefore used to
 1537 make statements about what occurred within a given collision event. This process is termed
 1538 *reconstruction*, and we will focus particularly on jets and flavor tagging, as the most relevant
 1539 pieces for this thesis work.

1540 **5.1 Jets**

1541 As discussed in Chapters 3 and 4, the production of particles with color charge from a
 1542 proton-proton interaction is complicated both by parton showering and by confinement: a
 1543 quark produced from a hard scatter is not seen as a quark, but rather, as a spray of particles
 1544 with a variety of hadrons in the final state, which subsequently shower upon interaction with
 1545 the calorimeter in a complicated way.

1546 For hard scatter electrons, photons, or muons on the other hand, the picture is much
 1547 clearer: there is no parton showering, and each has a distinct signature in the detector:
 1548 photons have no tracks and a very localized calorimeter shower, electrons are associated
 1549 with tracks and are similarly localized in the calorimeter, and muons are associated with
 1550 tracks, pass through the calorimeter due to their large mass, and leave signatures in the muon
 1551 spectrometer.

Jets are a tool to deal with the messiness of quarks and gluons. The basic concept is to group the multitude of particles produced by hadronization into a single object. Such an object then has associated properties, including a four-vector, which may be identified with the corresponding initial state particle. In practice a variety of information from the ATLAS detector is used for such a reconstruction. The analysis considered in this thesis uses particle flow jets [74], which combines information from both the tracker and the calorimeter, where the combined objects may be identified with underlying particles. However, jets built from clusters of calorimeter cells [75] as well as from charged particle tracks [76] have also been used very effectively.

A variety of algorithms are used to associate detector level objects to a given jet. The most commonly used in ATLAS is the anti- k_T algorithm [77], which is a successor to the k_T algorithm, among others [78], and develops as follows. Both algorithms are sequential recombination algorithms, which begin with the smallest distance, d_{ij} between considered objects (e.g. particles or intermediate groupings of particles). If d_{ij} is less than a parameter d_{iB} (B for “beam”) object i is combined with object j , the distance d_{ij} is recomputed, and the process repeats. This proceeds until $d_{ij} \geq d_{iB}$, at which point the jet is “complete” and removed from the list of considered objects.

The definitional difference between k_T and anti- k_T is these distance parameters. In general form, these are defined as

$$d_{ij} = \min(p_{Ti}^{2p}, p_{Tj}^{2p}) \frac{\Delta R_{ij}^2}{R^2} \quad (5.1)$$

$$d_{iB} = p_{Ti}^{2p} \quad (5.2)$$

where p_{Ti} is the transverse momentum of object i , ΔR_{ij} is the angular distance between objects i and j , R is a radius parameter, and p controls the tradeoff between the p_T and angular distance terms. For the k_T algorithm $p = 1$; for the anti- k_T algorithm, $p = -1$. This is a simple change, but results in significantly different behavior.

The anti- k_T algorithm can be understood as follows: for a single high p_T particle (p_{T1}) surrounded by a bunch of low p_T particles, the low p_T particles will be clustered with the

high p_T one if

$$d_{1j} = \frac{1}{p_{T1}^2} \frac{\Delta R_{1j}^2}{R^2} < \frac{1}{p_{T1}^2} \quad (5.3)$$

$$\implies \Delta R_{1j} < R. \quad (5.4)$$

1573 Therefore, a single high p_T particle (p_{T1}) surrounded by a bunch of low p_T particles results in
 1574 a perfectly conical jet. This shape may change with the presence of other high momentum
 1575 particles, but the key feature of the dynamics is that the jet shape is determined by high p_T
 1576 objects due to the $\frac{1}{p_T}$ nature of this definition. In contrast, the k_T algorithm results in jets
 1577 influenced by low momentum particles, which results in a less regular shape. This property,
 1578 of regular jet shapes determined by high momentum objects, as well as demonstrated good
 1579 practical performance, makes the anti- k_T algorithm the favored jet algorithm in ATLAS.

1580 Because jets are composed of multiple objects, a useful property of jets is jet *substructure*,
 1581 that is, acknowledging that jets are composite objects, analyzing the structure of a given
 1582 jet to infer physics information. This leads to the use of *subjets*; that is, after running jet
 1583 clustering, often to create a “large-R”, $R = 1.0$ anti- k_T jet, a smaller radius jet clustering
 1584 algorithm is run within the jet. Subjets are often chosen using the k_T algorithm, which again
 1585 is sensitive to lower momentum particles, with $R = 0.2$ or 0.3 . For the boosted version of this
 1586 thesis analysis, such a strategy is used, in which the subjets are *variable radius* and depend
 1587 on the momentum of the (proto)jet in question. Beyond this thesis work, substructure is
 1588 used in a large variety of analyses, with a set of associated variables and tools developed for
 1589 exploiting this structure *TODO: Cite some?*.

1590 5.2 Flavor Tagging

1591 For this this thesis, the physics process being considered is $HH \rightarrow b\bar{b}b\bar{b}$. From the previous
 1592 section, we know that the standard practice is to identify these b quarks (or, rather, the
 1593 resulting B hadrons, due to confinement) with jets – in our case, these b -*jets* are $R=0.4$
 1594 anti- k_T particle flow jets (see Chapter 7). However, not all jets produced at the LHC are
 1595 from B hadrons; rather, there are a variety of different types of jets corresponding to different

1596 flavors of quarks. These are often classified as light jets (from u , d , or s quarks, or gluons)
 1597 or as other *heavy flavor* jets, e.g. c -jets, involving c quarks. Distinguishing between these
 1598 different categories is a very active area of work in ATLAS, termed *flavor tagging*, with much
 1599 focus on *b-tagging* in particular, that is, the identification of jets from B hadron decays. We
 1600 here briefly describe the techniques used for flavor tagging in ATLAS.

1601 What distinguishes a b -jet from any other jet? This question is fundamental to the
 1602 design of the various b -tagging algorithms, and has two major answers: (1) B hadrons have
 1603 long lifetimes, and (2) B hadrons have large masses. It is most illustrative to compare
 1604 the B hadron properties to a common light meson, e.g. π^0 , the neutral pion, with quark
 1605 content $\frac{1}{\sqrt{2}}(u\bar{u} - d\bar{d})$. B hadrons have lifetimes around 1.5 ps, corresponding to a decay length
 1606 $c\tau \approx 0.45$ mm. In contrast, π^0 has a lifetime of 8.4×10^{-5} ps, which is around 20,000 times
 1607 shorter! Theoretically, this comes from CKM suppression of the b to c transition, which
 1608 dominates the B decay modes. Experimentally, this difference pops up as shown in Figure
 1609 5.1 – light flavor initiated jets decay almost immediately at the proton-proton interaction
 1610 point, whereas b -jets are distinguished by a displaced secondary vertex, corresponding to
 1611 the 5 mm decay length calculated above. This displaced vertex falls short of the detector
 1612 itself, but may be inferred from larger transverse (perpendicular to beam) and longitudinal
 1613 (parallel to beam) impact parameters of the resulting tracks, termed d_0 and z_0 respectively.

1614 Coming to the mass, B mesons have masses of around 5.2 GeV, whereas the π^0 mass
 1615 is around 0.134 GeV, (around 40 times lighter). This higher mass gives access to a larger
 1616 decay phase space, leading to a high multiplicity for b -jets (average of 5 charged particles per
 1617 decay).

1618 One final distinguishing feature of B hadrons is their *fragmentation function*, a function
 1619 describing the production of an observed final state. For B hadrons, this is particularly
 1620 “hard”, with the B hadrons themselves contributing to an average of around 75 % of the b -jet
 1621 energy. Thus, the identification of b -jets with B hadrons is, in some sense, descriptive.

1622 We have contrasted b -jets and light jets, demonstrating that there are several handles
 1623 available for making this distinction. c -jets are slightly more similar to b -jets, but the same

1624 handles still apply – c -hadron lifetimes are between 0.5 and 1 ps, a factor of 2 smaller than B
1625 hadrons. Their mass is around 1.9 GeV, 2 to 3 times smaller than B hadrons, and c -hadrons
1626 contribute to an average of around 55 % of c -jet energy. Therefore, while the gap is slightly
1627 smaller, a distinction may still be made.

1628 The ATLAS flavor tagging framework [80] relies on developing a suite of “low-level”
1629 taggers, which use a variety of information about tracks and vertices as inputs. The output
1630 of these lower level taggers are then fed into a higher level tagger, which aggregates these
1631 results into a high level discriminant. Each of these taggers is described below.

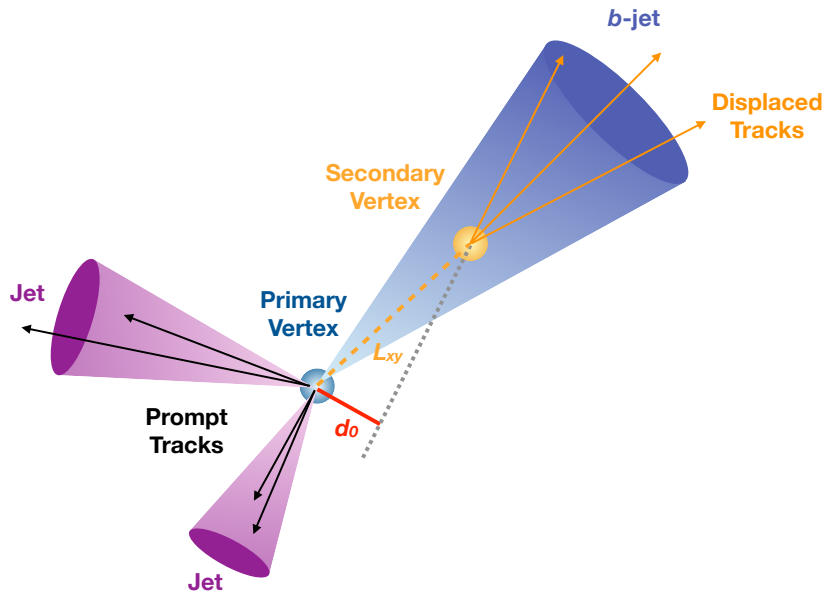


Figure 5.1: Illustration of an interaction producing two light jets and one b -jet in the transverse plane. While the light jets decay “promptly”, coinciding with the primary vertex of the proton-proton interaction, the longer lifetime of B hadrons leads to a secondary decay vertex, displaced from the primary vertex by length L_{xy} . This is typically a few mm, and therefore is not directly visible in the detector, but leads to a large transverse impact parameter, d_0 , for the resulting tracks. [79]

1632 5.2.1 IP2D/3D

1633 IP2D and IP3D are taggers based on the large track impact parameter (IP) nature of B
 1634 hadron decays. Both are based on histogram templates derived from Monte Carlo simulation,
 1635 which are used as probability density functions to construct log-likelihood discriminants.
 1636 IP2D incorporates just the transverse impact parameter information using 1D histogram
 1637 templates, whereas IP3D uses both transverse and longitudinal impact parameters in a 2D
 1638 template, which accounts for correlations. Importantly, these are *signed* impact parameters,
 1639 with sign based on the angle between the impact parameter and the considered jet – positive
 1640 impact parameters are consistent with a track extrapolation in front of the jet (angle between
 1641 impact parameter line and jet $< 90^\circ$), and therefore more consistent with tracks originating
 1642 from a displaced decay.

1643 Rather than using the impact parameters directly, an impact parameter *significance*
 1644 is used which incorporates an uncertainty on the impact parameter – tracks with a lower
 1645 uncertainty but the same impact parameter will contribute more in the calculation. This
 1646 signed significance is what is used to sample from the PDF templates, with the resulting
 1647 discriminants the sum of probability ratios between given jet hypotheses over tracks associated
 1648 to a given jet, namely $\sum_{i=1}^N \log \frac{p_b}{p_{light}}$ between b -jet and light jet hypotheses, where p_b and
 1649 p_{light} are the per-track probabilities. Similar discriminants are defined between b - and c -jets
 1650 and c and light jets. *TODO: show distributions?*

1651 5.2.2 SV1

1652 SV1 is an algorithm which aims to find a secondary vertex (SV) in a given jet. Operating
 1653 on all vertices associated with a considered jet, the algorithm discards tracks based on a
 1654 variety of cleaning requirements. It then proceeds to first construct all two-track vertices,
 1655 and then iterates over all the tracks involved in these two track vertices to try to fit a single
 1656 secondary vertex, which would then be identified with the secondary vertex from the b or c
 1657 hadron decay. This fit proceeds by evaluating a χ^2 for the association of a track and vertex,

removing the track with the largest χ^2 , and iterating until the χ^2 is acceptable and the vertex has an invariant mass of less than 6 GeV (for consistency with b or c hadron decay).

A variety of discriminating variables may then be constructed, including (1) invariant mass of the secondary vertex, (2) number of tracks associated with the secondary vertex, (3) number of two-track vertices, (4) energy fraction of the tracks associated to the secondary vertex (relative to all of the tracks associated to the jet), and various metrics associated with the secondary vertex position and decay length, including (5) transverse distance between the primary and secondary vertex, (6) distance between the primary and secondary vertex (7) distance between the primary and secondary vertex divided by its uncertainty, and (8) ΔR between the jet axis and the direction of the secondary vertex relative to the primary vertex.

While all eight of these variables are used as inputs to the higher level taggers, the number of two-track vertices, the vertex mass, and the vertex energy fraction are additionally used with 3D histogram templates to evaluate flavor tagging performance by constructing log-likelihood discriminants, similar to the procedure for IP2D/3D.

5.2.3 JetFitter

Rather than focusing on a particular aspect of the B hadron or D hadron decay topology (e.g impact parameter or secondary vertex), the third low level tagger, JETFITTER [81], tries to reconstruct the full decay chain, including all involved vertices. This is structured around a Kalman filter formalism [82], and has the strong underlying assumption that all tracks which stem from B and D hadron decay must intersect a common flight path. This assumption provides significant constraints, allowing for the reconstruction of vertices from even a single track, reducing the number of degrees of freedom in the fit, and allowing the use of “downstream” information, e.g., compatibility of tracks with a $B \rightarrow D$ -like decay. The constructed topology, including primary vertex location and B -hadron flight path, is iteratively updated over tracks associated to a given jet, and a variety of discriminating variables related to the resulting topology and reconstructed decay are used as inputs to the high level taggers.

1685 5.2.4 *RNNIP*

1686 The IP2D and IP3D algorithms rely on per-track probabilities, and the final discriminating
 1687 variables (and inputs to the higher level taggers) are sums (products) over these independently
 1688 considered quantities. In practice, however, the tracks are not independent – this is merely a
 1689 simplifying assumption to allow for the use of a binned likelihood, as treatment of all of the
 1690 interdependencies in such a framework quickly becomes intractable. To address this issue, a
 1691 recurrent neural network-based algorithm, RNNIP [83], is used, which takes as input a variety
 1692 of per-track variables, including the signed impact parameter significances (as in IP3D) as
 1693 well as track momentum fraction relative to the jet and ΔR between the track and the jet.
 1694 RNNs are sequence-based, and vectors of input variables corresponding to tracks for a given
 1695 jet are ordered by magnitude of transverse impact parameter significance and then passed
 1696 to the network, which outputs class probabilities corresponding to b-jet, c-jet, light-jet, and
 1697 τ -jet hypotheses. Such a procedure allows the network to learn interdependencies between
 1698 tracks, improving performance.

1699 5.2.5 *MV2 and DL1*

1700 Outputs from the above taggers are combined into high level taggers to aggregate all of the
 1701 information and improve discriminating power relative to the respective individual taggers as,
 1702 as shown in Figure 5.2. These high level taggers are primarily in two forms: MV2, which
 1703 uses a Boosted Decision Tree (BDT) for this aggregation, and DL1, which uses a deep neural
 1704 network. For the baseline versions of these taggers, only inputs from IP2D, IP3D, SV1, and
 1705 JetFitter are used. The tagger used for this thesis analysis, DL1r, additionally incorporates
 1706 RNNIP, demonstrating improved performance over the baseline DL1, as shown in Figure 5.3.
 1707 All high level taggers also include jet p_T and $|\eta|$.

DL1 offers a variety of improvements over MV2. Rather than a single discriminant output, as with MV2, DL1 has a multidimensional output, corresponding to probabilities for a jet to be a *b*-jet, *c*-jet, or light jet. This allows the trained network to be used for both *b*- and *c*-jet

tagging. The final discriminant for b -tagging with DL1 correspondingly takes the form

$$D_{\text{DL1}} = \ln \left(\frac{p_b}{f_c \cdot p_c + (1 - f_c) \cdot p_{\text{light}}} \right) \quad (5.5)$$

where p_b , p_c , and p_{light} are the output b , c , and light jet probabilities, and f_c corresponds to an effective c -jet fraction, which may be tuned to optimize performance.

DL1 further includes an additional set of JETFITTER input variables relative to MV2 which correspond to c -tagging – notably properties of secondary and tertiary vertices, as would be seen in a $B \rightarrow D$ decay chain.

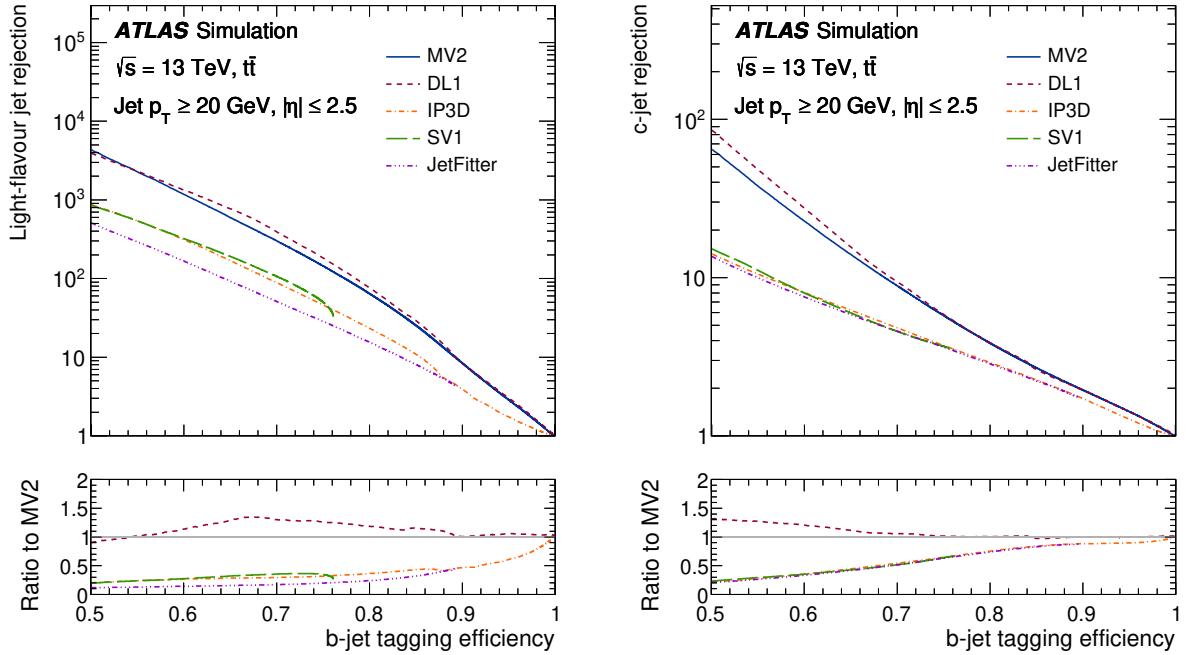


Figure 5.2: Performance of the various low and high level flavor tagging algorithms in $t\bar{t}$ simulation, demonstrating the tradeoff between b -jet efficiency and light and c -jet rejection. The high level taggers demonstrate significantly better performance than any of the individual low level taggers, with DL1 offering slight improvements over MV2 due to the inclusion of additional input variables.

Figure 5.2 shows a comparison of the performance of the various taggers. The b -tagging performance of DL1 and MV2 is found to be similar, with some improvements in light jet and c -jet rejection from the additional variables used in DL1. The performance of these high level taggers additionally is seen to be significantly better than any of the individual low level ones, even in regimes where only a single low level tagger is relevant (such as high b -tagging efficiencies, where SV1 and JETFITTER are limited by selections on tracks entering the respective algorithms).

The inclusion of RNNIP offers a significant improvement on top of baseline DL1, as shown in Figure 5.3, strongly motivating the choice of DL1r for this thesis.

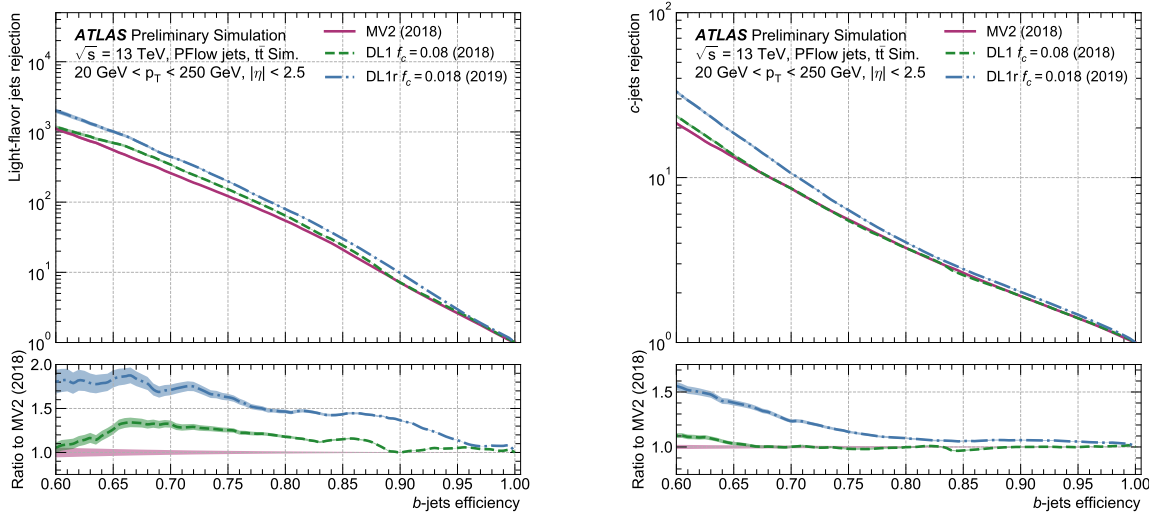


Figure 5.3: Performance of the MV2, DL1, and DL1r algorithms in $t\bar{t}$ simulation, demonstrating the tradeoff between b -jet efficiency and light and c -jet rejection. f_c controls the importance of c -jet rejection in the discriminating variable, and values shown have been optimized separately for each DL1 configuration. DL1r demonstrates a significant improvement in both light and c jet rejection over MV2 and DL1. [84]

1722 5.2.6 *Some Practical Notes*

1723 The b -tagging metrics presented in Figures 5.2 and 5.3 correspond to evaluating a tradeoff
1724 between b -jet efficiency and light jet and c -jet rejection. In this case, b -jet efficiency is defined
1725 such that, e.g. for a 77 % efficiency, 77 % of the real b -jets will be tagged as such. Somewhat
1726 counterintuitively, this means that a lower b -jet efficiency corresponds to a more aggressive
1727 (“tighter”) selection on the discriminating variable, while a higher b -jet efficiency corresponds
1728 to a less aggressive (“looser”) cut (100 % efficiency means no cut). Light and c jet efficiencies
1729 are defined similarly, with rejection defined as 1/ the corresponding efficiency.

1730 In ATLAS, the respective b -tagging efficiencies are used to define various b -tagging working
1731 points. The working point used for the nominal b -jet identification in this thesis is 77 % with
1732 DL1r. A loosened (less aggressive) selection at the 85 % working point is additionally used.
1733 See Chapter 7 for further details.

1734

Chapter 6

1735

THE ANATOMY OF AN LHC SEARCH

1736 In this thesis so far, we have set the theoretical foundation for the work carried out at the
 1737 LHC. We have described how one may translate between this theoretical foundation and what
 1738 we are actually able to observe with the ATLAS detector. We have further stepped through
 1739 the process of simulating production of specific physics processes and their appearance in
 1740 our detector, allowing us to describe how a hypothetical physics model would be seen in
 1741 our experiment. The question then becomes: all of these pieces are on the table, what do
 1742 we do with them? This chapter attempts to answer exactly that, setting up a roadmap for
 1743 assembling these pieces into a statement about the universe.

1744 ***6.1 Object Selection and Identification***

1745 As described in Chapter 5, there is a complicated set of steps for going from electrical signals
 1746 in a detector to physics objects.

1747 ***6.2 Defining a Signal Region***

1748 ***6.3 Background Estimation***

1749 ***6.4 Uncertainty Estimation***

1750 ***6.5 Hypothesis Testing***

1751

Chapter 7

1752

SEARCH FOR PAIR PRODUCTION OF HIGGS BOSONS IN THE $b\bar{b}b\bar{b}$ FINAL STATE

1753

This chapter presents two complementary searches for pair production of Higgs bosons in the final state. Such searches are separated based on the signal models being considered: resonant production, in which a new spin-0 or spin-2 particle is produced and decays to two Standard Model Higgs bosons, and non-resonant production, which is sensitive to the value of the Higgs self-coupling λ_{HHH} . Further information on the theory behind both channels can be found in Chapter 2.

While the searches face many similar challenges and proceed (in broad strokes) in a very similar manner, separate optimizations are performed to maximize the respective sensitivities for these two very different sets of signal hypotheses. More particularly, resonant signal hypotheses are (1) very peaked in values of the mass of the HH candidate system near the value of the resonance mass considered and (2) considered across a very broad range of signal mass hypotheses. The resonant searches are therefore split into resolved and boosted topologies based on Lorentz boost of the decay products, with the resolved channel as one of the primary focuses of this thesis. Further, several analysis design decisions are made to allow for sensitivity to a broad range of masses – in particular, though sensitivity is limited at lower values of m_{HH} relative to other channels *TODO: Combination, bbyy* due to the challenging background topology, retaining and properly reconstructing these low mass events allows the $b\bar{b}b\bar{b}$ channel to retain sensitivity as low as the kinematic threshold at 250 GeV.

In contrast, non-resonant signal hypotheses are quite broad in m_{HH} , and have a much more limited mass range, with Standard Model production peaking near 400 GeV, and the majority of the analysis sensitivity able to be captured with a resolved topology. Even for

1775 Beyond the Standard Model signal hypotheses, which may have more events at low m_{HH} ,
 1776 the non-resonant nature of the production allows the $b\bar{b}b\bar{b}$ channel to retain sensitivity while
 1777 discarding much of the challenging low mass background. Such freedom allows for decisions
 1778 which focus on improved background modeling for the middle to upper HH mass regime,
 1779 resulting in improved modeling and smaller uncertainties than would be obtained with a
 1780 more generic approach.

1781 Both searches are presented in the following, with emphasis on particular motivations for,
 1782 and consequences of, the various design decisions involved for each respective set of signal
 1783 hypotheses.

1784 The analyses improve upon previous work [1] in several notable ways. The resonant search
 1785 leverages a Boosted Decision Tree (BDT) based pairing algorithm, offering improved HH
 1786 pairing efficiency over a broad mass spectrum. The non-resonant adopts a different approach,
 1787 with a simplified algorithm based on the minimum angular distance (ΔR) between jets in
 1788 a Higgs candidate. Such an approach very efficiently discards low mass background events,
 1789 resulting in an easier to estimate background with reduced systematic uncertainties.

1790 A particular contribution of this thesis is the background estimation, which uses a novel,
 1791 neural network based approach, offering improved modeling over previous methods, as well
 1792 as the ability to model correlations between observables. While all aspects of the analysis of
 1793 course contribute to the final result, the author of this thesis wishes to emphasize that the
 1794 background estimate, with the corresponding uncertainties and all other associated decisions,
 1795 really is the core of the $HH \rightarrow b\bar{b}b\bar{b}$ analysis – the development of this procedure, and all
 1796 associated decisions, is similarly the core of this thesis work.

1797 ATLAS has performed a variety of searches in complementary decay channels as well,
 1798 notably for early Run 2 in the $b\bar{b}W^+W^-$ [85], $b\bar{b}\tau^+\tau^-$ [86], $W^+W^-W^+W^-$ [87], $b\bar{b}\gamma\gamma$ [88],
 1799 and $W^+W^-\gamma\gamma$ [89] final states, which were combined along with $b\bar{b}b\bar{b}$ in [24]. ATLAS has
 1800 also released a variety of full Run 2 results, including boosted $b\bar{b}\tau^+\tau^-$ [90], VBF $b\bar{b}b\bar{b}$ [20],
 1801 $b\bar{b}\ell\nu\ell\nu$ [91], and $b\bar{b}\gamma\gamma$ [92].

1802 CMS has also performed searches for resonant production of Higgs boson pairs in the

1803 $b\bar{b}b\bar{b}$ final state (among others) at $\sqrt{s} = 8$ TeV [93] and $\sqrt{s} = 13$ TeV [94]. CMS have also
1804 performed a combination of their searches in the $b\bar{b}b\bar{b}$, $b\bar{b}\tau^+\tau^-$, $b\bar{b}\gamma\gamma$, and $b\bar{b}VV$ channels
1805 in [95].

1806 This analysis also benefits from improvements to ATLAS jet reconstruction and calibration,
1807 and flavor tagging [80]. In particular, this analysis benefits from the introduction of particle
1808 flow jets [74]. These make use of tracking information to supplement calorimeter energy
1809 deposits, improving the angular and transverse momentum resolution of jets by better
1810 measuring these quantities for charged particles in those jets.

1811 The analysis also benefits from the new DL1r ATLAS flavor tagging algorithm. Whereas
1812 the flavor tagging algorithm used in the previous analysis (MV2) used a boosted decision tree
1813 (BDT) to combine the output of various low level algorithms, DL1r (and the baseline DL1
1814 algorithm) uses a deep neural network to do this combination. In addition to the low level
1815 algorithms used as inputs to MV2, DL1 includes a variety of additional variables used for
1816 c -tagging. DL1r further incorporates RNNIP, a recurrent neural network designed to identify
1817 b -jets using the impact parameters, kinematics, and quality information of the tracks in the
1818 jets, while also taking into account the correlations between the track features.

1819 The overall analysis sensitivity further benefits from a factor of ~ 4.6 increase in integrated
1820 luminosity.

1821 7.1 Data and Monte Carlo Simulation

1822 Both the resonant and non-resonant searches are performed on the full ATLAS Run 2 dataset,
1823 consisting of $\sqrt{s} = 13$ TeV proton-proton collision data taken from 2016 to 2018 inclusive.
1824 Data taken in 2015 is not used due to a lack of trigger jet matching information and b -jet
1825 trigger scale factors. The integrated luminosity collected and usable in this analysis¹ was:

- 1826
- 24.6 fb^{-1} in 2016

¹approximately 9 fb^{-1} of data was collected but could not be used in this analysis due to an inefficiency in the b -jet triggers at the start of 2016 [96]

- 1827 • 43.65 fb^{-1} in 2017

- 1828 • 57.7 fb^{-1} in 2018

1829 This gives a total integrated luminosity of 126 fb^{-1} . This is lower than the 139 fb^{-1} ATLAS
 1830 collected during Run 2 [97] due to the inefficiency described in footnote 1 as well as the
 1831 3.2 fb^{-1} of 2015 data which is unused due to the trigger scale factor issue mentioned above.

1832 In this analysis, Monte Carlo samples are used purely for modelling signal processes. The
 1833 background is strongly dominated by events produced by QCD multijet processes, which
 1834 are difficult to correctly model in simulation. This necessitates the use of a data-driven
 1835 background modelling technique, which is described in Section 7.6.

1836 The scalar resonance signal model is simulated at leading order in α_s using MADGRAPH
 1837 [55]. Hadronization and parton showering are done using HERWIG 7 [56][57] with EVTGEN [59],
 1838 and the nominal PDF is NNPDF 2.3 LO. In practice this is implemented as a two Higgs
 1839 doublet model where the new neutral scalar is produced through gluon fusion and required
 1840 to decay to a pair of SM Higgs bosons. The heavy scalar is assigned a width much smaller
 1841 than detector resolution, and the other 2HDM particles do not enter the calculation.

1842 Scalar samples are produced at resonance masses between 251 and 900 GeV and the
 1843 detector simulation is done using AtlFast-II [64]. In addition the samples at 400 GeV and
 1844 900 GeV are also fully simulated to verify that the use of AtlFast-II is acceptable. For higher
 1845 masses, as well as for the boosted analysis, samples are produced between 1000 and 5000 GeV,
 1846 and the detector is fully simulated. As discussed in Chapter 4, an outstanding issue with
 1847 AtlFast-II is the modeling of jet substructure. While such variables are not used for the
 1848 resolved analysis, the boosted analysis begins at 900 GeV, motivating the different detector
 1849 simulation in these two regimes.

1850 The spin-2 resonance signal model is also simulated at LO in α_s using MADGRAPH.
 1851 Hadronization and parton showering are done using PYTHIA 8 [58] with EVTGEN, and the
 1852 nominal PDF is NNPDF 2.3 LO. In practice this is implemented as a Randall-Sundrum
 1853 graviton with $c = 1.0$.

1854 Spin-2 resonance samples are produced at masses between 251 and 5000 GeV, and these
1855 samples are all produced with full detector simulation.

1856 For the non-resonant search, samples are produced at values of $\kappa_\lambda = 1.0$ and 10.0, and are
1857 simulated using POWHEG BOX v2 generator [52–54] at next-to-leading order (NLO), with full
1858 NLO corrections with finite top mass, using the PDF4LHC [98] parton distribution function
1859 (PDF) set. Parton showers and hadronization are simulated with PYTHIA 8.

1860 Alternative ggF samples are simulated at NLO using POWHEG BOX v2, but instead using
1861 HERWIG 7 [99] for parton showering and hadronization. The comparison between these two
1862 is used to assess an uncertainty on the parton showering.

1863 7.2 Triggers and Object Definitions

1864 To maximize analysis sensitivity, a combination of multi- b -jet triggers is used. Due to the use
1865 of events with two b -tagged jets in the background estimate, such triggers have a maximum
1866 requirement of two b -tagged jets. For the resonant analysis, a combination of triggers of
1867 various topologies is used, namely

1868 • 2b + HT, which requires two b -tagged jets and a minimum value of of H_T , defined to
1869 be the scalar sum of p_T across all jets in the event.

1870 • 2b + 2j, which requires two b -tagged jets and two other jets matching some kinematic
1871 requirements

1872 • 2b + 1j, which requires two b -tagged jets and one other jet matching some kinematic
1873 requirements

1874 • 1b, which requires one b -tagged jet

1875 Due to minimal contributions from some of these triggers for the Standard Model non-resonant
1876 signal, a simplified strategy relying entirely on 2b + 1j and 2b + 2j triggers is used for the
1877 non-resonant search.

1878 While the use of multiple triggers is beneficial for analysis sensitivity, it comes with some
 1879 complications. Namely, a set of scale factors must be assigned to simulated events to account
 1880 for differences in trigger efficiency between real and simulated events. Because these scale
 1881 factors may differ between triggers, the use of multiple triggers becomes complicated: an event
 1882 may pass more than one trigger, while trigger scale factors are only provided for individual
 1883 triggers.

1884 To simplify this calculation, a set of hierarchical offline selections is applied, closely
 1885 mimicking the trigger selection. Based on these selections, events are sorted into categories
 1886 (*trigger buckets*), after which the decision of a *single trigger* is checked.

1887 The resonant search applies such categorization in the following way, with selections
 1888 considered in order:

- 1889 1. If the leading jet is b -tagged with $p_T > 325 \text{ GeV}$, the event is in the $1b$ trigger category.
- 1890 2. Otherwise, if the leading jet is not b -tagged, but has $p_T > 168.75 \text{ GeV}$, the event is in
 1891 the $2b + 1j$ trigger category.
- 1892 3. If neither of the first two selections pass, if the scalar sum of jet p_T s, $H_T > 900 \text{ GeV}$,
 1893 the event falls into the $2b + HT$ trigger category.
- 1894 4. Events that do not pass any of the above offline selections are in the $2b + 2j$ trigger
 1895 category.

1896 Corresponding triggers are then checked in each category, and the final set of events consists
 1897 of those events that pass the trigger decision in their respective categories.

1898 For the resonant search, the $2b + 1j$ and $2b + 2j$ triggers are the dominant categories,
 1899 containing roughly 26 % and 49 % of spin-2 events, evaluated on MC16d samples with
 1900 resonance masses between 300 and 1200 GeV. Notably, the $1b$ trigger efficiency is largest at
 1901 high ($> 1 \text{ TeV}$) resonance masses.

1902 For the non-resonant search, it was noted that the $1b$ trigger has minimal contribution,
 1903 while the $2b + HT$ events are largely captured by the $2b + 2j$ trigger. Therefore, a simplified
 1904 scheme is considered, with selections:

- 1905 1. If the 1st leading jet has $p_T > 170 \text{ GeV}$ and the 3rd leading jet has $p_T > 70 \text{ GeV}$, the
 1906 event is in the $2b + 1j$ trigger category.
- 1907 2. Otherwise, the event is in the $2b + 2j$ trigger category.

1908 **7.3 Analysis Selection**

1909 After the trigger selections of Section 7.2, a variety of selections on the analysis objects are
 1910 made, with the goal of (1) reconstructing a HH -like topology and (2) suppressing contributions
 1911 from background processes.

1912 Both analyses begin with a common pre-selection, requiring at least four $R = 0.4$ anti- k_T
 1913 jets with $|\eta| < 2.5$ and $p_T > 40 \text{ GeV}$. The $|\eta| < 2.5$ requirement is necessary for b -tagging
 1914 due to the coverage of the ATLAS tracking detector (see Chapter 3), while the $p_T > 40 \text{ GeV}$
 1915 requirement is motivated by the trigger thresholds. A low p_T category, which would include
 1916 events failing the analysis selection due to this p_T cut, was considered for the non-resonant
 1917 search, but was found to contribute minimal sensitivity. At least two of the jets passing this
 1918 pre-selection are required to be b -tagged, and additional b -tagging requirements are made to
 1919 define the following regions:

- 1920 • “ $2b$ Region”: require exactly two b -tagged jets, used for background estimation
- 1921 • “ $4b$ Region”: require at least (but possibly more) four b -tagged jets, used as a signal
 1922 region for both resonant and non-resonant searches

1923 The non-resonant analysis additionally defines two $3b$ regions:

- 1924 • “ $3b+1$ loose Region”: require exactly three b -tagged jets which pass the 77 % b-tagging
 1925 working point (nominal) and one additional jet that fails the 77 % b-tagging working

1926 point but passes the *looser* 85 % b-tagging working point. Used as a signal region for
1927 the non-resonant search.

- 1928 • “3 b +1 fail Region”: complement of 3 b +1 loose. Require exactly three b -tagged jets
1929 which pass the 77 % b-tagging working point, but require that none of the remaining jets
1930 pass the 85 % b-tagging working point. Used as a validation region for the non-resonant
1931 search.

1932 After these requirements, four jets are chosen, ranked first by b -tagging requirement and then
1933 by p_T (e.g. for the 2 b region, the jets chosen are the two b -tagged jets and the two highest p_T
1934 non-tagged jets; for the 4 b region, the jets are the four highest p_T b -tagged jets). To match
1935 the topology of a $HH \rightarrow b\bar{b}b\bar{b}$ event, these four jets are then *paired* into *Higgs candidates*: the
1936 four jets are split into two sets of two, and each of these pairs is used to define a reconstructed
1937 object that is a proxy for a Higgs in a HH event.

1938 For four jets there are three possible pairings. For signal events, a correct pairing can be
1939 identified (provided all necessary jets pass pre-selection) using the truth information of the
1940 Monte Carlo simulation, and such information may be used to design/select an appropriate
1941 pairing algorithm. This is only part of the story, however. The vast majority of the events in
1942 data do *not* include a real HH decay (this is a search for a reason!), either because the event
1943 originates from a background process (e.g. for 4 b events), or because the selection is not
1944 designed to maximize the signal (e.g. 2 b events). As the pairing is part of the selection, it must
1945 still be run on such events, such that various algorithms which achieve similar performance
1946 in terms of pairing efficiency may have vastly different impacts in terms of the shape of the
1947 background and the biases inherent in the background estimation procedure. The interplay
1948 between these two facets of the pairing is an important part of the choices made for this
1949 analysis.

1950 A comparison of different shapes due to three different paring strategies is shown in Figure
1951 7.1.

1952 7.3.1 *Resonant Pairing Strategy*

1953 For the resonant analysis, a Boosted Decision Tree (BDT) is used for the pairing. The boosted
 1954 decision tree is given the total separation between the two jets in each of the two pairs (ΔR_1
 1955 and ΔR_2), the pseudo-rapidity separation between the two jets in each pair ($\Delta\eta_1$ and $\Delta\eta_2$),
 1956 and the angular separation between the two jets in each pair in the $x - y$ plane ($\Delta\phi_1$ and
 1957 $\Delta\phi_2$). The total separations (ΔR_s) are provided in addition to the components in order to
 1958 avoid requiring the boosted decision tree to reconstruct these variables in order to use them.
 1959 For these variables, pair 1 is the pair with the highest scalar sum of jet p_{T} s, and pair 2 the
 1960 other pair.

1961 The boosted decision tree is also parameterized on the di-Higgs mass (m_{HH}) by providing
 1962 this as an additional feature. Since the boosted decision tree is trained on correct and
 1963 incorrect pairings in signal events, there will be exactly one correct pairing and two incorrect
 1964 pairings in the training set for each m_{HH} value present in that set. As a result, this variable
 1965 cannot, in itself, distinguish a correct pairing from an incorrect pairing, and therefore the
 1966 inclusion of this variable simply serves to parameterize the BDT on m_{HH} ².

1967 The boosted decision tree was trained on one quarter of the total AFII simulated scalar
 1968 MC statistics, using the Gradient-based One Side Sampling (GOSS) algorithm which allows
 1969 rapid training with very large datasets. A preselection was applied requiring events to have
 1970 four jets with a p_{T} of at least 35 GeV. Note that this is a looser requirement than the 40 GeV
 1971 used in the analysis selection, and is meant to increase the available statistics for events with
 1972 low m_{HH} and to ensure a better performance as a function of that variable. Events were also
 1973 required to have four distinct jets that could be geometrically matched (to within $\Delta R \leq 0.4$)
 1974 to the b -quarks. The events used to train the BDT were not included when the analysis was
 1975 run on these signal simulations. The boosted decision tree was constructed with the following
 1976 hyperparameters:

1977 `min_data_in_leaf=50,`

²That is, the conditions placed on the other variables by the BDT vary with m_{HH} .

1978 num_leaves=180,
 1979 learning_rate=0.01

1980 These hyperparameters were optimized using a Bayesian optimization procedure [100].
 1981 Three fold cross-validation was used to perform this optimization without the need for an
 1982 additional sample, while avoiding over-training on signal events.

1983 *7.3.2 Non-resonant Pairing Strategy*

1984 For the non-resonant analysis, a simpler pairing algorithm is used, which proceeds as follows:
 1985 in a given event, Higgs candidates for each possible pairing are sorted by the p_T of the vector
 1986 sum of constituent jets. The angular separation, ΔR is computed between jets in the each of
 1987 the leading Higgs candidates, and the pairing with the smallest separation (ΔR_{jj}) is selected.
 1988 This method will be referred to as $\min \Delta R$ in the following.

1989 The primary motivation for the use of this pairing in the non-resonant search is a *smooth*
 1990 *mass plane*: by efficiently discarding low mass events, $\min \Delta R$ removes the background peak
 1991 present in the resonant search while maintaining good pairing efficiency for the Standard
 1992 Model non-resonant signal. This facilitates a background estimate with small kinematic bias
 1993 – the region in which the background estimate is derived is more similar to the signal region.

1994 Along with discarding low mass background, there is a corresponding loss of low mass
 1995 signal. This predominantly impacts points away from the Standard Model (see Figure 7.2),
 1996 but, because the $4b$ channel has the strongest contribution near the Standard Model and
 1997 because of the large low mass background present with other pairing methods, the impact on
 1998 analysis sensitivity is mitigated. The $\min \Delta R$ pairing is thus adopted for the non-resonant
 1999 search.

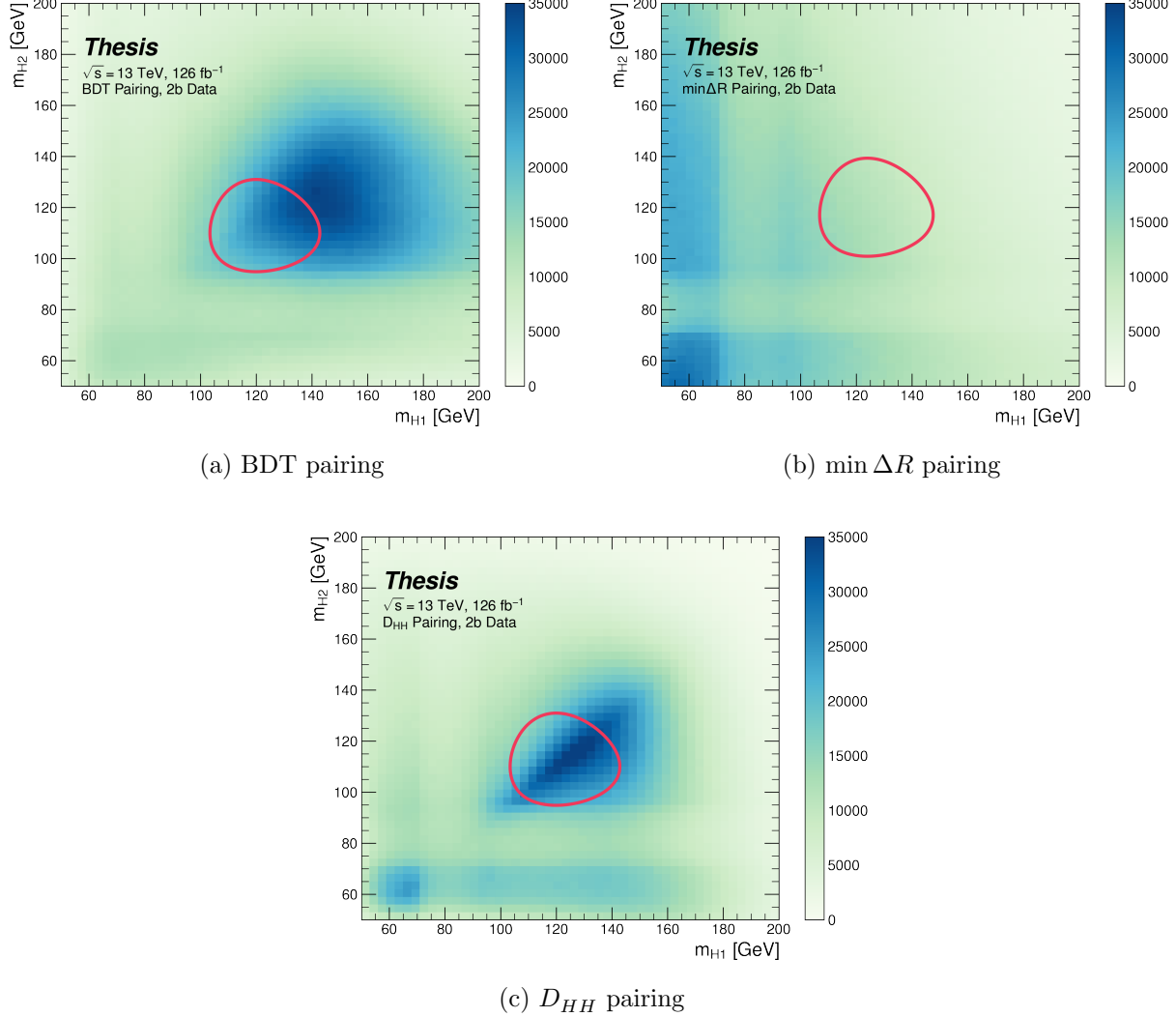


Figure 7.1: Comparison of m_{H1} vs m_{H2} planes for the full Run 2 $2b$ dataset with different pairings. As evidenced, this choice significantly impacts where events fall in this plane, and therefore which events fall into the various kinematic regions defined in this plane (see Section 7.5). The signal regions for the resonant/early Run 2 analysis are shown for reference for the BDT and D_{HH} pairings, while the the min ΔR signal region shifted is shifted slightly up and to the right to match the non-resonant selection. Note that the band structure around 80 GeV in both m_{H1} and m_{H2} is introduced by the top veto described in Section 7.4.

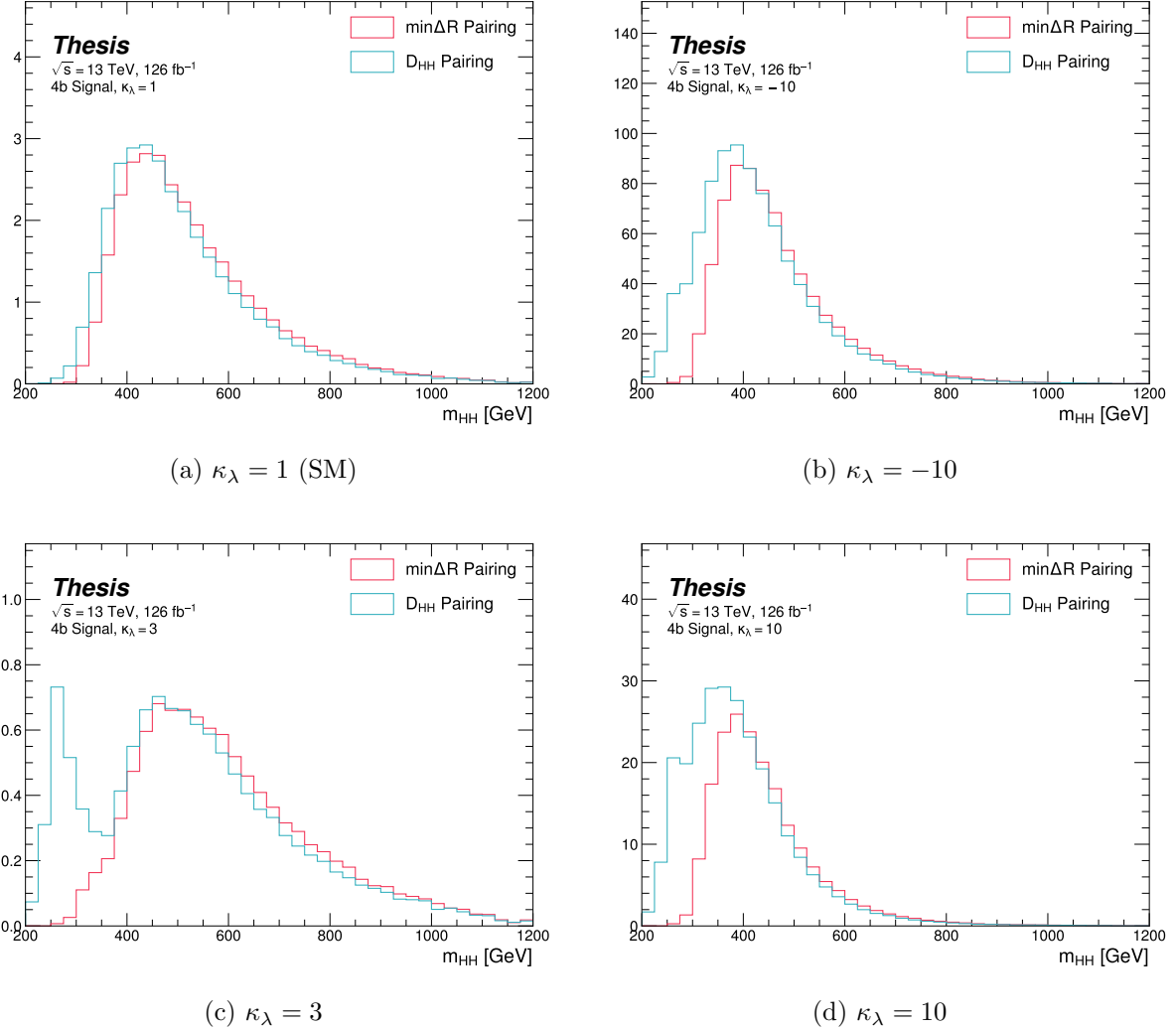


Figure 7.2: Comparison of signal distributions in the respective signal regions for the $\min \Delta R$ and D_{HH} pairing for various values of the Higgs trilinear coupling in the respective signal regions. The distributions are quite similar at the Standard Model point, but for other variations, $\min \Delta R$ does not pick up the low mass features.

2000 **7.4 Background Reduction and Top Veto**

2001 Choosing a pairing of the four b-tagged jets fully defines the di-Higgs candidate system used
2002 for each event in the remainder of the analysis chain. A requirement of $|\Delta\eta_{HH}| < 1.5$ on this
2003 di-Higgs candidate system mitigates QCD multijet background.

2004 In order to mitigate the hadronic $t\bar{t}$ background, a top veto is then applied, removing
2005 events consistent with a $t \rightarrow b(W \rightarrow q_1\bar{q}_2)$ decay.

2006 The jets in the event are separated into *HC jets* which are the four jets used to build the
2007 Higgs candidates, and *non-*HC jets**, the other jets (passing the p_T and $|\eta|$ requirements) in
2008 the event.

2009 W candidates are built by forming all possible pairs of all jets in each event. With n jets,
2010 there are $\binom{n}{2}$ such pairs. t candidates are then built by pairing each W candidate with each
2011 HC jet (for $4\binom{n}{2}$ combinations). Note that all jets in a t candidate must be distinct (i.e. a
2012 HC jet may not be used both on its own and in a W candidate).

With m_t denoting the invariant mass of the t candidate, and m_W the invariant mass of the W candidate, the quantity

$$X_{Wt} = \sqrt{\left(\frac{m_W - 80.4 \text{ GeV}}{0.1 \cdot m_W}\right)^2 + \left(\frac{m_t - 172.5 \text{ GeV}}{0.1 \cdot m_t}\right)^2} \quad (7.1)$$

2013 is constructed for each combination.

2014 Events are then vetoed if the minimum X_{Wt} over all combinations is less than 1.5.

2015 The same definitions and procedures are used for both the resonant and non-resonant
2016 analyses. However, for the non-resonant search, the top candidates considered for X_{Wt} have
2017 the additional requirement that the jet used for the b is *b*-tagged. While this is identical to
2018 the resonant analysis by definition for 4*b* events, it does change the set of events considered in
2019 lower tag regions, in particular for the 2*b* events considered in the derivation of the background
2020 estimate. Such a change is found to reduce the impact of background systematics by increasing
2021 2*b* support in the high X_{Wt} kinematic region. *TODO: Insert plots of variables*

2022 **7.5 Kinematic Region Definition**

As has been mentioned, an important piece of the analysis is the plane defined by the two Higgs candidate masses (the *Higgs candidate mass plane*). After the selection described above, a signal region is defined by requiring $X_{HH} < 1.6$, where:

$$X_{HH} = \sqrt{\left(\frac{m(H_1) - c_1}{0.1 \cdot m(H_1)}\right)^2 + \left(\frac{m(H_2) - c_2}{0.1 \cdot m(H_2)}\right)^2} \quad (7.2)$$

2023 with $m(H_1)$, $m(H_2)$ the leading and subleading Higgs candidate masses, c_1 and c_2 correspond
2024 to the center of the signal region, and the denominator provides a Higgs candidate mass
2025 dependent resolution of 10 %. For consistency with the HH decay hypothesis, c_1 and c_2
2026 are nominally (125 GeV, 125 GeV). However, these are allowed to vary due to energy loss,
2027 with specific values chosen described below. The selection of these values is one of several
2028 significant differences between the regions defined for the resonant and non-resonant search.
2029 We describe both below.

2030 **7.5.1 Resonant Kinematic Regions**

2031 For the resonant analysis, the signal region is centered at (120 GeV, 110 GeV) to account for
2032 energy loss leading to the Higgs masses being under-reconstructed. Note that leading and
2033 subleading Higgs candidates are defined according to the *scalar sum* of constituent jet p_T .

For the background estimation, two regions are defined which are roughly concentric around the signal region: a *validation region* which consists of those events not in the signal region, but which do pass

$$\sqrt{(m(H_1) - 1.03 \times 120 \text{ GeV})^2 + (m(H_2) - 1.03 \times 110 \text{ GeV})^2} < 30 \text{ GeV} \quad (7.3)$$

and a *control region* which consists of those events not in the signal or validation regions, but which do pass

$$\sqrt{(m(H_1) - 1.05 \times 120 \text{ GeV})^2 + (m(H_2) - 1.05 \times 110 \text{ GeV})^2} < 45 \text{ GeV} \quad (7.4)$$

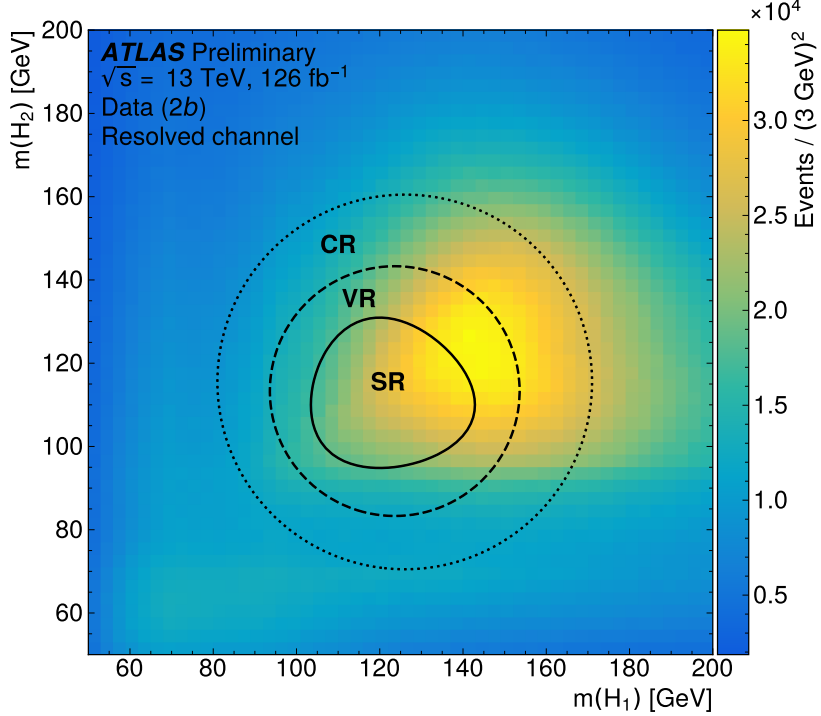


Figure 7.3: Regions used for the resonant search, shown on the $2b$ data mass plane. The outermost region (the “control region”) is used for derivation of the nominal background estimate. The innermost region is the signal region, where the signal extraction fit is performed. The region in between (the “validation region”) is used for the assessment of an uncertainty.

2034 For simplicity, the SR/VR/CR definitions from the early Run 2 paper [1] were chosen for
 2035 the resonant analysis, and were found to be close to optimal. These regions are shown in
 2036 Figure 7.3.

2037 7.5.2 Non-resonant Kinematic Regions

2038 For the non-resonant analysis the signal region is centered at (124 GeV, 117 GeV), corre-
 2039 sponding to the means of *correctly paired* Standard Model signal events. The shape of the
 2040 signal region (other than this change of center) was found to remain optimal.

2041 For the non-resonant search, leading and subleading Higgs candidates are defined according
 2042 to the *vector sum* of constituent jet p_T , more closely corresponding to the $1 \rightarrow 2$ decay
 2043 assumption behind the min ΔR pairing algorithm.

2044 Two areas for improvement were identified in the resonant analysis, which will be discussed
 2045 in more detail below: *signal contamination* of the validation region (which impacts the
 2046 uncertainty assessed due to extrapolation) and *large nuisance parameter pulls* for this
 2047 uncertainty, corresponding to a rough assumption that the validation region is closer to the
 2048 signal region in the mass plane, and so offers a better estimate of the signal region. Extensive
 2049 cross-checks were performed for the resonant search, which demonstrated minimal bias due
 2050 to the signal contamination and healthy behavior of the signal extraction fit, despite the
 2051 large pulls. However, these large pulls imply that the nominal estimate may be improved by
 2052 incorporating some of the information entering the definition of the extrapolation uncertainty.
 2053 Further, the resonant search benefits from a set of highly peaked signals, such that the
 2054 smooth nature of the background helps to mitigate signal contamination bias. With the
 2055 broad non-resonant signals, a bias due to signal contamination becomes more of a concern,
 2056 such that addressing this is highly motivated.

A redesign of the control and validation regions is therefore performed for the non-resonant analysis. The outer boundary defined by the shifted resonant control region:

$$\sqrt{(m(H_1) - 1.05 \times 124 \text{ GeV})^2 + (m(H_2) - 1.05 \times 117 \text{ GeV})^2} < 45 \text{ GeV} \quad (7.5)$$

2057 is kept, roughly corresponding to combining the regions used for the resonant analysis. In
 2058 order to assess the variation of the background estimate, two sets of regions are desired, so
 2059 this combined region is split into *quadrants*, that is, divided into four pieces along axes that
 2060 intersect with the signal region center. To avoid kinematic bias, quadrants on opposite sides
 2061 of the signal region are paired, with these pairs corresponding to the non-resonant control
 2062 and validation regions.

2063 The particular orientation of the regions is chosen such that region centers align with the
 2064 leading and subleading Higgs candidate masses, corresponding to a set of axes rotated at

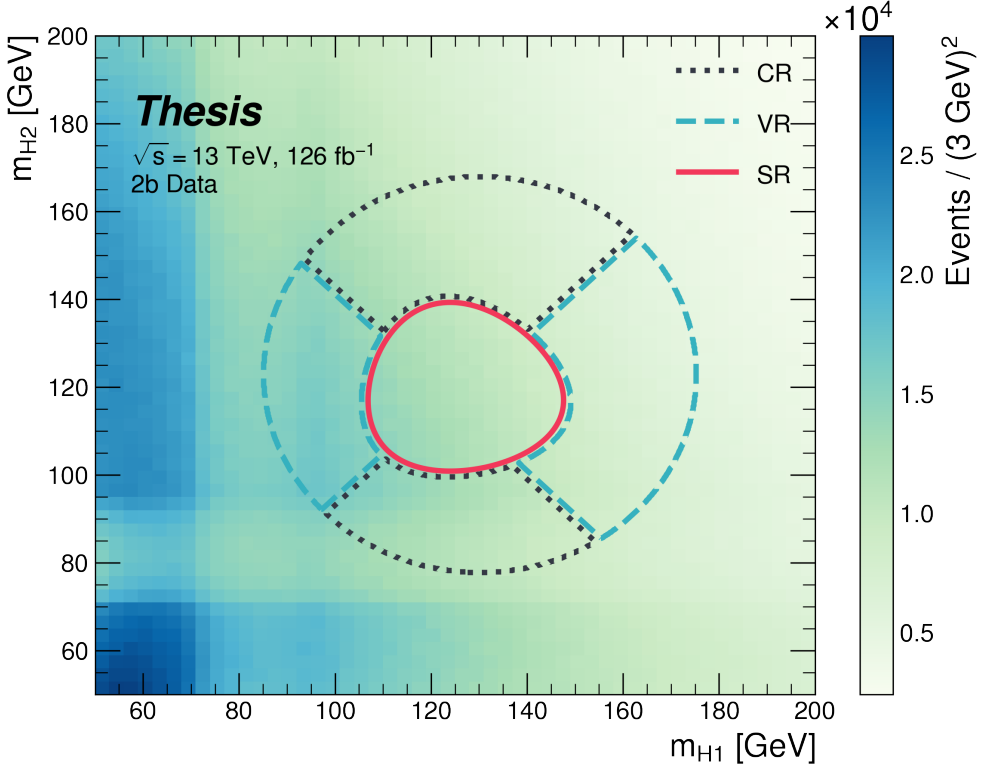


Figure 7.4: Regions used for the non-resonant search. The “top” and “bottom” quadrants together comprise the control region, in which the nominal background estimate is derived. The “left” and “right” quadrants together comprise the validation region, which is used to assess an uncertainty. The signal region, in the center, is where the signal extraction fit is performed.

2065 45° , with the “top” and “bottom” quadrants together comprising the control region, and the
2066 other set (“left” and “right”) the validation region. These regions are shown in Figure 7.4

2067 This design of regions includes a set of events closer to the signal region in the mass plane,
2068 leveraging the assumption that these events are more similar to signal region events, while
2069 also including events further away from the signal region, mitigating signal contamination.
2070 This region selection is found to have good performance in alternate validation regions (see
2071 Section 7.8).

2072 7.5.3 Discriminating Variable

2073 The discriminant used for the resonant analysis is *corrected* m_{HH} . This variable is calculated
 2074 by re-scaling the Higgs candidate four vectors such that each $m_H = 125$ GeV. These re-scaled
 2075 four-vectors are then summed, and their invariant mass is the corrected m_{HH} . These re-scaled
 2076 four-vectors are not used for any other purpose. The effect of this correction, which sharpens
 the m_{HH} peak and correctly centers it, is shown in Figure 7.5.

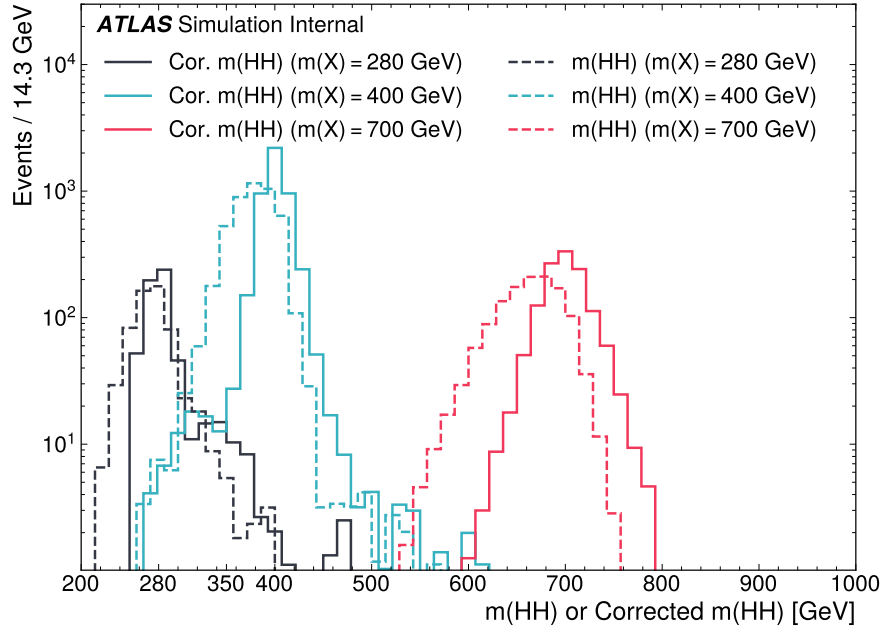


Figure 7.5: Impact of the m_{HH} correction on a range of spin-0 resonant signals. The corrected m_{HH} distributions (solid lines) are much sharper and more centered on the corresponding resonance masses than the uncorrected m_{HH} distributions (dashed).

2077

2078 For the non-resonant analysis, due to the broad nature of the signal in m_{HH} , such a
 2079 correction is not as motivated, and, indeed, is found to have very minimal impact. The
 2080 uncorrected m_{HH} (just referred to as m_{HH}) is therefore used as a discriminant. To maximize

2081 sensitivity, the non-resonant analysis additionally uses two variables for categorization: $\Delta\eta_{HH}$,
2082 an angular variable which, along with m_{HH} , fully characterizes the HH system [101], and
2083 X_{HH} , the variable used for the signal region definition, which leverages the peaked structure of
2084 the signal in the $(m(H_1), m(H_2))$ plane to split the signal extraction fit into lower and higher
2085 purity regions (highest purity near $X_{HH} = 0$, the center of the signal region). Distributions
2086 of these variables are shown in *TODO: plots*. The categorization used for this thesis has been
2087 optimized to be 2×2 in these variables, with corresponding selections $0 \leq \Delta\eta_{HH} \leq 0.75$ and
2088 $0.75 \leq \Delta\eta_{HH} \leq 1.5$ for $\Delta\eta_{HH}$, and $0 \leq X_{HH} \leq 0.95$ and $0.95 \leq X_{HH} \leq 1.6$ for X_{HH} .

2089 **7.6 Background Estimation**

2090 After the event selection described above, there are two major backgrounds, QCD and $t\bar{t}$.
2091 A very similar approach is used for both the resonant and the non-resonant analyses, with
2092 some small modifications. This approach is notably fully data-driven, which is warranted due
2093 to the flexibility of the estimation method, as well as the high relative proportion of QCD
2094 background ($> 90\%$), and allows for the use of machine learning methods in the construction
2095 of the background estimate. However, it sacrifices an explicit treatment of the $t\bar{t}$ component.
2096 Performance of the background estimate on the $t\bar{t}$ component is checked explicitly, and
2097 minimal impact due to $t\bar{t}$ mis-modeling is seen.

2098 Contributions of single Higgs processes and ZZ are found to be negligible, and the
2099 Standard Model HH background is found to have no impact on the resonant search.

2100 The foundation of the background estimate lies in the derivation of a reweighting function
2101 which matches the kinematics of events with exactly two b -tagged jets to those of events in
2102 the higher tagged regions (events with three or four b -tagged jets). The reweighting function
2103 and overall normalization are derived in the control region. Systematic bias of this estimate
2104 is assessed in the validation region.

2105 For the resonant analysis, the systematic bias is a bias due to extrapolation: the validation
2106 region lies between the control and signal regions. For the non-resonant analysis, the bias
2107 instead comes from different possible interpolations of the signal region kinematics – given the
2108 choice of nominal estimate, the validation region is a conceptually equivalent, but maximally
2109 different, signal region estimate.

2110 **7.6.1 The Two Tag Region**

2111 Events in data with exactly two b -tagged jets are used for the data driven background estimate.
2112 The hypothesis here is that, due to the presence of multiple b -tagged jets, the kinematics of
2113 such events are similar to the kinematics of events in higher b -tagged regions (i.e. events
2114 with three and four b -tagged jets, respectively), and any differences can be corrected by a

2115 reweighting procedure. The region with three b -tagged jets is split into two b -tagging regions,
 2116 as described in Section 7.3, with the $3b + 1$ loose region used as an additional signal region.
 2117 The lower tagged $3b$ component ($3b + 1$ fail) is reserved for validation of the background
 2118 modelling procedure. Events with fewer than two b -tagged jets are not used for this analysis,
 2119 as they are relatively more different from the higher tag regions.

2120 The nominal event selection requires at least four jets in order to form Higgs candidates.
 2121 For the four tag region, these are the four highest p_T b -tagged jets. For the three tag regions,
 2122 these jets are the three b -tagged jets, plus the highest p_T jet satisfying a loosened b -tagging
 2123 requirement. Similarly, and following the approach of the resonant analysis, the two tag region
 2124 uses the two b -tagged jets and the two highest p_T non-tagged jets to form Higgs candidates.
 2125 Combinatoric bias from selection of different numbers of b -tagged jets is corrected as a part
 2126 of the kinematic reweighting procedure through the reweighting of the total number of jets in
 2127 the event. In this way, the full event selection may be run on two tagged events.

2128 7.6.2 Kinematic Reweighting

2129 The set of two tagged data events is the fundamental piece of the data driven background
 2130 estimate. However, kinematic differences from the four tag region exist and must be corrected
 2131 in order for this estimate to be useful. Binned approaches based on ratios of histograms
 2132 have been previously considered [1], [20], but are limited in their handling of correlations
 2133 between variables and by the “curse of dimensionality”, i.e. the dataset becomes sparser and
 2134 sparser in “reweighting space” as the number of dimensions in which to reweight increases,
 2135 limiting the number of variables used for reweighting. This leads either to an unstable fit
 2136 result (overfitting with finely grained bins) or a lower quality fit result (underfitting with
 2137 coarse bins).

2138 Note that even some machine learning methods such as Boosted Decision Trees (BDTs) [102],
 2139 may suffer from this curse of dimensionality, as the depth of each decision tree used is limited
 2140 by the available statistics after each set of corresponding selections (cf. binning in a more
 2141 sophisticated way), limiting the expressivity of the learned reweighting function.

2142 To solve these issues, a neural network based reweighting procedure is used here. This
2143 is a truly multivariate approach, allowing for proper treatment of variable correlations. It
2144 further overcomes the issues associated with binned approaches by learning the reweighting
2145 function directly, allowing for greater sensitivity to local differences and helping to avoid the
2146 curse of dimensionality.

2147 *Neural Network Reweighting*

Let $p_{4b}(x)$ and $p_{2b}(x)$ be the probability density functions for four and two tag data respectively across some input variables x . The problem of learning the reweighting function between two and four tag data is then the problem of learning a function $w(x)$ such that

$$p_{2b}(x) \cdot w(x) = p_{4b}(x) \quad (7.6)$$

from which it follows that

$$w(x) = \frac{p_{4b}(x)}{p_{2b}(x)}. \quad (7.7)$$

This falls into the domain of density ratio estimation, for which there are a variety of approaches. The method considered here is modified from [103, 104], and depends on a loss function of the form

$$\mathcal{L}(R(x)) = \mathbb{E}_{x \sim p_{2b}}[\sqrt{R(x)}] + \mathbb{E}_{x \sim p_{4b}}\left[\frac{1}{\sqrt{R(x)}}\right]. \quad (7.8)$$

where $R(x)$ is some estimator dependent on x and $\mathbb{E}_{x \sim p_{2b}}$ and $\mathbb{E}_{x \sim p_{4b}}$ are the expectation values with respect to the 2b and 4b probability densities. A neural network trained with such a loss function has the objective of finding the estimator, $R(x)$, that minimizes this loss. It is straightforward to show that

$$\arg \min_R \mathcal{L}(R(x)) = \frac{p_{4b}(x)}{p_{2b}(x)} \quad (7.9)$$

2148 which is exactly the form of the desired reweighting function.

In practice, to avoid imposing explicit positivity constraints, the substitution $Q(x) \equiv \log R(x)$ is made. The loss function then takes the equivalent form

$$\mathcal{L}(Q(x)) = \mathbb{E}_{x \sim p_{2b}}[\sqrt{e^{Q(x)}}] + \mathbb{E}_{x \sim p_{4b}}\left[\frac{1}{\sqrt{e^{Q(x)}}}\right], \quad (7.10)$$

with solution

$$\arg \min_Q \mathcal{L}(Q(x)) = \log \frac{p_{4b}(x)}{p_{2b}(x)}. \quad (7.11)$$

2149 Taking the exponent then results in the desired reweighting function.

2150 Note that similar methods for density ratio estimation are available [105], e.g. from a

2151 more standard binary cross-entropy loss. However, these were found to perform no better
2152 than the formulation presented here.

2153 *Variables and Results*

2154 The neural network is trained on a variety of variables sensitive to two vs. four tag differences.

2155 To help bring out these differences, the natural logarithm of some of the variables with a
2156 large, local change is taken. The set of training variables used for the resonant analysis is

2157 1. $\log(p_T)$ of the 4th leading Higgs candidate jet

2158 2. $\log(p_T)$ of the 2nd leading Higgs candidate jet

2159 3. $\log(\Delta R)$ between the closest two Higgs candidate jets

2160 4. $\log(\Delta R)$ between the other two Higgs candidate jets

2161 5. Average absolute value of η across the four Higgs candidate jets

2162 6. $\log(p_T)$ of the di-Higgs system.

2163 7. ΔR between the two Higgs candidates

2164 8. $\Delta\phi$ between the jets in the leading Higgs candidate

2165 9. $\Delta\phi$ between the jets in the subleading Higgs candidate

2166 10. $\log(X_{Wt})$, where X_{Wt} is the variable used for the top veto

2167 11. Number of jets in the event.

2168 The non-resonant analysis uses an identical set of variables with two notable changes

2169 1. The definition of X_{Wt} differs from the resonant definition (as described in Section 7.4).

2170 2. An integer encoding of the two trigger categories is used as an input (variable which
 2171 takes on the value 0 or 1 corresponding to each of the two categories). This was found
 2172 to improve a mis-modeling near the tradeoff in m_{HH} of the two buckets.

2173 The neural network used for both resonant and non-resonant reweighting has three densely
 2174 connected hidden layers of 50 nodes each with ReLU activation functions and a single node
 2175 linear output. This configuration demonstrates good performance in the modelling of a variety
 2176 of relevant variables, including m_{HH} , when compared to a range of networks of similar size.

2177 In practice, a given training of the reweighting neural network is subject to variation
 2178 due to training statistics and initial conditions. An uncertainty is assigned to account for
 2179 this (Section 7.7), which relies on training an ensemble of reweighting networks [106]. To
 2180 increase the stability of the background estimate, the median of the predicted weight for each
 2181 event is calculated across the ensemble. This median is then used as the nominal background
 2182 estimate. This approach is indeed seen to be much more stable and to demonstrate a better
 2183 overall performance than a single arbitrary training. Each ensemble used for this analysis
 2184 consists of 100 neural networks, trained as described in Section 7.7.

2185 The training of the ensemble used for the nominal estimate is done in the kinematic
 2186 Control Region. The prediction of these networks in the Signal Region is then used for the
 2187 nominal background estimate. In addition, a separate ensemble of networks is trained in the
 2188 Validation Region. The difference between the prediction of the nominal estimate and the

2189 estimate from the VR derived networks in the Signal Region is used to assign a systematic
 2190 uncertainty. Further details on this systematic uncertainty are discussed in Section 7.7. Note
 2191 that although the same procedure is used for both Control and Validation Region trained
 2192 networks, only the median estimate from the VR derived reweighting is used for assessing a
 2193 systematic – no additional “uncertainty on the uncertainty” from VR ensemble variation is
 2194 applied.

2195 Each reweighted estimate is normalized such that the reweighted $2b$ yield matches the $4b$
 2196 yield in the corresponding training region. Note that this applies to each of the networks used
 2197 in each ensemble, where the normalization factor is also subject to the procedure described in
 2198 Section 7.7. As the median over these normalized weights is not guaranteed to preserve this
 2199 normalization, a further correction is applied such that the $2b$ yield, after the median weights
 2200 are applied, matches the $4b$ yield in the corresponding training region. As no preprocessing
 2201 is applied to correct for the class imbalance between $2b$ and $4b$ events entering the training,
 2202 this ratio of number of $4b$ events ($n(4b)$) over number of $2b$ events ($n(2b)$) is folded into the
 2203 learned weights. Correspondingly, the set of normalization factors described above is near 1
 2204 and the learned weights are centered around $n(4b)/n(2b)$ (roughly 0.01 over the full dataset).
 2205 This normalization procedure applies for all instances of the reweighting (e.g. those used for
 2206 validations in Section 7.8), with appropriate substitutions of reweighting origin (here $2b$) and
 2207 reweighting target (here $4b$).

2208 Note that, due to different trigger and pileup selections during each year, the reweighting
 2209 is trained on each year separately. An approach of training all of the years together with
 2210 a one-hot encoding was explored, but was found to have minimal benefit over the split
 2211 years approach, and in fact to increase the systematic bias of the corresponding background
 2212 estimate. Because of this, and because trigger selections for each year significantly impact
 2213 the kinematics of each year, such that categorizing by year is expected to reflect groupings
 2214 of kinematically similar events and to provide a meaningful degree of freedom in the signal
 2215 extraction fit, the split-year approach is kept.

2216 The control region closure for the 2018 dataset is shown for the resonant search in Figures

2217 7.6 through 7.14 and for the non-resonant search in Figures 7.24 through 7.32 for 4b and
 2218 Figures 7.42 through 7.50 for 3b1l. The impact of this control region derived reweighting
 2219 on the validation region is shown in Figures 7.15 through 7.23 for the resonant search and
 2220 Figures 7.33 through 7.41 for 4b and Figures 7.51 through 7.59 for 3b1l for the non-resonant
 2221 search. 2018 is chosen because it is the largest subset of the data on which the year-by-year
 2222 reweighting is trained. The other years are omitted here for brevity, but demonstrate very
 2223 similar results. Generally good performance is seen, with some occasional mis-modeling. For
 2224 the resonant search, this is most notable in the case of individual jet p_T . Such mis-modeling
 2225 may be corrected by including the variables in the input set, but this was found to not
 2226 improve the modeling of m_{HH} , and so is not done here. This mis-modeling is notable for the
 2227 non-resonant search in the leading Higgs candidate jet p_T , and is a direct consequence of the
 2228 trigger category input, which improves modeling of m_{HH} . Results are similar for other years,
 2229 but are not included here for brevity.

2230 One other salient feature of the non-resonant plots is the distributions of m_{H1} and m_{H2} ,
 2231 which emphasize the quadrant region definitions – the control region has a peak around
 2232 125 GeV in m_{H1} , which may be thought of as “signal region-like”, motivating this alignment,
 2233 though consequently the distribution of m_{H2} is quite bimodal. The reverse is true for the
 2234 validation region.

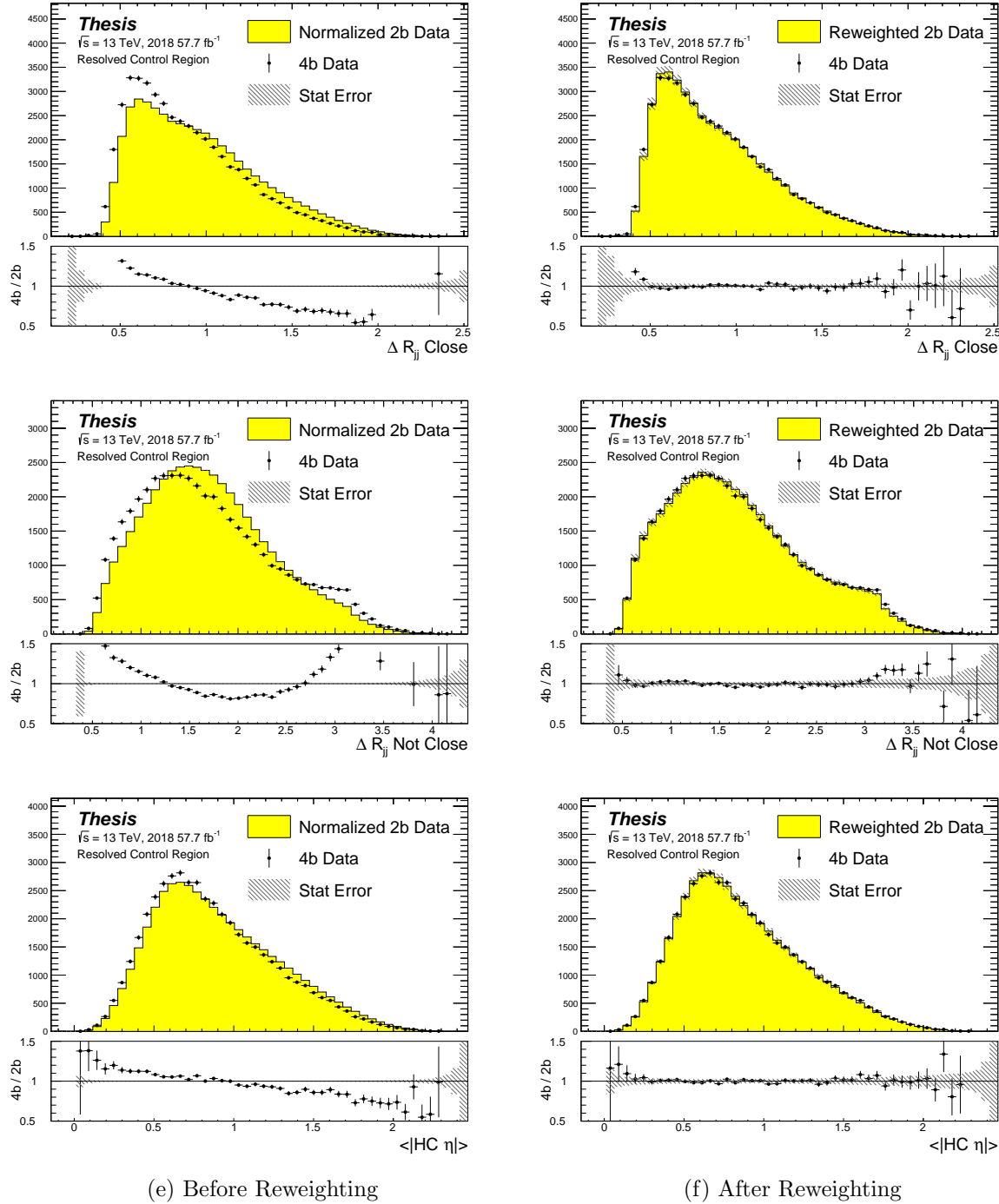


Figure 7.6: **Resonant Search:** Distributions of ΔR between the closest Higgs Candidate jets, ΔR between the other two, and average absolute value of HC jet η before (left) and after (right) CR derived reweighting for the 2018 Control Region.

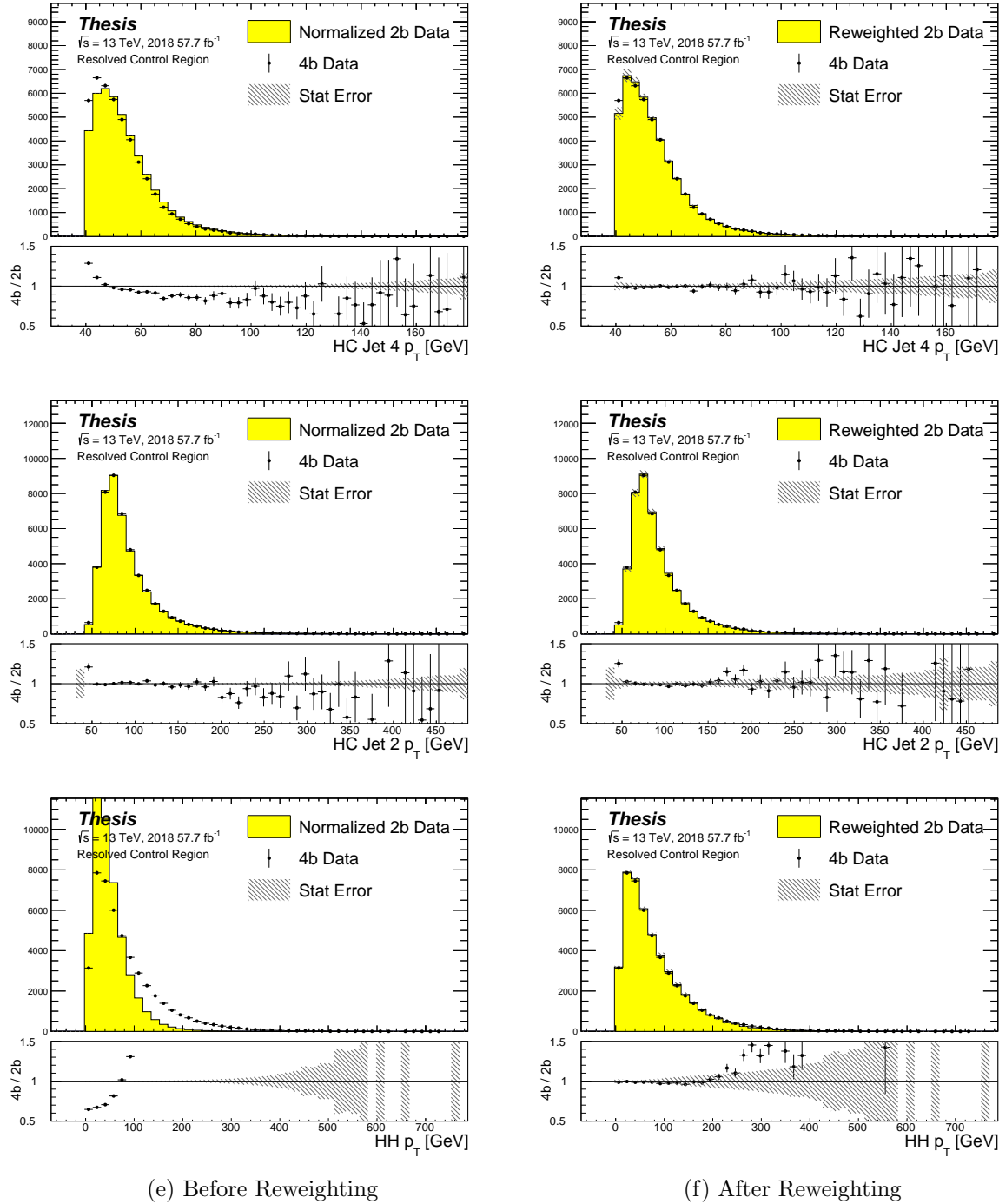


Figure 7.7: **Resonant Search:** Distributions of p_T of the 2nd and 4th leading Higgs Candidate jets and the p_T of the di-Higgs system before (left) and after (right) CR derived reweighting for the 2018 Control Region.

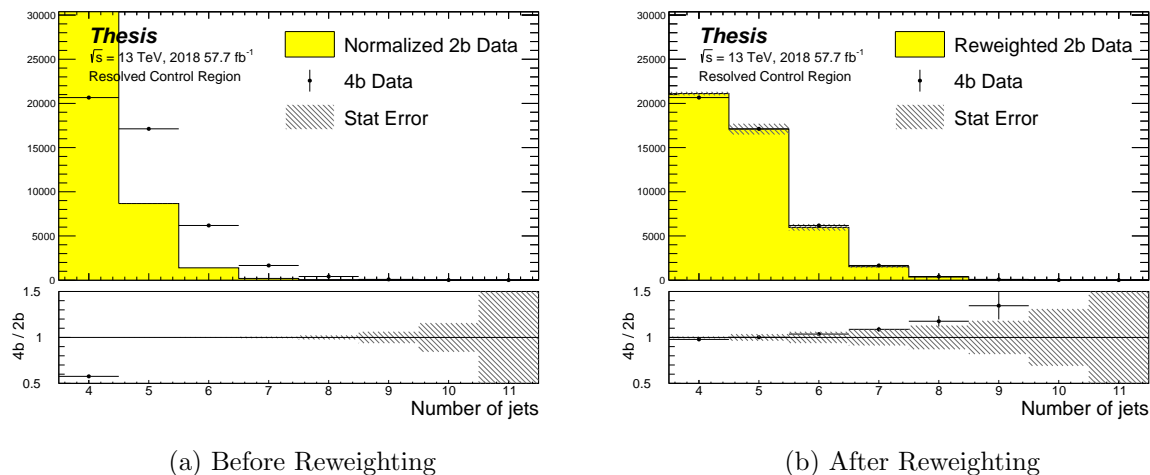


Figure 7.8: **Resonant Search:** Distributions of the number of jets before (left) and after (right) CR derived reweighting for the 2018 Control Region. A minimum of 4 jets is required in each event in order to form Higgs candidates.

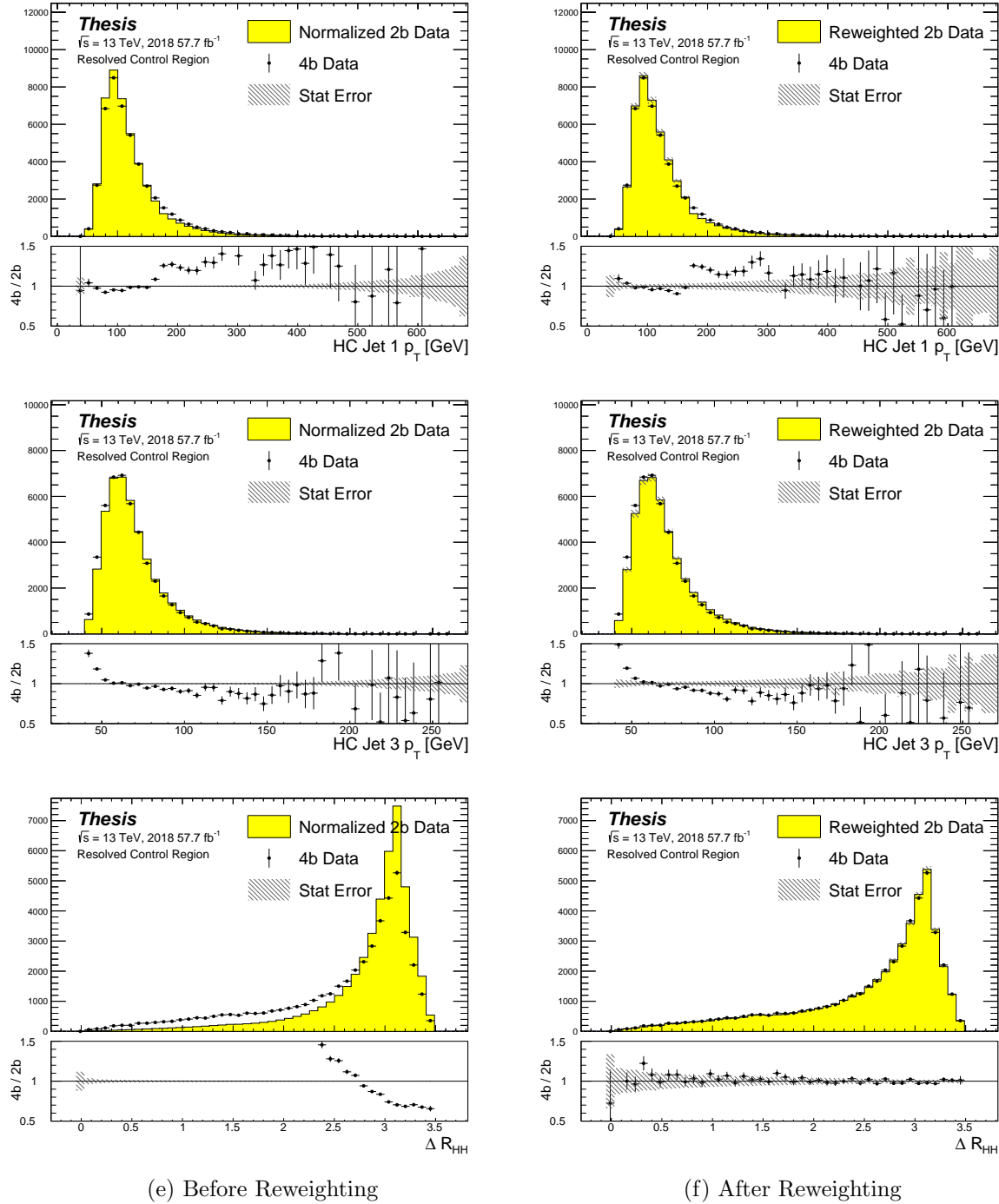


Figure 7.9: **Resonant Search:** Distributions of p_T of the 1st and 3rd leading Higgs Candidate jets and ΔR between Higgs candidates before (left) and after (right) CR derived reweighting for the 2018 Control Region.

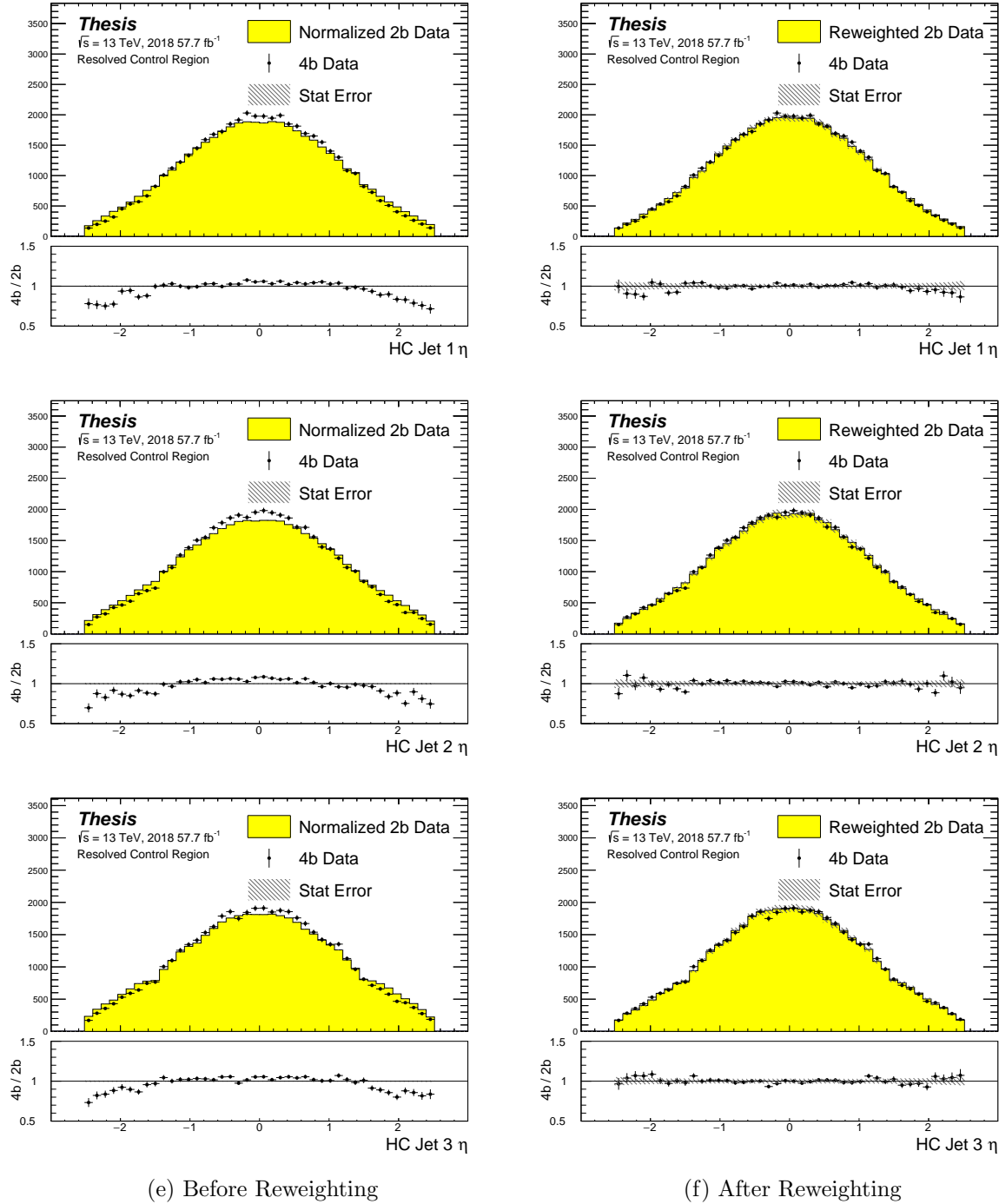


Figure 7.10: **Resonant Search:** Distributions of η of the 1st, 2nd, and 3rd leading Higgs Candidate jets before (left) and after (right) CR derived reweighting for the 2018 Control Region.

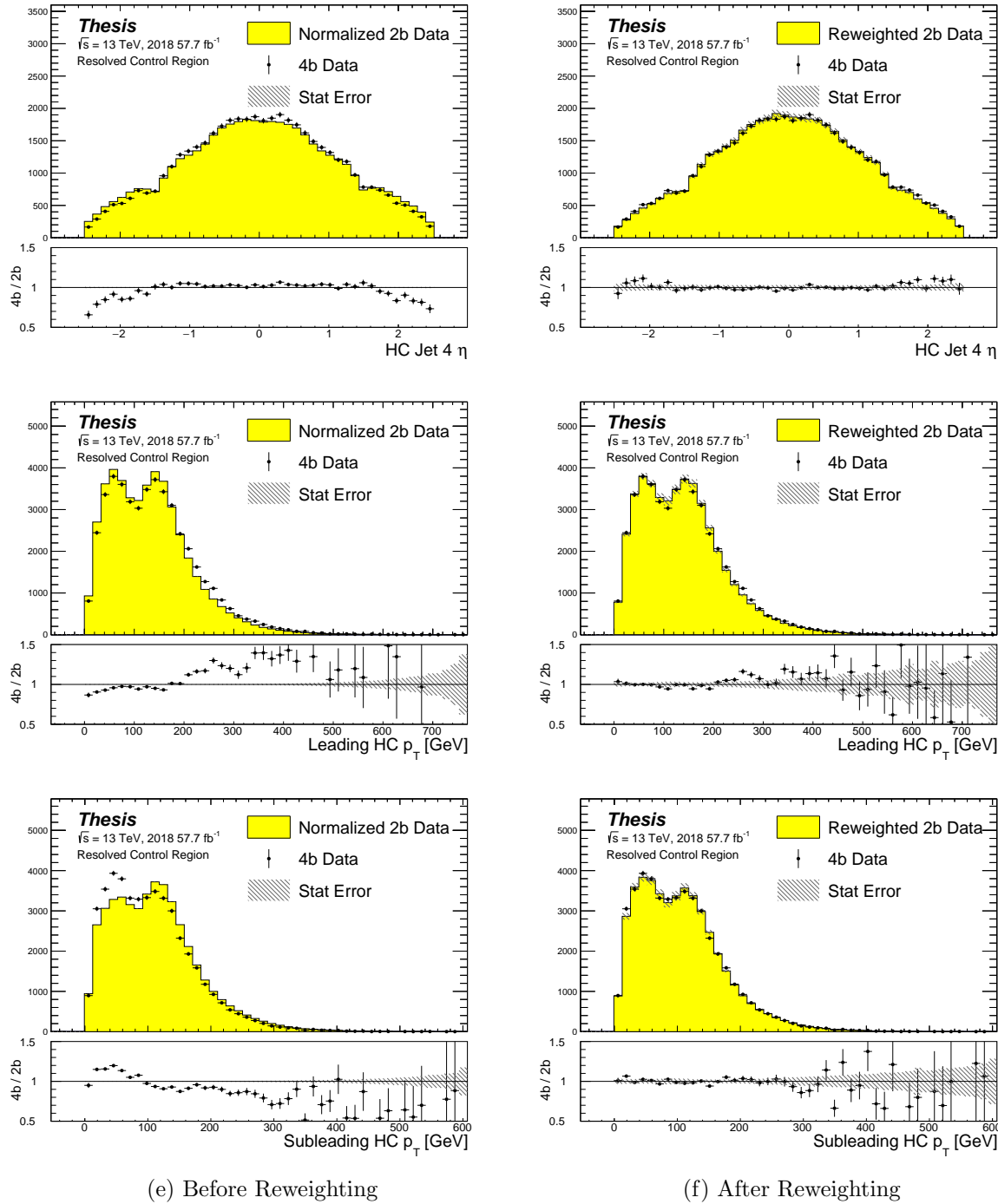


Figure 7.11: **Resonant Search:** Distributions of η of the 4th leading Higgs Candidate jet and the p_T of the leading and subleading Higgs candidates before (left) and after (right) CR derived reweighting for the 2018 Control Region.

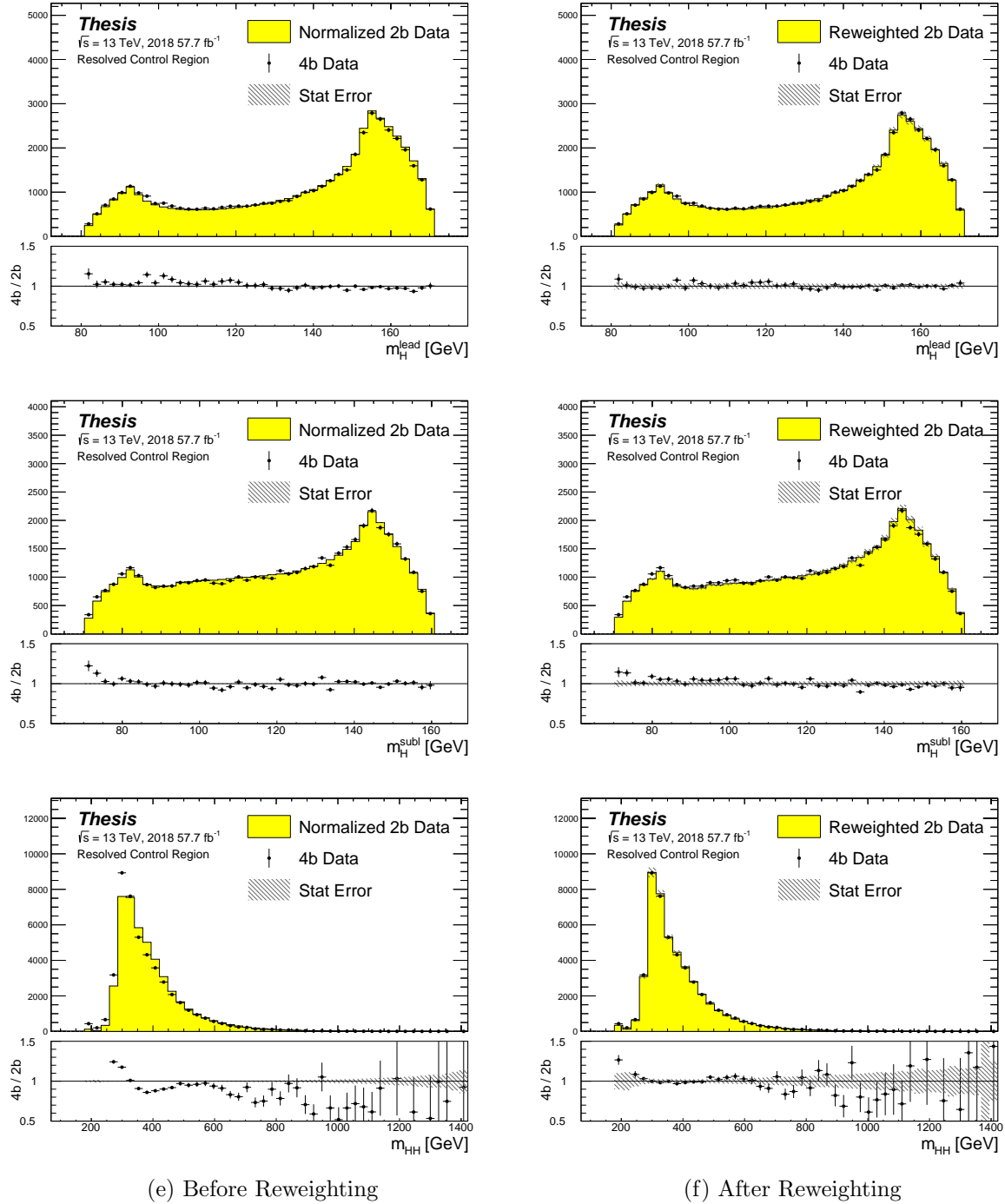


Figure 7.12: **Resonant Search:** Distributions of mass of the leading and subleading Higgs candidates and of the di-Higgs system before (left) and after (right) CR derived reweighting for the 2018 Control Region.

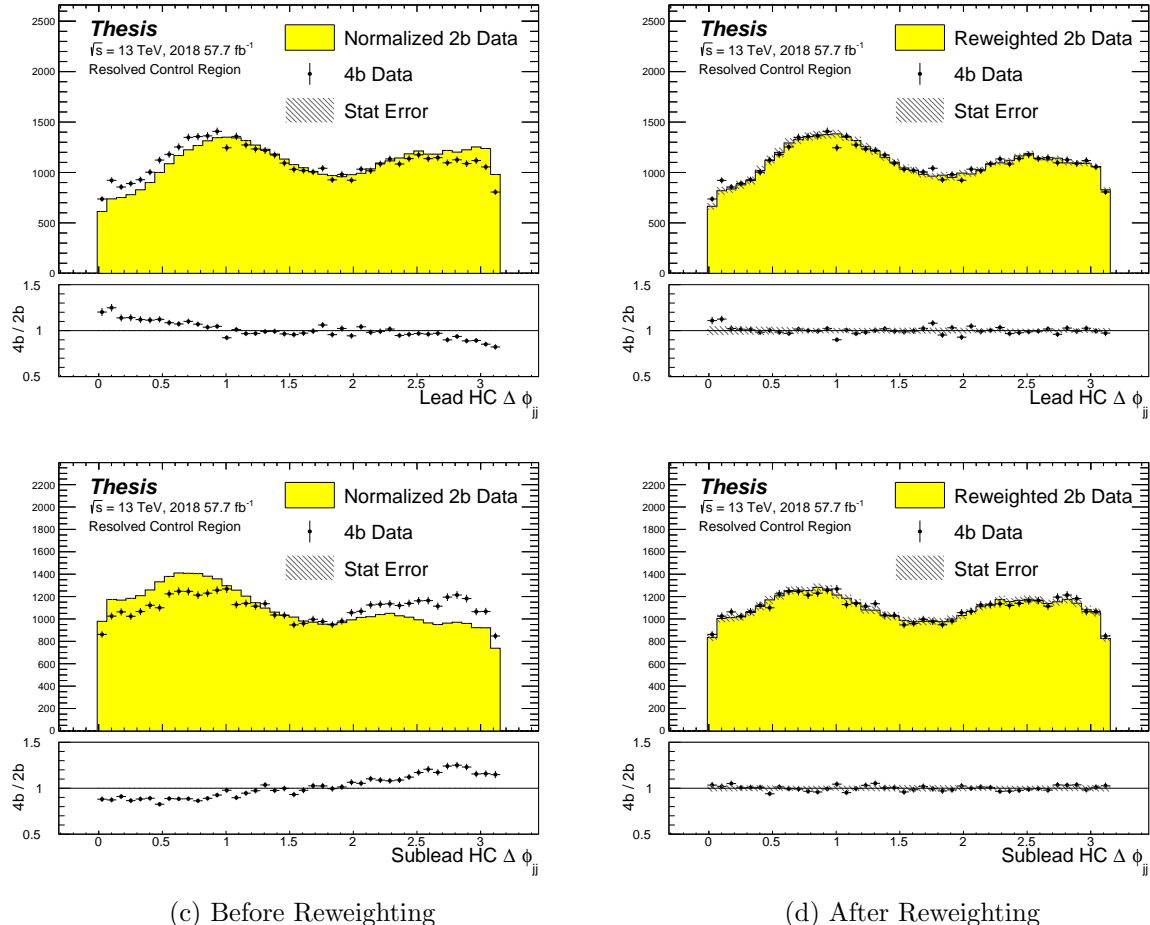


Figure 7.13: **Resonant Search:** Distributions of $\Delta\phi$ between jets in the leading and subleading Higgs candidates before (left) and after (right) CR derived reweighting for the 2018 Control Region.

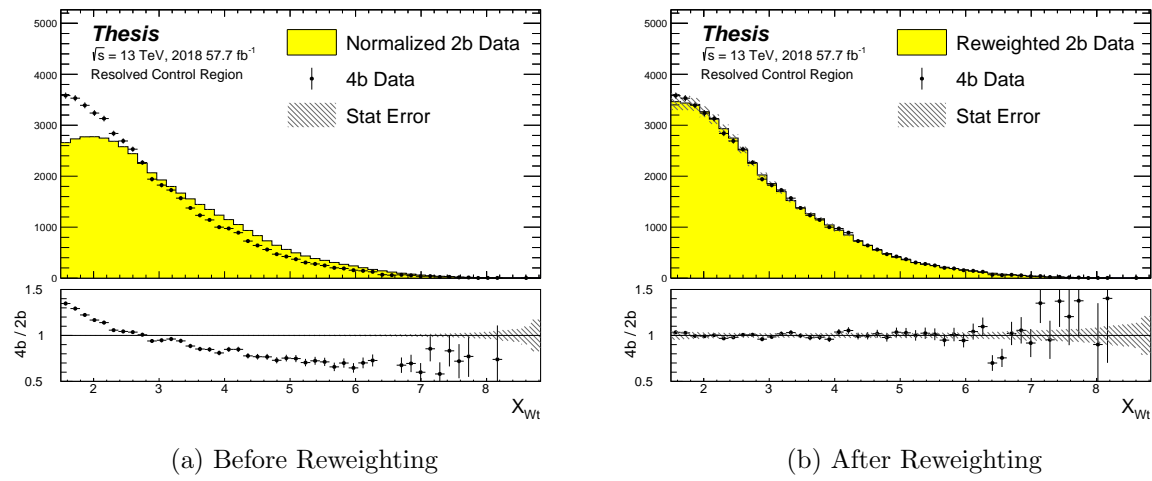


Figure 7.14: **Resonant Search:** Distributions of the top veto variable, X_{Wt} , before (left) and after (right) CR derived reweighting for the 2018 Control Region. Reweighting is done after the cut on this variable is applied

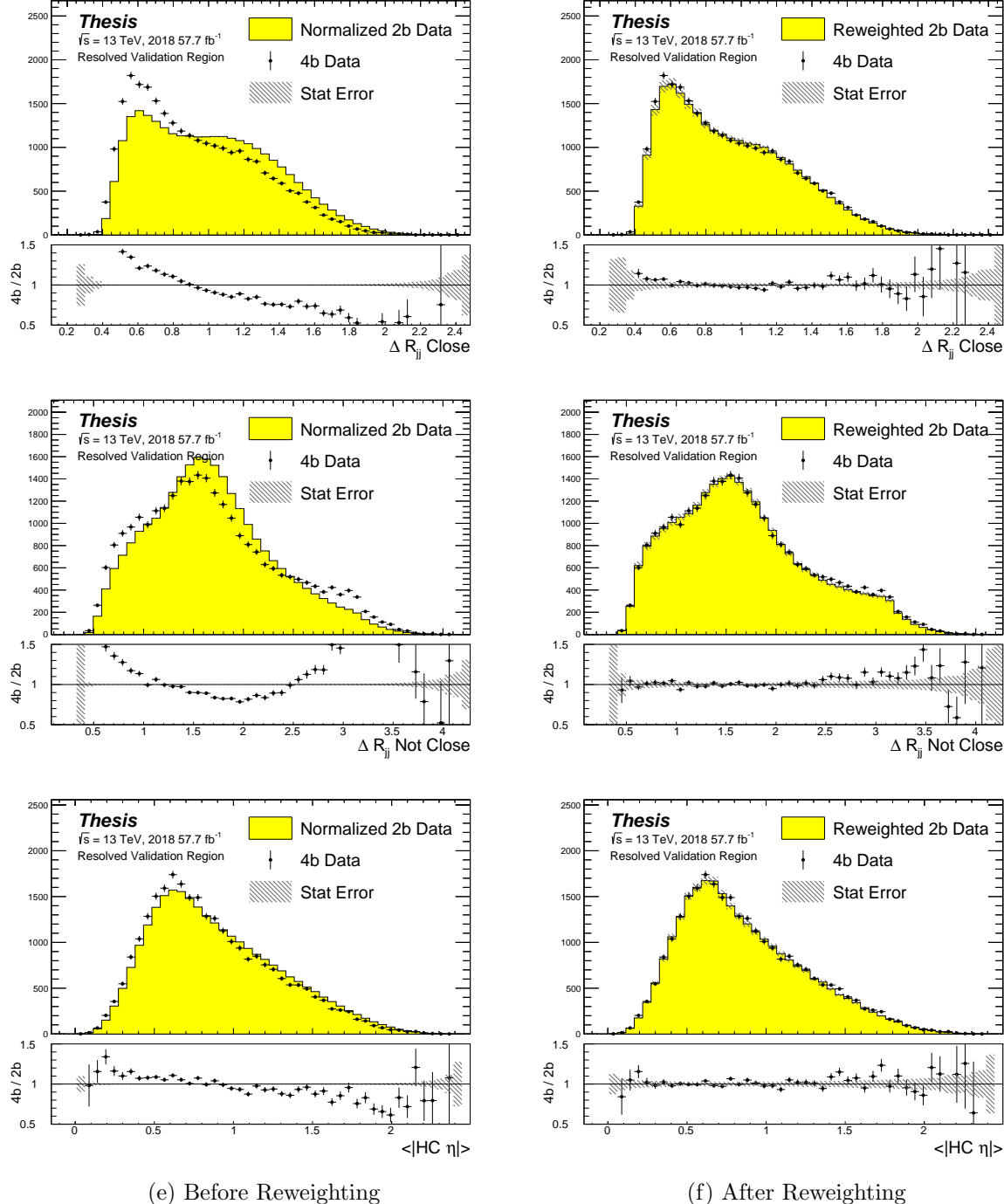


Figure 7.15: **Resonant Search:** Distributions of ΔR between the closest Higgs Candidate jets, ΔR between the other two, and average absolute value of HC jet η before (left) and after (right) CR derived reweighting for the 2018 Validation Region.

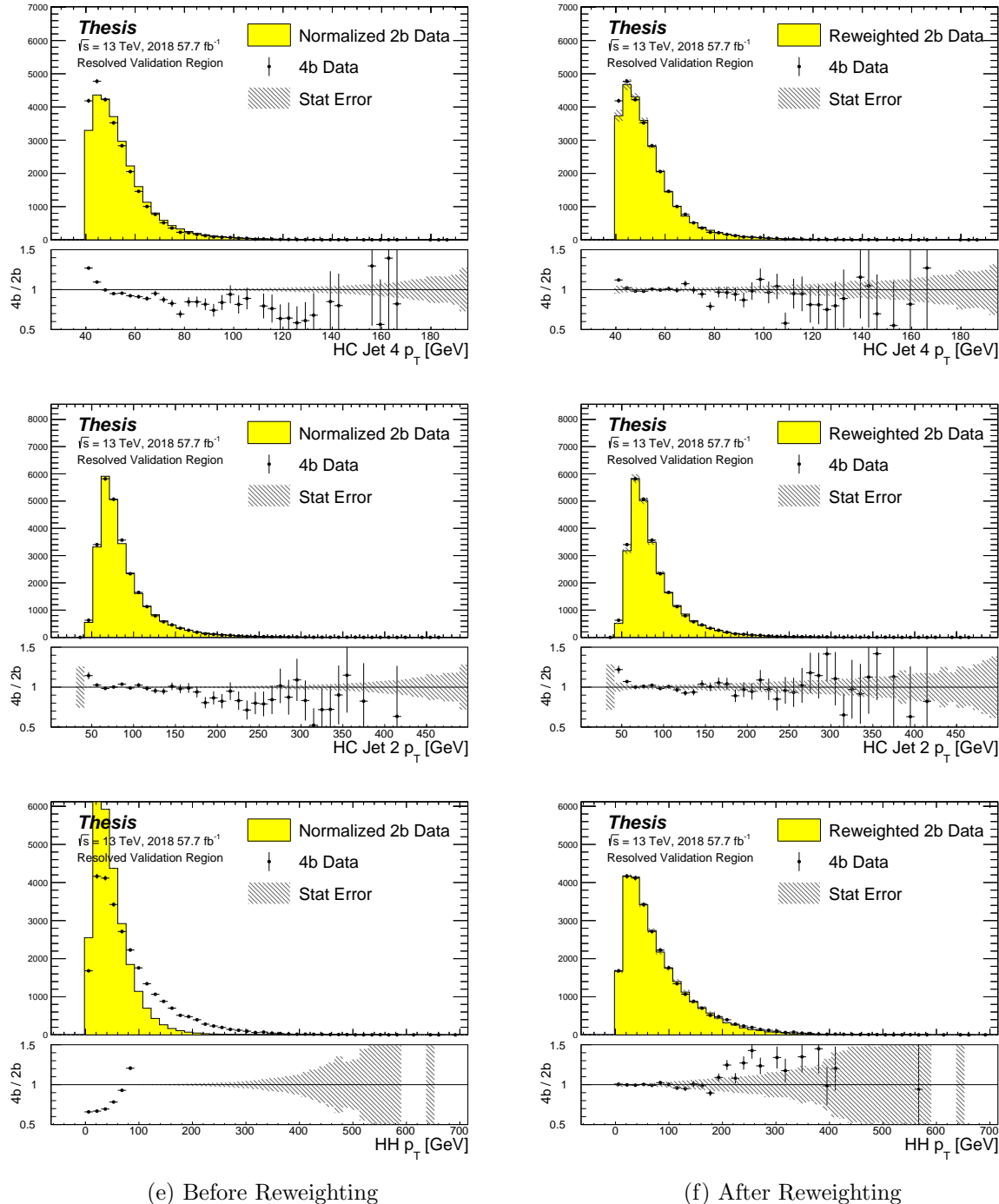


Figure 7.16: **Resonant Search:** Distributions of p_T of the 2nd and 4th leading Higgs Candidate jets and the p_T of the di-Higgs system before (left) and after (right) CR derived reweighting for the 2018 Validation Region.

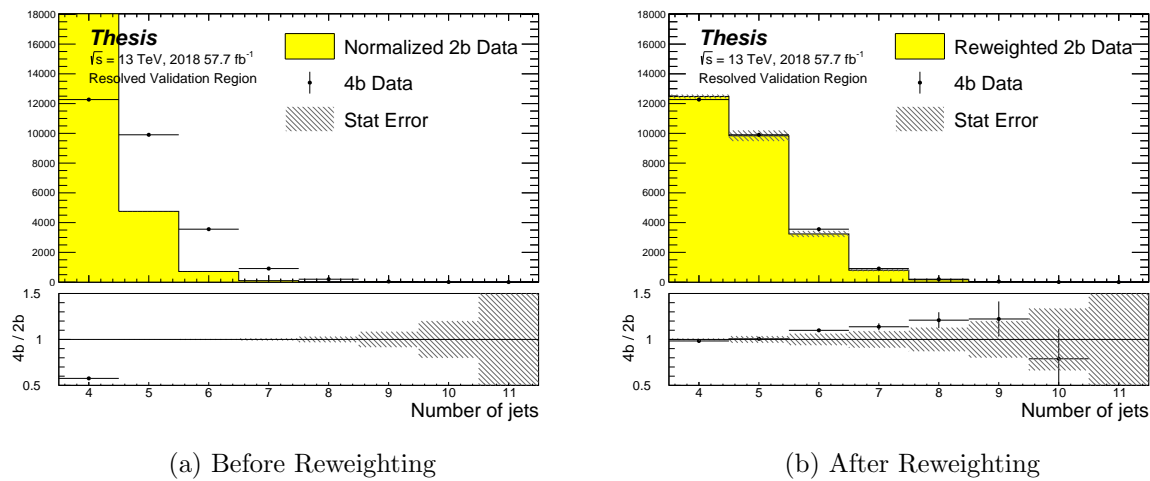


Figure 7.17: **Resonant Search:** Distributions of the number of jets before (left) and after (right) CR derived reweighting for the 2018 Validation Region. A minimum of 4 jets is required in each event in order to form Higgs candidates.

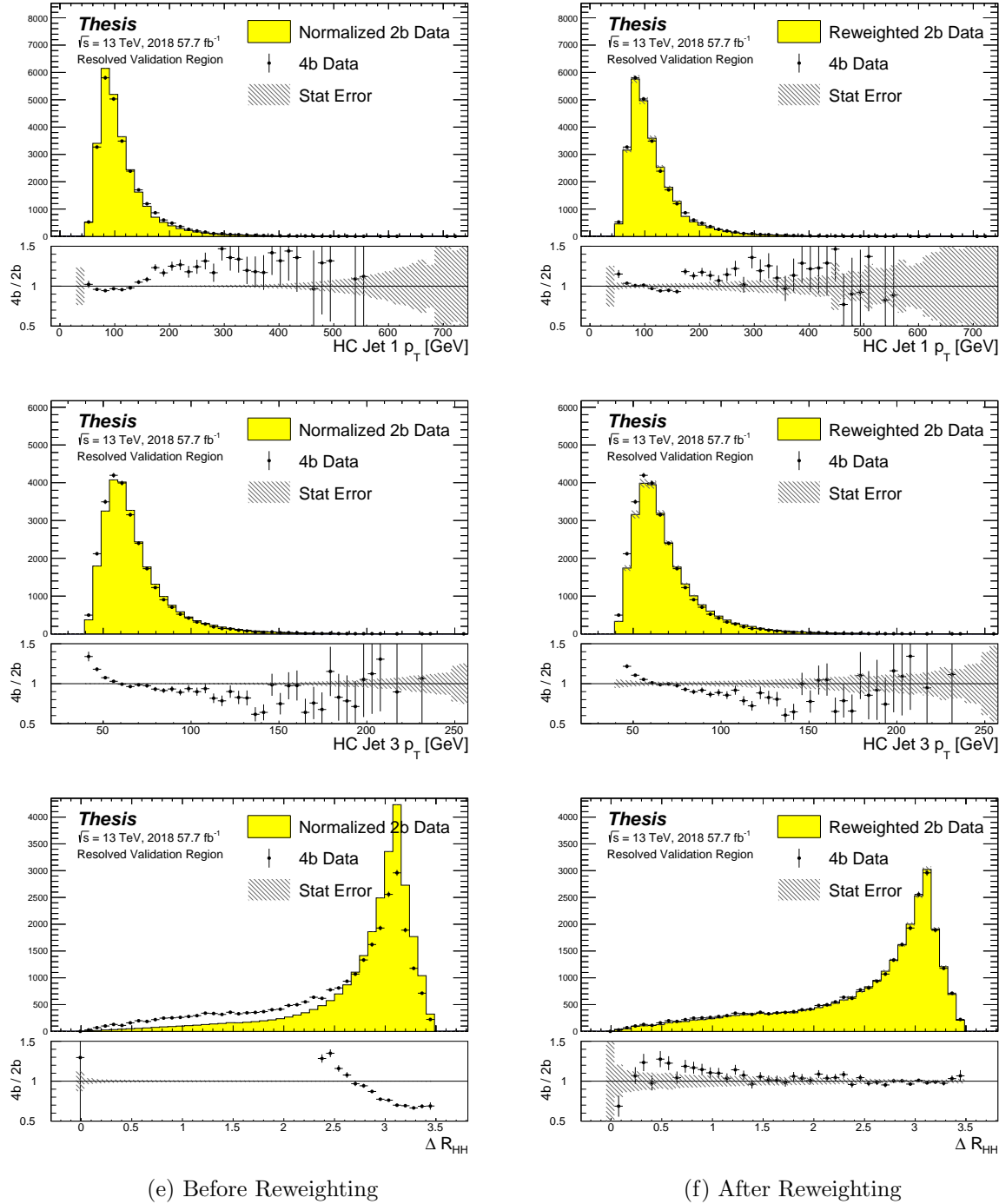


Figure 7.18: **Resonant Search:** Distributions of p_T of the 1st and 3rd leading Higgs Candidate jets and ΔR between Higgs candidates before (left) and after (right) CR derived reweighting for the 2018 Validation Region.

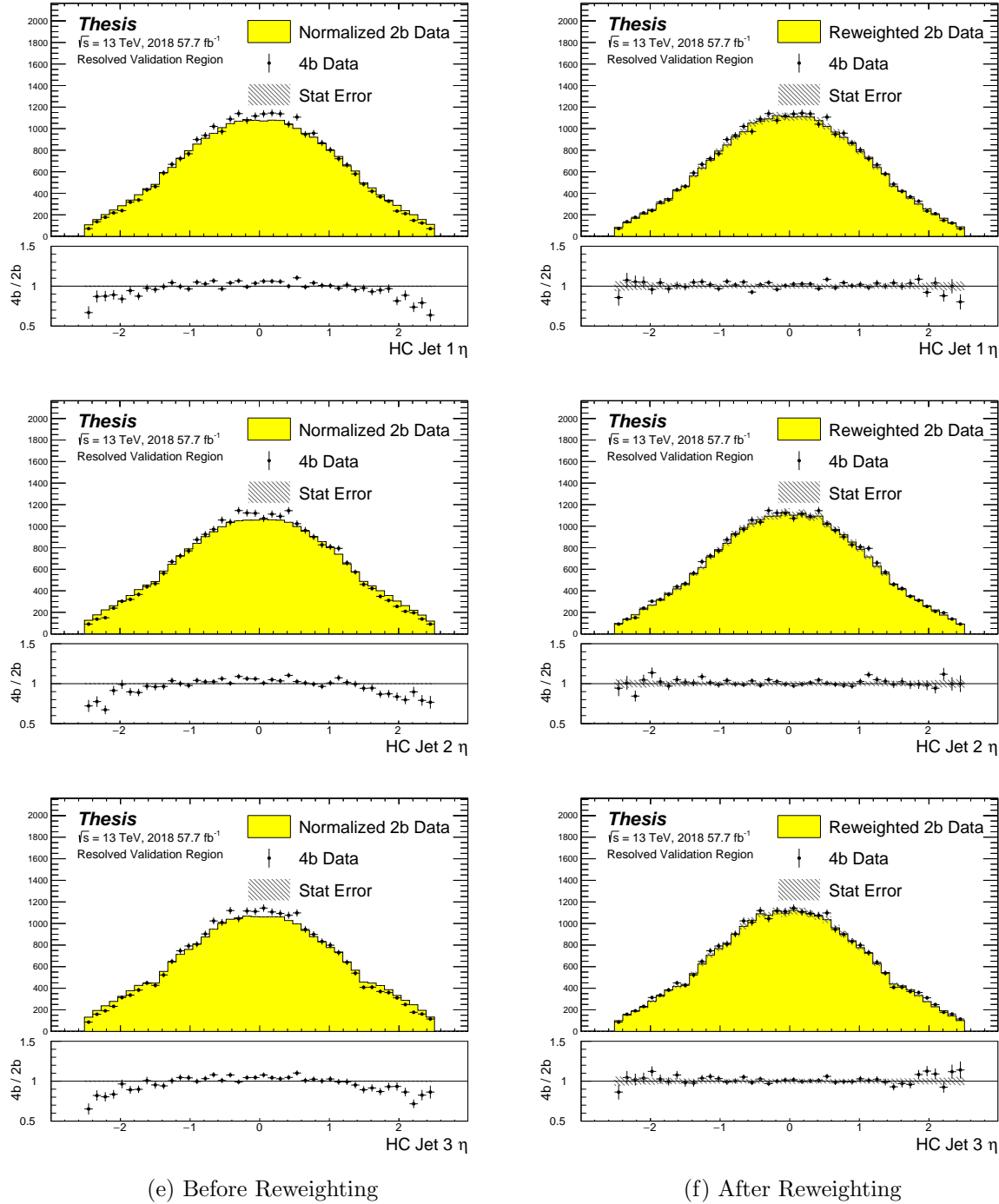


Figure 7.19: **Resonant Search:** Distributions of η of the 1st, 2nd, and 3rd leading Higgs Candidate jets before (left) and after (right) CR derived reweighting for the 2018 Validation Region.

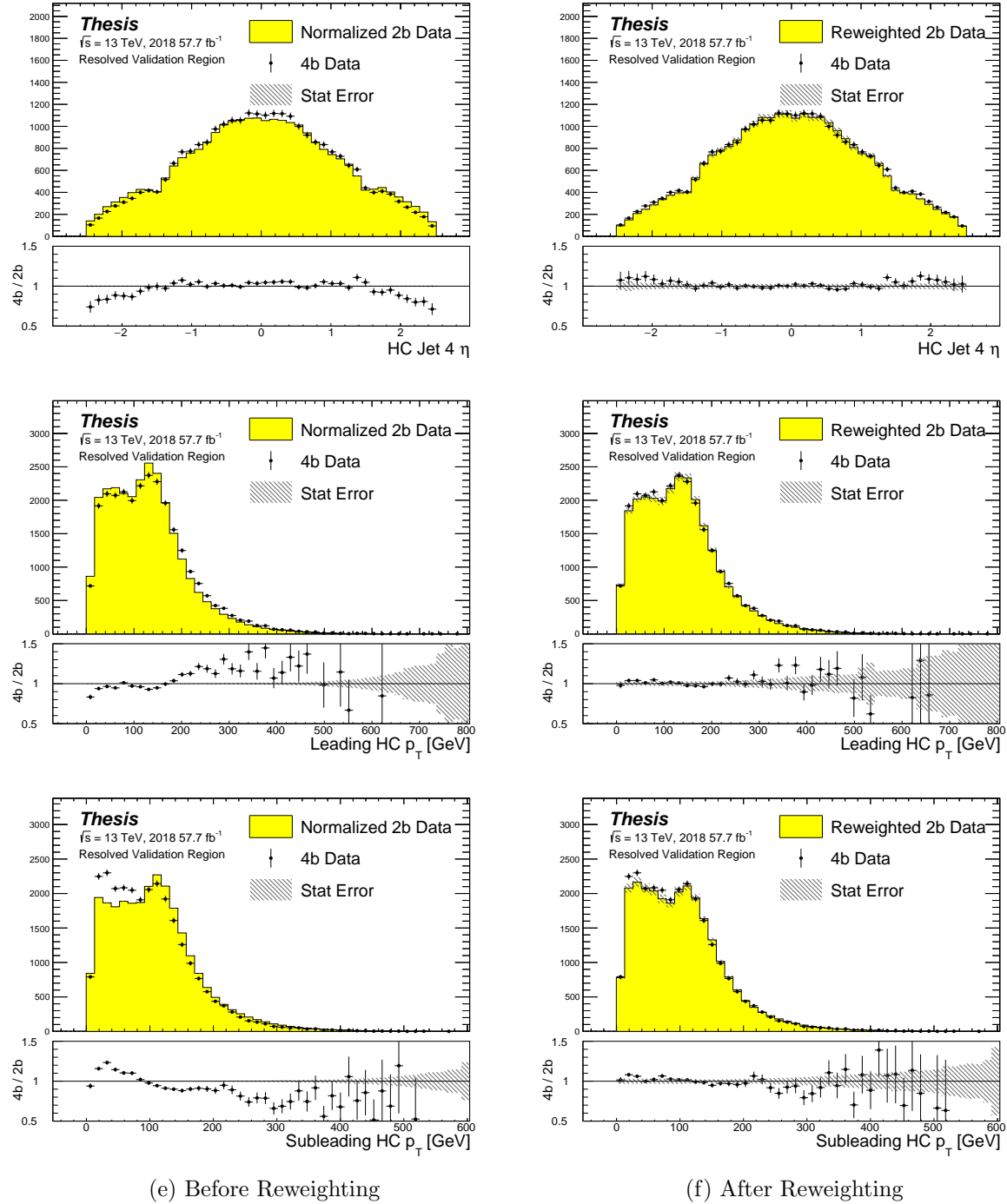


Figure 7.20: **Resonant Search:** Distributions of η of the 4th leading Higgs Candidate jet and the p_T of the leading and subleading Higgs candidates before (left) and after (right) CR derived reweighting for the 2018 Validation Region.

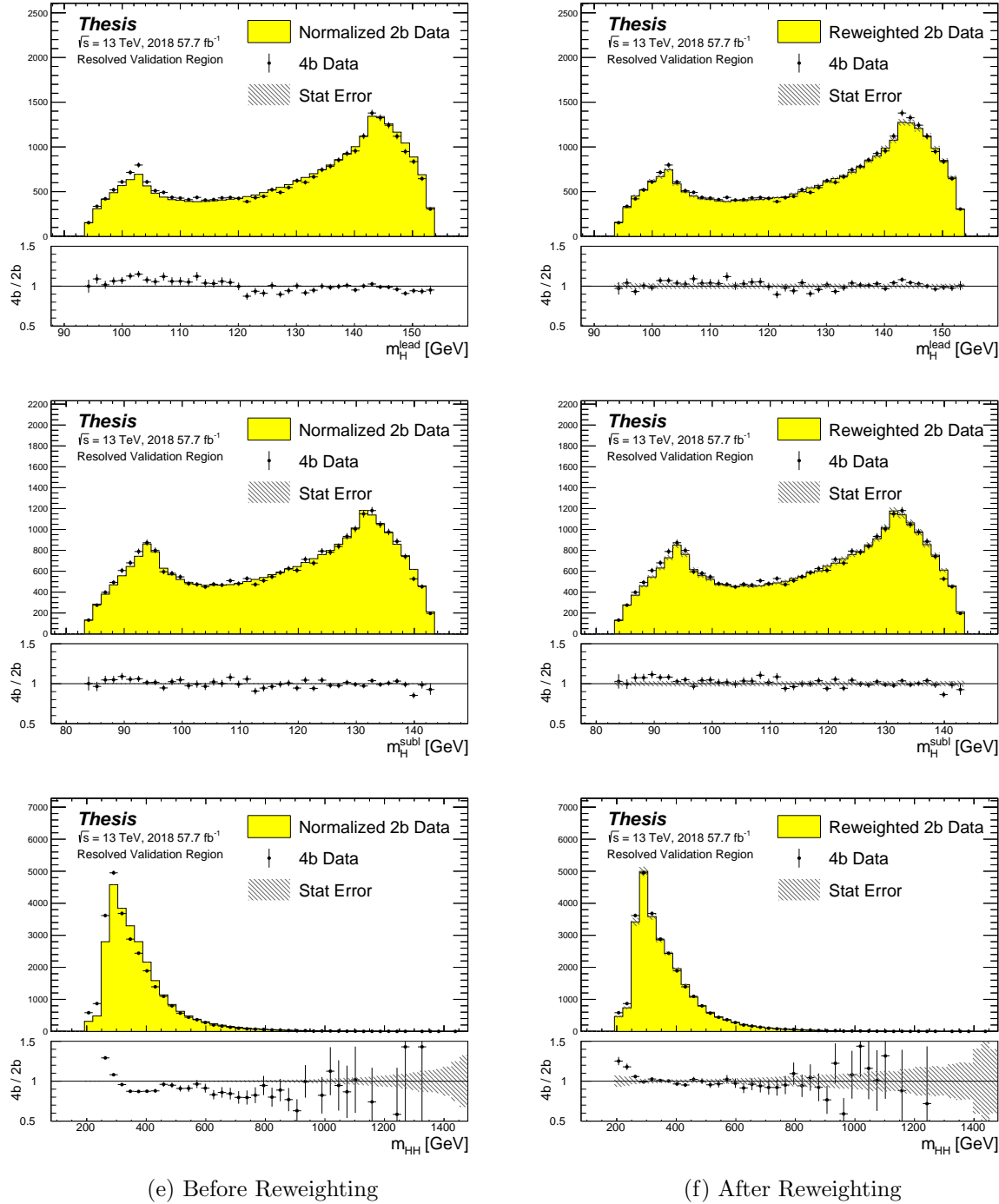


Figure 7.21: **Resonant Search:** Distributions of mass of the leading and subleading Higgs candidates and of the di-Higgs system before (left) and after (right) CR derived reweighting for the 2018 Validation Region.

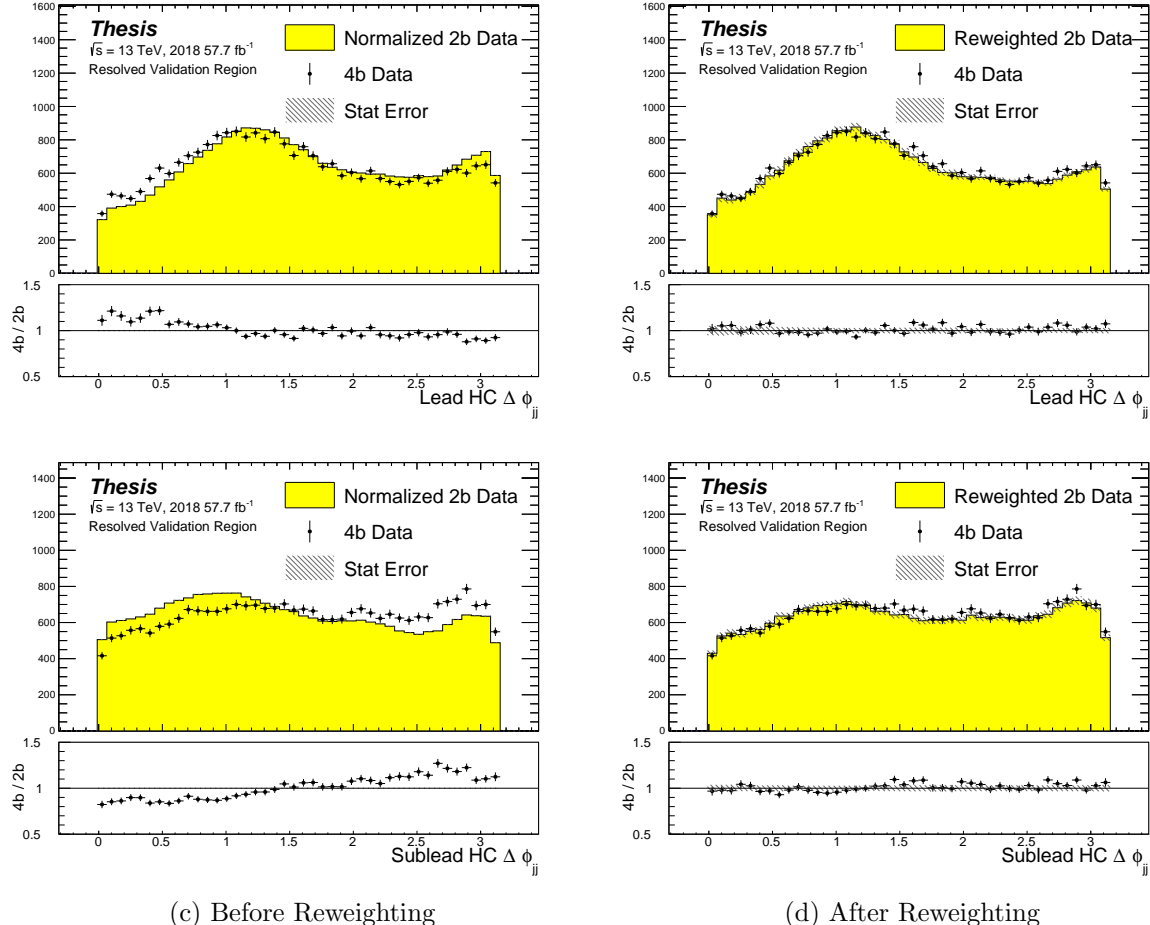


Figure 7.22: **Resonant Search:** Distributions of $\Delta\phi$ between jets in the leading and subleading Higgs candidates before (left) and after (right) CR derived reweighting for the 2018 Validation Region.

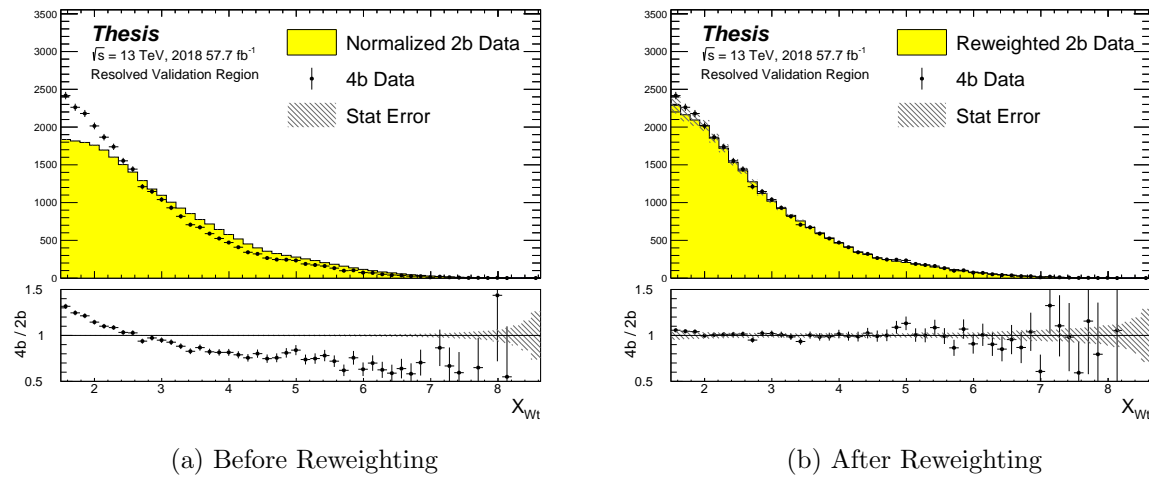


Figure 7.23: **Resonant Search:** Distributions of the top veto variable, X_{Wt} , before (left) and after (right) CR derived reweighting for the 2018 Validation Region. Reweighting is done after the cut on this variable is applied

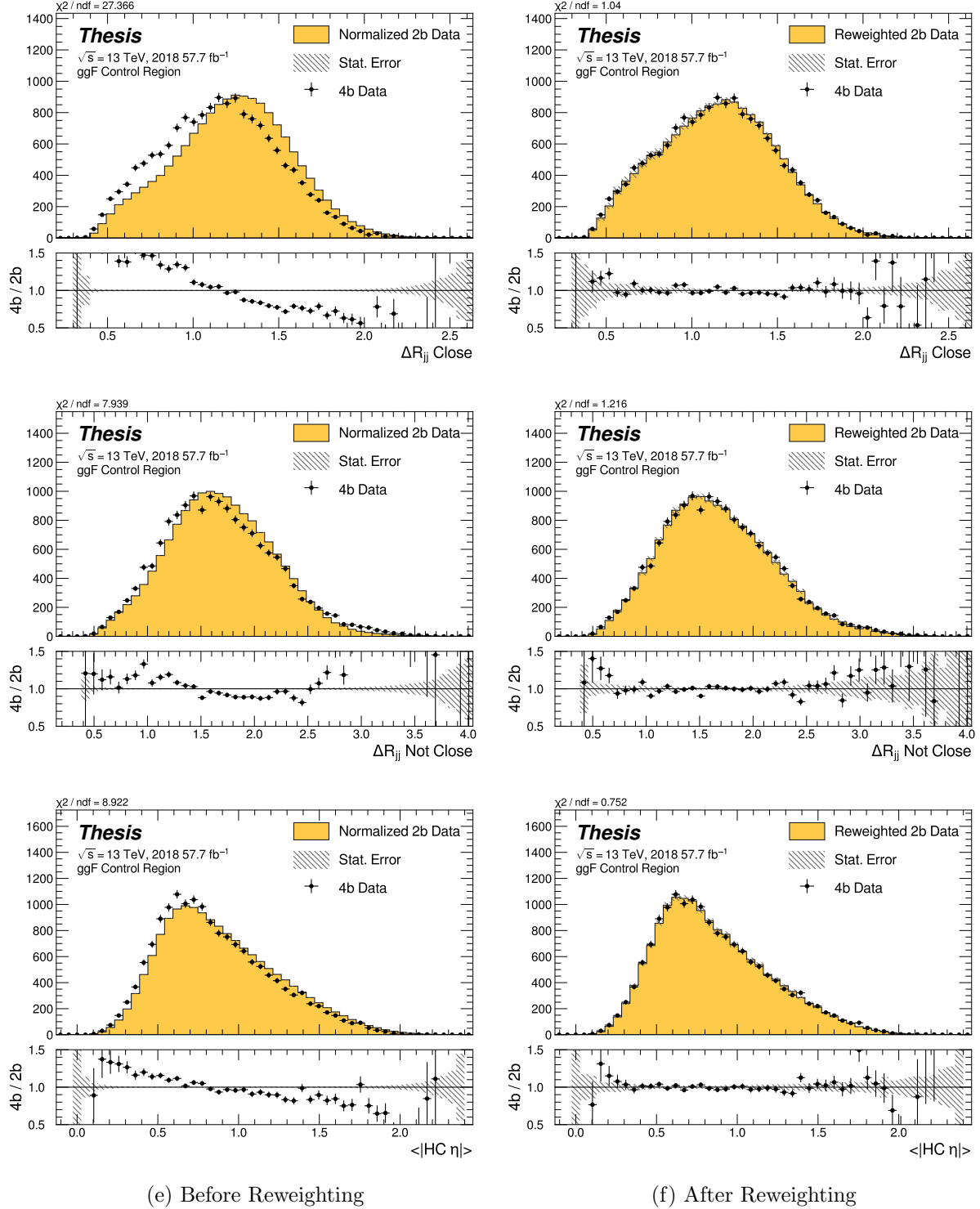


Figure 7.24: **Non-resonant Search (4b):** Distributions of ΔR between the closest Higgs Candidate jets, ΔR between the other two, and average absolute value of HC jet η before (left) and after (right) CR derived reweighting for the 2018 4b Control Region.

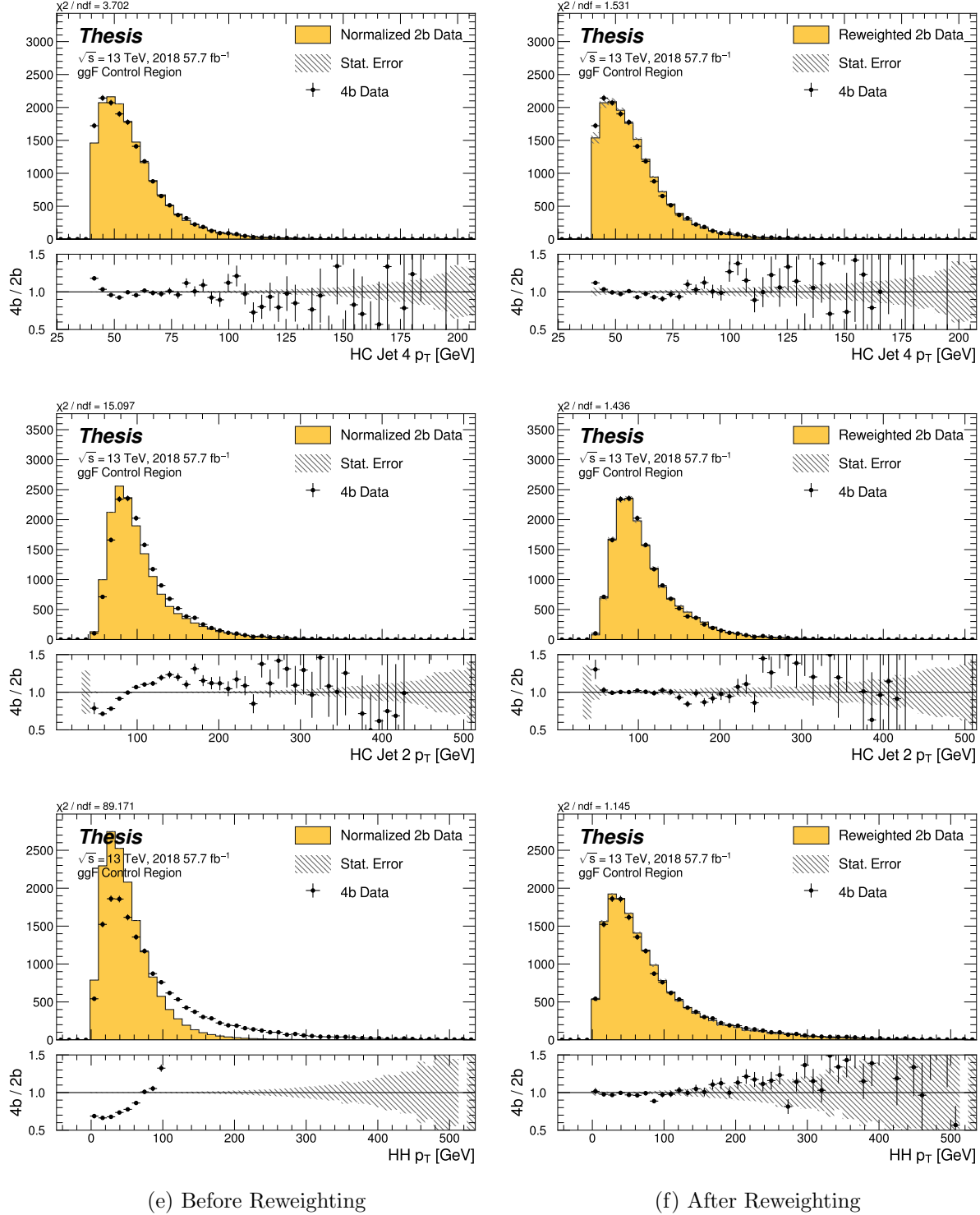


Figure 7.25: **Non-resonant Search (4b):** Distributions of p_T of the 2nd and 4th leading Higgs Candidate jets and the p_T of the di-Higgs system before (left) and after (right) CR derived reweighting for the 2018 4b Control Region.

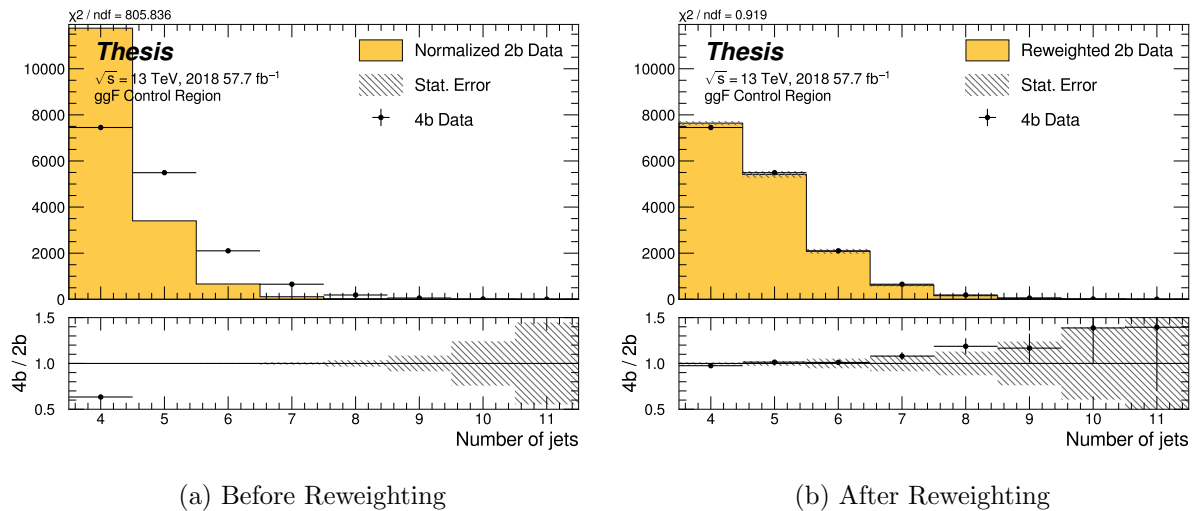


Figure 7.26: **Non-resonant Search (4b)**: Distributions of the number of jets before (left) and after (right) CR derived reweighting for the 2018 4b Control Region. A minimum of 4 jets is required in each event in order to form Higgs candidates.

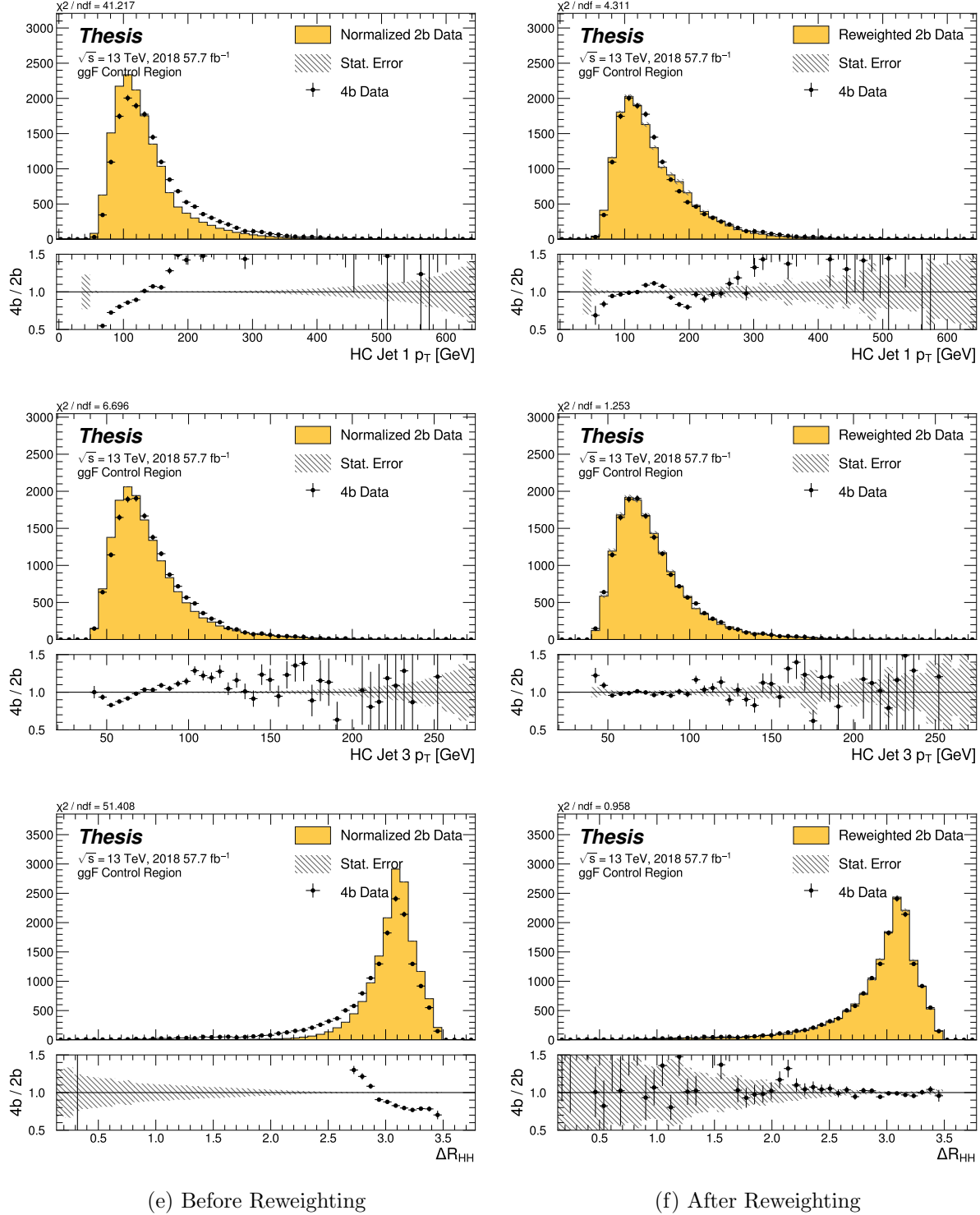


Figure 7.27: **Non-resonant Search (4b):** Distributions of p_T of the 1st and 3rd leading Higgs Candidate jets and ΔR between Higgs candidates before (left) and after (right) CR derived reweighting for the 2018 4b Control Region.

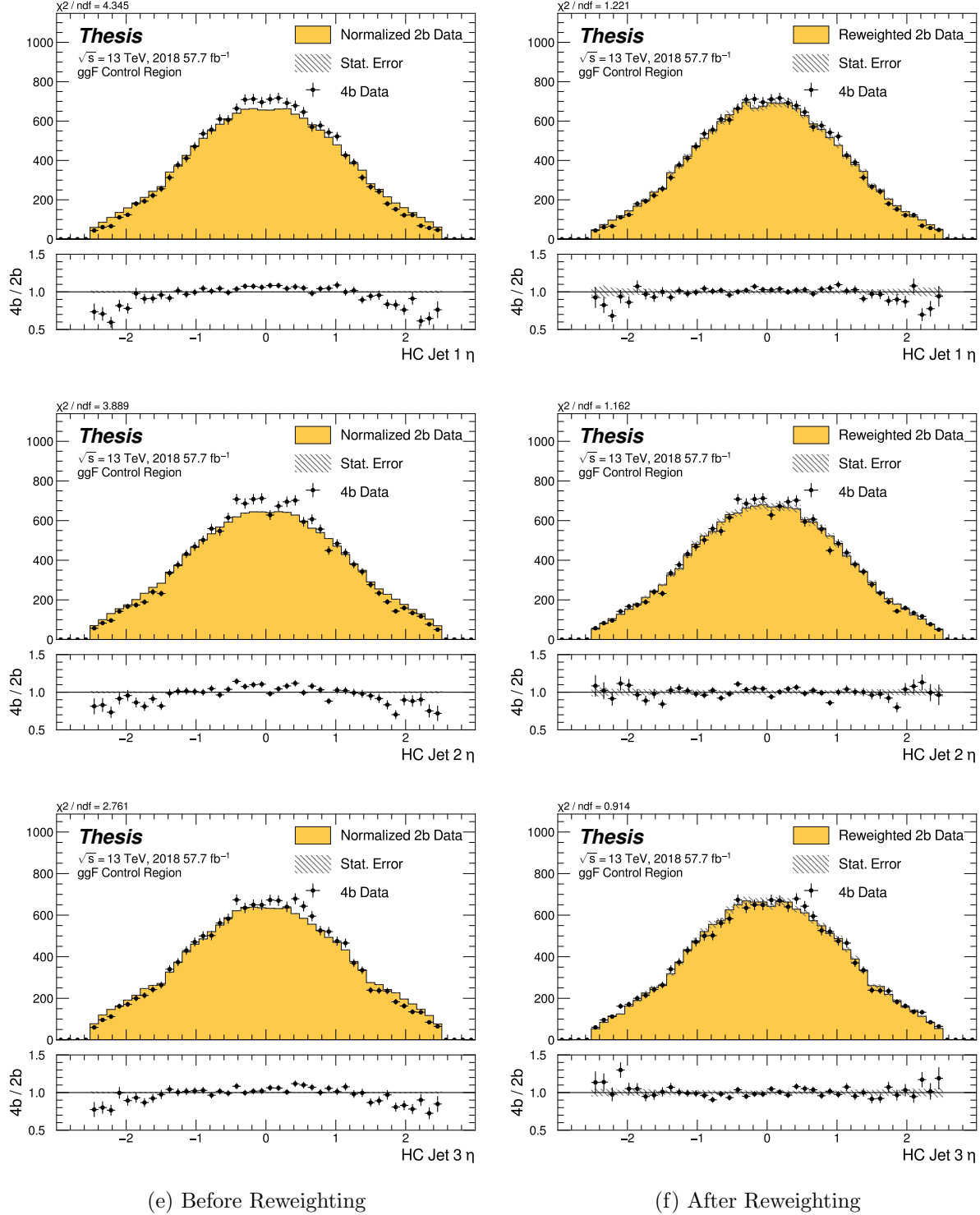


Figure 7.28: **Non-resonant Search (4b):** Distributions of η of the 1st, 2nd, and 3rd leading Higgs Candidate jets before (left) and after (right) CR derived reweighting for the 2018 4b Control Region.

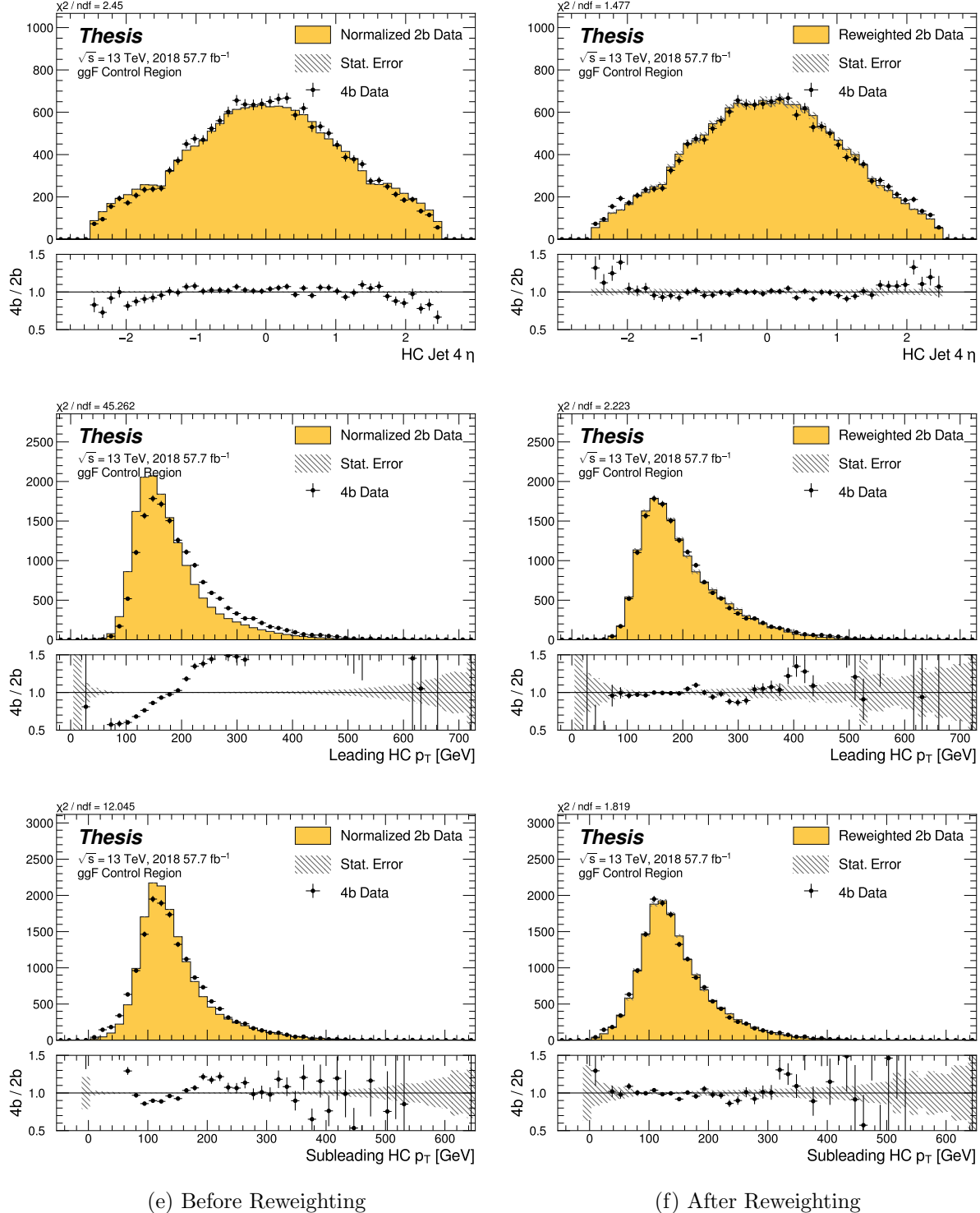


Figure 7.29: **Non-resonant Search (4b):** Distributions of η of the 4th leading Higgs Candidate jet and the p_T of the leading and subleading Higgs candidates before (left) and after (right) CR derived reweighting for the 2018 4b Control Region.

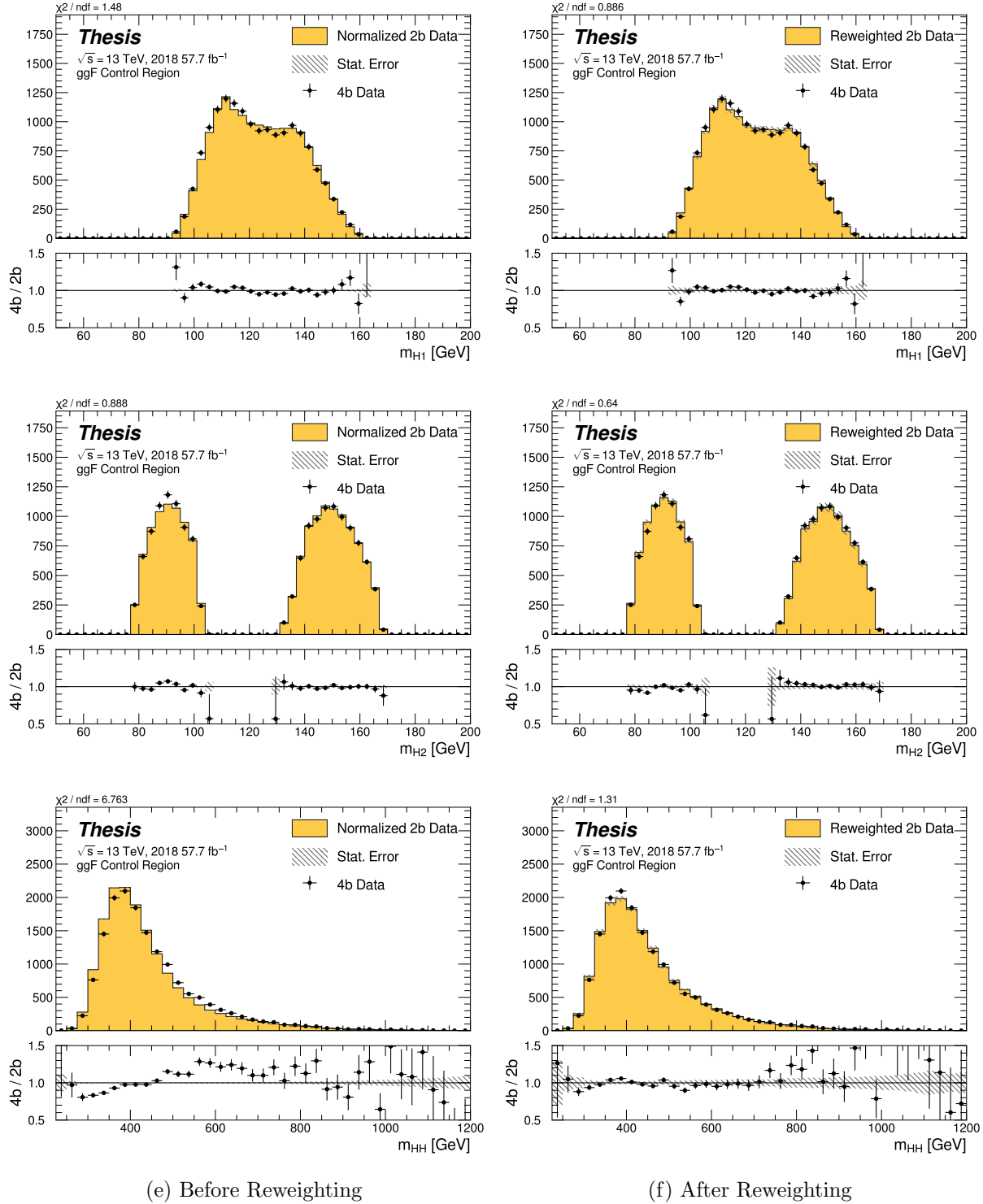


Figure 7.30: **Non-resonant Search (4b):** Distributions of mass of the leading and subleading Higgs candidates and of the di-Higgs system before (left) and after (right) CR derived reweighting for the 2018 4b Control Region.

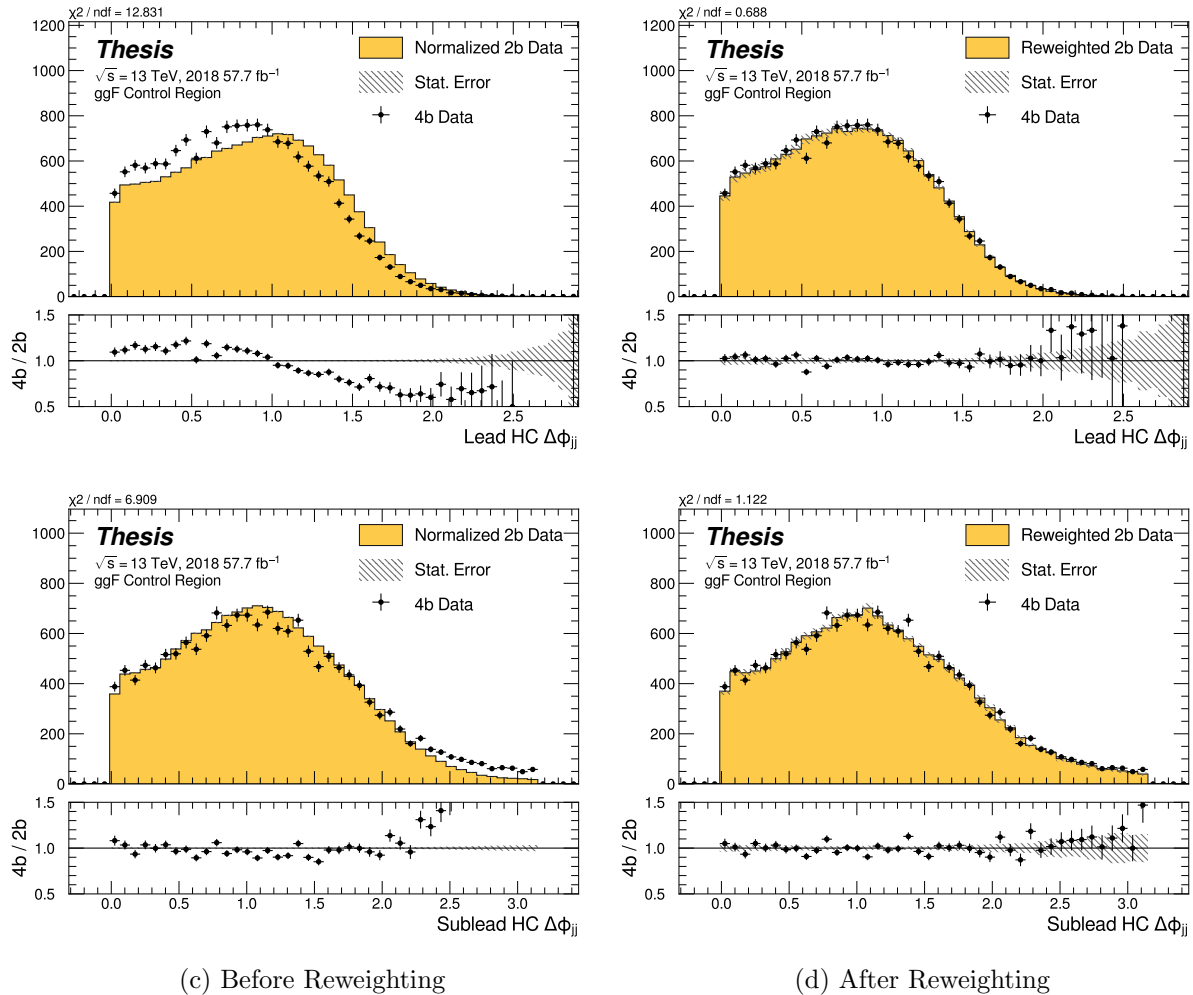


Figure 7.31: **Non-resonant Search (4b):** Distributions of $\Delta\phi$ between jets in the leading and subleading Higgs candidates before (left) and after (right) CR derived reweighting for the 2018 4b Control Region.

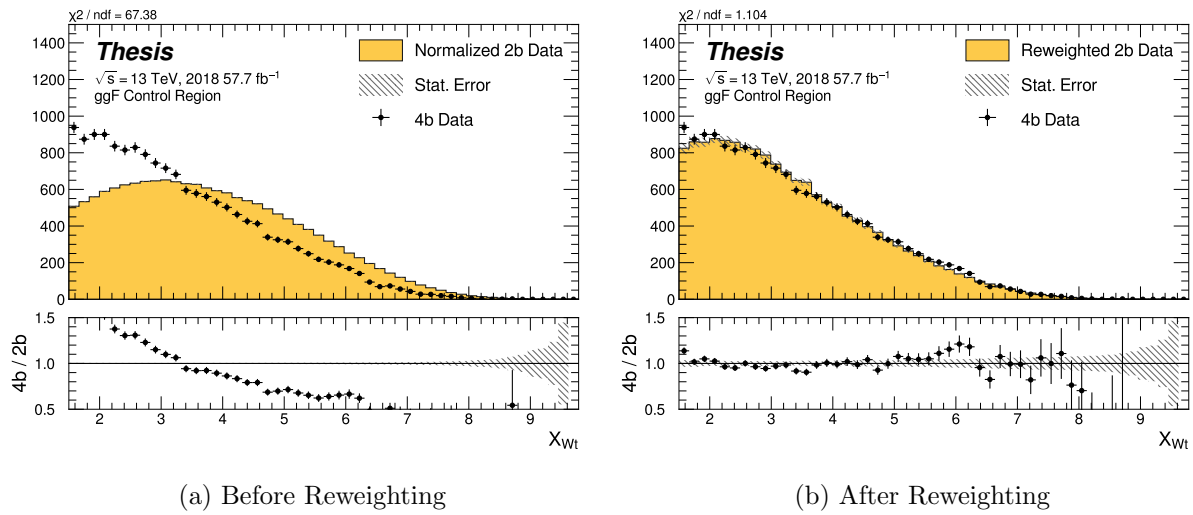


Figure 7.32: **Non-resonant Search (4b):** Distributions of the top veto variable, X_{Wt} , before (left) and after (right) CR derived reweighting for the 2018 4b Control Region. Reweighting is done after the cut on this variable is applied.

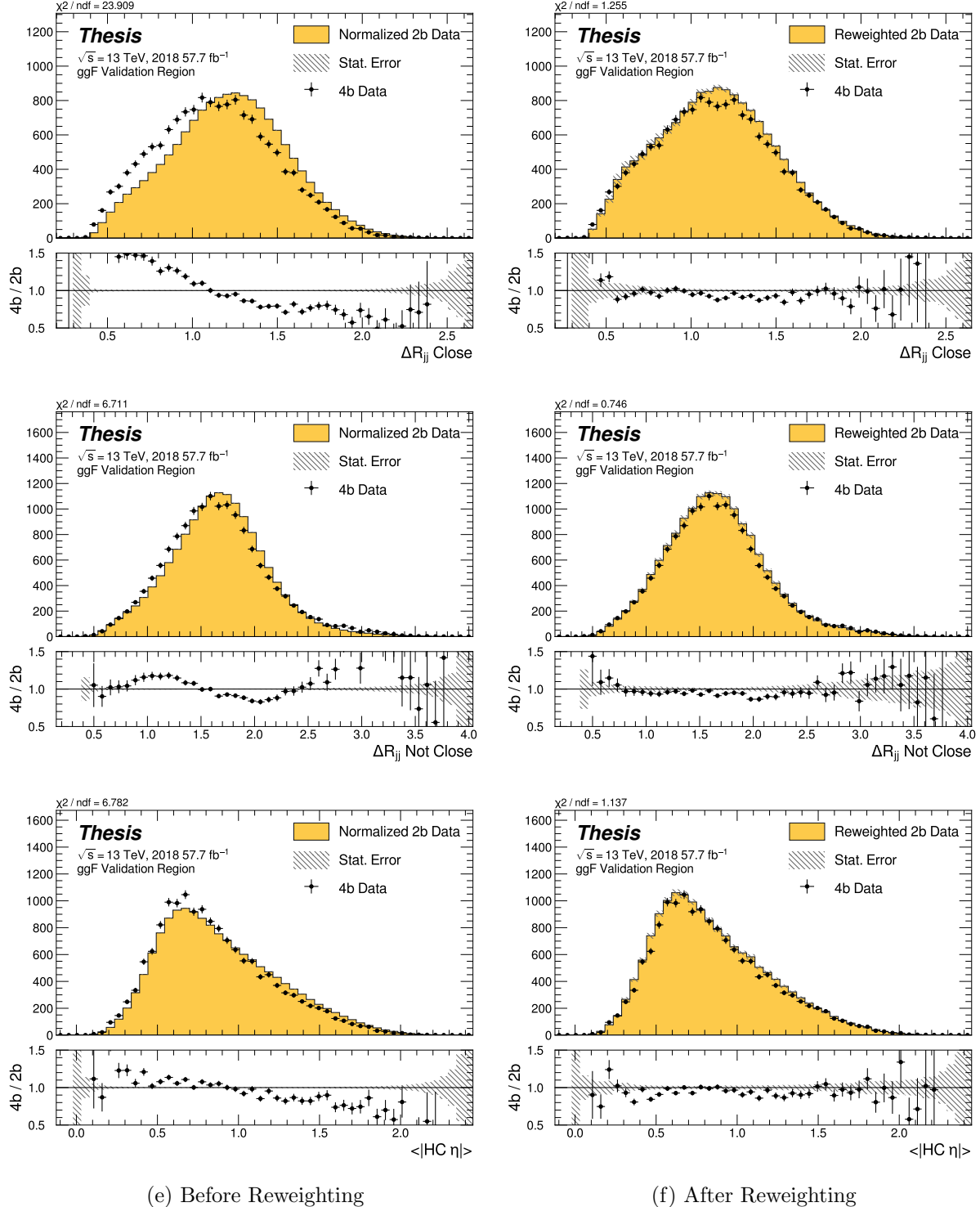


Figure 7.33: **Non-resonant Search (4b):** Distributions of ΔR between the closest Higgs Candidate jets, ΔR between the other two, and average absolute value of HC jet η before (left) and after (right) CR derived reweighting for the 2018 4b Validation Region.

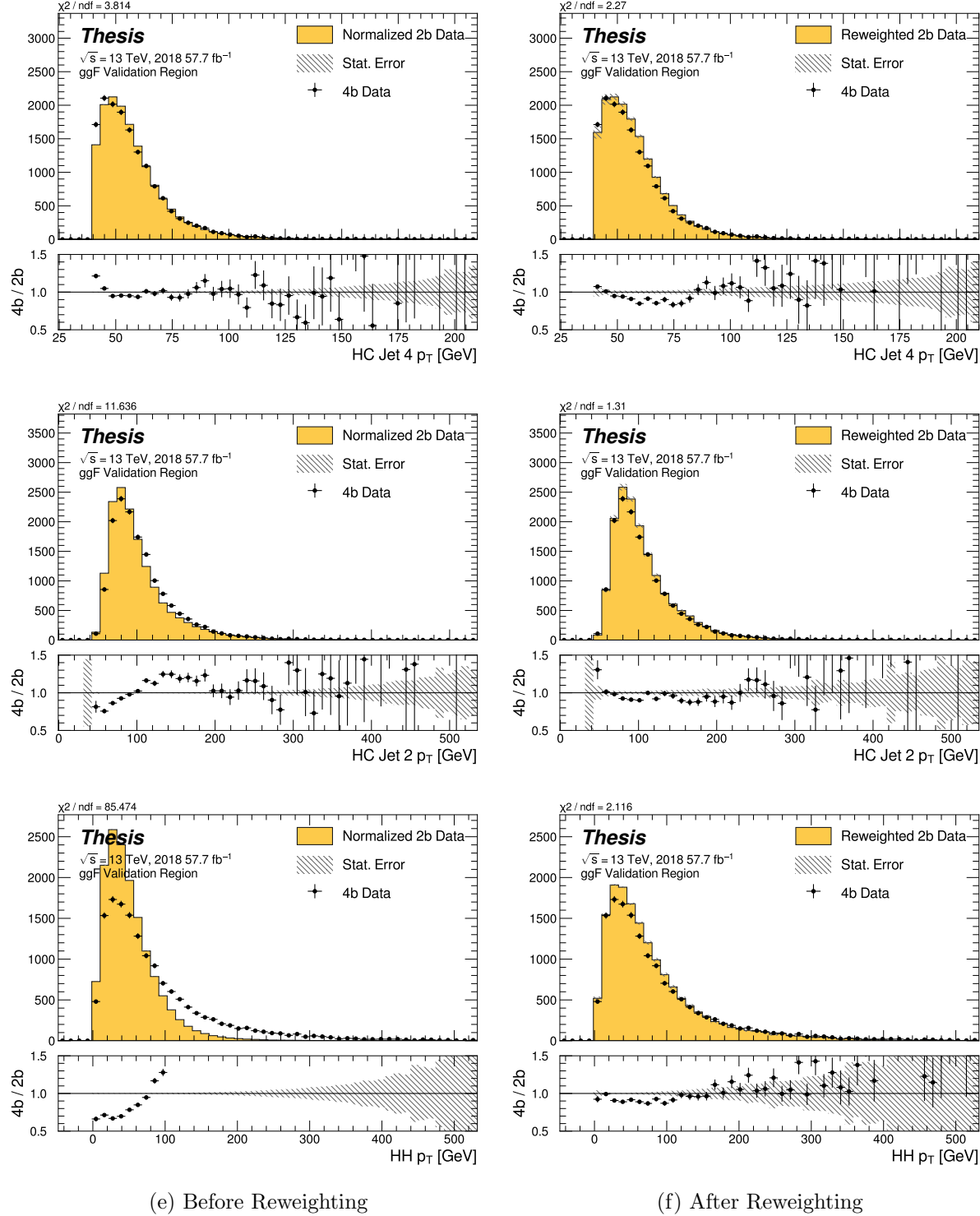


Figure 7.34: **Non-resonant Search (4b):** Distributions of p_T of the 2nd and 4th leading Higgs Candidate jets and the p_T of the di-Higgs system before (left) and after (right) CR derived reweighting for the 2018 4b Validation Region.

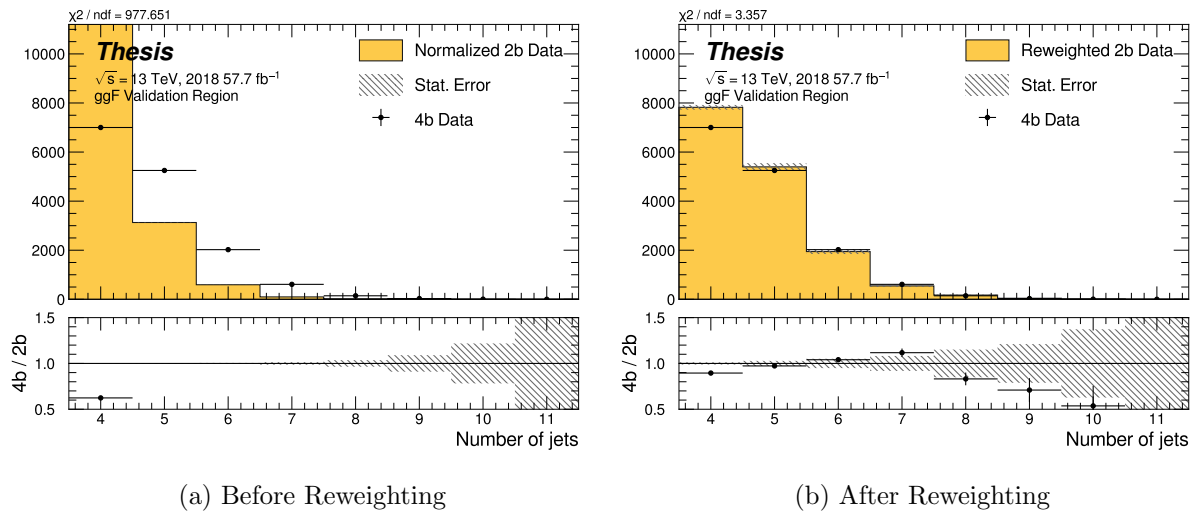


Figure 7.35: **Non-resonant Search (4b)**: Distributions of the number of jets before (left) and after (right) CR derived reweighting for the 2018 4b Validation Region. A minimum of 4 jets is required in each event in order to form Higgs candidates.

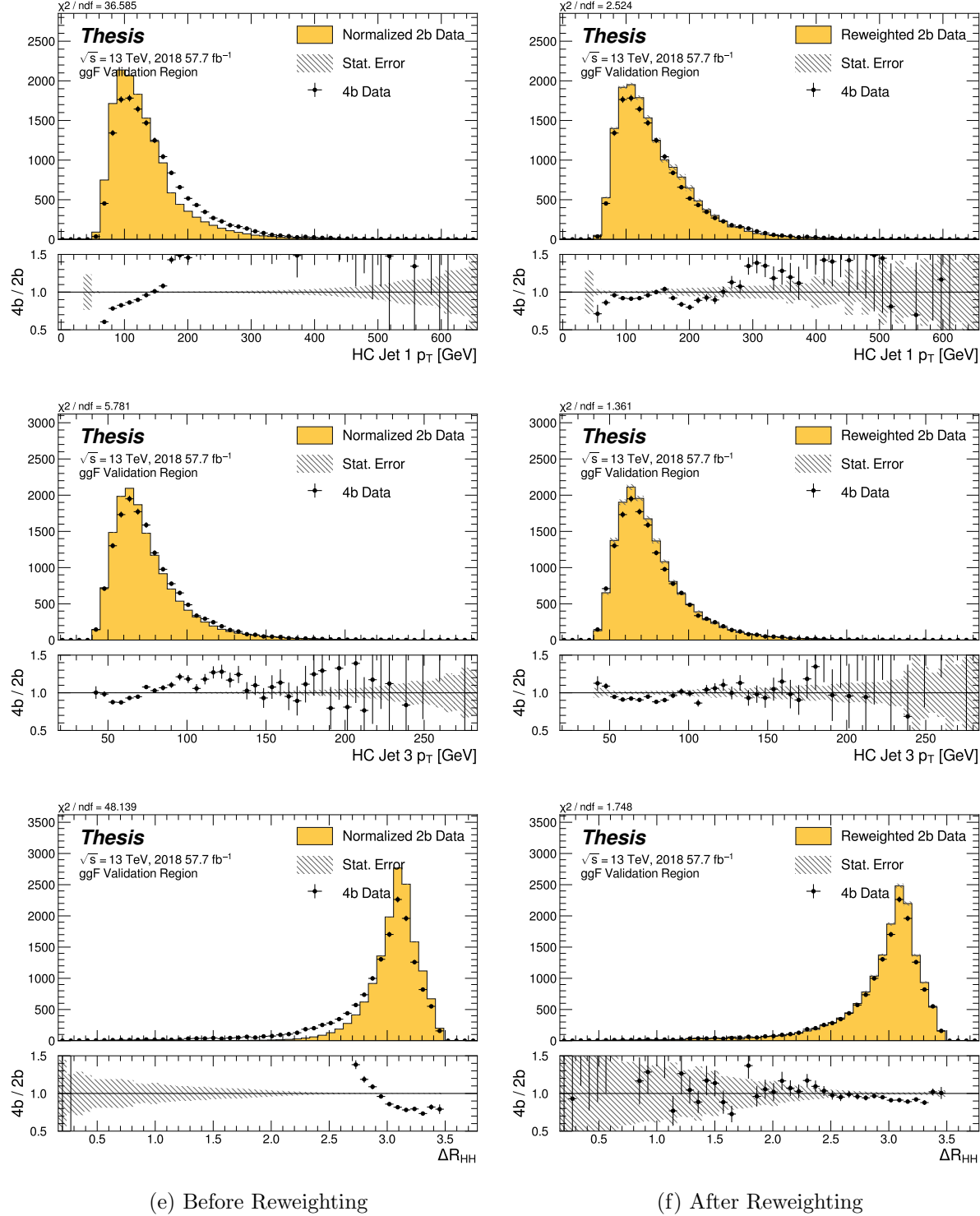


Figure 7.36: **Non-resonant Search (4b):** Distributions of p_T of the 1st and 3rd leading Higgs Candidate jets and ΔR between Higgs candidates before (left) and after (right) CR derived reweighting for the 2018 4b Validation Region.

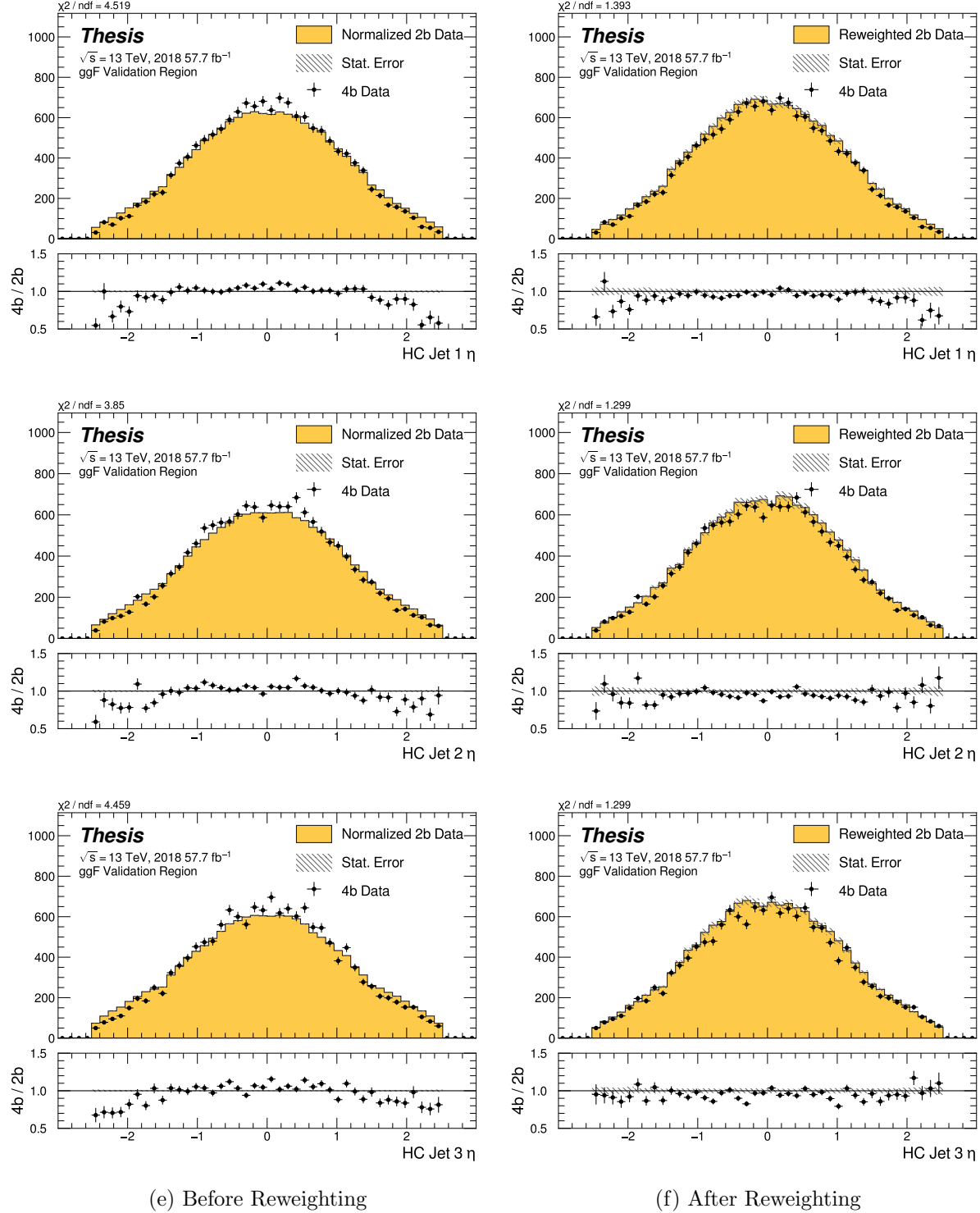


Figure 7.37: **Non-resonant Search (4b):** Distributions of η of the 1st, 2nd, and 3rd leading Higgs Candidate jets before (left) and after (right) CR derived reweighting for the 2018 4b Validation Region.

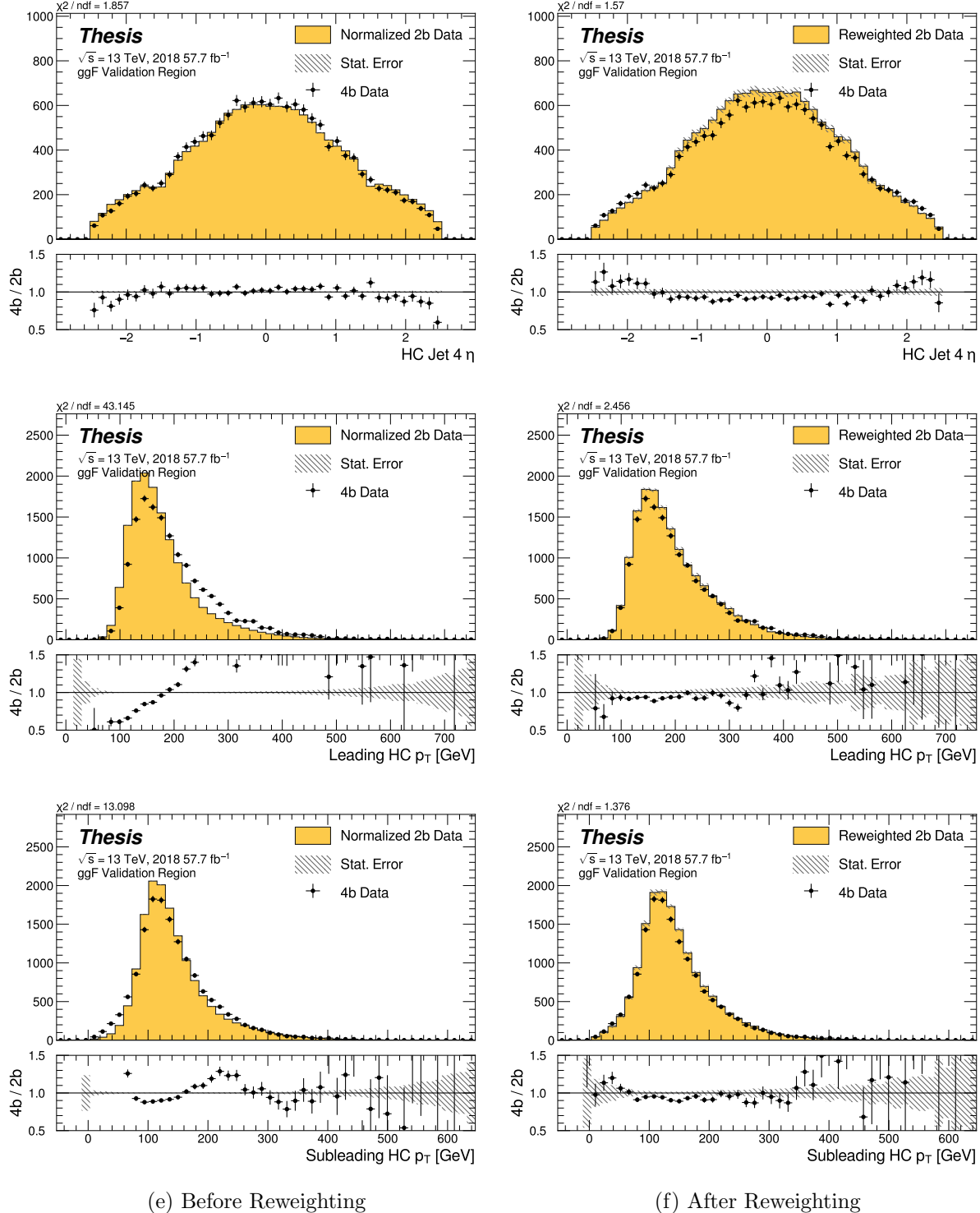


Figure 7.38: **Non-resonant Search (4b):** Distributions of η of the 4th leading Higgs Candidate jet and the p_T of the leading and subleading Higgs candidates before (left) and after (right) CR derived reweighting for the 2018 4b Validation Region.

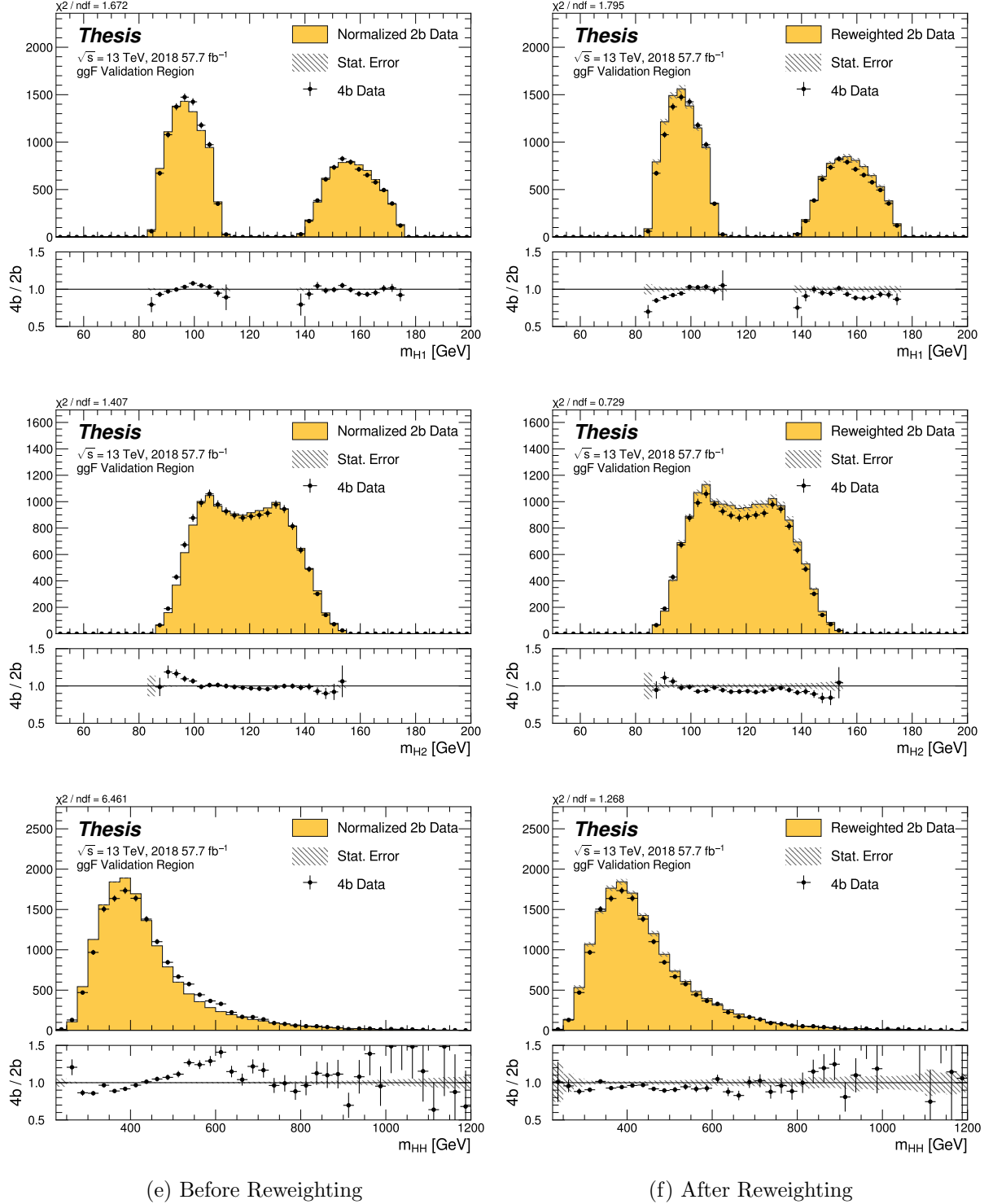


Figure 7.39: **Non-resonant Search (4b):** Distributions of mass of the leading and subleading Higgs candidates and of the di-Higgs system before (left) and after (right) CR derived reweighting for the 2018 4b Validation Region.

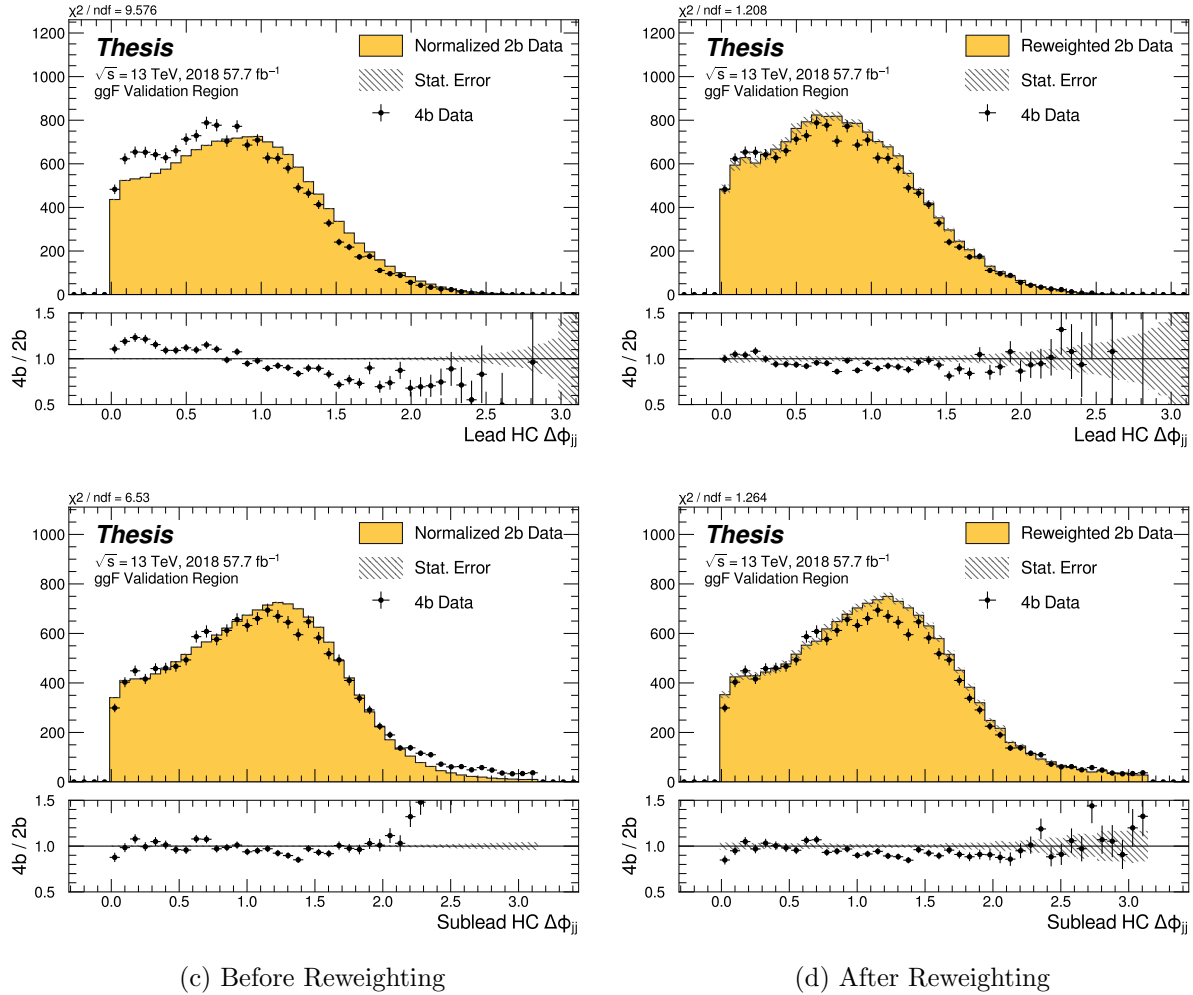


Figure 7.40: **Non-resonant Search (4b):** Distributions of $\Delta\phi$ between jets in the leading and subleading Higgs candidates before (left) and after (right) CR derived reweighting for the 2018 4b Validation Region.

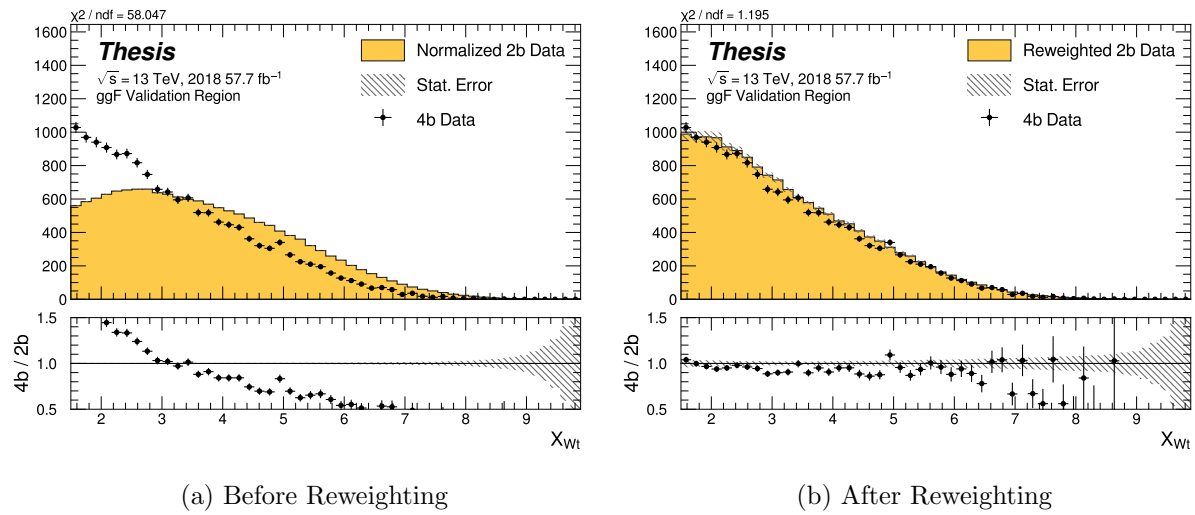


Figure 7.41: **Non-resonant Search (4b):** Distributions of the top veto variable, X_{Wt} , before (left) and after (right) CR derived reweighting for the 2018 4b Validation Region. Reweighting is done after the cut on this variable is applied.

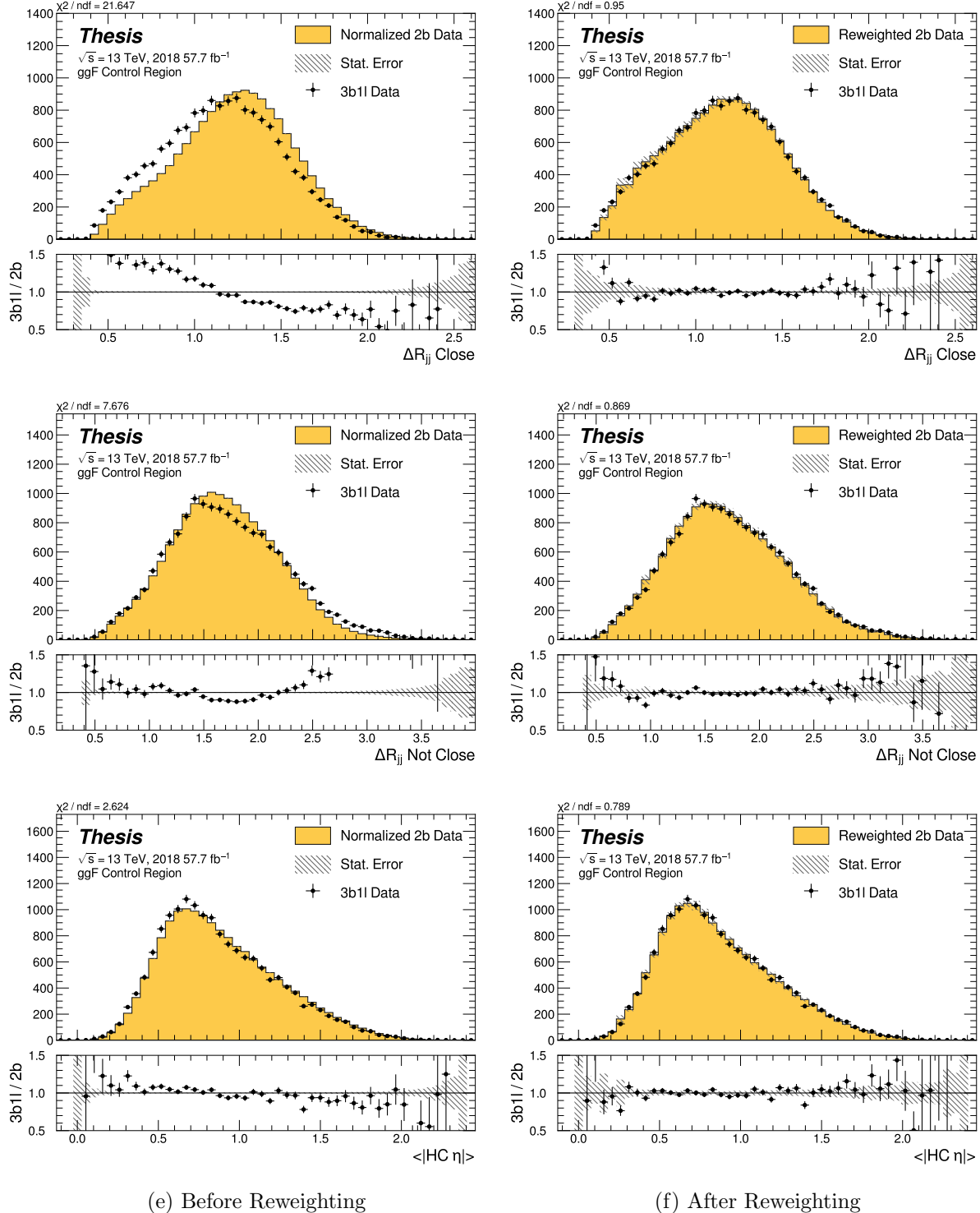


Figure 7.42: **Non-resonant Search (3b1l):** Distributions of ΔR between the closest Higgs Candidate jets, ΔR between the other two, and average absolute value of HC jet η before (left) and after (right) CR derived reweighting for the 2018 3b1l Control Region.

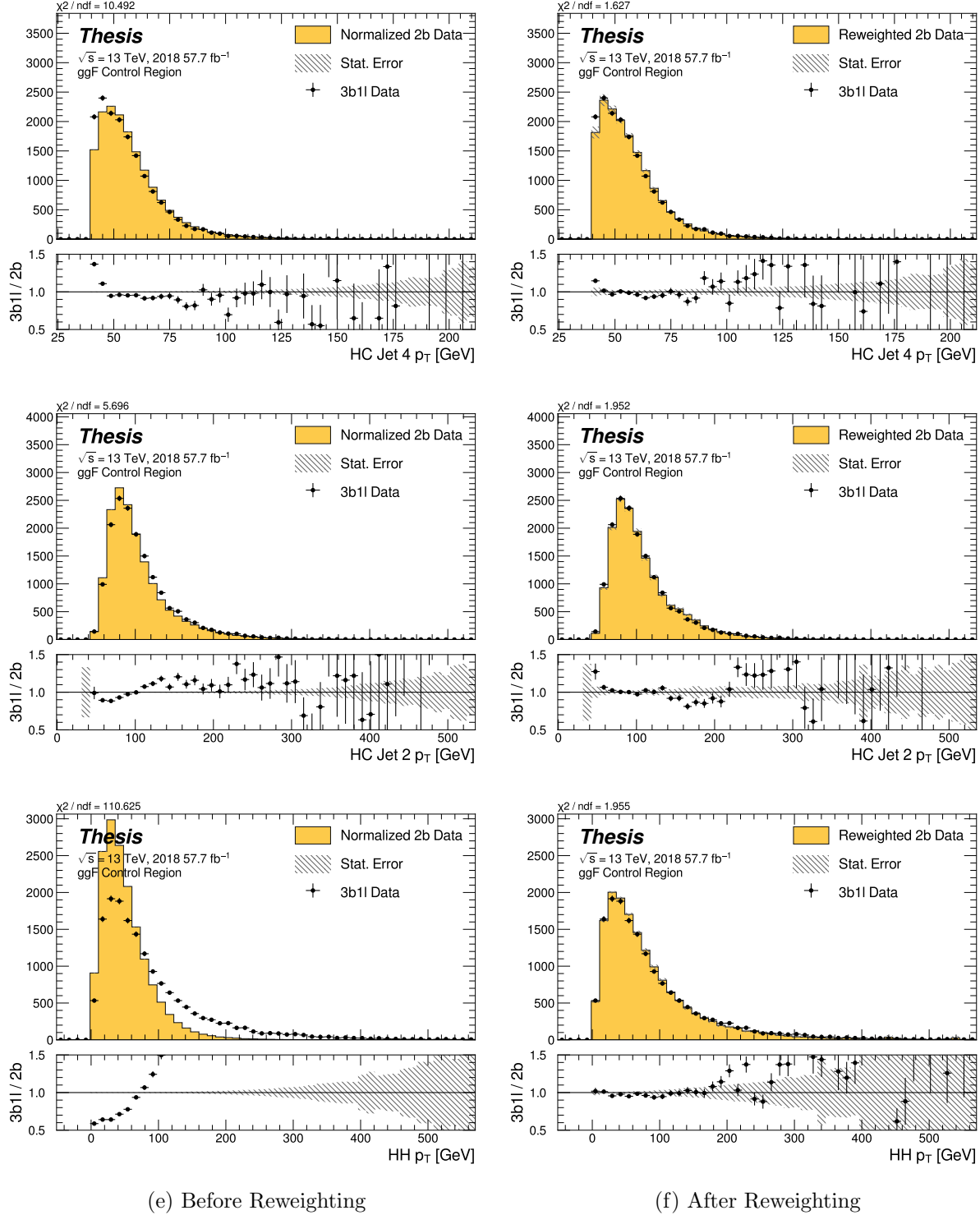


Figure 7.43: **Non-resonant Search (3b1l):** Distributions of p_T of the 2nd and 4th leading Higgs Candidate jets and the p_T of the di-Higgs system before (left) and after (right) CR derived reweighting for the 2018 3b1l Control Region.

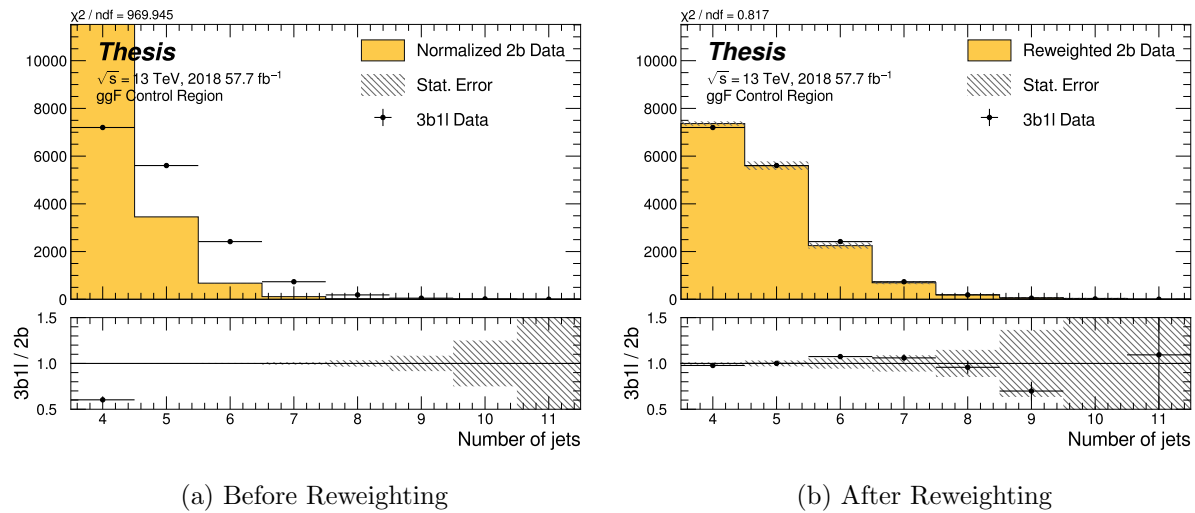


Figure 7.44: **Non-resonant Search (3b1l)**: Distributions of the number of jets before (left) and after (right) CR derived reweighting for the 2018 3b1l Control Region. A minimum of 4 jets is required in each event in order to form Higgs candidates.

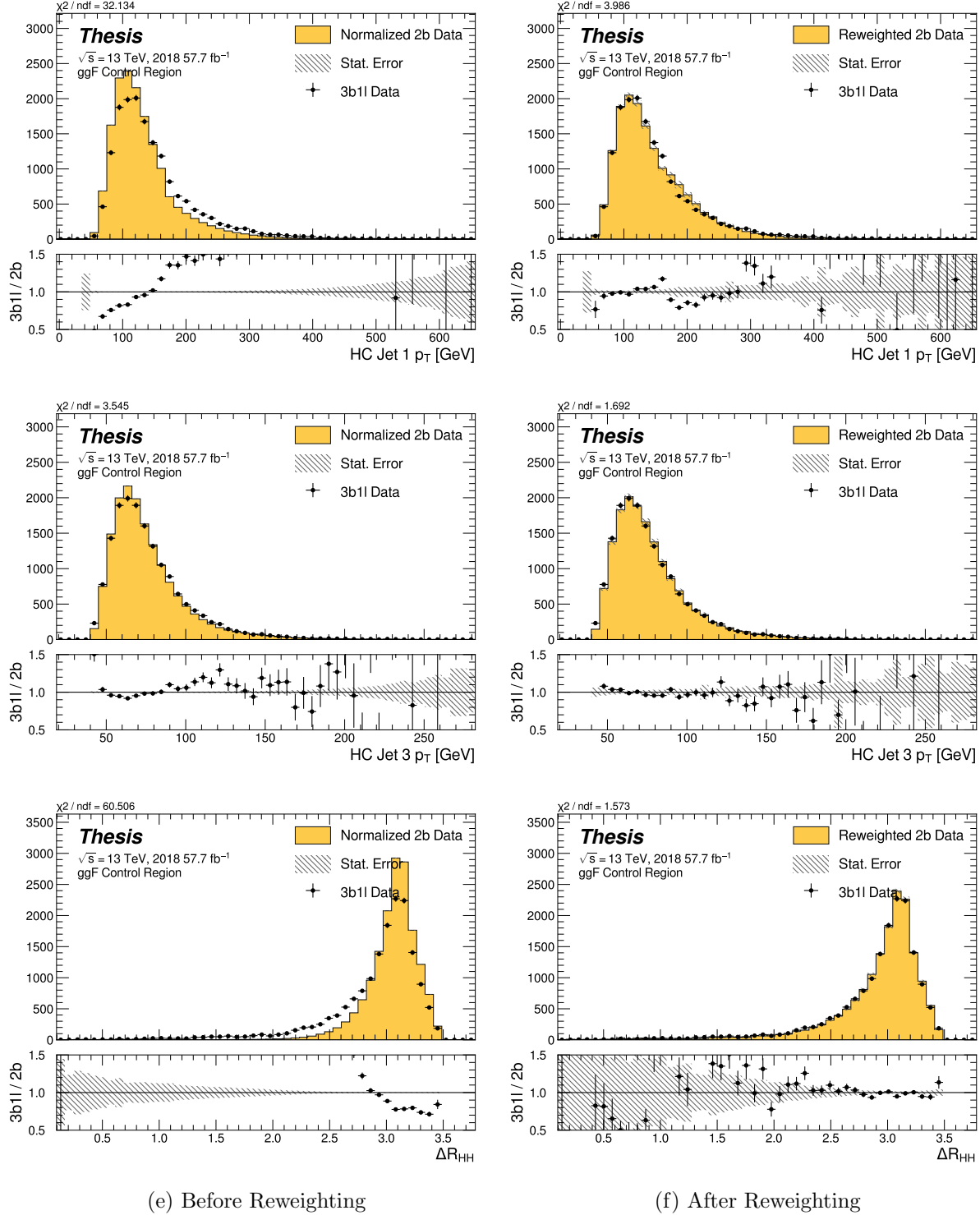


Figure 7.45: **Non-resonant Search (3b1l):** Distributions of p_T of the 1st and 3rd leading Higgs Candidate jets and ΔR between Higgs candidates before (left) and after (right) CR derived reweighting for the 2018 3b1l Control Region.

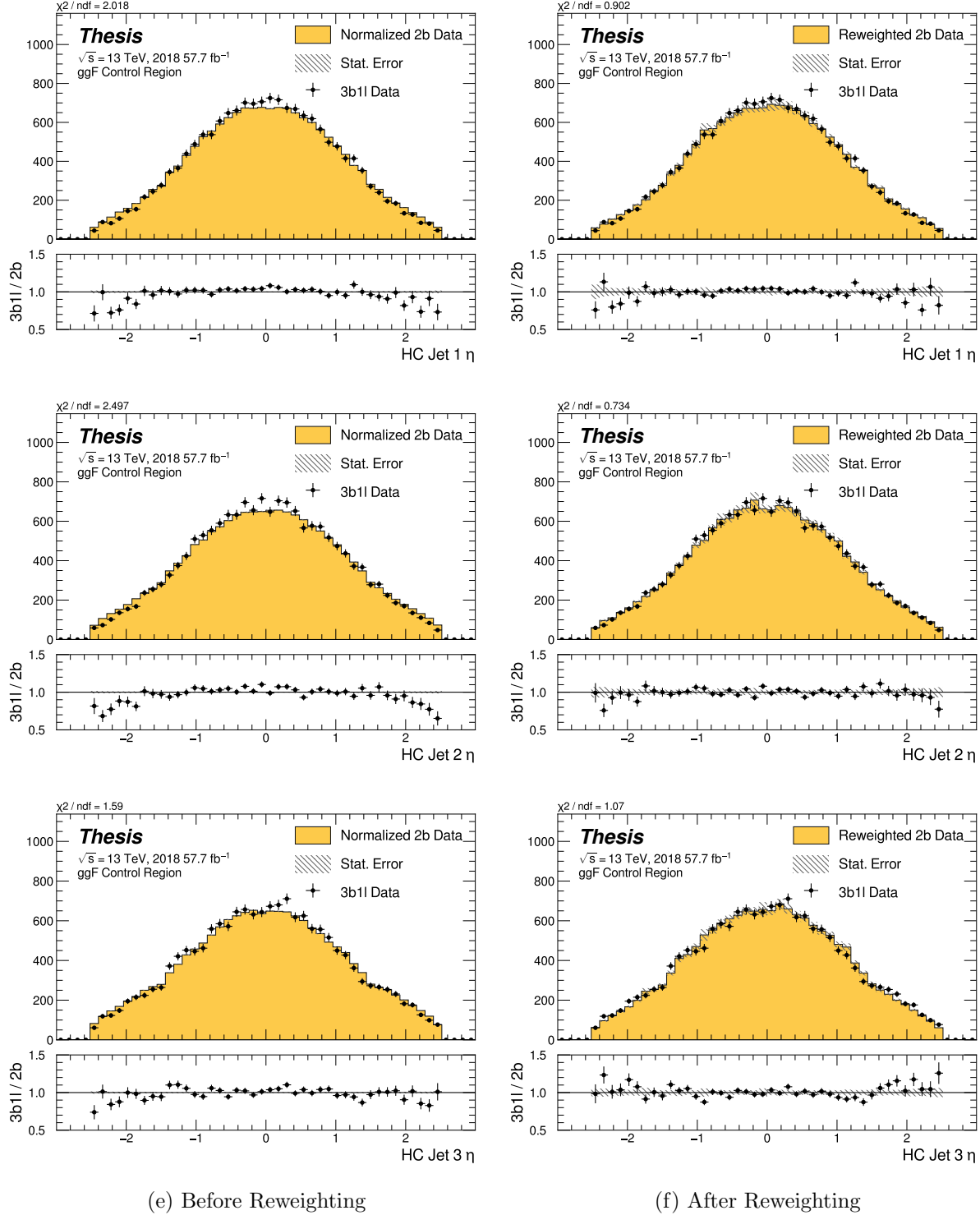


Figure 7.46: **Non-resonant Search (3b1l):** Distributions of η of the 1st, 2nd, and 3rd leading Higgs Candidate jets before (left) and after (right) CR derived reweighting for the 2018 3b1l Control Region.

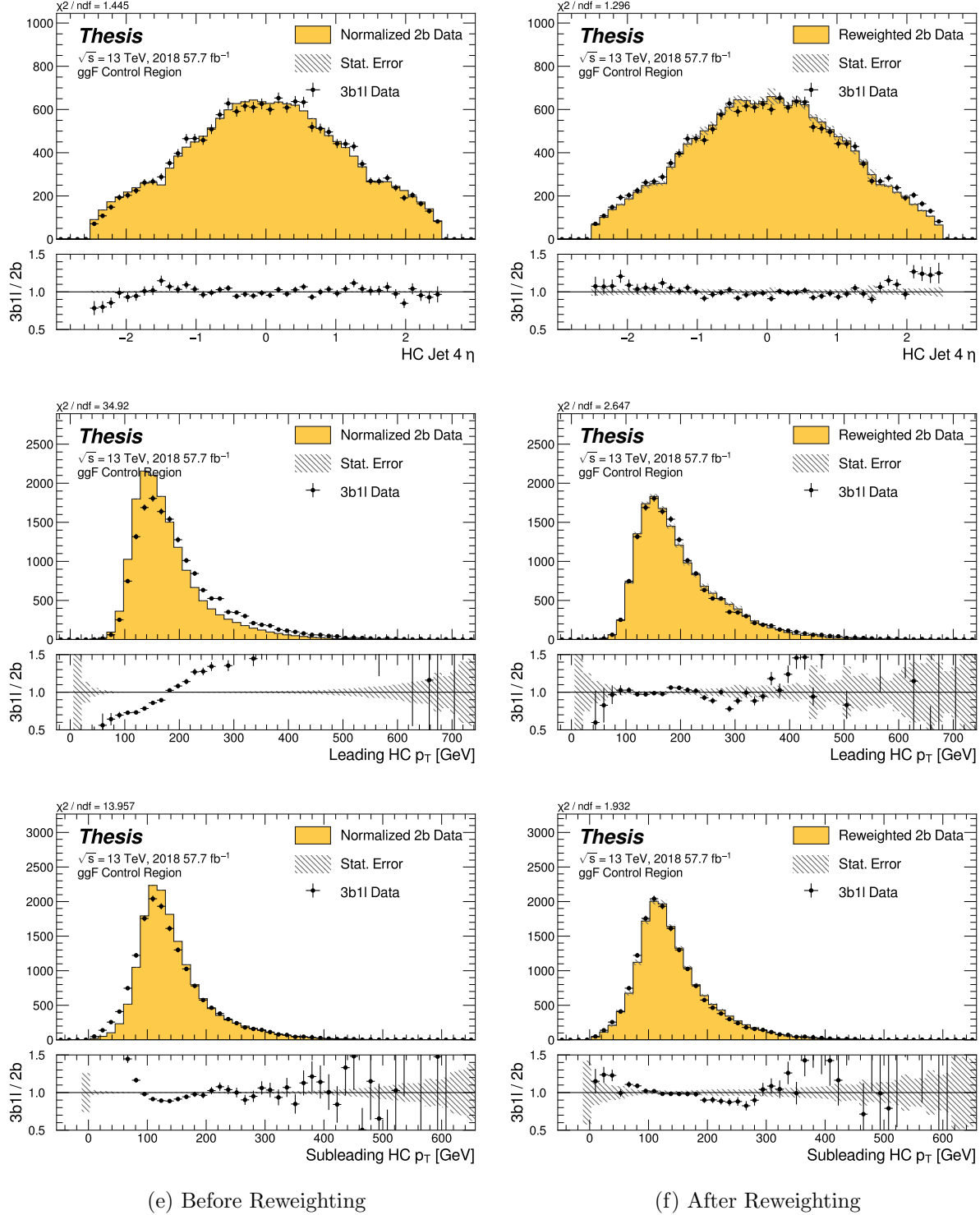


Figure 7.47: **Non-resonant Search (3b1l):** Distributions of η of the 4th leading Higgs Candidate jet and the p_T of the leading and subleading Higgs candidates before (left) and after (right) CR derived reweighting for the 2018 3b1l Control Region.

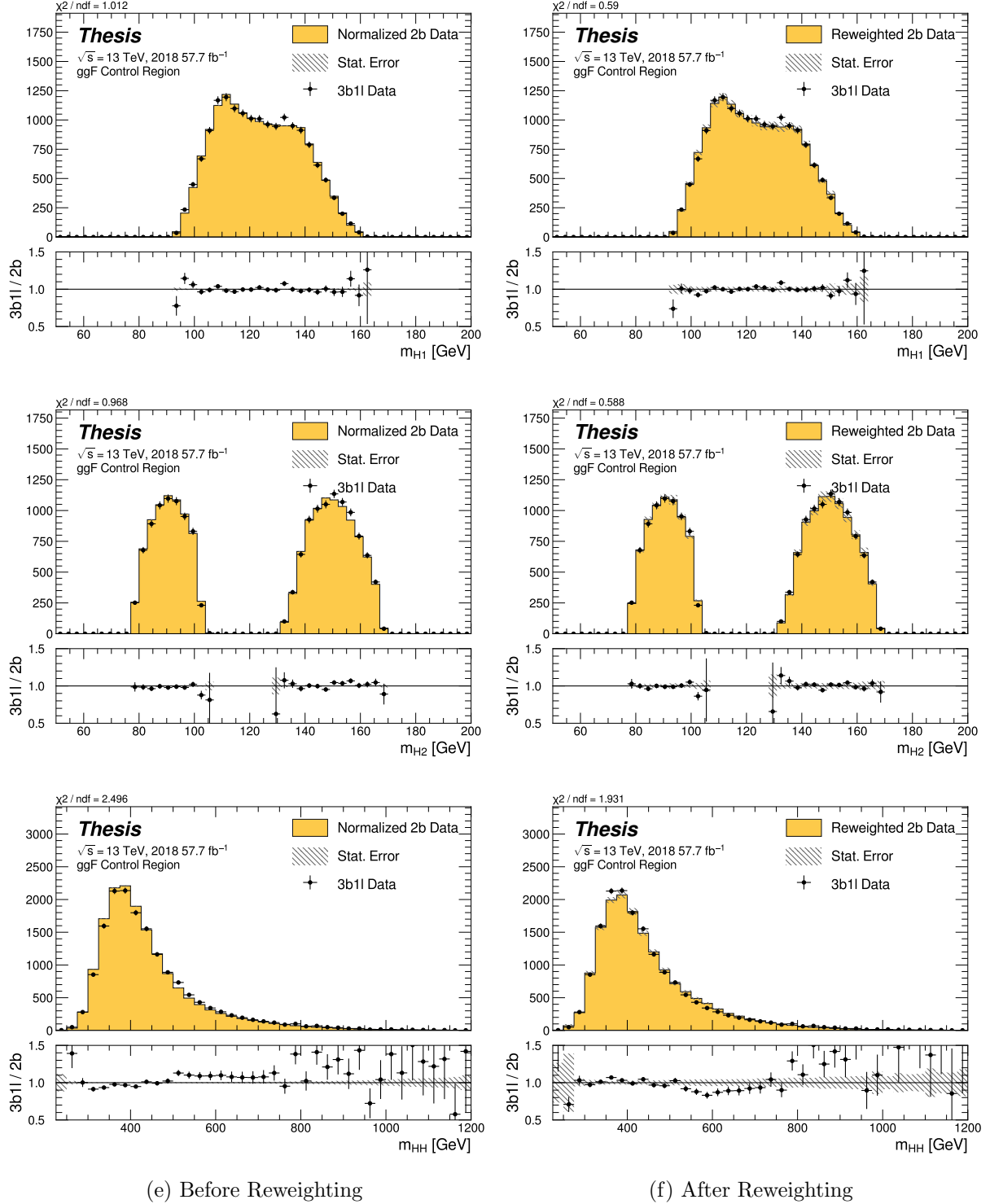


Figure 7.48: **Non-resonant Search (3b1l):** Distributions of mass of the leading and subleading Higgs candidates and of the di-Higgs system before (left) and after (right) CR derived reweighting for the 2018 3b1l Control Region.

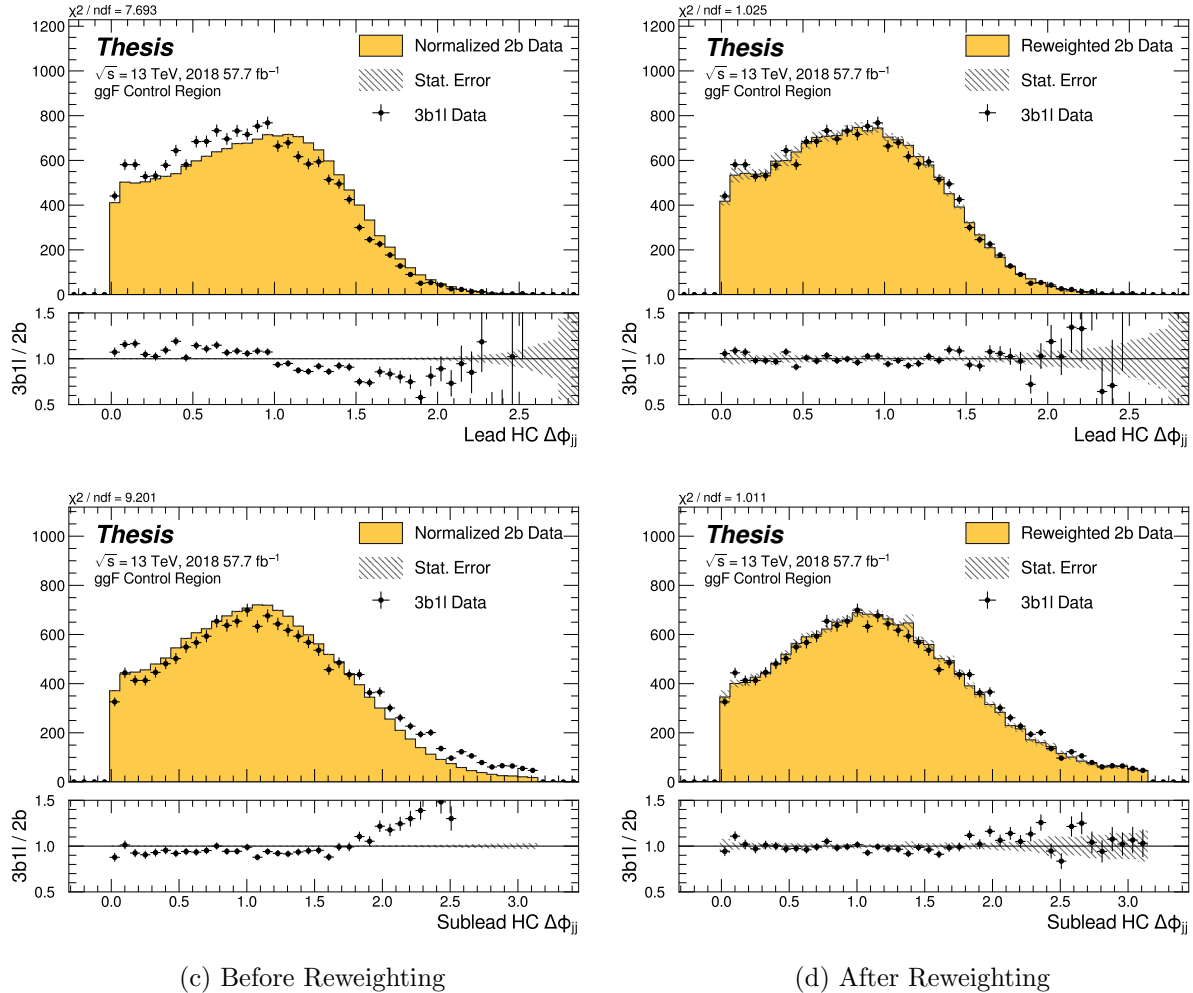


Figure 7.49: **Non-resonant Search (3b1l):** Distributions of $\Delta\phi$ between jets in the leading and subleading Higgs candidates before (left) and after (right) CR derived reweighting for the 2018 3b1l Control Region.

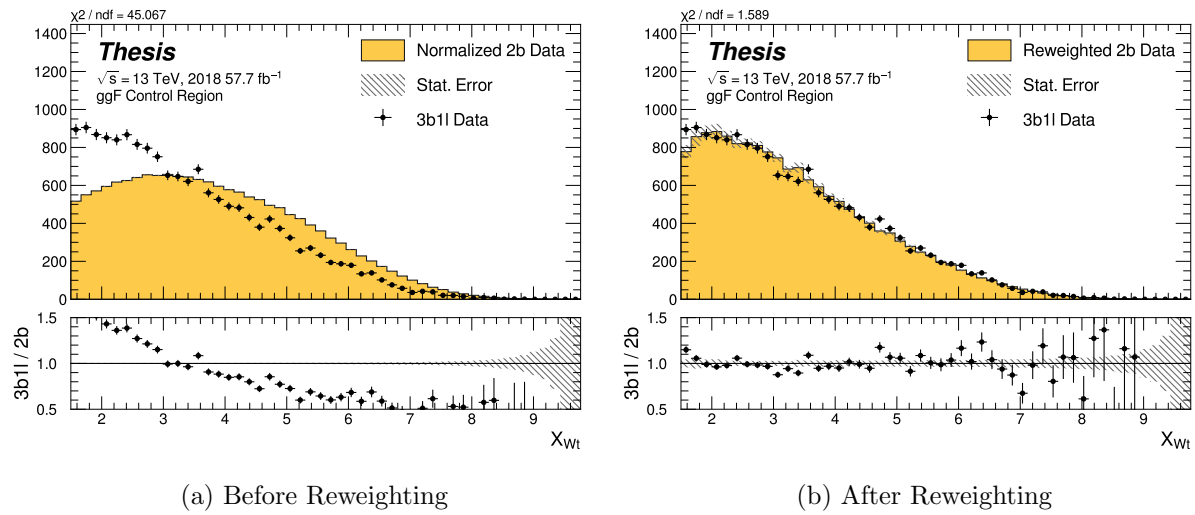


Figure 7.50: **Non-resonant Search (3b1l):** Distributions of the top veto variable, X_{Wt} , before (left) and after (right) CR derived reweighting for the 2018 3b1l Control Region. Reweighting is done after the cut on this variable is applied.

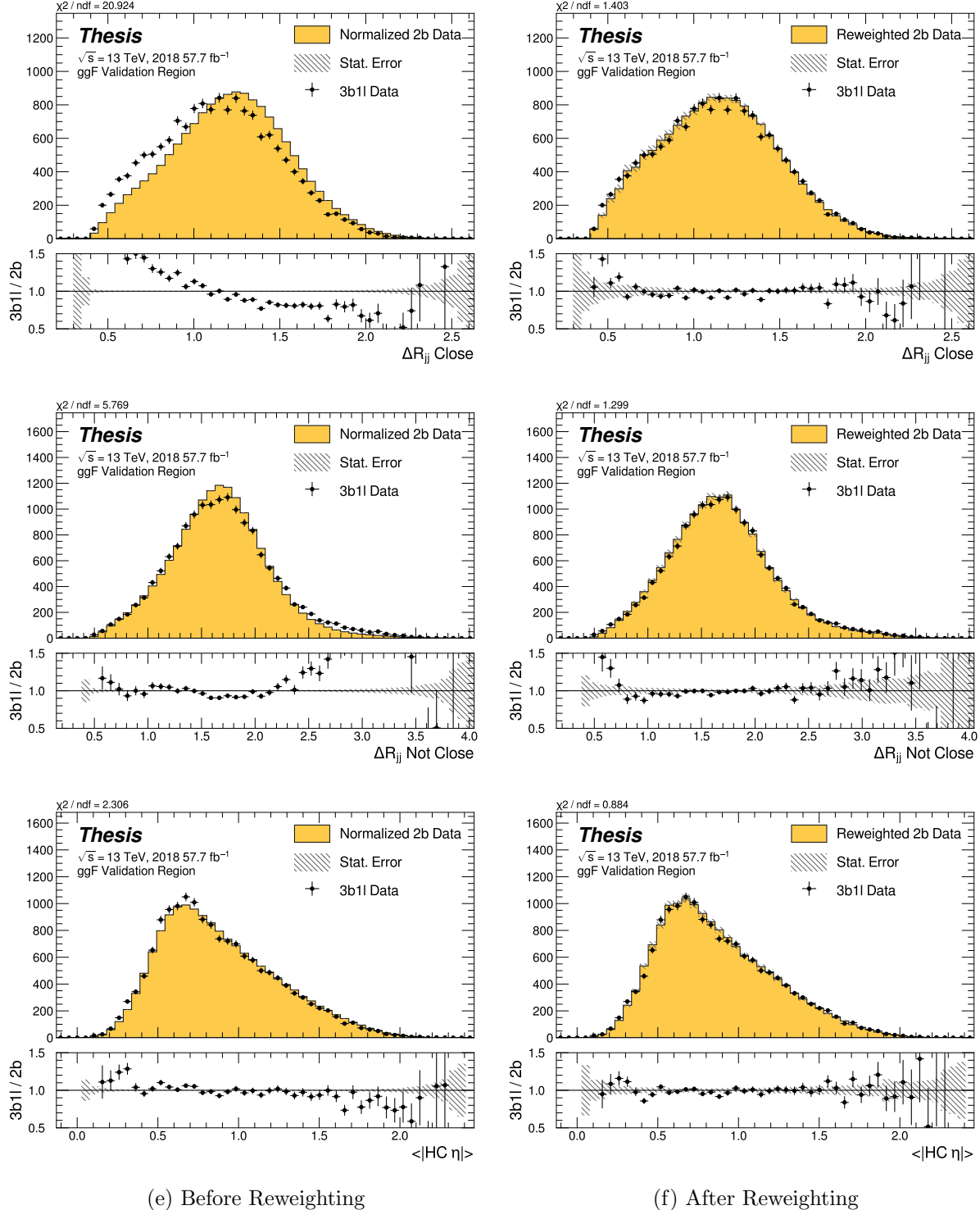


Figure 7.51: **Non-resonant Search (3b1l):** Distributions of ΔR between the closest Higgs Candidate jets, ΔR between the other two, and average absolute value of HC jet η before (left) and after (right) CR derived reweighting for the 2018 3b1l Validation Region.

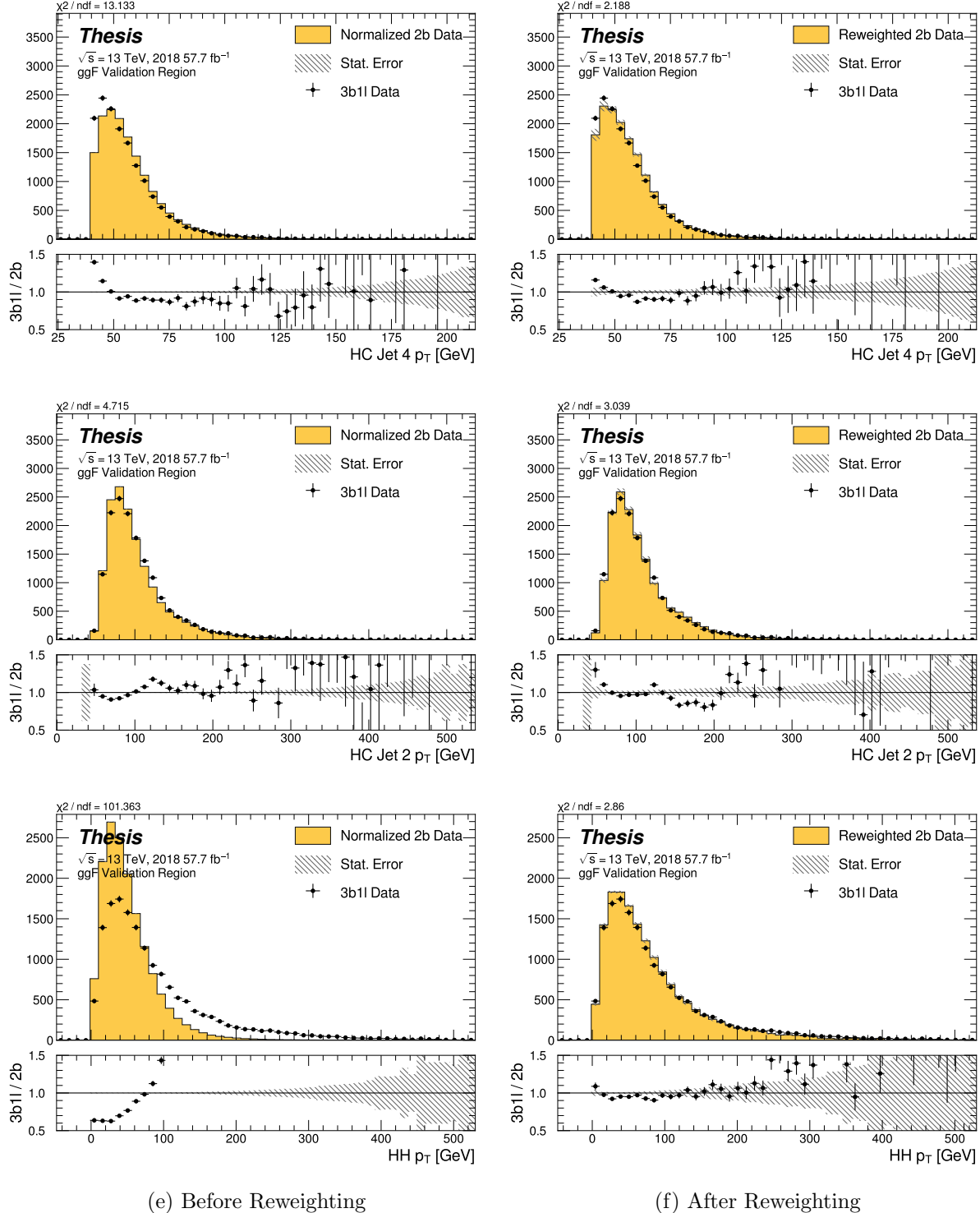


Figure 7.52: **Non-resonant Search (3b1l):** Distributions of p_T of the 2nd and 4th leading Higgs Candidate jets and the p_T of the di-Higgs system before (left) and after (right) CR derived reweighting for the 2018 3b1l Validation Region.

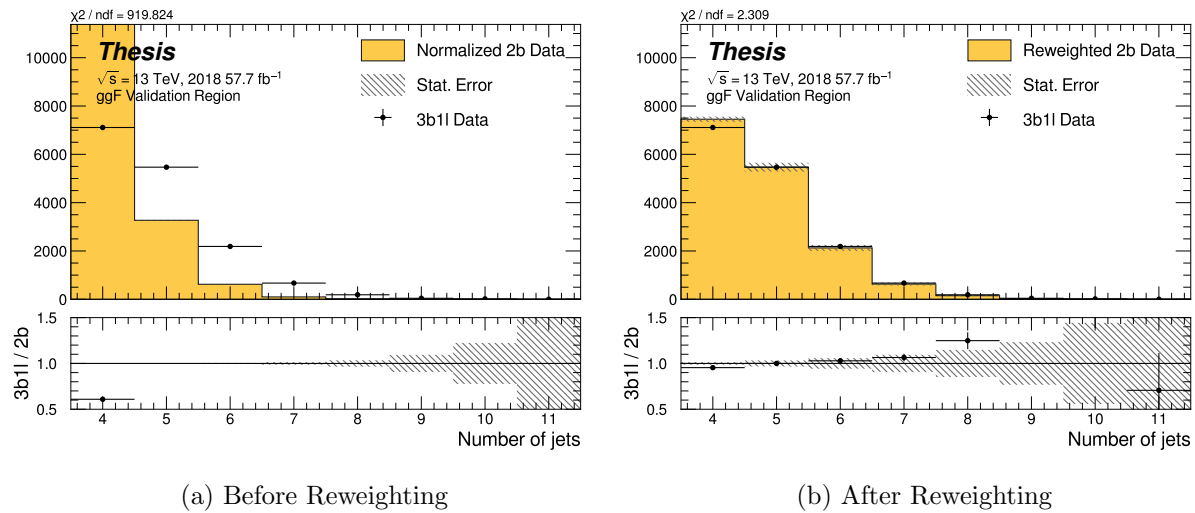


Figure 7.53: **Non-resonant Search (3b1l)**: Distributions of the number of jets before (left) and after (right) CR derived reweighting for the 2018 3b1l Validation Region. A minimum of 4 jets is required in each event in order to form Higgs candidates.

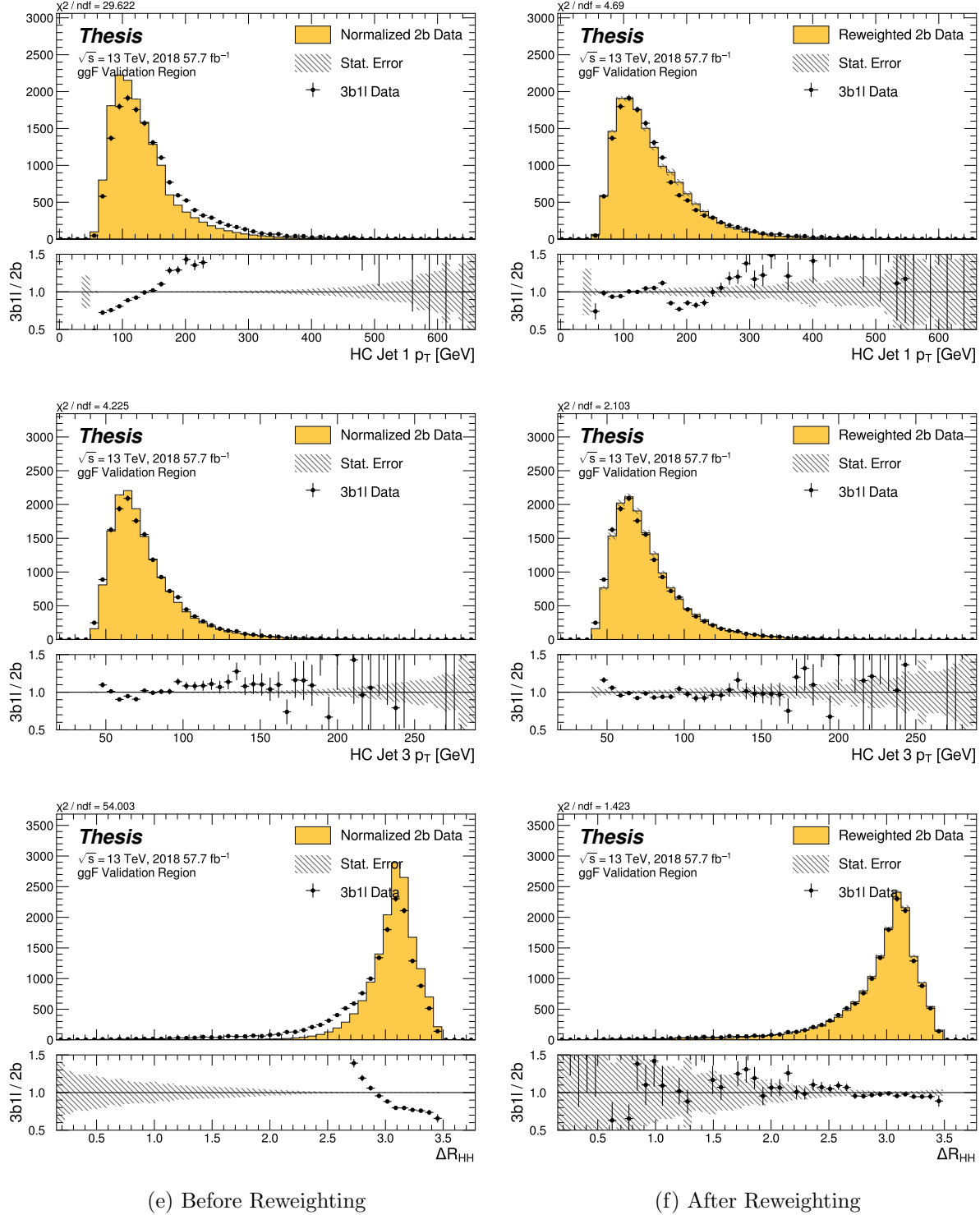


Figure 7.54: **Non-resonant Search (3b1l):** Distributions of p_T of the 1st and 3rd leading Higgs Candidate jets and ΔR between Higgs candidates before (left) and after (right) CR derived reweighting for the 2018 3b1l Validation Region.

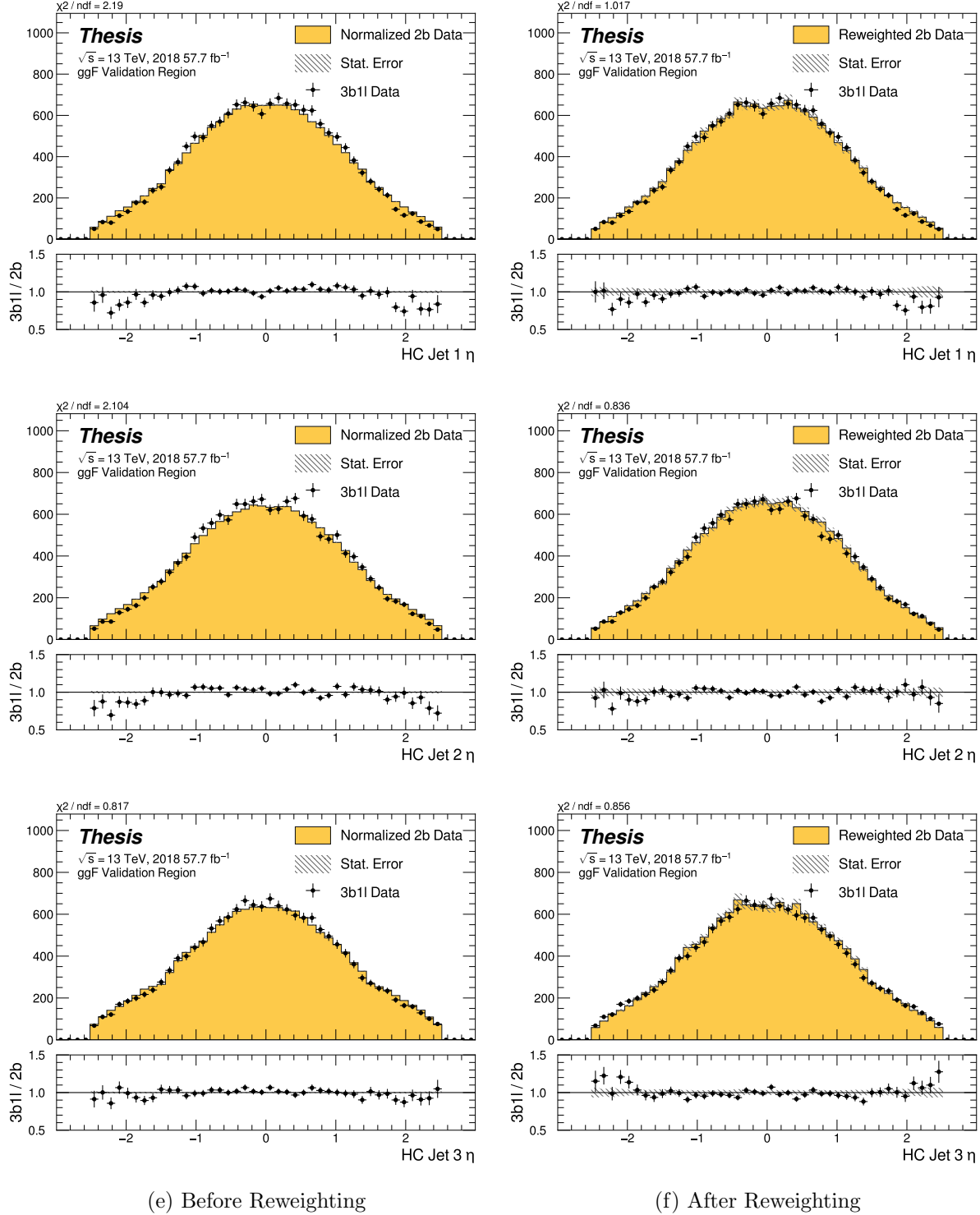


Figure 7.55: **Non-resonant Search (3b1l):** Distributions of η of the 1st, 2nd, and 3rd leading Higgs Candidate jets before (left) and after (right) CR derived reweighting for the 2018 3b1l Validation Region.

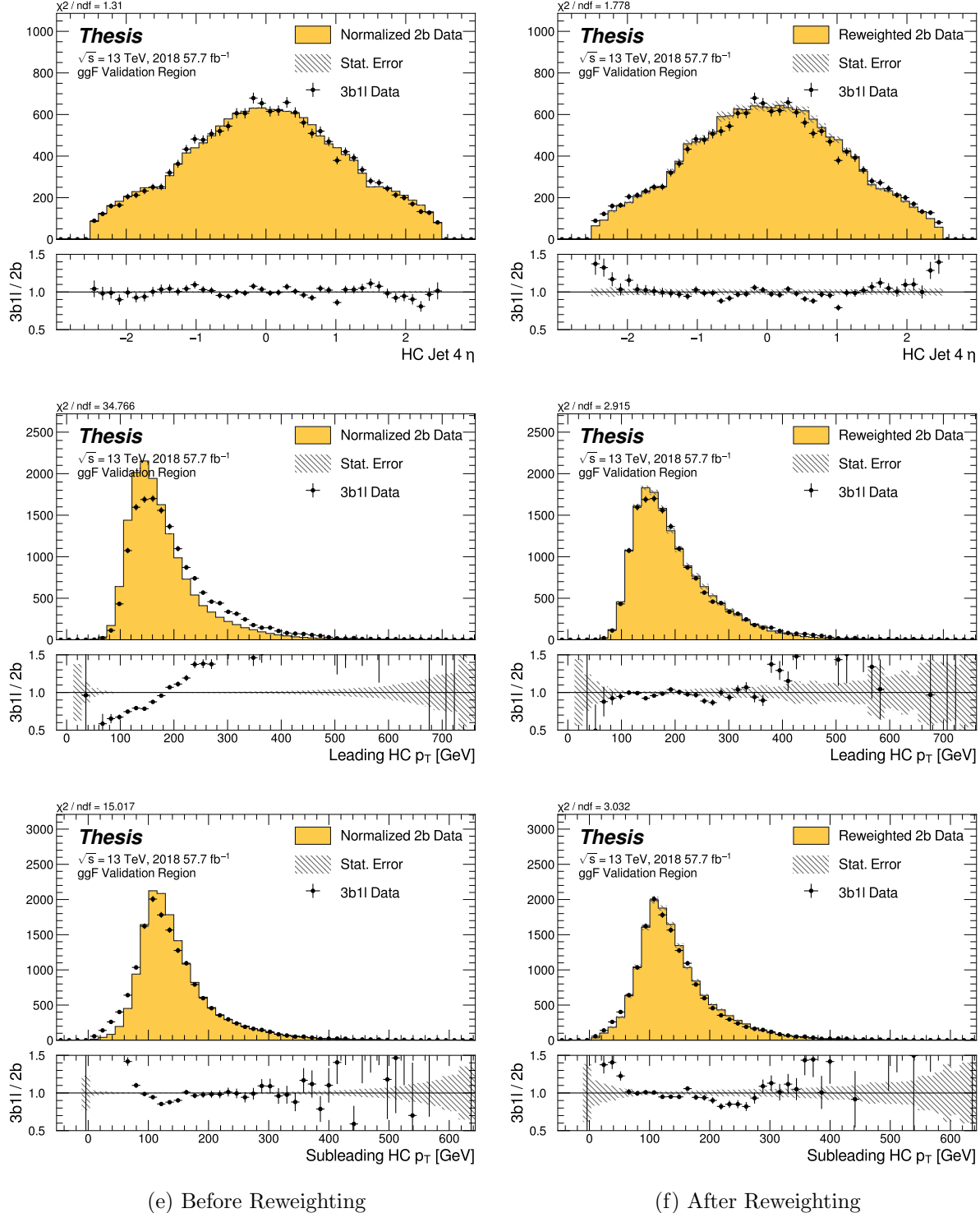


Figure 7.56: **Non-resonant Search (3b1l):** Distributions of η of the 4th leading Higgs Candidate jet and the p_T of the leading and subleading Higgs candidates before (left) and after (right) CR derived reweighting for the 2018 3b1l Validation Region.

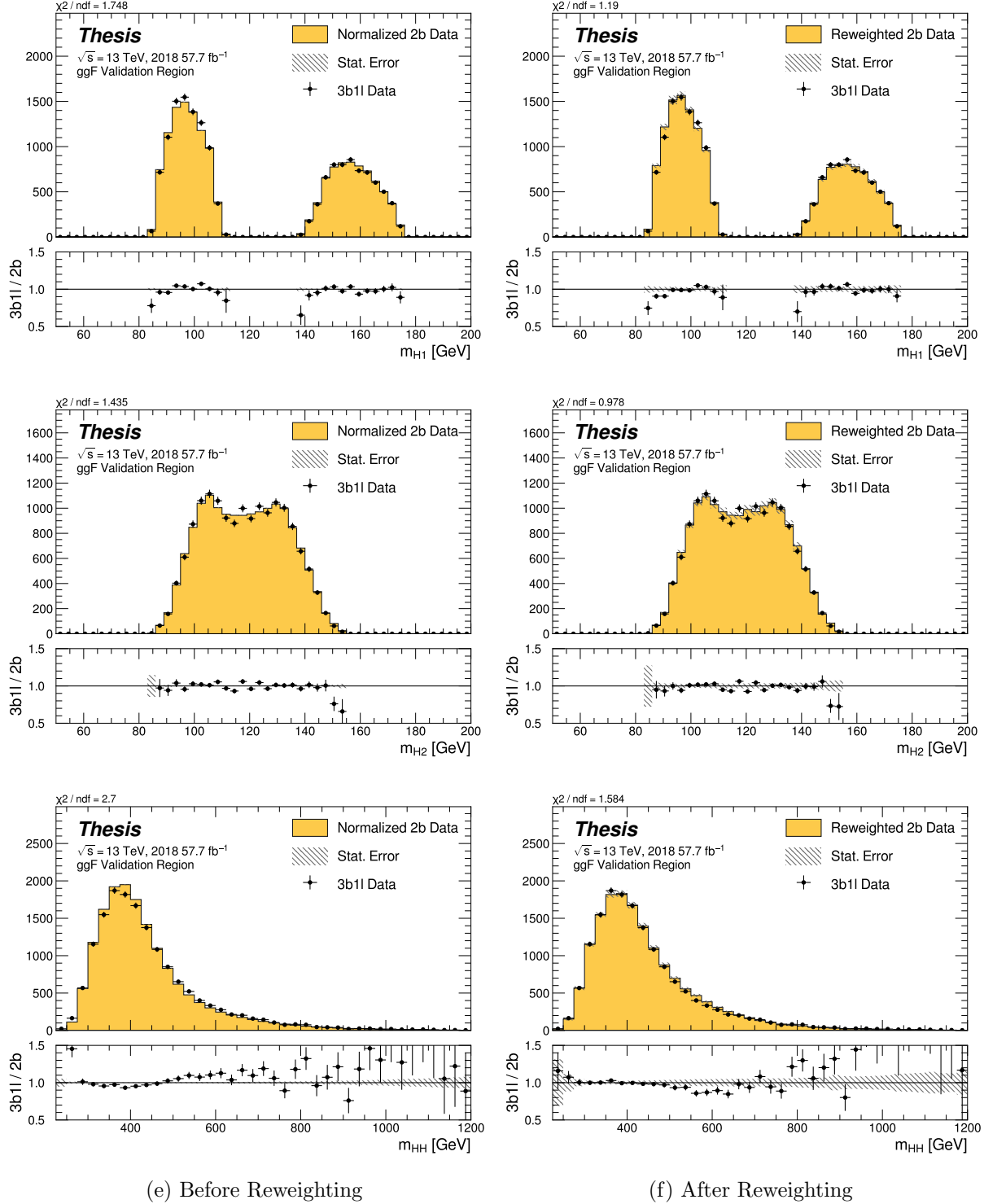


Figure 7.57: **Non-resonant Search (3b1l):** Distributions of mass of the leading and subleading Higgs candidates and of the di-Higgs system before (left) and after (right) CR derived reweighting for the 2018 3b1l Validation Region.

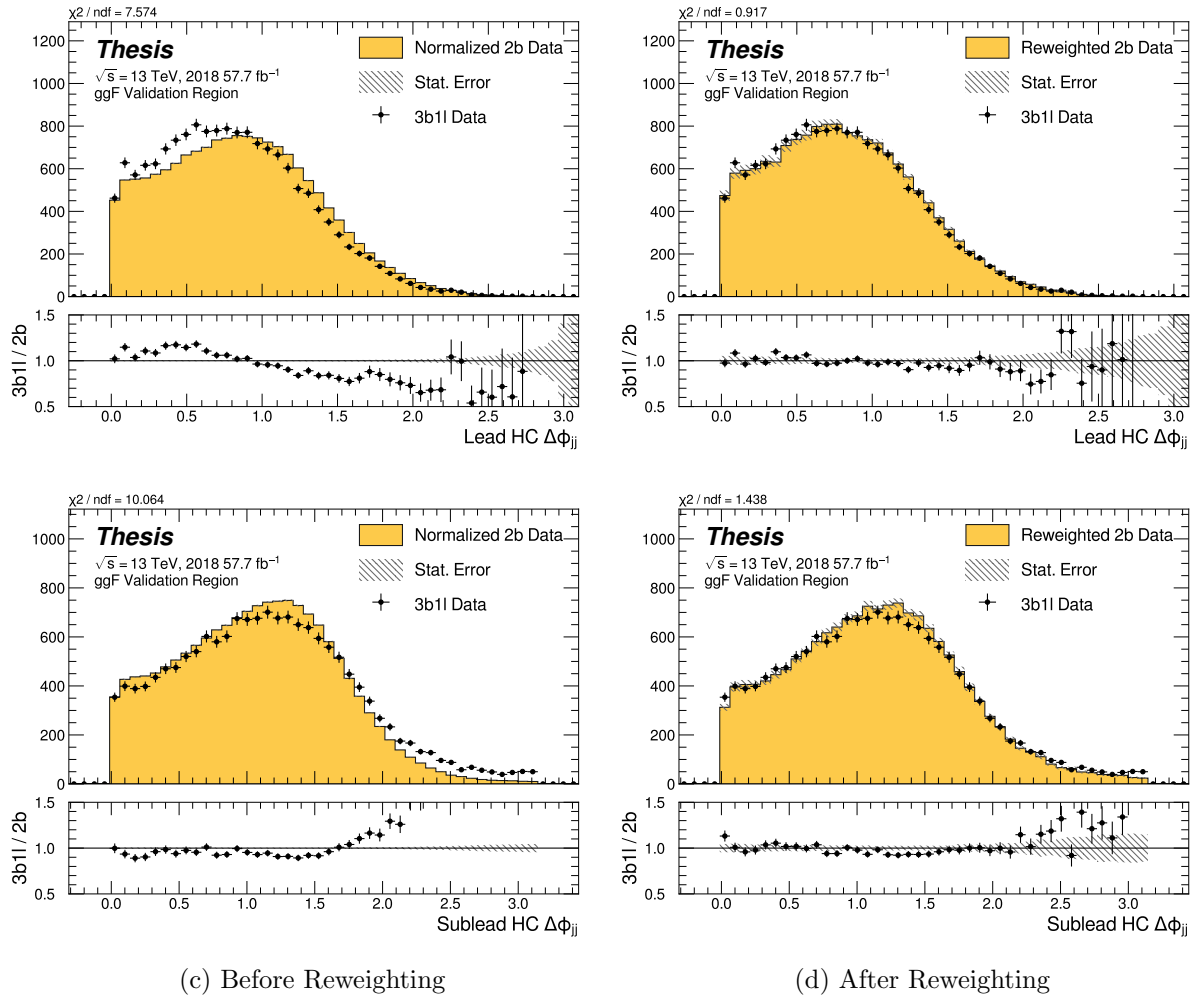


Figure 7.58: **Non-resonant Search (3b1l):** Distributions of $\Delta\phi$ between jets in the leading and subleading Higgs candidates before (left) and after (right) CR derived reweighting for the 2018 3b1l Validation Region.

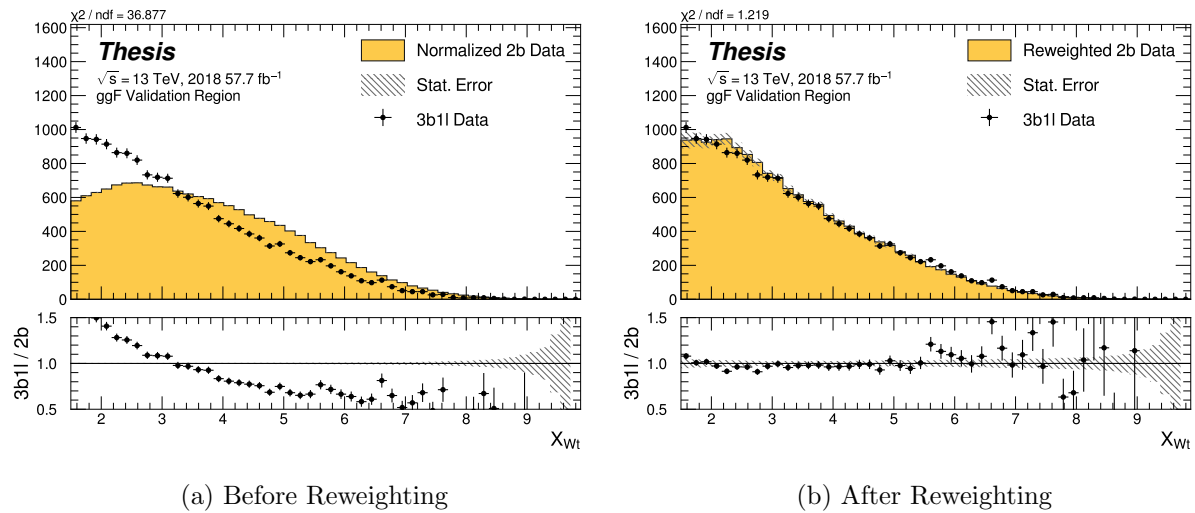


Figure 7.59: **Non-resonant Search (3b1l):** Distributions of the top veto variable, X_{Wt} , before (left) and after (right) CR derived reweighting for the 2018 3b1l Validation Region. Reweighting is done after the cut on this variable is applied.

2235 **7.7 Uncertainties**

2236 A variety of uncertainties are assigned to account for known biases in the underlying methods,
2237 calibrations, and objects used for this analysis. The largest such uncertainty is associated
2238 with the kinematic bias inherent in deriving the background estimate outside of the signal
2239 region. However, a statistical biasing of this same estimate also has a significant impact.
2240 Additionally, due to the use of Monte Carlo for signal modelling and b -tagging calibration,
2241 uncertainties related to mis-modelings in simulation must also be accounted for. Note that
2242 the results for the non-resonant analysis presented here are preliminary and only include
2243 background systematic, such that the discussion of the signal systematics *only* applies for
2244 the resonant search. However, these background systematics are expected to be by far the
2245 dominant uncertainties.

2246 *7.7.1 Statistical Uncertainties and Bootstrapping*

2247 There are two components to the statistical error for the neural network background estimate.
2248 The first is standard Poisson error, i.e., a given bin, i , in the background histogram has value
2249 $n_i = \sum_{j \in i} w_j$, where w_j is the weight for an event j which falls in bin i . Standard techniques
2250 then result in statistical error $\delta n_i = \sqrt{\sum_{j \in i} w_j^2}$, which reduces to the familiar \sqrt{N} Poisson error
2251 when all w_j are equal to 1.

2252 However, this procedure does not take into account the statistical uncertainty on the
2253 w_j due to the finite training dataset. Due to the large size difference between the two tag
2254 and four tag datasets, it is the statistical uncertainty due to the four tag training data that
2255 dominates that on the background. A standard method for estimating this uncertainty is the
2256 bootstrap resampling technique [107]. Conceptually, a set of statistically equivalent sets is
2257 constructed by sampling with replacement from the original training set. The reweighting
2258 network is then trained on each of these separately, resulting in a set of statistically equivalent
2259 background estimates. Each of these sets is below referred to as a replica.

2260 In practice, as the original training set is large, the resampling procedure is able to

2261 be simplified through the relation $\lim_{n \rightarrow \infty} \text{Binomial}(n, 1/n) = \text{Poisson}(1)$, which dictates that
 2262 sampling with replacement is approximately equivalent to applying a randomly distributed
 2263 integer weight to each event, drawn from a Poisson distribution with a mean of 1.

2264 Though the network configuration itself is the same for each bootstrap training, the
 2265 network initialization is allowed to vary. It should therefore be noted that the bootstrap
 2266 uncertainties implicitly capture the uncertainty due to this variation in addition to the
 2267 previously mentioned training set variation.

2268 The variation from this bootstrapping procedure is used to assign a bin-by-bin uncertainty
 2269 which is treated as a statistical uncertainty in the fit. Due to practical constraints, a
 2270 procedure for approximating the full bootstrap error band is developed which demonstrates
 2271 good agreement with the full bootstrap uncertainty. This procedure is described below.

2272 *Calculating the Bootstrap Error Band*

2273 The standard procedure to calculate the bootstrap uncertainty would proceed as follows: first,
 2274 each network trained on each bootstrap replica dataset would be used to produce a histogram
 2275 in the variable of interest. This would result in a set of replica histograms (e.g. for 100
 2276 bootstrap replicas, 100 histograms would be created). The nominal estimate would then be
 2277 the mean of bin values across these replica histograms, with errors set by the corresponding
 2278 standard deviation.

2279 In practice, such an approach is inflexible and demanding both in computation and in
 2280 storage, in so far as we would like to produce histograms in many variables, with a variety
 2281 of different cuts and binnings. This motivates a derivation based on event-level quantities.
 2282 However, due to non-trivial correlations between replica weights, simple linear propagation of
 2283 event weight variation is not correct.

2284 We therefore adopt an approach which has been empirically found to produce results
 2285 (for this analysis) in line with those produced by generating all of the histograms, as in the
 2286 standard procedure. This approach is described below. Note that, for robustness to outliers
 2287 and weight distribution asymmetry, the median and interquartile range (IQR) are used for

2288 the central value and width respectively (as opposed to the mean and standard deviation).

2289 The components involved in the calculation have been mentioned in Section 7.6 and are
2290 as follows:

2291 1. Replica weight (w_i): weight predicted for a given event by a network trained on replica
2292 dataset i .

2293 2. Replica norm (α_i): normalization factor for replica i . This normalizes the reweighting
2294 prediction of the network trained on replica dataset i to match the corresponding target
2295 yield.

2296 3. Median weight (w_{med}): median weight for a given event across replica datasets, used
2297 for the nominal estimate. Defined (for 100 bootstrap replicas) as

$$w_{med} \equiv \text{median}(\alpha_1 w_1, \dots, \alpha_{100} w_{100}) \quad (7.12)$$

2296 4. Normalization correction (α_{med}): normalization factor to match the predicted yield of
2297 the median weights (w_{med}) to the target yield in the training region.

2298 As mentioned in Section 7.6, the *nominal estimate* is constructed from the set of median
2299 weights and the normalization correction, i.e. $\alpha_{med} \cdot w_{med}$.

2300 For the bootstrap error band, a “varied” histogram is then generated by applying, for
2301 each event, a weight equal to the median weight (with no normalization correction) plus half
2302 the interquartile range of the replica weights: $w_{varied} = w_{med} + \frac{1}{2} \text{IQR}(w_1, \dots, w_{100})$.

2303 This varied histogram is scaled to match the yield of the nominal estimate. To account
2304 for variation of the nominal estimate yield, a normalization variation is calculated from the
2305 interquartile range of the replica norms: $\frac{1}{2} \text{IQR}(\alpha_1, \dots, \alpha_{100})$. This variation, multiplied into
2306 the nominal estimate, is used to set a baseline for the varied histogram described above.

Denoting $H(\text{weights})$ as a histogram constructed from a given set of weights, $Y(\text{weights})$

as the predicted yield for a given set of weights, the final varied histogram is thus:

$$H(w_{med} + \frac{1}{2} \text{IQR}(w_1, \dots, w_{100})) \cdot \frac{Y(\alpha_{med} w_{med})}{Y(w_{med} + \frac{1}{2} \text{IQR}(w_1, \dots, w_{100}))} + \frac{1}{2} \text{IQR}(\alpha_1, \dots, \alpha_{100}) \cdot H(\alpha_{med} w_{med}) \quad (7.13)$$

where the first term roughly describes the behavior of the bootstrap variation across the distribution of the variable of interest while the second term describes the normalization variation of the bootstrap replicas.

The difference between the varied histogram and the nominal histogram is then taken to be the bootstrap statistical uncertainty on the nominal histogram.

Figure 7.60 demonstrates how each of the components described above contribute to the uncertainty envelope for the non-resonant 2017 Control Region and compares this approximate band to the variation of histograms from individual bootstrap estimates. The error band constructed from the above procedure is seen to provide a good description of the bootstrap variation.

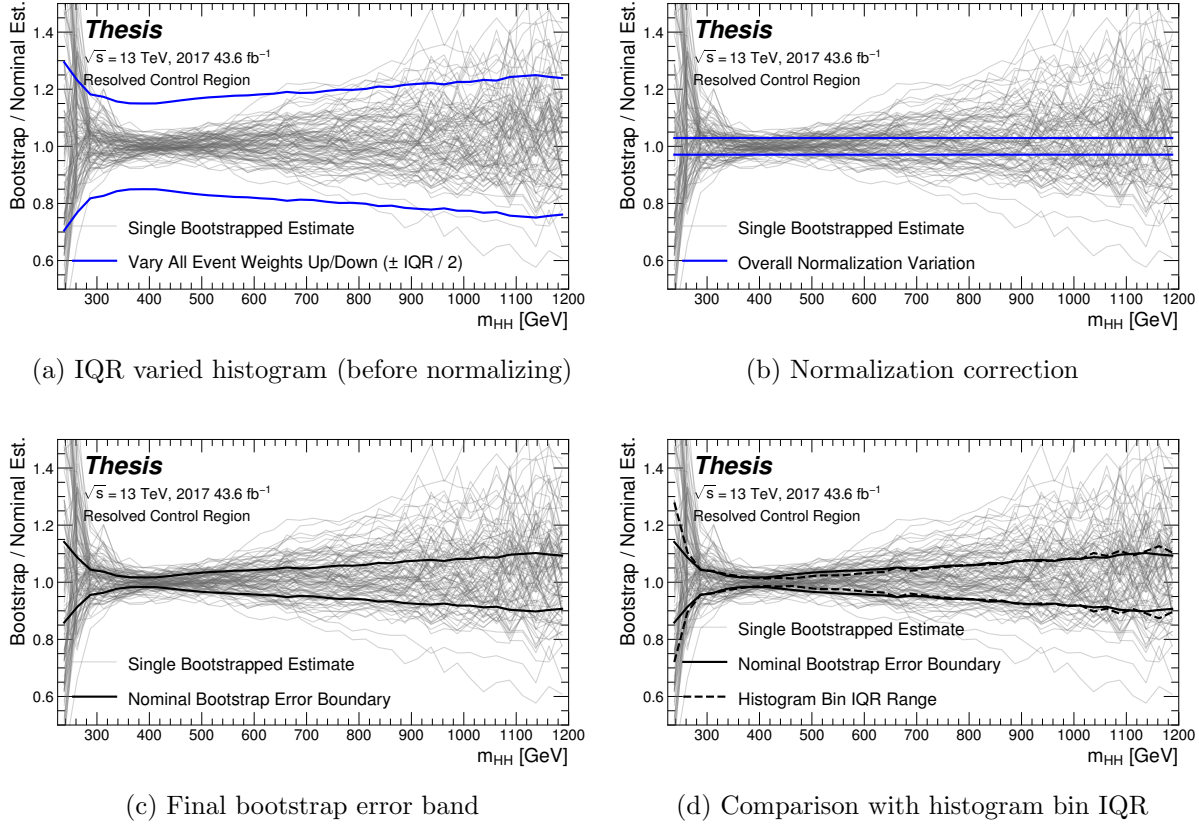


Figure 7.60: Illustration of the approximate bootstrap band procedure, shown as a ratio to the nominal estimate for the 2017 non-resonant background estimate. Each grey line is from the m_{HH} prediction for a single bootstrap training. Figure 7.60(a) shows the variation histograms constructed from median weight \pm the IQR of the replica weights. It can be seen that this captures the rough shape of the bootstrap envelope, but is not good estimate for the overall magnitude of the variation. Figure 7.60(b) demonstrates the applied normalization correction, and Figure 7.60(c) shows the final band (normalized Figure 7.60(a) + Figure 7.60(b)). Comparing this with the IQR variation for the prediction from each bootstrap in each bin in Figure 7.60(d), the approximate envelope describes a very similar variation.

2317 7.7.2 *Background Shape Uncertainties*

2318 To account for the systematic bias associated with deriving the reweighting function in the
2319 control region and extrapolating to the signal region, an alternative background model is
2320 derived in the validation region. Because of the fully data-driven nature of the background
2321 model, this is an uncertainty assessed on the full background. The alternative model and
2322 the baseline are consistent with the observed data in their training regions, and differences
2323 between the alternative and baseline models are used to define a shape uncertainty on the
2324 m_{HH} spectrum, with a two-sided uncertainty defined by symmetrizing the difference about
2325 the baseline.

2326 For the resonant analysis, this uncertainty is split into two components to allow for two
2327 independent variations of the m_{HH} spectrum: a low- H_T and a high- H_T component, where
2328 H_T is the scalar sum of the p_T of the four jets constituting the Higgs boson candidates, and
2329 serves as a proxy for m_{HH} , while avoiding introducing a sharp discontinuity. The boundary
2330 value is 300 GeV. The low- H_T shape uncertainty primarily affects the m_{HH} spectrum below
2331 400 GeV (close to the kinematic threshold) by up to around 5%, and the high- H_T uncertainty
2332 mainly m_{HH} above this by up to around 20% relative to nominal. These separate m_{HH}
2333 regimes are by design – the H_T split is introduced to prevent low mass bins from constraining
2334 the high mass uncertainty and vice-versa.

2335 This was the *status quo* shape uncertainty decomposition from the Early Run 2 analysis.
2336 A decomposition in terms of orthogonal polynomials, which would provide increased flexibility,
2337 was also evaluated. This study revealed that both decompositions are able to account for the
2338 systematic deviations between four tag data and the background estimate (evaluated in the
2339 kinematic validation region), and produce almost identical limits. The simpler *status quo*
2340 decomposition is therefore kept.

2341 For the non-resonant analysis, the quadrant nature of the background estimation leads to
2342 a natural breakdown of the nuisance parameters: quadrants are defined in the signal region
2343 along the same axes as those used for the control and validation region definitions. Variations

2344 are then assessed in each of these signal region quadrants, corresponding to regions that
 2345 are “closer to” and “further away from” the nominal and alternate estimate regions, fully
 2346 leveraging the power of the two equivalent but systematically different estimates.

2347 Figure 7.61 shows an example of the variation in each H_T region for the 2018 resonant
 2348 analysis. Figure 7.62 shows the example quadrant variation for the 2018 4 b non-resonant
 analysis.

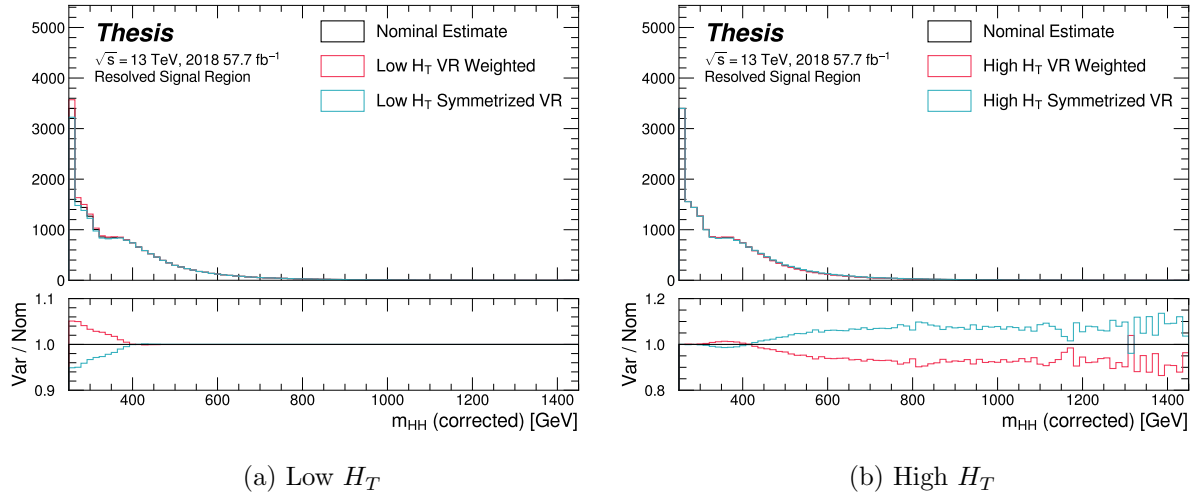
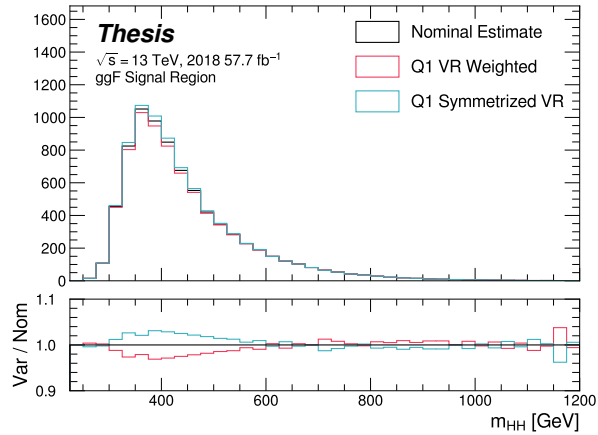
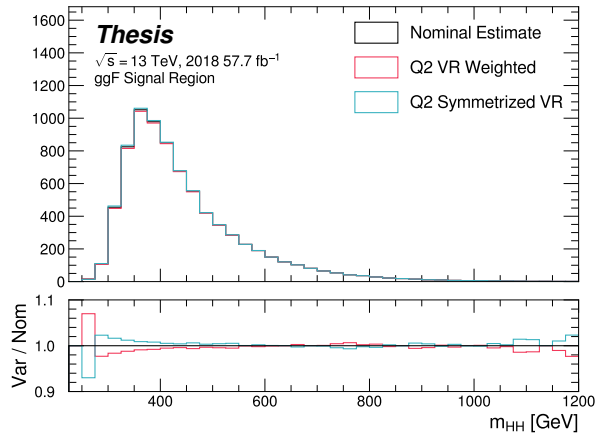


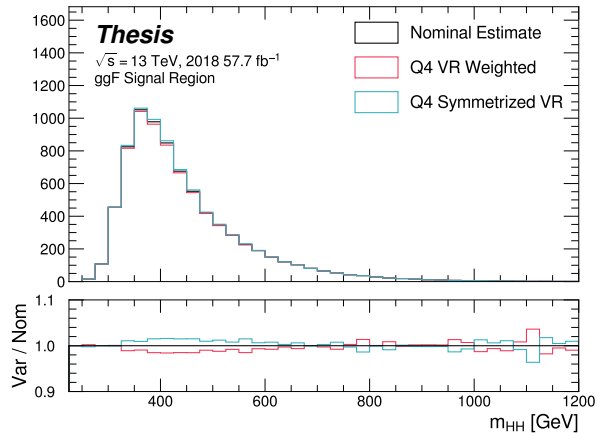
Figure 7.61: **Resonant Search:** Example of CR vs VR variation in each H_T region for 2018.
 The variation nicely factorizes into low and high mass components.



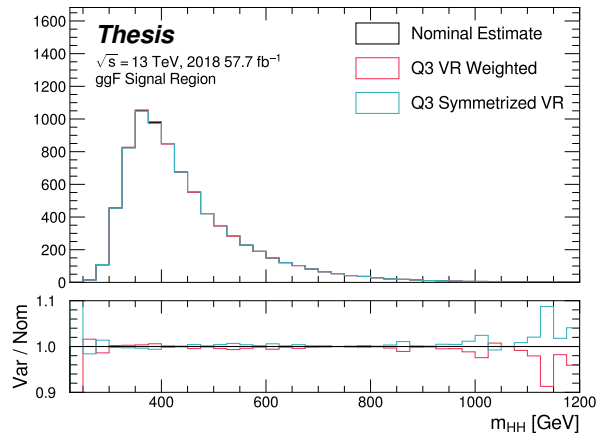
(a) Q1 (top)



(b) Q2 (left)



(c) Q4 (right)



(d) Q3 (bottom)

Figure 7.62: **Non-resonant Search (4b):** Example of CR vs VR variation in each signal region quadrant for 2018. Significantly different behavior is seen between quadrants, with the largest variation in quadrant 1 and the smallest in quadrant 4.

2350 7.7.3 *Signal Uncertainties*

2351 A variety of uncertainties are assessed on the the signal Monte Carlo simulation. As the
2352 background estimate is fully data driven, such uncertainties are not needed for the background
2353 estimate. Note again that the results presented for the non-resonant search only include the
2354 background systematics described above.

2355 Detector modeling and reconstruction uncertainties account for differences between Monte
2356 Carlo simulation and real data due to mis-modeling of the detector as well as due to the
2357 different performance of algorithms on simulation compared to data. In this analysis they
2358 consist of uncertainties related to jet properties and uncertainties stemming from the flavor
2359 tagging procedure. The jet uncertainties are treated according to the prescription in [108] and
2360 are implemented as variations of the jet properties. These cover uncertainty in jet energy scale
2361 and resolution. Uncertainties in b -tagging efficiency are treated according to the prescription
2362 in Ref. [80] and implemented as scale factors applied to the Monte Carlo event weights. A
2363 systematic related to the PtReco b -jet energy correction has been studied in the $HH \rightarrow \gamma\gamma b\bar{b}$
2364 analysis [109] and found to be negligible compared to the other jet uncertainties. Following
2365 this example, such a systematic is therefore neglected here.

2366 Trigger uncertainties stem from imperfect knowledge of the ratio between the efficiency of
2367 a given trigger in data to its efficiency in Monte Carlo simulation. This ratio is applied as a
2368 scale factor to all simulated events, with the systematic variations produced by varying the
2369 scale factor up or down by one sigma. Such variations are evaluated based on measurements
2370 of per-jet online efficiencies for both jet reconstruction and b -tagging, and these are used to
2371 compute event-level uncertainties. These are then applied as overall weight variations on the
2372 simulated events.

2373 An uncertainty on the total integrated luminosity used in this analysis is also applied, ans
2374 is measured to be 1.7% [97], obtained using the LUCID-2 detector for the primary luminosity
2375 measurements [110].

2376 A variety of theoretical uncertainties are also assessed on the signal. Such uncertainties

2377 are assessed by generating samples following the configuration of the baseline samples, but
 2378 with modifications to probe various aspects of the simulation. These include uncertainties in
 2379 the parton density functions (PDFs); uncertainties due to missing higher order terms in the
 2380 matrix elements; and uncertainties in the modelling of the underlying event, which includes
 2381 multi-parton interactions, of hadronic showers and of initial and final state radiation.

2382 Uncertainties due to modelling of the parton shower and the underlying event are eval-
 2383 uated by comparing results from using two different generators, namely HERWIG 7.1.3 and
 2384 PYTHIA 8.235. No significant dependence on the variable of interest, m_{HH} , is observed.
 2385 Therefore, a 5% flat systematic uncertainty is assigned to all signal samples, extracted from
 2386 the acceptance comparison for the full 4-tag selection.

2387 Uncertainties in the matrix element calculation are evaluated by varying the factorization
 2388 and renormalization scales used in the generator up and down by a factor of two, both
 2389 independently and simultaneously. This results in an effect smaller than 1% for all variations
 2390 and all masses; the impact of such uncertainties is therefore neglected.

2391 PDF uncertainties are evaluated using the PDF4LHC_NLO_MC set [98] by calculating
 2392 the signal acceptance for each PDF replica and taking the standard deviation. In all cases,
 2393 these uncertainties result in an effect smaller than 1% on the signal acceptance; therefore
 2394 these are also neglected.

2395 Theoretical uncertainties on the $H \rightarrow b\bar{b}$ branching ratio [111] are also included.

2396 **7.8 Background Validation**

2397 In addition to checking the performance of the background estimate in the control and
2398 validation regions, a variety of alternative selections are defined to allow for a full “dress
2399 rehearsal” of the background estimation procedure.

2400 Both the resonant and non-resonant analyses make use of a *reversed* $\Delta\eta$ region, in which
2401 the kinematic cut on $\Delta\eta_{HH}$ is reversed, so that events are required to have $\Delta\eta_{HH} > 1.5$.
2402 This is orthogonal to the nominal signal region and has minimal sensitivity, allowing for the
2403 comparison of the background estimate $4b$ data in the corresponding “signal region”. For
2404 this validation, a new reweighting is trained following nominal procedures, but entirely in the
2405 $\Delta\eta_{HH} > 1.5$ region.

2406 The non-resonant analysis additionally makes use of the $3b + 1$ fail region mentioned
2407 above, which again is orthogonal to the nominal signal regions and has minimal sensitivity.
2408 The reweighting in this case is between $2b$ and $3b + 1$ fail events rather than between $2b$
2409 and $3b + 1$ loose or $2b$ and $4b$. However, the kinematic selections of signal region events are
2410 otherwise identical, allowing for a complementary test of the background estimate.

2411 *TODO: Add shifted regions if they’re ready*

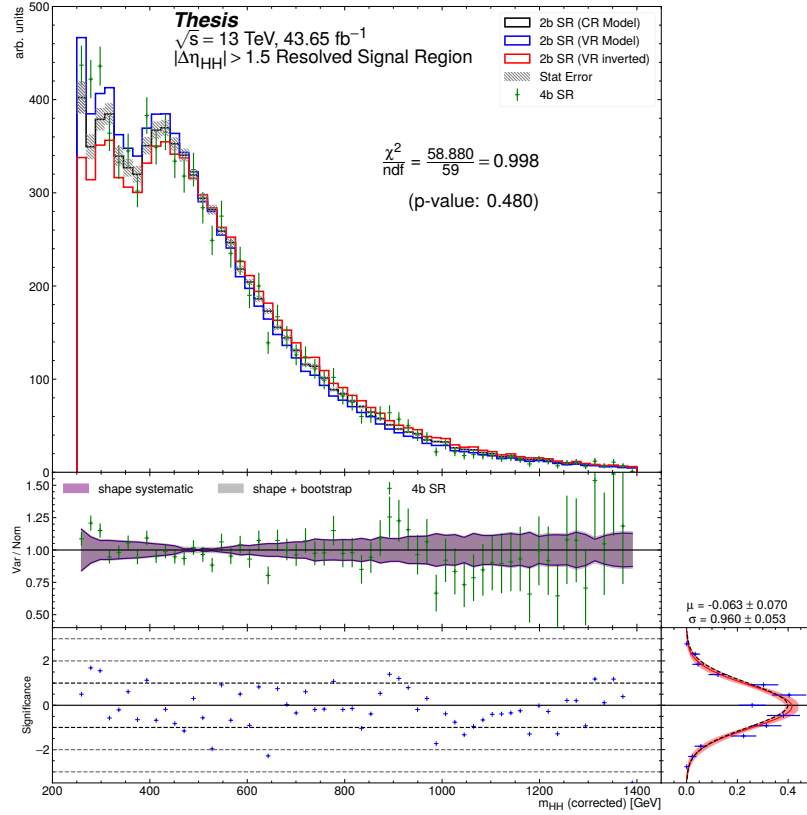


Figure 7.63: **Resonant Search:** Performance of the background estimation method in the resonant analysis reversed $\Delta\eta_{HH}$ kinematic signal region. A new background estimate is trained following nominal procedures entirely within the reversed $\Delta\eta_{HH}$ region, and the resulting model, including uncertainties, is compared with $4b$ data in the corresponding signal region. Good agreement is shown. The quoted p -value uses the χ^2 test statistic, and demonstrates no evidence that the data differs from the assessed background.

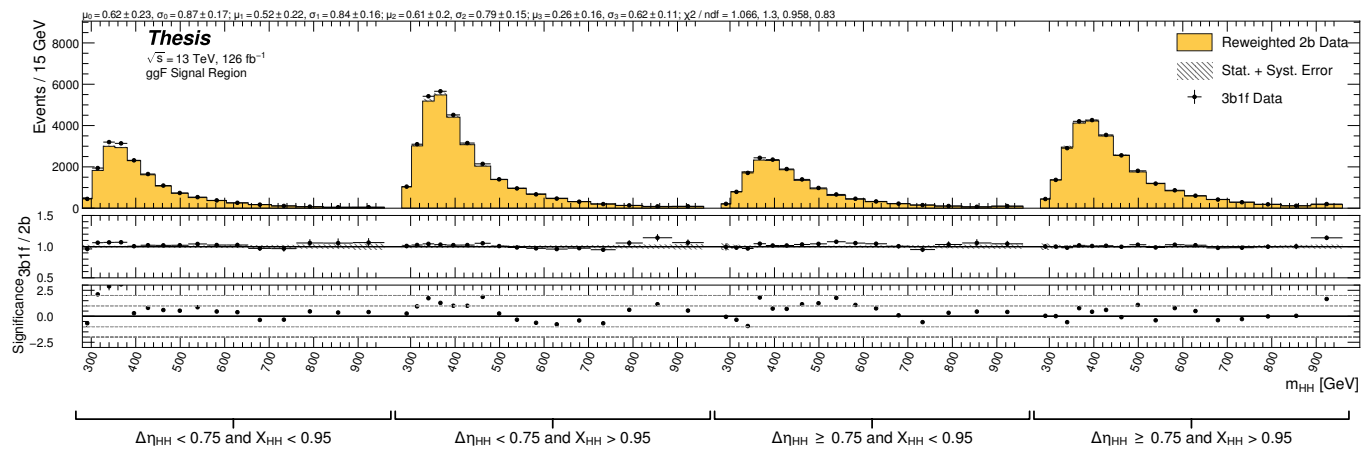


Figure 7.64: **Non-resonant Search:** Performance of the background estimation method in the $3b + 1$ fail validation region. A new background estimate is trained following nominal procedures but with a reweighting from $2b$ to $3b + 1$ fail events. Generally good agreement is seen, though there is some deviation at very low masses in the low $\Delta\eta_{HH}$ low X_{HH} category.

2412 **7.9 Overview of Other $b\bar{b}b\bar{b}$ Channels**

2413 The results discussed above have been developed in conjunction with (1) a boosted channel
2414 for the resonant search and (2) a vector boson fusion (VBF) channel for the non-resonant
2415 search. Detailed discussions of these two channels are beyond the scope of this thesis, though
2416 a combined set of resolved and boosted results are presented below. The VBF results are not
2417 included in this thesis, but much of this thesis work has been useful in the development of
2418 that result. For completeness, we therefore briefly summarize both analyses here.

2419 **7.9.1 Resonant: Boosted Channel**

2420 The boosted analysis selection targets resonance masses from 900 GeV to 5 TeV. In such
2421 events, H decays have a high Lorentz boost, such that the $b\bar{b}$ decays are very collimated. The
2422 resolved analysis fails to reconstruct such HH events, as the $R = 0.4$ jets start to overlap.

2423 The boosted analysis instead reconstructs H decays as large radius, $R = 1.0$ jets, with
2424 corresponding b -quarks identified with variable radius subjets, that is jets with a radius that
2425 scales as ρ/p_T , the p_T is that of the jet in question, and ρ is a fixed parameter, here chosen
2426 to be 30 GeV, which is optimized to maintain truth-level double b -labeling efficiency across
2427 the full range of Higgs jet p_T [76].

2428 Due to limited boosted b -tagging efficiency and to maintain sensitivity even when b -jets
2429 are highly collimated, the boosted analysis is divided into three categories based on the
2430 number of b -tagged jets associated to each large radius jet:

- 2431 • 4 b category: two b -tagged jets in each
- 2432 • 2 $b - 1$ category: two b -tagged jets in one, one in the other
- 2433 • 1 $b - 1$ category: one b -tagged jet in each

2434 The analysis then proceeds in each of these categories.

2435 The resolved and boosted channels are combined for resonance masses from 900 GeV to
2436 1.5 TeV inclusive. To keep the channels statistically independent, the boosted channel vetoes
2437 events passing the resolved analysis selection.

2438 *7.9.2 Non-resonant: VBF Channel*

2439 The vector boson fusion channel is only considered for the non-resonant search. While the
2440 sensitivity is in general much more limited than the gluon-gluon fusion analysis due to the
2441 much smaller production cross section, VBF is sensitive to a variety of Beyond the Standard
2442 Model physics, both complementary and orthogonal to the theoretical scope of gluon-gluon
2443 fusion.

2444 The VBF channel proceeds very similarly to the ggF, with the primary differences being
2445 the kinematic selections and the categorization, which are impacted by the presence of two
2446 *VBF jets*, resulting from the two initial state quarks. The ggF channel result presented here
2447 includes a veto on VBF events, such that if events pass the full VBF selection, they are not
2448 included in the set of events considered for the ggF result.

2449 Beginning with the assumption of four *HH* jets and two VBF jets, the VBF channel first
2450 requires an event to have a minimum six jets. The VBF jets are reconstructed as the two jets
2451 with the highest di-jet invariant mass, m_{jj} , out of the set of all non-tagged jets in the event.
2452 If no such pair exists (i.e., there are less than two non-tagged jets), the event is placed in the
2453 ggF channel. To reduce the number of background events, three cuts are then applied, VBF
2454 jets are required to have $\Delta\eta > 3$ and a combined invariant mass of $m_{jj} > 1000$ GeV. *HH*
2455 jets are identified as in the ggF channel, and the vector sum of the p_T of the *HH* and VBF
2456 jets is required to be less than 65 GeV. The remainder of the analysis proceeds similarly to
2457 the ggF channel, and events failing any stage of this selection are considered for ggF.

2458 Note that the background estimation for the VBF channel is inherited from the resonant
2459 and ggF analyses, a significant additional contribution of this thesis work.

2460 **7.10 m_{HH} Distributions**

2461 *7.10.1 Resonant Search*

2462 The final discriminant used for the resonant search is corrected m_{HH} . Histogram binning
2463 was optimized for the resonant search to be 84 equal width bins from 250 GeV to 1450 GeV,
2464 corresponding to a bin width of 14.3 GeV, and overflow events (events above 1450 GeV) are
2465 included in the last bin. A demonstration of the performance of the reweighting on this
2466 distribution is shown in Figure 7.65 for the control region and Figure 7.66 for the validation region. A background-only profile likelihood fit is run for the distribution in the
2467 signal region, and results with spin-0 signals overlaid are shown in Figure 7.67. Note that the
2468 plots show the sum across all years, but the signal extraction fit and background estimate
2469 are run with the years separately. Agreement is generally good throughout.
2470

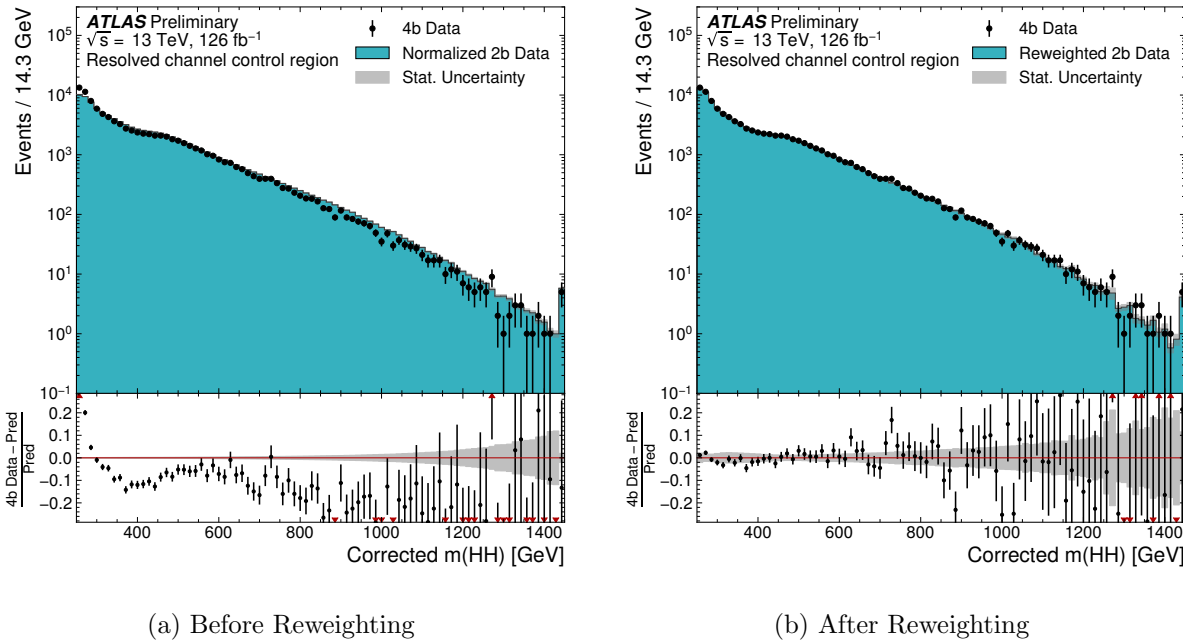


Figure 7.65: **Resonant Search:** Demonstration of the performance of the nominal reweighting in the control region on corrected m_{HH} , with Figure 7.65(a) showing $2b$ events normalized to the total $4b$ yield and Figure 7.65(b) applying the reweighting procedure. Agreement is much improved with the reweighting. Note that overall reweighted $2b$ yield agrees with $4b$ yield in the control region by construction.

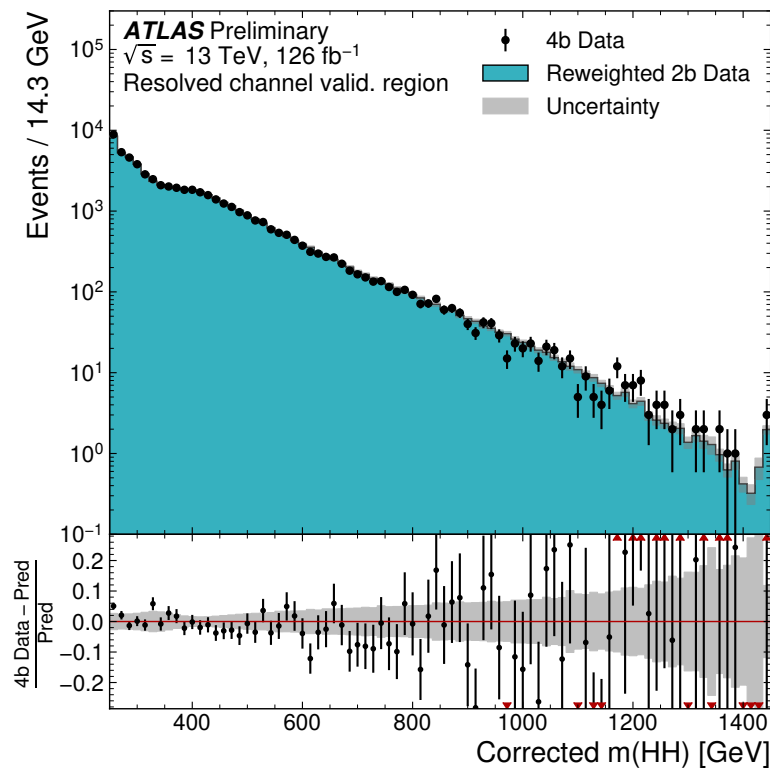


Figure 7.66: **Resonant Search:** Demonstration of the performance of the control region derived reweighting in the validation region on corrected m_{HH} . Agreement is generally good for this extrapolated estimate. Note that the uncertainty band includes the extrapolation systematic, which is defined by a reweighting trained in the validation region.

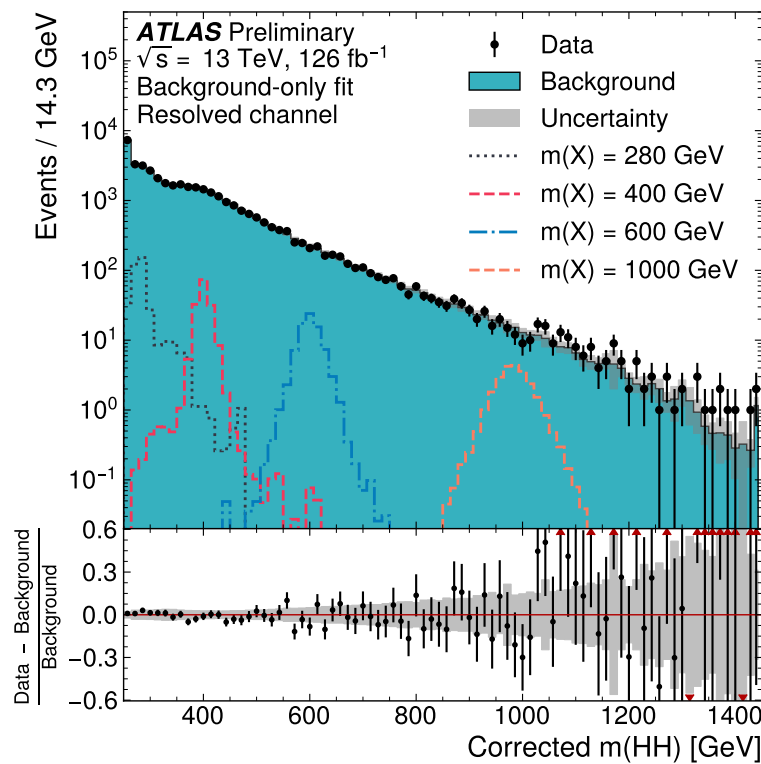


Figure 7.67: **Resonant Search:** Signal region agreement of the background estimate and observed data after a background-only profile likelihood fit. The closure is generally quite good, though there is an evident deficit in the background estimate relative to the data for higher values of corrected m_{HH} .

2471 7.10.2 Non-resonant Search

As discussed above, the non-resonant search splits the signal extraction into two categories of $\Delta\eta_{HH}$ ($0 \leq \Delta\eta_{HH} < 0.75$ and $0.75 \leq \Delta\eta_{HH} < 1.5$), and two categories of X_{HH} ($0 \leq X_{HH} < 0.95$ and $0.95 \leq X_{HH} < 1.6$). To maintain reasonable statistics in each bin entering the signal extraction fit, a variable width binning is considered defined by a resolution parameter, r , and a set range in m_{HH} , where bin edges are determined iteratively as

$$b_{low}^{i+1} = b_{low}^i + r \cdot b_{low}^i, \quad (7.14)$$

2472 where b_{low}^i is the low edge of bin i . The parameters used here are $r = 0.08$ over a range
2473 from 280 GeV to 975 GeV, and underflow and overflow are included in the initial and final
2474 bin contents respectively. m_{HH} with no correction is used as the final discriminant in each
2475 category.

2476 A demonstration of the performance of the reweighting on distributions unrolled across
2477 categories is shown in Figures 7.68 and 7.69 for the control region and Figures 7.70
2478 and 7.71 for the validation region. A background-only profile likelihood fit is run for the
2479 distribution in the signal region, and results with the Standard Model HH signal and $\kappa_\lambda = 6$
2480 signal overlaid are shown for $4b$ in Figure 7.72 and $3b1l$ in Figure 7.73. Note that the plots
2481 show the sum across all years, but the signal extraction fit and background estimate are run
2482 with the years separately. All bins are normalized to represent a density of Events / 15 GeV.

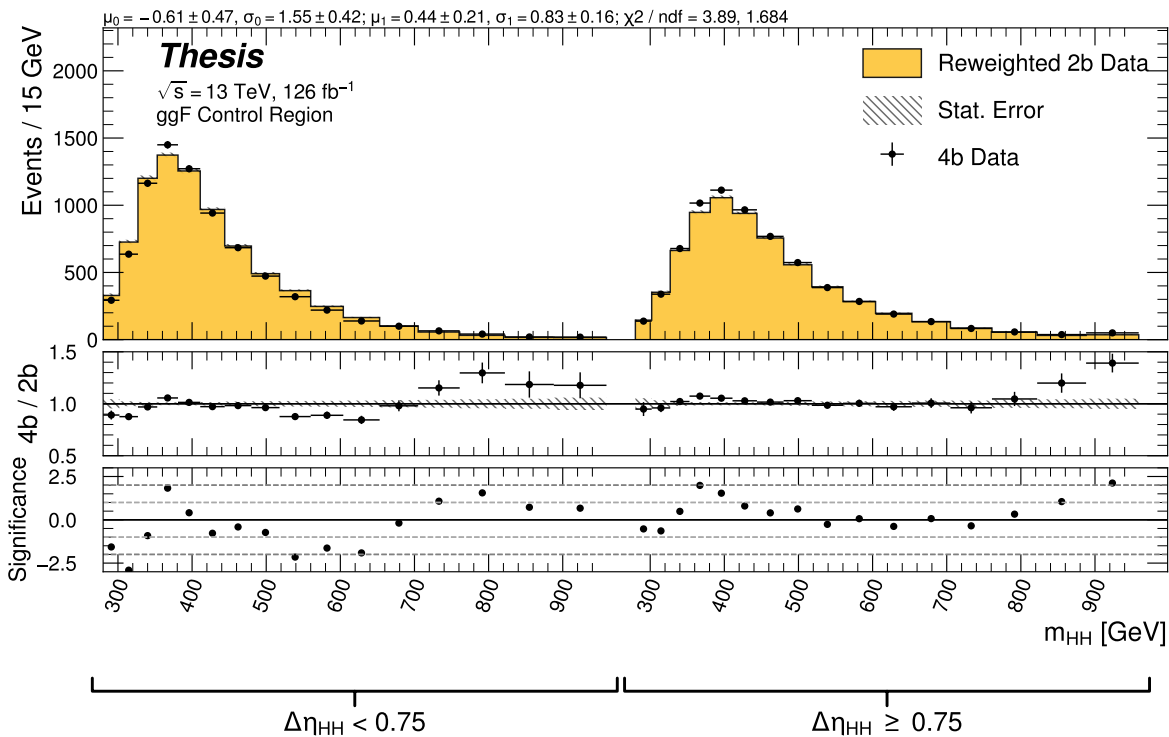


Figure 7.68: **Non-resonant Search (4b)**: Demonstration of the performance of the nominal reweighting in the control region on m_{HH} , split into the two $\Delta\eta_{HH}$ regions. Closure is generally good, with some residual mis-modeling in the low $\Delta\eta_{HH}$ region near 600 GeV.

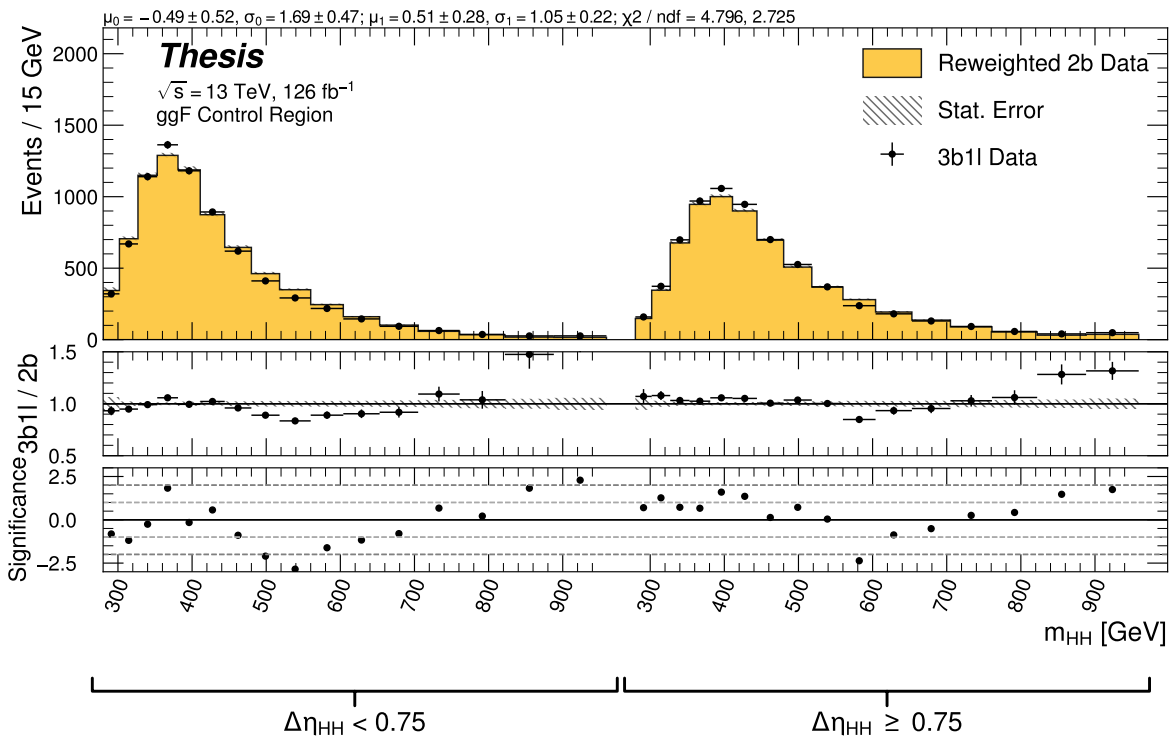


Figure 7.69: **Non-resonant Search (3b1l):** Demonstration of the performance of the nominal reweighting in the control region on m_{HH} , split into the two $\Delta\eta_{HH}$ regions. Closure is generally good, with similar conclusions as for the $4b$ region.

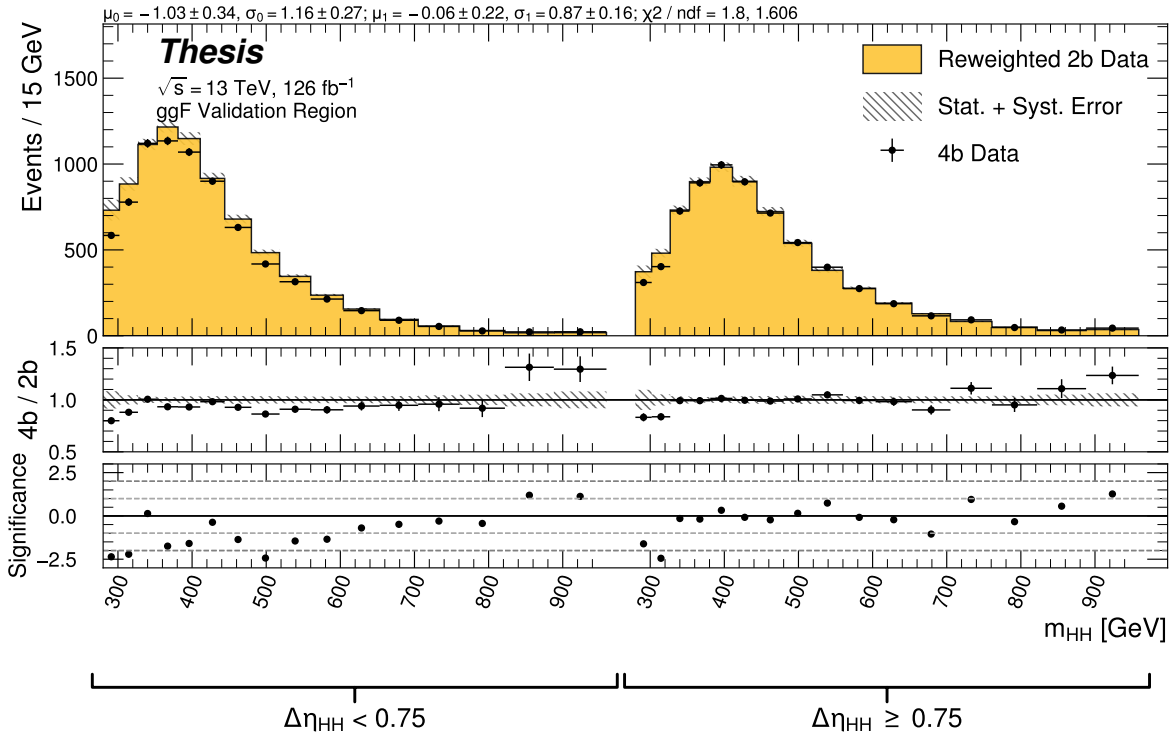


Figure 7.70: **Non-resonant Search (4b)**: Demonstration of the performance of the nominal reweighting in the validation region on m_{HH} , split into the two $\Delta\eta_{HH}$ regions. The low $\Delta\eta_{HH}$ region is consistently overestimated, but, systematic uncertainties are defined via the difference between VR and CR estimates.

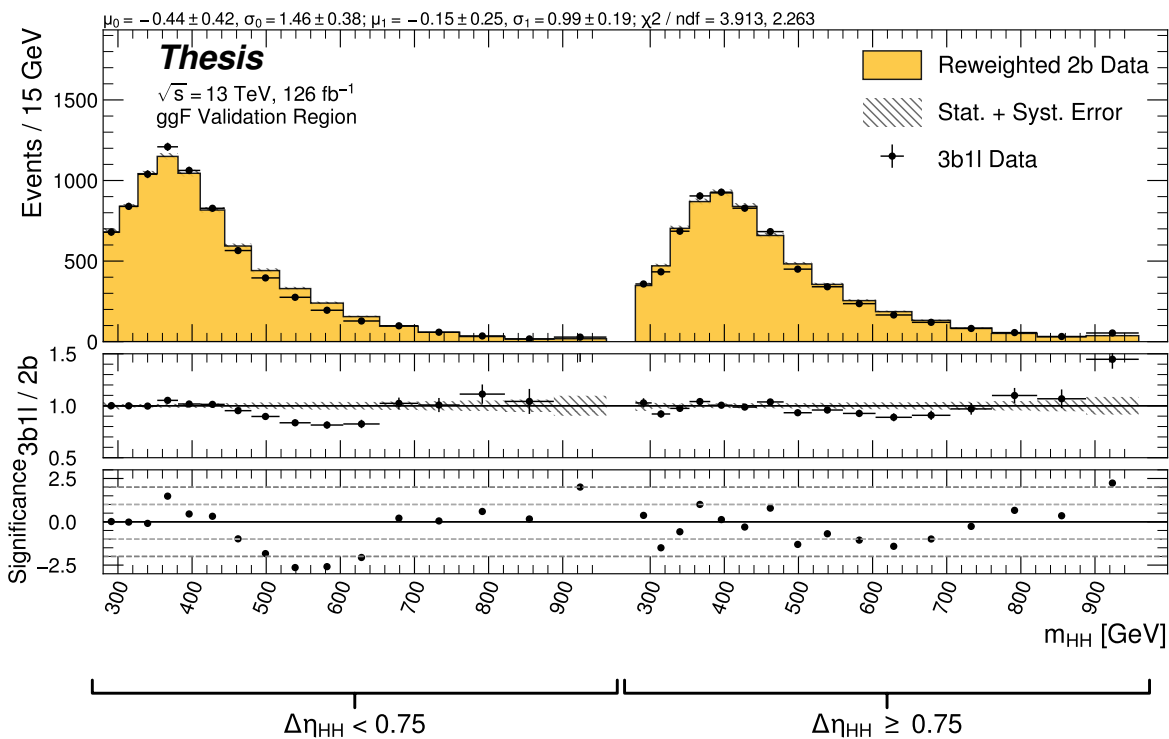


Figure 7.71: **Non-resonant Search (3b1l):** Demonstration of the performance of the nominal reweighting in the validation region on m_{HH} , split into the two $\Delta\eta_{HH}$ regions. A deficit is present near 600 GeV, but agreement is fairly good otherwise.

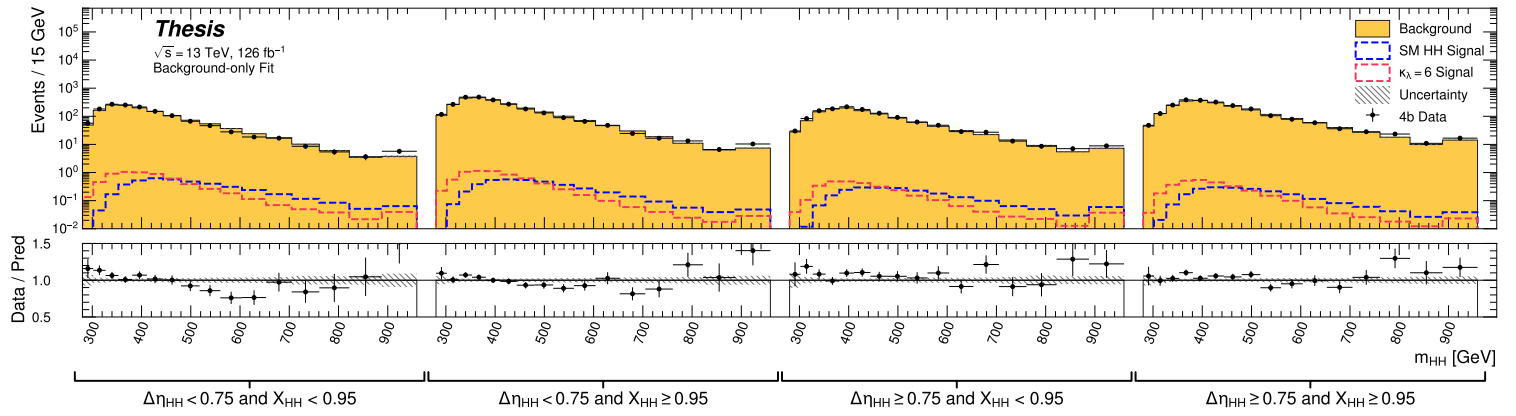


Figure 7.72: **Non-resonant Search (4b):** Signal region agreement of the background estimate and observed data after a background-only profile likelihood fit for the 4b channels, with Standard Model and $\kappa_\lambda = 6$ signal overlaid for reference. Modeling is generally quite good near the Standard Model peak, but disagreements are seen at very low and high masses. A deficit is present in low $\Delta\eta_{HH}$ bins near 600 GeV.

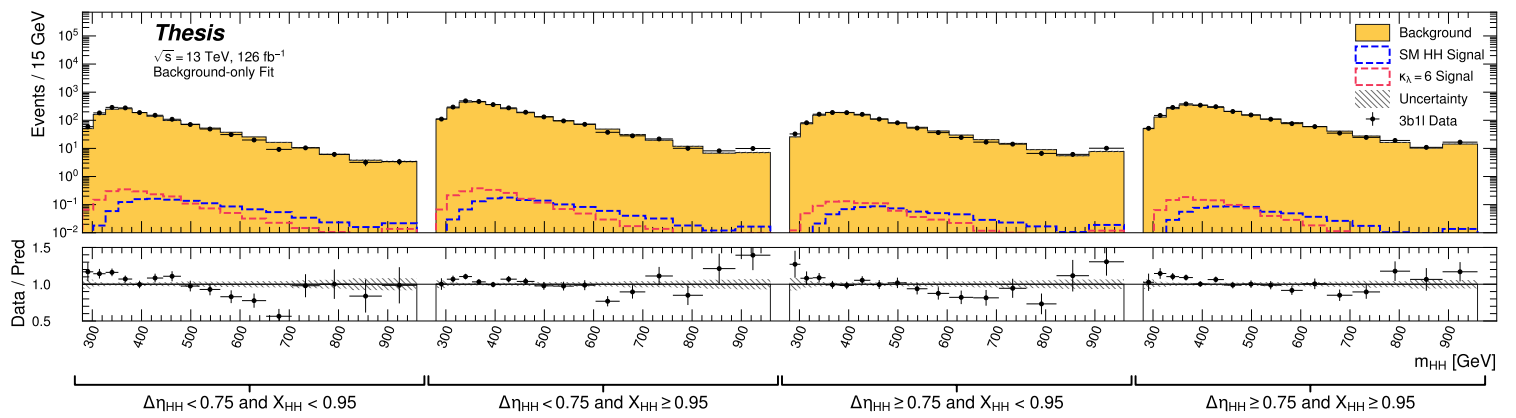


Figure 7.73: **Non-resonant Search (3b1l):** Signal region agreement of the background estimate and observed data after a background-only profile likelihood fit for the 3b1l channels, with Standard Model and $\kappa_\lambda = 6$ signal overlaid for reference. Conclusions are very similar to the 4b channels, with generally good modeling near the Standard Model peak, but disagreements at very low and high masses. A deficit is present near 600 GeV.

2483 **7.11 Statistical Analysis**

2484 The resonant analysis is used to set a 95% confidence level upper limit on the $pp \rightarrow X \rightarrow$
2485 $HH \rightarrow b\bar{b}b\bar{b}$ and $pp \rightarrow G_{KK}^* \rightarrow HH \rightarrow b\bar{b}b\bar{b}$ cross-sections, while the non-resonant analysis
2486 is used to set a 95% confidence level upper limit on the $pp \rightarrow HH \rightarrow b\bar{b}b\bar{b}$ cross sections for
2487 a variety of values of the trilinear Higgs coupling.

2488 The upper limit is extracted using the CL_s method [112]. The test statistic used is q_μ
2489 [113], where μ is the signal strength, and θ represents the nuisance parameters. A single
2490 hat represents the maximum likelihood estimate of a parameter, while $\hat{\theta}(x)$ represents the
2491 conditional maximum likelihood estimate of the nuisance parameters if the signal cross-section
2492 is fixed at x .

$$q_\mu = \begin{cases} -2 \ln \left(\frac{\mathcal{L}(\mu, \hat{\theta}(\mu))}{\mathcal{L}(\hat{\mu}, \hat{\theta})} \right) & \hat{\mu} \leq \mu \\ 0 & \hat{\mu} > \mu \end{cases} \quad (7.15)$$

2493 CL_s for some test value of μ is then defined by

$$CL_s = \frac{CL_{s+b}}{CL_b} = \frac{p(q_\mu \geq q_{\mu, \text{obs}} | s+b)}{p(q_\mu \geq q_{\mu, \text{obs}} | b)}, \quad (7.16)$$

2494 where the p -values are calculated in the asymptotic approximation [113], which is valid in
2495 the large sample limit.

2496 The signal cross-section μ fb is excluded at the 95% confidence level if $CL_s < 0.05$.

Observed	-2σ	-1σ	Expected	$+1\sigma$	$+2\sigma$
4.4	3.1	4.2	5.9	8.2	11.0

Table 7.1: Limits on Standard Model $HH \rightarrow b\bar{b}b\bar{b}$ production, presented in units of the predicted Standard Model cross section. Results include background systematics only.

2497 7.12 Results

2498 Figure 7.74 shows the expected limit for the spin-0 and spin-2 resonant search. The resolved
 2499 channel covers the range between 251 and 1500 GeV and is combined with the boosted channel
 2500 between 900 and 1500 GeV. The boosted channel then extends to 3 TeV. The most significant
 2501 excess is seen for a signal mass of 1100 GeV, with local significance of 2.6σ for the spin-0
 2502 signal and 2.7σ for the spin-2 signal. This is reduced to 1.0σ and 1.2σ globally.

2503 The spin-2 bulk Randall-Sundrum model with $k/\overline{M}_{\text{Pl}} = 1$ is excluded for graviton masses
 2504 between 298 and 1440 GeV.

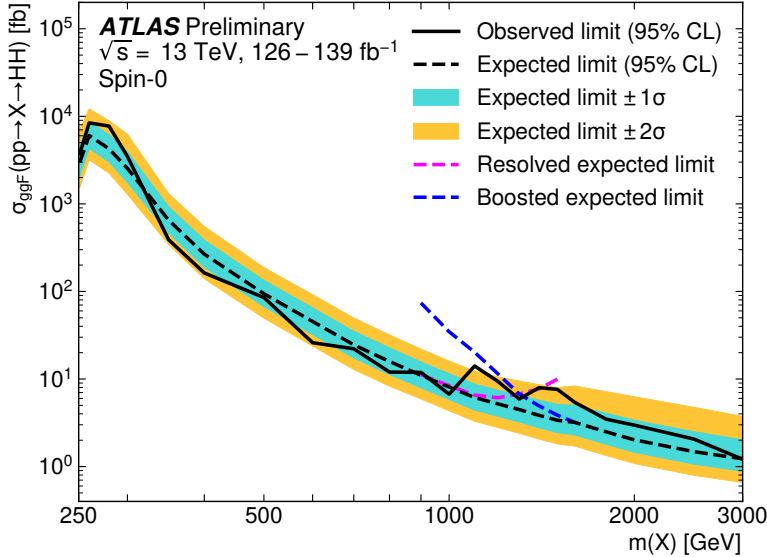
2505 Preliminary results are presented here for the gluon-gluon fusion non-resonant search,
 2506 combining results from the $4b$ and $3b + 1l$ signal regions in the 2×2 category scheme in
 2507 $\Delta\eta_{HH}$ and X_{HH} . These results will be further combined with a VBF channel as discussed,
 2508 but this is left for future work. Results shown here include background systematics only.
 2509 Limits are set for κ_λ values from -20 to 20 . The cross section limit for HH production is set
 2510 at 140 fb (180 fb) observed (expected), corresponding to an observed (expected) limit of 4.4
 2511 (5.9) times the Standard Model prediction (see Table 7.1). κ_λ is constrained to be within the
 2512 range $-4.9 \leq \kappa_\lambda \leq 14.4$ observed ($-3.9 \leq \kappa_\lambda \leq 10.9$ expected). These results are shown in
 2513 Figure 7.75.

2514 We note that this is a significant improvement over the early Run 2 result, which achieved
 2515 an observed (expected) limit of 12.9 (20.7) times the Standard Model prediction. The dataset
 2516 is 4.6 times larger, and a naive scaling of the early Run 2 result (Poisson statistics \implies a factor
 2517 of $1/\sqrt{4.6}$) would predict an observed (expected) limit of 6.0 (9.7) times the Standard Model.

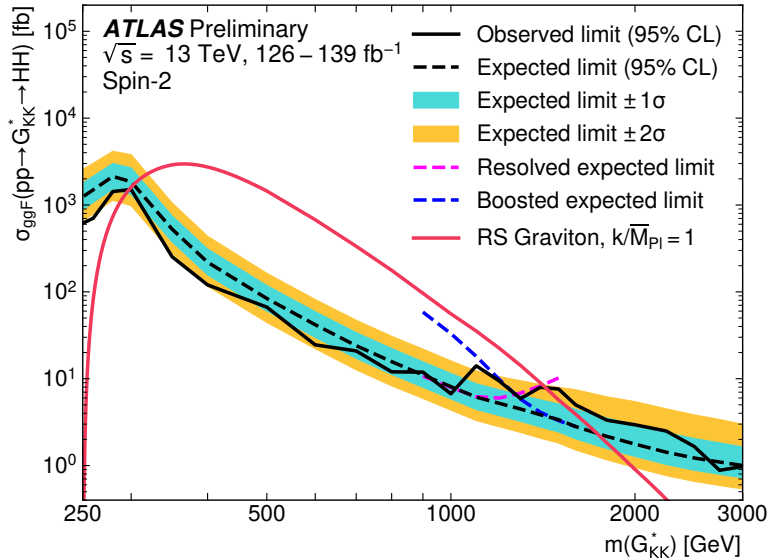
2518 The result of 4.4 (5.9) observed (expected) presented here is therefore both an improvement
 2519 by a factor of 3 (3.5) over the previous result and also beats the statistical scaling by around
 2520 30 (40) %, demonstrating the impact of the various analysis improvements presented here.
 2521 We note again that these results do not include the complete set of uncertainties – however
 2522 we expect the addition of the remaining uncertainties to have no more than a few percent
 2523 impact.

2524 The observed limits presented in Figure 7.75 are consistently above the 2σ band for values
 2525 of $\kappa_\lambda \geq 5$, peaking at a local significance of 3.8σ for $\kappa_\lambda = 6$. As this analysis is optimized for
 2526 points near the Standard Model, and as there is no excess present in more sensitive channels
 2527 in this same region (e.g. $HH \rightarrow bb\gamma\gamma$ *TODO: include comparison*), we do not believe this is a
 2528 real effect, but is rather due to a mis-modeling of the background at low mass, where the
 2529 min ΔR pairing has poor signal efficiency and the assumption of well behaved background in
 2530 the mass plane breaks down. This is consistent with the location of the $\kappa_\lambda = 6$ signal in m_{HH} ,
 2531 as shown in Figures 7.72 and 7.73. It was considered, but not implemented, for this analysis
 2532 to impose a cut on m_{HH} near 350 or 400 GeV to avoid such a low mass modeling issue.

2533 To check the impact of if we would have imposed such a cut, and to verify that the excess
 2534 is due to the low mass regime, we therefore run the same set of limits without the low mass
 2535 bins. In this case, we choose to simply drop the first few bins in m_{HH} such that everything
 2536 else, including the higher mass bin edges, is kept the same. Due to the variable width binning,
 2537 this corresponds to an m_{HH} cut of 381 GeV. The results of this check are shown in Figure
 2538 7.76, overlaid with the limits of Figure 7.75 for reference. With the m_{HH} cut imposed, there
 2539 is a slight degradation in the expected limits for larger positive and negative values of κ_λ ,
 2540 but the points near the Standard Model are nearly identical. Further, the observed excess is
 2541 significantly reduced, with observed limits for $\kappa_\lambda \geq 5$ now falling entirely within the expected
 2542 1σ band. Due to the preliminary nature of these results, further study is left for future
 2543 work. However, we believe, in conjunction with the $HH \rightarrow bb\gamma\gamma$ results and our expectations
 2544 about the difficulty of the background estimation at low mass, that this is demonstrative of a
 2545 mis-modeling rather than a real excess.



(a)



(b)

Figure 7.74: Expected (dashed black) and observed (solid black) 95% CL upper limits on the cross-section times branching ratio of resonant production for spin-0 ($X \rightarrow HH$) and spin-2 $G_{KK}^* \rightarrow HH$. The $\pm 1\sigma$ and $\pm 2\sigma$ ranges for the expected limits are shown in the colored bands. The resolved channel expected limit is shown in dashed pink and covers the range from 251 and 1500 GeV. It is combined with the boosted channel (dashed blue) between 900 and 1500 GeV. The theoretical prediction for the bulk RS model with $k/\bar{M}_{Pl} = 1$ [23] (solid red line) is shown, with the decrease below 350 GeV due to a sharp reduction in the $G_{KK}^* \rightarrow HH$ branching ratio. The nominal $H \rightarrow b\bar{b}$ branching ratio is taken as 0.582.

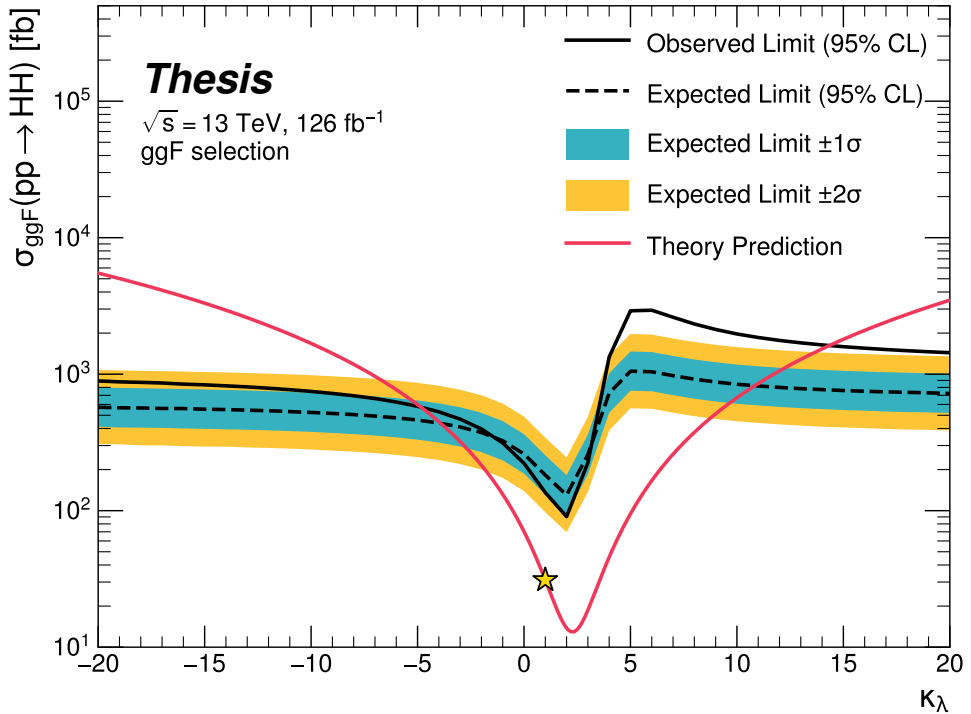


Figure 7.75: Expected (dashed black) and observed (solid black) 95% CL upper limits on the cross-section times branching ratio of non-resonant production for a range of values of the Higgs self-coupling, with the Standard Model value ($\kappa_\lambda = 1$) illustrated with a star. The $\pm 1\sigma$ and $\pm 2\sigma$ ranges for the expected limits are shown in the colored bands. The cross section limit for HH production is set at 140 fb (180 fb) observed (expected), corresponding to an observed (expected) limit of 4.4 (5.9) times the Standard Model prediction. κ_λ is constrained to be within the range $-4.9 \leq \kappa_\lambda \leq 14.4$ observed ($-3.9 \leq \kappa_\lambda \leq 10.9$ expected). The nominal $H \rightarrow b\bar{b}$ branching ratio is taken as 0.582. We note that the excess present for $\kappa_\lambda \geq 5$ is thought to be due to a low mass background mis-modeling, present due to the optimization of this analysis for the Standard Model point, and is not present in more sensitive channels in this same region (e.g. $HH \rightarrow bb\gamma\gamma$).

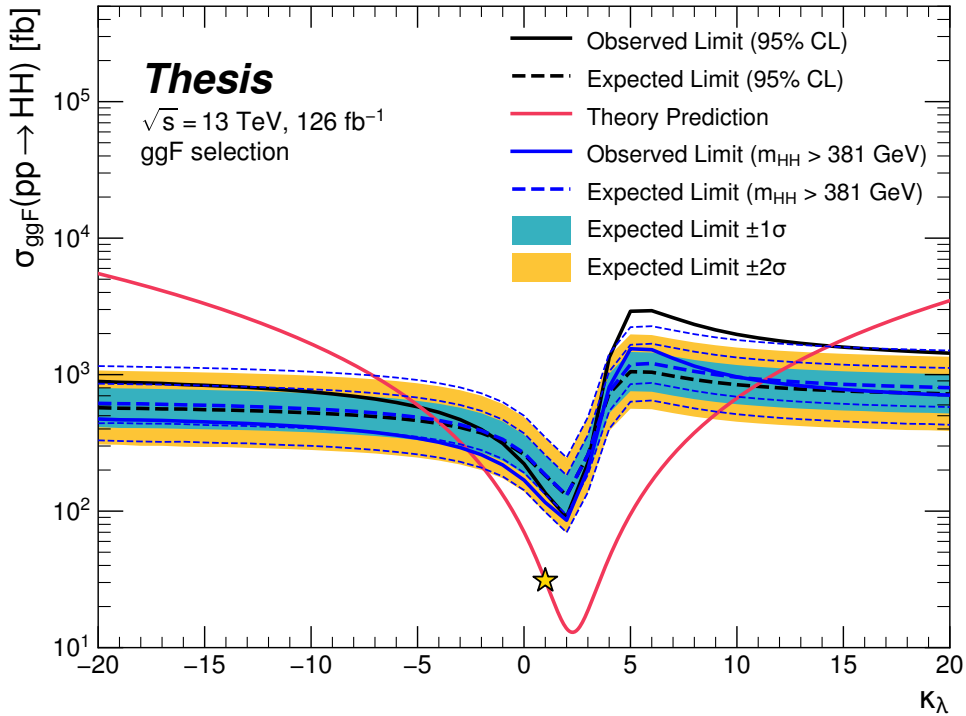


Figure 7.76: Comparison of the limits in Figure 7.75 with an equivalent set of limits that drop the m_{HH} bins below 381 GeV, with the value of 381 GeV determined by the optimized variable width binning. The expected limit band with this mass cut is shown in dashed blue, and the observed is shown in solid blue. The excess at and above $\kappa_\lambda = 5$ is significantly reduced, demonstrating that this is driven by low mass. Notably, there is minimal impact on the expected sensitivity with this m_{HH} cut.

2546

Chapter 8

2547

FUTURE IDEAS FOR $HH \rightarrow b\bar{b}b\bar{b}$

2548 The searches presented in this thesis make use of a large suite of sophisticated techniques,
 2549 selected through careful study and validation. During this process, a variety of interesting
 2550 directions for the $HH \rightarrow b\bar{b}b\bar{b}$ analysis were explored by this thesis author, in collaboration
 2551 with a few others¹, but were not used due to a variety of constraints. We present two
 2552 such interesting directions here, with the hope of encouraging further exploration of these
 2553 techniques in future work.

2554 **8.1 pairAGraph: A New Method for Jet Pairing**

2555 As discussed in Chapter 7, one of the main problems to solve is the pairing of b -jets into
 2556 Higgs candidates. Figure 7.1 demonstrates that the choice of the pairing method, while
 2557 important for achieving good reconstruction of signal events, also significantly impacts the
 2558 structure of non- HH events, leading to various biases in the background estimate. Evaluation
 2559 of the pairing method therefore must take both of these factors into account. While we have
 2560 presented some advantages in respective contexts for the pairing methods considered here,
 2561 we of course would like to explore further improvements to this important component of the
 2562 analysis.

2563 To that end, we note that all of the pairing methods considered here share a common
 2564 feature: four jets are selected, and the pairing is some discrimination between the available
 2565 three pairings of these four jets. For the methods used in this analysis, the jet selection
 2566 proceeds via a simple p_T ordering, with b -tagged jets receiving a higher priority than non-

¹Notably Nicole Hartman (SLAC), who spearheaded much of the development and proof of concept work, in collaboration with Michael Kagan and Rafael Teixeira De Lima.

2567 tagged jets.

2568 With the advent of a variety of machine learning methods for dealing with a variable number
2569 of inputs (e.g. recurrent neural networks [114], deep sets [115], graph neural networks [116],
2570 and transformers [117]), a natural place to improve on the pairing is to consider more than
2571 just four jets. The pairing and jet selection is then performed simultaneously, allowing for
2572 the incorporation of more event information in the pairing decision and the incorporation of
2573 jet correlation structure in the jet selection.

2574 In practice, the majority of $HH \rightarrow b\bar{b}b\bar{b}$ events have either four or five jets which pass the
2575 kinematic preselection, and any gain from this additional freedom would come from events
2576 with greater than or equal to five jets. However, this five jet topology is particularly exciting
2577 for scenarios such as events with initial state radiation (ISR), in which the $HH \rightarrow 4b$ jets are
2578 offset by a single jet with p_T similar in magnitude to that of the $HH \rightarrow 4b$ system. Such
2579 events have explicit event level information which is not encoded with the inclusion of only
2580 the $HH \rightarrow 4b$ jets, and are pathological if the ISR jet happens to pass b -tagging requirements.

2581 Additionally, with the use of lower tagged regions for background estimation and alternate
2582 signal regions, this extra flexibility in jet selection may provide a very useful bias – since the
2583 algorithm is trained on signal, the selected jets for the pairing will be the most “4b-like” jets
2584 available in the considered set.

2585 For the studies considered here, a transformer [117] based architecture is used. This is
2586 best visualized by considering the event as a graph with jets corresponding to nodes and edges
2587 corresponding to potential connections – for this reason, we term this algorithm “pairAGraph”.
2588 The approach is as follows: each jet, i , is represented by some vector of input variables, \vec{x}_i ,
2589 in our case the four-vector information, (p_T, η, ϕ, E) of each jet, plus information on the
2590 b -tagging decision. A multi-layer perceptron (MLP) is used to create a latent embedding,
2591 $\mathbf{h}(\vec{x}_i)$, of this input vector.

To describe the relationship between various jets in the event, we then define a vector \vec{z}_i

for each jet as

$$\vec{z}_i = \sum_j w_{ij} \mathbf{h}(\vec{x}_j) \quad (8.1)$$

where j runs over all jets in the event (including $i = j$), the w_{ij} can be thought of as edge weights, and $\mathbf{h}(\vec{x}_j)$ is the latent embedding for jet j mentioned above.

Within this formula, both \mathbf{h} and the w_{ij} are learnable. To learn an appropriate latent mapping and set of edge weights, we define a similarity metric corresponding to each possible jet pairing:

$$\vec{z}_{1a} \cdot \vec{z}_{1b} + \vec{z}_{2a} \cdot \vec{z}_{2b} \quad (8.2)$$

where subscripts $1a$ and $1b$ correspond to the two jets in pair 1, $2a$ and $2b$ to the jets in pair 2 for a given pairing of four distinct jets.

This similarity metric is calculated for all possible pairings, which are then passed through a softmax [118] activation function, which compresses these scores to between 0 and 1 with sum of 1, lending an interpretation as probability of each pairing.

In training, the ground truth pairing is set by *truth matching* jets to the b -jets in the HH signal simulation – a jet is considered to match if it is < 0.3 in ΔR away from a b -jet in the simulation record. Given this ground truth, a cross-entropy loss *TODO: cite* is used on the softmax outputs, and w_{ij} and \mathbf{h} are updated correspondingly. Training in such a way corresponds to updating w_{ij} and \mathbf{h} to maximize the similarity metric for the correct pairing.

In evaluation, the pairings with a higher score (and therefore higher softmax output) given the trained h and w_{ij} therefore correspond to the pairings that are most “ HH -like”. The maximum over these scores is therefore the pairing used as the predicted result from the algorithm.

Because the majority of $HH \rightarrow b\bar{b}b\bar{b}$ events have either four or five jets, it was found to be sufficient to only consider a maximum of 5 jets. Consideration of more is in principle possible, but the quickly expanding combinatorics leads to a rapidly more difficult problem. The jets considered are the five leading jets in p_T . Notably, this set of jets may include jets which are not b -tagged, even for the nominal 4 b region – therefore events with 4 b -tagged jets

2613 are not required to use all of them in the construction of Higgs candidates, in contrast to the
2614 other algorithms used in this thesis.

2615 A comparison of the pairAGraph jet selection with the baseline selection used in Chapter 7
2616 is considered in Table 8.1 for the MC16a Standard Model non-resonant signal. As a reminder,
2617 the baseline selection orders jets by p_T , selecting first the highest p_T b -tagged jets (according
2618 to the b -tag region definition) and then the highest p_T non-tagged jets. The first four jets in
2619 this ordering are used.

2620 For the comparison presented in Table 8.1, only the leading five jets are considered in
2621 applying both algorithms in order to compare results on more equal footing. The numbers
2622 shown are the percent of the time that the correct jets are selected for the Higgs candidates
2623 by each algorithm, given that the correct jets fall within these leading five jets, where “correct”
2624 here means truth matched to the corresponding b -quarks. pairAGraph demonstrates a slight
2625 improvement over the baseline for $4b$, which widens when considering lower b -tag categories.
2626 Given that four b -quarks are present in all of these categories, this suggests that pairAGraph
2627 is able to recover information in the case of, e.g., mis-tagged jets.

2628 Table 8.2 compares the HH pairing accuracy of a few different pairing algorithms for
2629 the Standard Model signal. Notably, pairAGraph demonstrates a higher pairing accuracy
2630 immediately after paring, but all methods are quite comparable after the full analysis selection.

2631

2632 As mentioned in Chapter 7, though the pairing is quite important for signal events, it also
2633 must be applied to events in data, where the overwhelming majority of events do not contain
2634 HH . Though in general, pairing methods select for an HH -like topology, the additional
2635 flexibility of pairAGraph to choose which jets enter the candidate HH system provides an
2636 additional handle to shape the kinematics of events in data. Examples of this impact are seen
2637 in Figures 8.1 and 8.2, which compare the $2b$ and $4b$ distributions of p_T of the HH candidate
2638 system between BDT pairing and pairAGraph pairing before and after reweighting. HH p_T
2639 was chosen as it is a variable which demonstrates both a large difference between $2b$ and $4b$
2640 and a residual mis-modeling after reweighting. As can be seen in Figure 8.1, the $2b$ and $4b$

4b correct jets	96.7%	96.0%
3b+1 loose correct jets	96.3%	95.2%
3b correct jets	91.6%	83.2%

Table 8.1: Percent of the time that the correct jets are selected for the Higgs candidates by each algorithm, given that the correct jets fall within the set of considered jets, where “correct” here means truth matched to the corresponding b -quarks. Only the leading five jets are considered in the assessment of both algorithms. Definitions of the $4b$ and $3b + 1$ loose categories are as described in Section 7.3, where $3b$ requires three b -tagged jets and the fourth jet is untagged. pairAGraph demonstrates a slight improvement over the baseline for $4b$, which widens when considering lower b -tag categories. Given that four b -quarks are present in all of these categories, this suggests that pairAGraph is able to recover information in the case of, e.g., mis-tagged jets.

	After Pairing	After Full Selection
D_{HH}	71.8%	93.6%
$\min \Delta R$	69.7%	94.7%
pairAGraph	78.4%	94.2%

Table 8.2: Pairing accuracy evaluated for the Standard Model signal (MC16a), comparing D_{HH} and $\min \Delta R$ (discussed in Chapter 7) with pairAGraph trained on the Standard Model signal. Numbers are shown both immediately after pairing and after the full analysis selection. pairAGraph demonstrates a 7-8% higher accuracy than the other algorithms immediately after pairing, but all methods are quite comparable after the full analysis selection.

distributions are more similar before reweighting with pairAGraph. Figure 8.2 further shows that the residual mis-modeling after reweighting is reduced, along with the corresponding uncertainty. While this is not fully conclusive, it provides a hint that the jets chosen for the 2b event HH candidate system may be more “4b-like” than the jets chosen with the baseline selection.

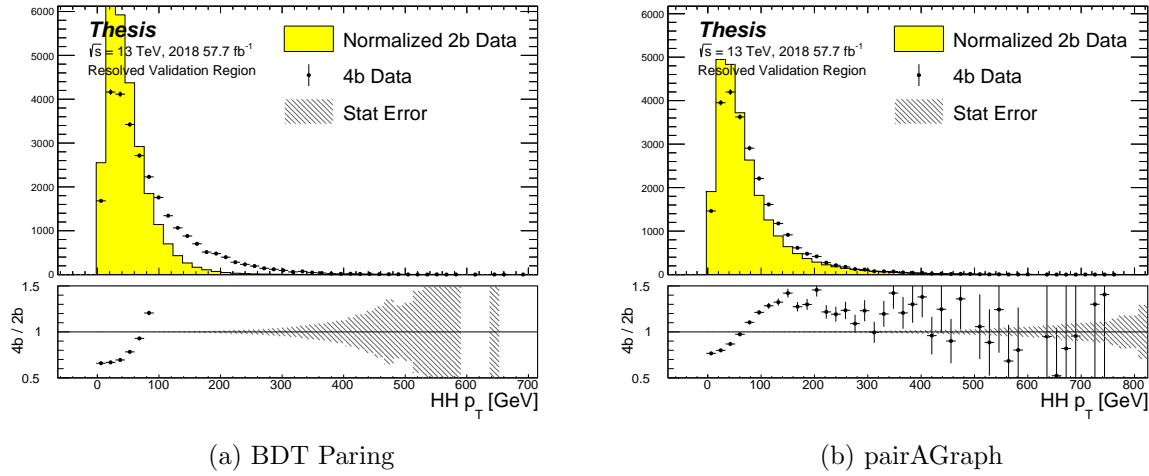


Figure 8.1: Comparison of distributions of $HH p_T$ in the 2018 resonant validation region before reweighting for BDT pairing (left) and pairAGraph (right). $HH p_T$ is a variable with a large difference between 2b and 4b, but the relative shapes seem to be more similar for pairAGraph than for BDT paring, corresponding to the hypothesis that pairAGraph chooses more “4b-like” jets.

2646 8.2 Background Estimation with Mass Plane Interpolation

2647 The choice of a pairing algorithm that results in a smooth mass plane (such as $\min \Delta R$)
 2648 opens up a variety of options for the background estimation. While the method based on
 2649 reweighting of 2b events used for this thesis performs well and has been extensively studied
 2650 and validated, it also relies on several assumptions. In particular, the reweighting is derived

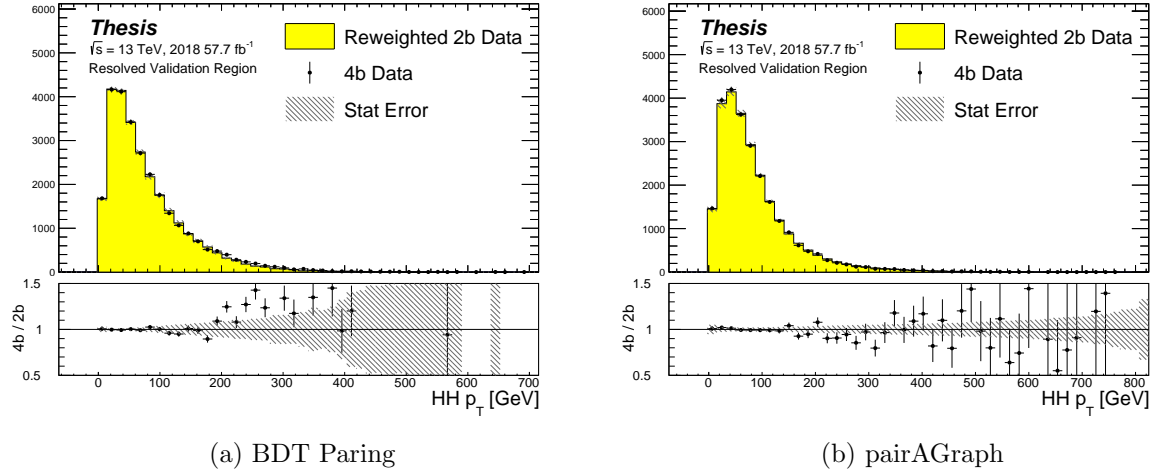


Figure 8.2: Comparison of distributions of $HH p_T$ in the 2018 resonant validation region after reweighting for BDT pairing (left) and pairAGraph (right). $HH p_T$ is a variable with a large difference between $2b$ and $4b$, and the reweighted agreement in the high p_T tail is significantly improved with pairAGraph, with a corresponding reduction in the assigned bootstrap uncertainty in that region.

2651 between e.g., $2b$ and $4b$ events *outside* of the signal region and then applied to $2b$ events *inside*
 2652 the signal region, with the assumption that the $2b$ to $4b$ transfer function will be sufficiently
 2653 similar in both regions of the mass plane. An uncertainty is assigned to account for the bias
 2654 due to this assumption, but the extrapolation in the mass plane is never explicitly treated in
 2655 the nominal estimate. While the approach of reweighting $2b$ events within the signal region
 2656 does have the advantage of incorporating explicit signal region information (that is, the $2b$
 2657 signal region events), the importance of the extrapolation bias motivates consideration of
 2658 a method that operates within the $4b$ mass plane. This additionally removes the reliance
 2659 on lower b -tagging regions, allowing for the use of, e.g. $3b$ triggers, and future-proofing the
 2660 analysis against trigger bandwidth constraints in the low tag regions.

2661 The pairAGraph pairing method discussed in the previous section was developed concur-

2662 rently with these studies and demonstrates good properties for an interpolated estimate (as
2663 shown below), and is therefore used in the following.

The method considered here relies on the following: for a given vector of input variables (event kinematics, etc), \vec{x} , the joint probability in the HH mass plane may be written as:

$$p(\vec{x}, m_{H1}, m_{H2}) = p(\vec{x}|m_{H1}, m_{H2})p(m_{H1}, m_{H2}) \quad (8.3)$$

2664 by the chain rule of probability. This means that the full dynamics of events in the HH mass
2665 plane may be described by (1) the conditional probability of considered variables \vec{x} , given
2666 values of m_{H1} and m_{H2} , and (2) the density of the mass plane itself.

2667 We present here an approach which uses normalizing flows [119] to model the conditional
2668 probabilities of events in the mass plane and Gaussian processes to model the mass plane
2669 density. These models are trained in a region around, but not including, the signal region,
2670 and the trained models are then used to construct an *interpolated* estimate of the signal
2671 region kinematics. This approach therefore explicitly treats event behavior within the mass
2672 plane, avoiding the concerns associated with a reweighted estimate. Validation of such a
2673 method, as well as assessing of closure and biases of the method, may be done in alternate
2674 b -tagging or kinematic regions, notably the now unused $2b$ region, results of which are shown
2675 below.

2676 8.2.1 Normalizing Flows

Normalizing flows model observed data $x \in X$, with $x \sim p_X$, as the output of an invertible, differentiable function $f : X \rightarrow Z$, with $z \in Z$ a latent variable with a simple prior probability distribution (often standard normal), $z \sim p_Z$. From a change of variables, given such a function, we may write

$$p_X(x) = p_Z(f(x)) \left| \det \left(\frac{d(f(x))}{dx} \right) \right| \quad (8.4)$$

2677 where $\left(\frac{d(f(x))}{dx} \right)$ is the Jacobian of f at x .

2678 The problem of normalizing flows then reduces to (1) choosing sets of f which are both
2679 tractable and sufficiently expressive to describe observed data, and (2) optimizing associated

2680 sets of functional parameters on observed data via maximum likelihood estimation using
 2681 the above formula. Sampling from the learned density is done by drawing from the latent
 2682 distribution $z \sim p_Z$ (cf. inverse transform sampling) – the corresponding sample is then
 2683 $x \sim p_X$ with $x = f^{-1}(z)$.

2684 A standard approach to the definition of these f is as a composition of affine transfor-
 2685 mations (e.g. RealNVP [120]), that is, transformations of the form $\alpha z + \beta$, with α and β
 2686 learnable parameter vectors. This can roughly be thought of as shifting and squeezing the
 2687 input prior density in order to match the data density. However, this has somewhat
 2688 limited expressivity, for instance in the case of a multi-modal density.

This work thus instead relies on neural spline flows [121] in which the functions considered are monotonic rational-quadratic splines, which have an analytic inverse. A rational quadratic function has the form of a quotient of two quadratic polynomials, namely,

$$f_j(x_i) = \frac{a_{ij}x_i^2 + b_{ij}x_{ij} + c_{ij}}{d_{ij}x_i^2 + e_{ij}x_i + f_{ij}} \quad (8.5)$$

2689 with six associated parameters (a_{ij} through f_{ij}) per each piecewise bin j of the spline and
 2690 each input dimension i . This is explicitly more flexible and expressive than a simple affine
 2691 transformation, allowing, e.g., the treatment of multi-modality via the piecewise nature of
 2692 the spline.

2693 The rational quadratic spline is defined on a set interval. The transformation outside of
 2694 this interval is set to the identity, with these linear tails allowing for unconstrained inputs.
 2695 The boundaries between bins of the spline are set by coordinates called *knots*, with $K + 1$
 2696 knots for K bins – the two endpoints for the spline interval plus the $K - 1$ internal boundaries.
 2697 The derivatives at these points are constrained to be positive for the internal knots, and
 2698 boundary derivatives are set to 1 to match the linear tails.

2699 The bin widths and heights are learnable ($2 \cdot K$ parameters) as are the internal knot
 2700 derivatives ($K - 1$ parameters), and these $3K - 1$ outputs of the neural network are sufficient
 2701 to define a monotonic rational-quadratic spline which passes through each knot and has the
 2702 given derivative value at each knot.

2703 In the context of the $HH \rightarrow 4b$ analysis, a neural spline flow is used to model the four
 2704 vector information of each Higgs candidate, conditional on their respective masses. The
 2705 resulting flow is therefore five dimensional, with inputs $x = (p_{T,H1}, p_{T,H2}, \eta_{H1}, \eta_{H2}, \Delta\phi_{HH})$,
 2706 where the ATLAS ϕ symmetry has been encoded by assuming $\phi_{H1} = 0$. Conditional variables
 2707 m_{H1} and m_{H2} are not modeled by the flow, but “come along for the ride”. A standard normal
 2708 distribution in 5 dimensions is used for the underlying prior. Modeling of the four vectors
 2709 was chosen in order to reduce bias from modeling m_{HH} directly.

2710 The trained flow model then gives a model for $p(x|m_{H1}, m_{H2})$ which may be sampled
 2711 from to reconstruct distributions of HH kinematics given values of m_{H1} and m_{H2} .

2712 8.2.2 Gaussian Processes

2713 The second piece of this background estimate is the modeling of the mass plane density,
 2714 $p(m_{H1}, m_{H2})$. This is done using Gaussian process regression – note that a similar procedure
 2715 is used to define a systematic in the boosted $4b$ analysis. Generally, Gaussian processes
 2716 are a collection of random variables in which every finite collection of said variables is
 2717 distributed according to a multivariate normal distribution. For the context of Gaussian
 2718 process regression, what we consider is a Gaussian process over function space, that is, for a
 2719 collection of points, x_1, \dots, x_N , the space of corresponding function values, $(f(x_1), \dots, f(x_N))$
 2720 is Gaussian process distributed, that is, described by an N dimensional normal distribution
 2721 with mean μ , covariance matrix Σ .

2722 For a single point, this would correspond to a function space described entirely by a
 2723 normal distribution, with various samples from that distribution yielding various candidate
 2724 functions. For multiple points, a covariance matrix describes the relationship between each
 2725 pair of points – correspondingly, it is represented via a *kernel function*, $K(x, x')$. As, in
 2726 practice, μ may always be set to 0 via a centering of the data, the kernel function fully defines
 2727 the considered family of functions.

The considered family of functions describes a Bayesian *prior* for the data. This prior
 may be conditioned on a set of training data points (X_1, \vec{y}_1) . This conditional *posterior* may

then be used to make predictions $\vec{y}_2 = f(X_2)$ at a set of new points X_2 . Because of the Gaussian process prior assumption, \vec{y}_1 and \vec{y}_2 are assumed to be jointly Gaussian. We may therefore write

$$\begin{pmatrix} \vec{y}_1 \\ \vec{y}_2 \end{pmatrix} \sim \mathcal{N} \left(\begin{pmatrix} 0 \\ 0 \end{pmatrix}, \begin{pmatrix} K(X_1, X_1) & K(X_1, X_2) \\ K(X_1, X_2) & K(X_2, X_2) \end{pmatrix} \right) \quad (8.6)$$

2728 where we have used that the kernel function is symmetric and assumed prior mean 0.

By standard conditioning properties of Gaussian distributions,

$$\vec{y}_2 | \vec{y}_1 \sim \mathcal{N}(K(X_2, X_1)K(X_1, X_1)^{-1}\vec{y}_1, K(X_2, X_2) - K(X_2, X_1)K(X_1, X_1)^{-1}K(X_1, X_2)) \quad (8.7)$$

2729 which is the sampling distribution for a Gaussian process given kernel K . In practice, the
2730 mean of this sampling distribution is used as the function estimate, with an uncertainty from
2731 the predicted variance at a given point.

The choice of kernel function has a very strong impact on the fitted curve, and must therefore be chosen to express the expected dynamics of the data. A common such choice is a radial basis function (RBF) kernel, which takes the form

$$K(x, x') = \exp \left(-\frac{d(x, x')^2}{2l^2} \right) \quad (8.8)$$

2732 where $d(\cdot, \cdot)$ is the Euclidean distance and $l > 0$ is a length scale parameter. Conceptually, as
2733 distances $d(x, x')$ increase relative to the chosen length scale, the kernel smoothly dies off –
2734 further away points influence each other less.

2735 Coming back to our case of the mass plane, the procedure runs as follows:

- 2736 1. A binned 2d histogram of the blinded mass plane is created in a window around the
2737 “standard” analysis regions. Bins which have any overlap with the signal region are
2738 excluded.
- 2739 2. A Gaussian process is trained using the bin centers, values as training points. The
2740 scikit-learn implementation [122] is used, with RBF kernel with anisotropic length scale
2741 (l is dimension 2). The length scale is initialized to (50, 50) to cover the signal region,

2742 and optimized by minimizing the negative log-marginal likelihood on the training data,
 2743 $-\log p(\vec{y}|\theta)$. Training data is centered and scaled to mean 0, variance 1, and a statistical
 2744 error is included in the fit.

2745 3. The Gaussian process is then used to predict the density $p(m_{H1}, m_{H2})$ in the signal
 2746 region. This may then be sampled from via an inverse transform sampling to generate
 2747 values (m_{H1}, m_{H2}) according to the density (specifically, according to the mean of the
 2748 Gaussian process posterior). Though in principle the Gaussian process sampling is not
 2749 limited to bin centers, this is kept for simplicity, with a uniform smearing applied within
 2750 each sampled bin to approximate the continuous estimate, namely, if a bin is sampled
 2751 from, the returned value is drawn uniformly at random within the sampled bin.

4. The sampling in the previous step can be arbitrary – to set the overall normalization,
 a Monte Carlo sampling of the Gaussian process is done to approximate the relative
 fraction of events predicted both inside (f_{in}) and outside (f_{out}) of the signal region,
 within the training box. The number of events outside of the signal region (n_{out}) is
 known, therefore, the number of events inside of the signal region, n_{in} , may be estimated
 as

$$n_{in} = \frac{n_{out}}{f_{out}} \cdot f_{in}. \quad (8.9)$$

2752 Note that the Monte Carlo sampling procedure is simply a set of samples of the Gaussian
 2753 process from uniformly random values of m_{H1}, m_{H2} , and is the most convenient approach
 2754 given the irregular shape of the signal region.

2755 This procedure results in a generated set of predicted m_{H1}, m_{H2} values for signal region
 2756 background events, along with an overall yield prediction.

2757 8.2.3 The Full Prediction

2758 Given the normalizing flow parametrization of $p(x|m_{H1}, m_{H2})$ and the Gaussian process
 2759 generation of $(m_{H1}, m_{H2}) \sim p(m_{H1}, m_{H2})$ and prediction of the signal region yield, all of the

2760 pieces are in place to construct an interpolation background estimate. Namely

- 2761 1. Gaussian process sampled (m_{H1}, m_{H2}) values are provided to the normalizing flow to
2762 predict the other variables for the Higgs candidate four-vectors. These are used to
2763 construct the HH system (notably m_{HH}).
- 2764 2. These final distributions are normalized according to the predicted background yield.

2765 *8.2.4 Results*

2766 All of the following results use the pairAGraph pairing algorithm, and reweighted results use
2767 the region definitions from the resonant analysis.

2768 The Gaussian process sampling procedure is trained on a small fraction (0.01) of $2b$ data
2769 to mimic the available $4b$ statistics. This fraction of $2b$ data is blinded, and the prediction of
2770 the estimate trained on this blinded region may then be compared to real $2b$ data in the signal
2771 region. The predictions for signal region m_{H1} and m_{H2} individually are shown in Figure 8.3,
2772 and the resulting mass planes are compared in Figure 8.4. Good agreement is seen.

2773 The $4b$ region is kept blinded for this work, meaning that a direct comparison of the
2774 Gaussian process estimate in the $4b$ signal region is not done. However, a Gaussian process is
2775 trained on the blinded $4b$ region and compared to the corresponding reweighted $2b$ estimate,
2776 trained per the nominal procedures from the analyses above. The predictions for signal
2777 region m_{H1} and m_{H2} individually are shown in Figure 8.5, compared to both the control and
2778 validation region derived reweighting estimates, and the resulting signal region mass planes
2779 are compared in Figure 8.6. The estimates are seen to be compatible.

2780 The Gaussian process estimate may then be used as an input to the normalizing flow
2781 estimate to form a complete background estimate. Figure 8.7 shows such an estimate for the
2782 subsampled $2b$ signal region. Results for the prediction of the normalizing flow with inputs of
2783 real $2b$ signal region m_{H1} and m_{H2} are compared to the results of using Gaussian process
2784 predicted m_{H1} and m_{H2} , and are seen to be consistent, demonstrating the above closure of

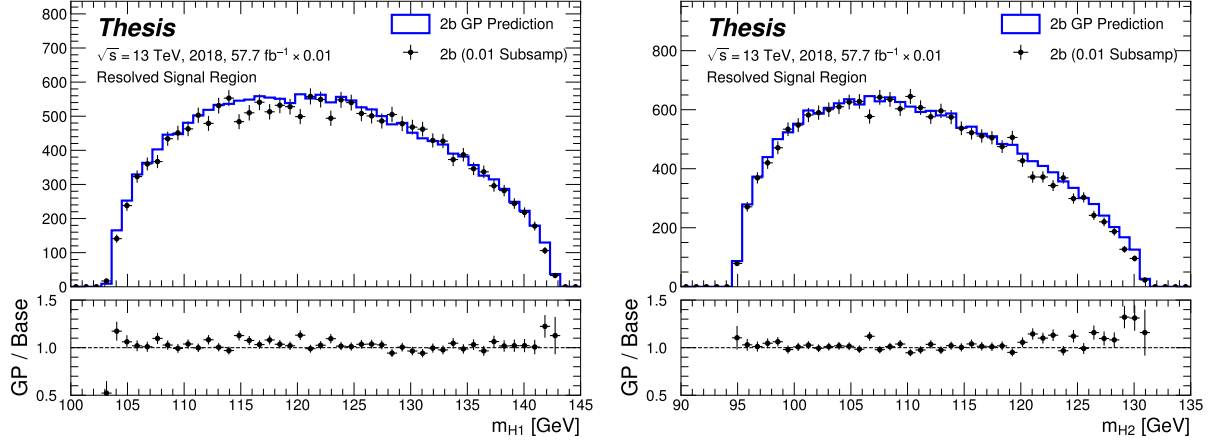


Figure 8.3: Gaussian process sampling prediction of marginals m_{H1} and m_{H2} for $2b$ signal region events compared to real $2b$ signal region events for the 2018 dataset. Good agreement is seen. Only a small fraction (0.01) of the $2b$ dataset is used for both training and this final comparison to mimic $4b$ statistics.

2785 the Gaussian process prediction. Reasonable agreement with real $2b$ signal region data is
2786 seen.

2787 Figure 8.8 demonstrates the application of this process to the $4b$ region, closely following
2788 how such an estimate would be used in the $HH \rightarrow b\bar{b}b\bar{b}$ analysis. As the $4b$ signal region
2789 is kept blinded for these studies, no direct evaluation is made, but results are compared to
2790 a resonant control region derived reweighting. Both signal region predictions are seen to
2791 be comparable, though there are some systematic differences. However, only the nominal
2792 estimates are compared here, with assessment of uncertainties on the interpolated estimate
2793 left for future work.

2794 8.2.5 Outstanding Points

2795 While good performance is demonstrated from the nominal interpolated background estimate,
2796 various uncertainties must be assigned according to the various stages of the estimate. These

2797 notably include

2798 • Assessing a statistical uncertainty on the normalizing flow training (cf. bootstrap
2799 uncertainty).

2800 • Propagation of the Gaussian process uncertainty through the sampling procedure.

2801 • Validation of the resulting estimate and assessment of necessary systematic uncertainties
2802 (e.g. from validation region non-closure).

2803 These are all quite tractable, but some, especially the choice of an appropriate systematic
2804 uncertainty, are certainly not obvious and require detailed study. In this respect, the
2805 reweighting validation work of the non-resonant analysis is certainly quite useful as a starting
2806 place in terms of the available regions and their correspondence to the nominal $4b$ signal
2807 region.

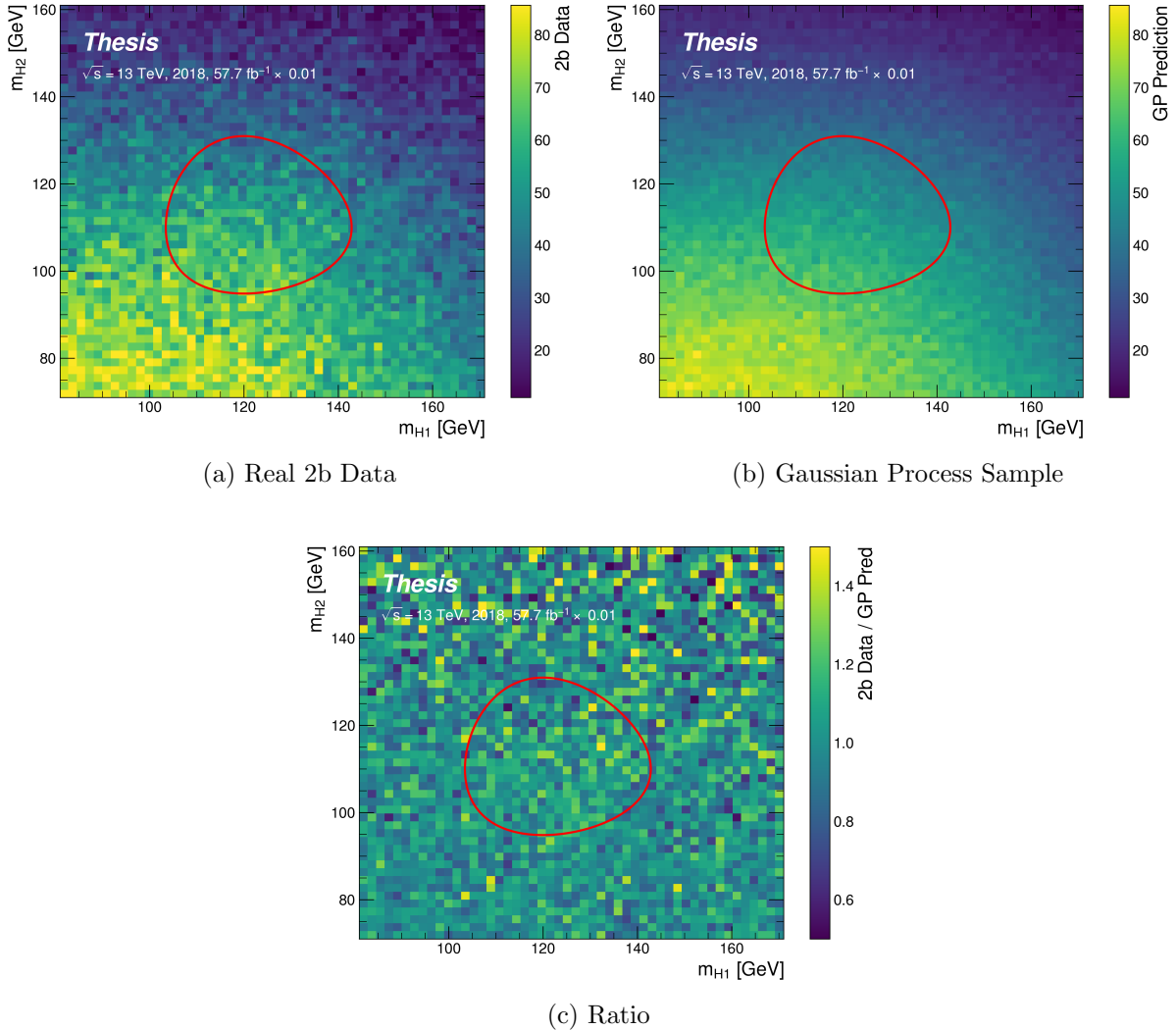


Figure 8.4: Gaussian process sampling prediction for the mass plane compared to the real 2b dataset for 2018. Only a small fraction (0.01) of the 2b dataset is used for both training and this final comparison to mimic 4b statistics. Good agreement is seen.

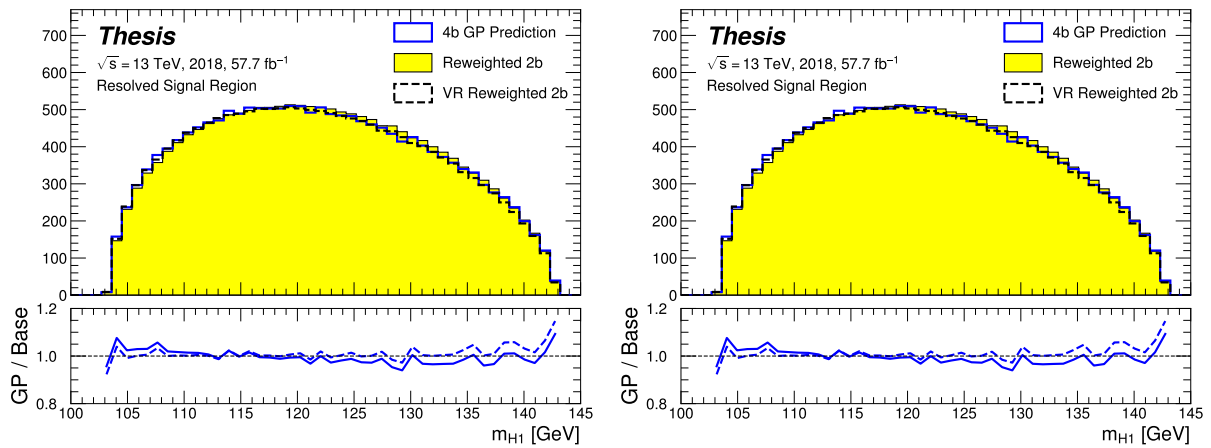


Figure 8.5: Gaussian process sampling prediction of marginals m_{H1} and m_{H2} for 4b signal region events compared to both control and validation reweighting predictions. While there are some differences, the estimates are compatible.

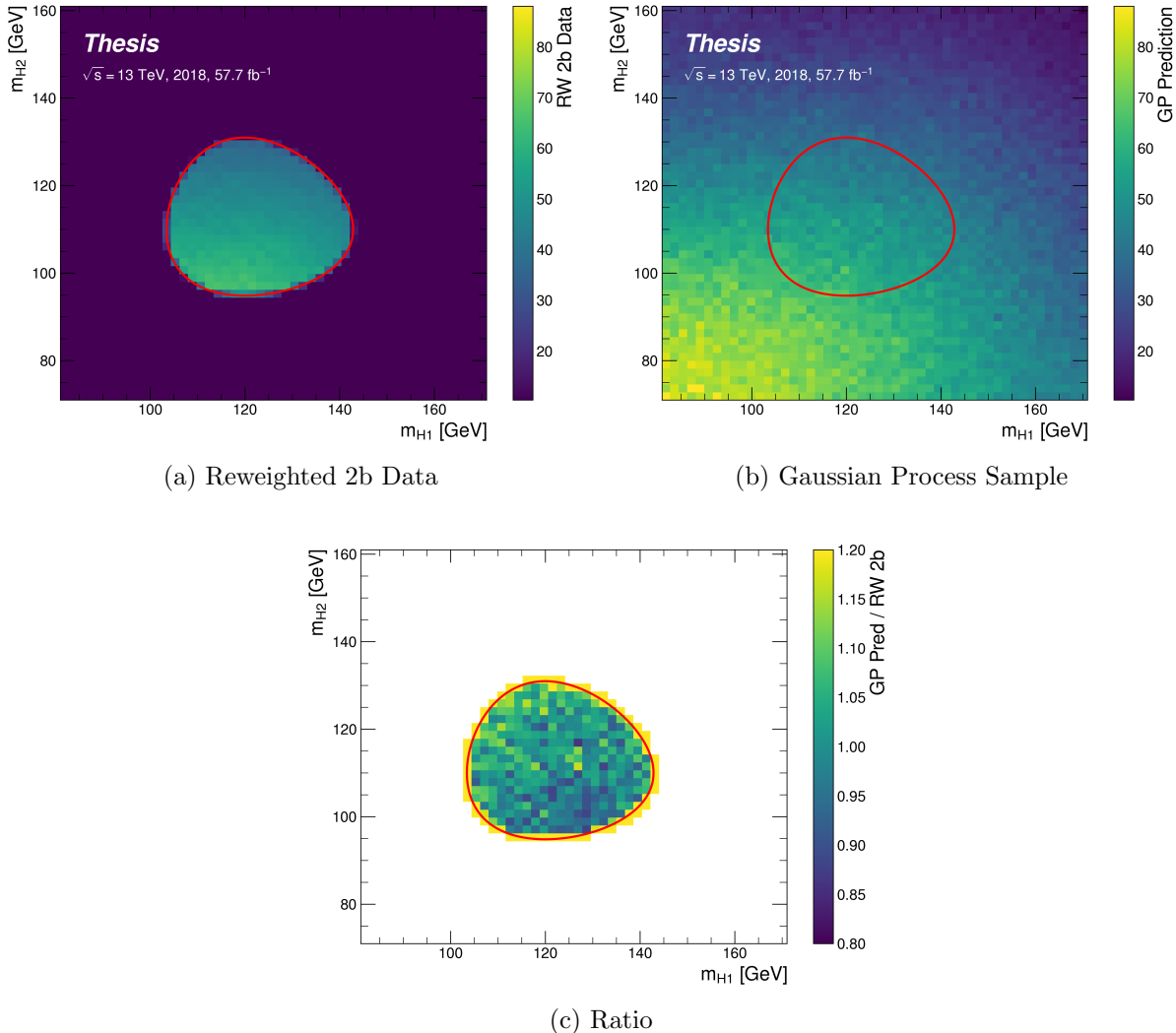


Figure 8.6: Gaussian process sampling prediction for the $4b$ mass plane compared to the reweighted $2b$ estimate in the signal region. Both estimates are compatible.

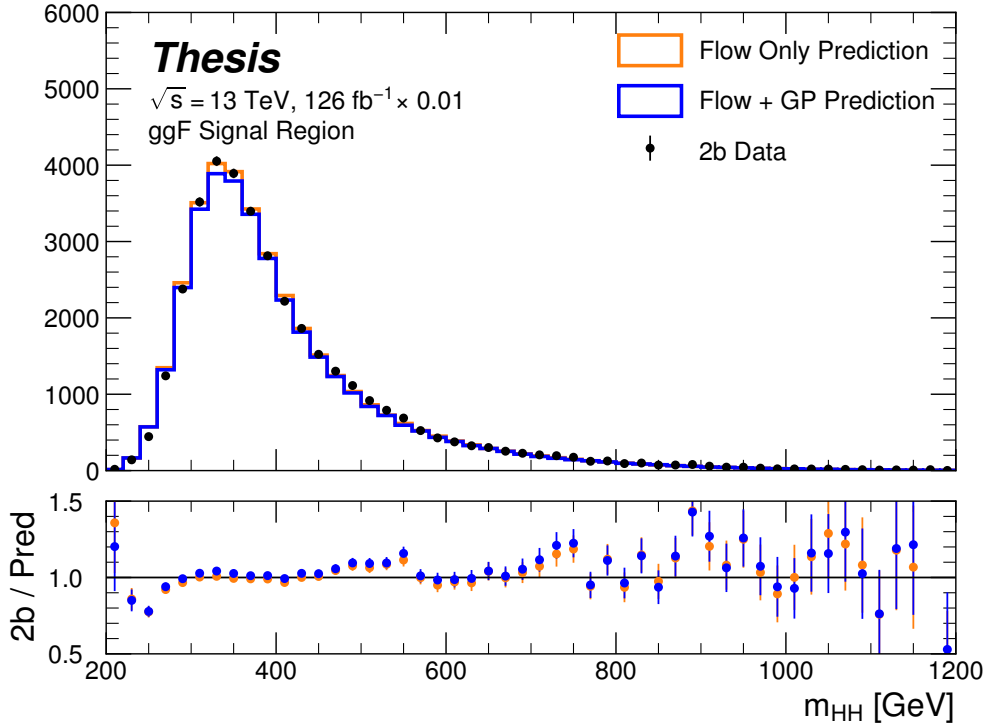


Figure 8.7: Comparison of the interpolation background estimate with real 2b data in the signal region. Only 1 % of 2b data is used in order to mimic 4b statistics, and results are presented here summed across years. The “Flow Only” prediction uses samples of actual 2b signal region data for the input values of m_{H_1} and m_{H_2} , whereas the “Flow + GP” prediction uses samples following the Gaussian process procedure above, more closely mimicking a the full background estimation procedure. The two predictions are quite comparable, demonstrating the closure of the Gaussian process estimate, and the predicted m_{HH} shape agrees well with 2b data. Only 2b statistical uncertainty is shown.

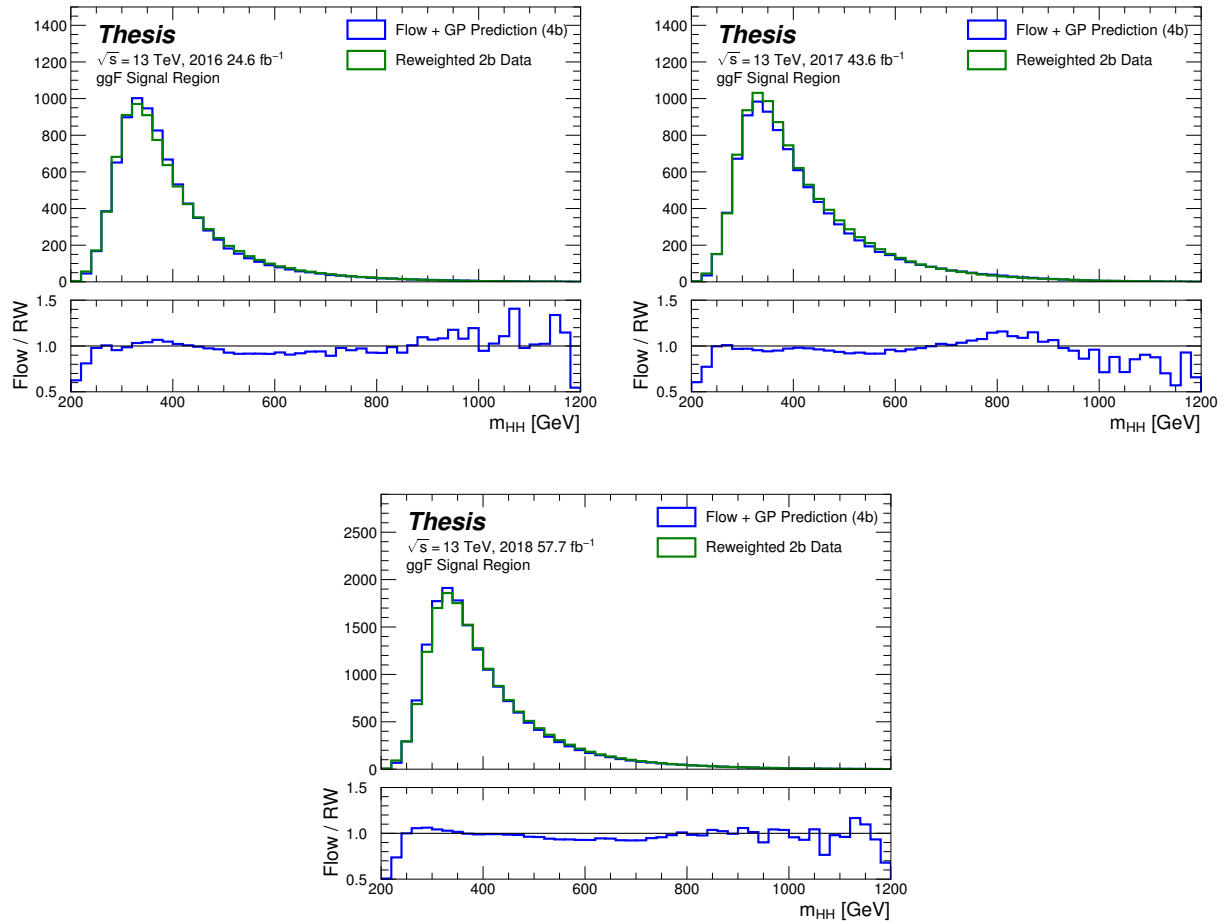


Figure 8.8: Comparison of the interpolation background estimate in the $4b$ signal region with the control region derived reweighted 2b estimate, shown for each year individually. Results are generally similar, within around 10 %.

2808

Chapter 9

2809

CONCLUSIONS

2810 This thesis has provided an overview of the Standard Model, with an emphasis on pair
2811 production of Higgs bosons and how this process may be used to both verify the Standard
2812 Model and to search for new physics. An overview of the Large Hadron Collider and the
2813 ATLAS detector has been provided, and the design and use of simulation infrastructure
2814 has been explained, including work to improve hadronic shower modeling in fast detector
2815 simulation. The translation of detector level information to analysis level information has
2816 been explained, with an emphasis on jets and the identification of B hadron decay. Finally,
2817 two searches for Higgs boson pair production have been presented, with a complete set of
2818 results for resonant production included, focusing on searches beyond the Standard Model,
2819 and a preliminary set of results for non-resonant production, targeting Standard Model
2820 production, with variations of the Higgs self-coupling. Two advanced techniques for the
2821 future of these analyses are further presented, along with proof-of-concept results.

2822

BIBLIOGRAPHY

- 2823 [1] ATLAS Collaboration, *Search for pair production of Higgs bosons in the $b\bar{b}b\bar{b}$ final*
 2824 *state using proton–proton collisions at $\sqrt{s} = 13$ TeV with the ATLAS detector*, JHEP
 2825 **01** (2019) 030, arXiv: [1804.06174 \[hep-ex\]](https://arxiv.org/abs/1804.06174) (cit. on pp. [xix](#), [78](#), [91](#), [97](#)).
- 2826 [2] A. Shmakov et al., *SPANet: Generalized Permutationless Set Assignment for Particle*
 2827 *Physics using Symmetry Preserving Attention*, 2021, arXiv: [2106.03898 \[hep-ex\]](https://arxiv.org/abs/2106.03898)
 2828 (cit. on p. [xix](#)).
- 2829 [3] D. M. Reiman, J. Tamanas, J. X. Prochaska, and D. Ďurovčíková, *Fully probabilistic*
 2830 *quasar continua predictions near Lyman- α with conditional neural spline flows*, 2020,
 2831 arXiv: [2006.00615 \[astro-ph.CO\]](https://arxiv.org/abs/2006.00615) (cit. on p. [xix](#)).
- 2832 [4] *A New Map of All the Particles and Forces*, [https://www.quantamagazine.org/a-](https://www.quantamagazine.org/a-new-map-of-the-standard-model-of-particle-physics-20201022/)
 2833 [new-map-of-the-standard-model-of-particle-physics-20201022/](https://www.quantamagazine.org/a-new-map-of-the-standard-model-of-particle-physics-20201022/), Accessed:
 2834 2021-07-23 (cit. on pp. [3](#), [27](#)).
- 2835 [5] J. D. Jackson, *Classical electrodynamics; 2nd ed.* Wiley, 1975 (cit. on p. [2](#)).
- 2836 [6] M. Thomson, *Modern particle physics*, Cambridge University Press, 2013, ISBN: 978-1-
 2837 107-03426-6 (cit. on p. [2](#)).
- 2838 [7] M. Srednicki, *Quantum Field Theory*, Cambridge Univ. Press, 2007 (cit. on p. [2](#)).
- 2839 [8] M. Gell-Mann, *A schematic model of baryons and mesons*, Physics Letters **8** (1964)
 2840 **214**, ISSN: 0031-9163, URL: <https://www.sciencedirect.com/science/article/pii/S0031916364920013> (cit. on p. [11](#)).
- 2842 [9] G. Zweig, *An SU_3 model for strong interaction symmetry and its breaking; Version 1*,
 2843 tech. rep., CERN, 1964, URL: <https://cds.cern.ch/record/352337> (cit. on p. [11](#)).

- 2844 [10] O. W. Greenberg, *Spin and Unitary-Spin Independence in a Paraquark Model of*
2845 *Baryons and Mesons*, Phys. Rev. Lett. **13** (20 1964) 598, URL: <https://link.aps.org/doi/10.1103/PhysRevLett.13.598> (cit. on p. 11).
- 2846
- 2847 [11] M. Y. Han and Y. Nambu, *Three-Triplet Model with Double SU(3) Symmetry*, Phys.
- 2848 Rev. **139** (4B 1965) B1006, URL: <https://link.aps.org/doi/10.1103/PhysRev.139.B1006> (cit. on p. 11).
- 2849
- 2850 [12] F. L. Wilson, *Fermi's Theory of Beta Decay*, American Journal of Physics **36** (1968)
- 2851 1150, eprint: <https://doi.org/10.1119/1.1974382>, URL: <https://doi.org/10.1119/1.1974382> (cit. on p. 14).
- 2852
- 2853 [13] *The Nobel Prize in Physics 1979*, <https://www.nobelprize.org/prizes/physics/1979/summary/>, Accessed: 2021-07-23 (cit. on p. 15).
- 2854
- 2855 [14] F. Englert and R. Brout, *Broken Symmetry and the Mass of Gauge Vector Mesons*,
2856 Phys. Rev. Lett. **13** (9 1964) 321, URL: <https://link.aps.org/doi/10.1103/PhysRevLett.13.321> (cit. on p. 20).
- 2857
- 2858 [15] P. W. Higgs, *Broken Symmetries and the Masses of Gauge Bosons*, Phys. Rev. Lett.
2859 **13** (16 1964) 508, URL: <https://link.aps.org/doi/10.1103/PhysRevLett.13.508> (cit. on p. 20).
- 2860
- 2861 [16] G. S. Guralnik, C. R. Hagen, and T. W. B. Kibble, *Global Conservation Laws and*
2862 *Massless Particles*, Phys. Rev. Lett. **13** (20 1964) 585, URL: <https://link.aps.org/doi/10.1103/PhysRevLett.13.585> (cit. on p. 20).
- 2863
- 2864 [17] ATLAS Collaboration, *Observation of a new particle in the search for the Standard*
2865 *Model Higgs boson with the ATLAS detector at the LHC*, Phys. Lett. B **716** (2012) 1,
2866 arXiv: [1207.7214 \[hep-ex\]](https://arxiv.org/abs/1207.7214) (cit. on p. 20).
- 2867
- 2868 [18] CMS Collaboration, *Observation of a new boson at a mass of 125 GeV with the CMS*
2869 *experiment at the LHC*, Phys. Lett. B **716** (2012) 30, arXiv: [1207.7235 \[hep-ex\]](https://arxiv.org/abs/1207.7235) (cit. on p. 20).
- 2869

- 2870 [19] S. Weinberg, *A Model of Leptons*, Phys. Rev. Lett. **19** (21 1967) 1264, URL: <https://link.aps.org/doi/10.1103/PhysRevLett.19.1264> (cit. on p. 25).
- 2871
- 2872 [20] ATLAS Collaboration, *Search for the $HH \rightarrow b\bar{b}b\bar{b}$ process via vector-boson fusion*
2873 *production using proton–proton collisions at $\sqrt{s} = 13$ TeV with the ATLAS detector*,
2874 JHEP **07** (2020) 108, arXiv: 2001.05178 [hep-ex] (cit. on pp. 30, 78, 97), Erratum:
2875 JHEP **01** (2021) 145.
- 2876 [21] G. Branco et al., *Theory and phenomenology of two-Higgs-doublet models*, Physics
2877 Reports **516** (2012) 1, Theory and phenomenology of two-Higgs-doublet models,
2878 ISSN: 0370-1573, URL: <http://www.sciencedirect.com/science/article/pii/S0370157312000695> (cit. on pp. 31, 32).
- 2879
- 2880 [22] K. Agashe, H. Davoudiasl, G. Perez, and A. Soni, *Warped gravitons at the CERN*
2881 *LHC and beyond*, Phys. Rev. D **76** (3 2007) 036006, URL: <https://link.aps.org/doi/10.1103/PhysRevD.76.036006> (cit. on pp. 31, 32).
- 2882
- 2883 [23] A. Carvalho, *Gravity particles from Warped Extra Dimensions, predictions for LHC*,
2884 2018, arXiv: 1404.0102 [hep-ph] (cit. on pp. 31, 32, 186).
- 2885
- 2886 [24] ATLAS Collaboration, *Combination of searches for Higgs boson pairs in pp collisions*
2887 *at $\sqrt{s} = 13$ TeV with the ATLAS detector*, Phys. Lett. B **800** (2020) 135103, arXiv:
1906.02025 [hep-ex] (cit. on pp. 32, 35, 78).
- 2888
- 2889 [25] P. D. Group et al., *Review of Particle Physics*, Progress of Theoretical and Experimental
2890 Physics **2020** (2020), 083C01, ISSN: 2050-3911, eprint: <https://academic.oup.com/ptep/article-pdf/2020/8/083C01/34673722/ptaa104.pdf>, URL: <https://doi.org/10.1093/ptep/ptaa104> (cit. on p. 34).
- 2891
- 2892 [26] T. van Ritbergen and R. G. Stuart, *On the precise determination of the Fermi coupling*
2893 *constant from the muon lifetime*, Nuclear Physics B **564** (2000) 343, ISSN: 0550-3213,
2894 URL: [http://dx.doi.org/10.1016/S0550-3213\(99\)00572-6](http://dx.doi.org/10.1016/S0550-3213(99)00572-6) (cit. on p. 34).

- 2895 [27] S. Dawson, A. Ismail, and I. Low, *What's in the loop? The anatomy of double Higgs*
 2896 *production*, Physical Review D **91** (2015), ISSN: 1550-2368, URL: <http://dx.doi.org/10.1103/PhysRevD.91.115008> (cit. on p. 34).
- 2898 [28] A. M. Sirunyan et al., *Measurement of the top quark Yukawa coupling from $t\bar{t}$ kinematic*
 2899 *distributions in the dilepton final state in proton-proton collisions at $\sqrt{s}=13$ TeV*,
 2900 Physical Review D **102** (2020), ISSN: 2470-0029, URL: <http://dx.doi.org/10.1103/PhysRevD.102.092013> (cit. on p. 34).
- 2902 [29] S. Dawson, S. Dittmaier, and M. Spira, *Neutral Higgs-boson pair production at hadron*
 2903 *colliders: QCD corrections*, Physical Review D **58** (1998), ISSN: 1089-4918, URL:
 2904 <http://dx.doi.org/10.1103/PhysRevD.58.115012> (cit. on p. 36).
- 2905 [30] S. Borowka et al., *Higgs Boson Pair Production in Gluon Fusion at Next-to-Leading*
 2906 *Order with Full Top-Quark Mass Dependence*, Physical Review Letters **117** (2016),
 2907 ISSN: 1079-7114, URL: <http://dx.doi.org/10.1103/PhysRevLett.117.012001>
 2908 (cit. on p. 36).
- 2909 [31] J. Baglio et al., *Gluon fusion into Higgs pairs at NLO QCD and the top mass*
 2910 *scheme*, The European Physical Journal C **79** (2019), ISSN: 1434-6052, URL: <http://dx.doi.org/10.1140/epjc/s10052-019-6973-3> (cit. on p. 36).
- 2912 [32] D. de Florian and J. Mazzitelli, *Higgs Boson Pair Production at Next-to-Next-to-*
 2913 *Leading Order in QCD*, Physical Review Letters **111** (2013), ISSN: 1079-7114, URL:
 2914 <http://dx.doi.org/10.1103/PhysRevLett.111.201801> (cit. on p. 36).
- 2915 [33] D. Y. Shao, C. S. Li, H. T. Li, and J. Wang, *Threshold resummation effects in Higgs*
 2916 *boson pair production at the LHC*, Journal of High Energy Physics **2013** (2013), ISSN:
 2917 1029-8479, URL: [http://dx.doi.org/10.1007/JHEP07\(2013\)169](http://dx.doi.org/10.1007/JHEP07(2013)169) (cit. on p. 36).
- 2918 [34] D. de Florian and J. Mazzitelli, *Higgs pair production at next-to-next-to-leading*
 2919 *logarithmic accuracy at the LHC*, 2015, arXiv: [1505.07122 \[hep-ph\]](https://arxiv.org/abs/1505.07122) (cit. on p. 36).

- [35] M. Grazzini et al., *Higgs boson pair production at NNLO with top quark mass effects*, Journal of High Energy Physics **2018** (2018), ISSN: 1029-8479, URL: [http://dx.doi.org/10.1007/JHEP05\(2018\)059](http://dx.doi.org/10.1007/JHEP05(2018)059) (cit. on p. 36).
- [36] J. Baglio et al., *gg → HH: Combined uncertainties*, Physical Review D **103** (2021), ISSN: 2470-0029, URL: <http://dx.doi.org/10.1103/PhysRevD.103.056002> (cit. on p. 36).
- [37] F. Dulat, A. Lazopoulos, and B. Mistlberger, *iHixs 2 — Inclusive Higgs cross sections*, Computer Physics Communications **233** (2018) 243, ISSN: 0010-4655, URL: <http://dx.doi.org/10.1016/j.cpc.2018.06.025> (cit. on p. 36).
- [38] ATLAS Collaboration, *Measurement prospects of the pair production and self-coupling of the Higgs boson with the ATLAS experiment at the HL-LHC*, ATL-PHYS-PUB-2018-053, 2018, URL: <https://cds.cern.ch/record/2652727> (cit. on p. 36).
- [39] D. de Florian, I. Fabre, and J. Mazzitelli, *Triple Higgs production at hadron colliders at NNLO in QCD*, Journal of High Energy Physics **2020** (2020), ISSN: 1029-8479, URL: [http://dx.doi.org/10.1007/JHEP03\(2020\)155](http://dx.doi.org/10.1007/JHEP03(2020)155) (cit. on p. 36).
- [40] A. Papaefstathiou, T. Robens, and G. Tetlamatzi-Xolocotzi, *Triple Higgs boson production at the Large Hadron Collider with Two Real Singlet scalars*, Journal of High Energy Physics **2021** (2021), ISSN: 1029-8479, URL: [http://dx.doi.org/10.1007/JHEP05\(2021\)193](http://dx.doi.org/10.1007/JHEP05(2021)193) (cit. on p. 36).
- [41] T. Robens, T. Stefaniak, and J. Wittbrodt, *Two-real-scalar-singlet extension of the SM: LHC phenomenology and benchmark scenarios*, The European Physical Journal C **80** (2020), ISSN: 1434-6052, URL: <http://dx.doi.org/10.1140/epjc/s10052-020-7655-x> (cit. on p. 36).
- [42] D. Egana-Ugrinovic, S. Homiller, and P. Meade, *Multi-Higgs boson production probes Higgs sector flavor*, Physical Review D **103** (2021), ISSN: 2470-0029, URL: <http://dx.doi.org/10.1103/PhysRevD.103.115005> (cit. on p. 36).

- 2946 [43] CERN, *CERN's accelerator complex*, <https://home.cern/science/accelerators/accelerator-complex>, Accessed: 27 July 2021 (cit. on p. 38).
- 2947
- 2948 [44] J. Pequenao, “Computer generated image of the whole ATLAS detector”, 2008, URL: <https://cds.cern.ch/record/1095924> (cit. on p. 40).
- 2949
- 2950 [45] ATLAS Collaboration, *The ATLAS Experiment at the CERN Large Hadron Collider*, JINST **3** (2008) S08003 (cit. on p. 41).
- 2951
- 2952 [46] J. Pequenao and P. Schaffner, “How ATLAS detects particles: diagram of particle paths in the detector”, 2013, URL: <https://cds.cern.ch/record/1505342> (cit. on p. 42).
- 2953
- 2954
- 2955 [47] ATLAS Collaboration, *ATLAS Insertable B-Layer: Technical Design Report*, ATLAS-TDR-19; CERN-LHCC-2010-013, 2010, URL: <https://cds.cern.ch/record/1291633> (cit. on p. 43), Addendum: ATLAS-TDR-19-ADD-1; CERN-LHCC-2012-009, 2012, URL: <https://cds.cern.ch/record/1451888>.
- 2956
- 2957
- 2958
- 2959 [48] B. Abbott et al., *Production and integration of the ATLAS Insertable B-Layer*, JINST **13** (2018) T05008, arXiv: [1803.00844 \[physics.ins-det\]](https://arxiv.org/abs/1803.00844) (cit. on p. 43).
- 2960
- 2961 [49] A. Outreach, “ATLAS Fact Sheet : To raise awareness of the ATLAS detector and collaboration on the LHC”, 2010, URL: <https://cds.cern.ch/record/1457044> (cit. on p. 45).
- 2962
- 2963
- 2964 [50] ATLAS Collaboration, *Performance of the ATLAS trigger system in 2015*, Eur. Phys. J. C **77** (2017) 317, arXiv: [1611.09661 \[hep-ex\]](https://arxiv.org/abs/1611.09661) (cit. on p. 46).
- 2965
- 2966 [51] ATLAS Collaboration, *The ATLAS Collaboration Software and Firmware*, ATL-SOFT-PUB-2021-001, 2021, URL: <https://cds.cern.ch/record/2767187> (cit. on p. 46).
- 2967
- 2968 [52] P. Nason, *A New method for combining NLO QCD with shower Monte Carlo algorithms*, JHEP **11** (2004) 040, arXiv: [hep-ph/0409146 \[hep-ph\]](https://arxiv.org/abs/hep-ph/0409146) (cit. on pp. 50, 81).
- 2969

- 2970 [53] S. Frixione, P. Nason and C. Oleari, *Matching NLO QCD computations with parton*
 2971 *shower simulations: the POWHEG method*, JHEP **11** (2007) 070, arXiv: [0709.2092](#)
 2972 [[hep-ph](#)] (cit. on pp. 50, 81).
- 2973 [54] S. Alioli, P. Nason, C. Oleari, and E. Re, *A general framework for implementing NLO*
 2974 *calculations in shower Monte Carlo programs: the POWHEG BOX*, JHEP **06** (2010)
 2975 043, arXiv: [1002.2581](#) [[hep-ph](#)] (cit. on pp. 50, 81).
- 2976 [55] J. Alwall et al., *The automated computation of tree-level and next-to-leading order*
 2977 *differential cross sections, and their matching to parton shower simulations*, Journal of
 2978 High Energy Physics **2014** (2014), URL: [https://doi.org/10.1007/jhep07\(2014\)](https://doi.org/10.1007/jhep07(2014)079)
 2979 (cit. on pp. 50, 80).
- 2980 [56] J. Bellm et al., *Herwig 7.0/Herwig++ 3.0 release note*, The European Physical Journal
 2981 C **76** (2016), URL: <https://doi.org/10.1140/epjc/s10052-016-4018-8> (cit. on
 2982 pp. 50, 80).
- 2983 [57] M. Bähr et al., *Herwig++ physics and manual*, The European Physical Journal C
 2984 **58** (2008) 639, URL: <https://doi.org/10.1140/epjc/s10052-008-0798-9> (cit. on
 2985 pp. 50, 80).
- 2986 [58] T. Sjöstrand et al., *An introduction to PYTHIA 8.2*, Computer Physics Communications
 2987 **191** (2015) 159, ISSN: 0010-4655, URL: <https://www.sciencedirect.com/science/article/pii/S0010465515000442> (cit. on pp. 50, 80).
- 2988 [59] D. J. Lange, *The EvtGen particle decay simulation package*, Nucl. Instrum. Meth. A
 2989 **462** (2001) 152 (cit. on pp. 50, 80).
- 2990 [60] S. Höche, *Introduction to parton-shower event generators*, 2015, arXiv: [1411.4085](#)
 2991 [[hep-ph](#)] (cit. on p. 51).
- 2992 [61] S. Agostinelli et al., *Geant4—a simulation toolkit*, Nuclear Instruments and Methods
 2993 in Physics Research Section A: Accelerators, Spectrometers, Detectors and Associated

- 2995 Equipment **506** (2003) 250, ISSN: 0168-9002, URL: <https://www.sciencedirect.com/science/article/pii/S0168900203013688> (cit. on p. 52).
- 2996
- 2997 [62] P. Calafiura, J. Catmore, D. Costanzo, and A. Di Girolamo, *ATLAS HL-LHC Computing Conceptual Design Report*, tech. rep., CERN, 2020, URL: <https://cds.cern.ch/record/2729668> (cit. on p. 52).
- 2998
- 2999
- 3000 [63] A. Collaboration, *Computing and Software - Public Results*, <https://twiki.cern.ch/twiki/bin/view/AtlasPublic/ComputingandSoftwarePublicResults>, Accessed:
- 3001
- 3002 27 July 2021 (cit. on p. 53).
- 3003 [64] ATLAS Collaboration, *The ATLAS Simulation Infrastructure*, *Eur. Phys. J. C* **70**
- 3004 (2010) 823, arXiv: [1005.4568 \[physics.ins-det\]](https://arxiv.org/abs/1005.4568) (cit. on pp. 52, 80).
- 3005 [65] ATLAS Collaboration, *The new Fast Calorimeter Simulation in ATLAS*, ATL-SOFT-
- 3006 PUB-2018-002, 2018, URL: <https://cds.cern.ch/record/2630434> (cit. on pp. 54,
- 3007 55).
- 3008 [66] ROOT, *TPrincipal Class Reference*, <https://root.cern.ch/doc/master/classTPrincipal.html>, Accessed: 27 July 2021 (cit. on p. 54).
- 3009
- 3010 [67] M. Aharrouche et al., *Energy linearity and resolution of the ATLAS electromagnetic*
- 3011 *barrel calorimeter in an electron test-beam*, *Nuclear Instruments and Methods in*
- 3012 *Physics Research Section A: Accelerators, Spectrometers, Detectors and Associated*
- 3013 *Equipment* **568** (2006) 601, ISSN: 0168-9002, URL: [http://dx.doi.org/10.1016/j.nima.2006.07.053](https://dx.doi.org/10.1016/j.nima.2006.07.053) (cit. on p. 55).
- 3014
- 3015 [68] ATLAS Collaboration, *Evidence for prompt photon production in pp collisions at*
- 3016 $\sqrt{s} = 7 \text{ TeV}$ *with the ATLAS detector*, ATLAS-CONF-2010-077, 2010, URL: <https://cds.cern.ch/record/1281368> (cit. on p. 55).
- 3017
- 3018 [69] S. Gasiorowski and H. Gray, *Fast Calorimeter Simulation in ATLAS*, *EPJ Web Conf.*
- 3019 **245** (2020) 02002. 7 p, URL: <https://cds.cern.ch/record/2756298> (cit. on p. 56).

- 3020 [70] D. P. Kingma and M. Welling, *Auto-Encoding Variational Bayes*, 2014, arXiv: [1312.6114 \[stat.ML\]](#) (cit. on p. 56).
- 3021
- 3022 [71] G. Aad et al., *Topological cell clustering in the ATLAS calorimeters and its performance*
3023 *in LHC Run 1*, *The European Physical Journal C* **77** (2017), ISSN: 1434-6052, URL:
3024 <http://dx.doi.org/10.1140/epjc/s10052-017-5004-5> (cit. on pp. 60, 61).
- 3025 [72] A. Ghosh and A. Collaboration, *Deep generative models for fast shower simulation*
3026 *in ATLAS*, *Journal of Physics: Conference Series* **1525** (2020) 012077, URL: <https://doi.org/10.1088/1742-6596/1525/1/012077> (cit. on p. 62).
- 3027
- 3028 [73] R. Di Sipio, M. F. Giannelli, S. K. Haghight, and S. Palazzo, *DijetGAN: a Generative-*
3029 *Adversarial Network approach for the simulation of QCD dijet events at the LHC*,
3030 *Journal of High Energy Physics* **2019** (2019), ISSN: 1029-8479, URL: [http://dx.doi.org/10.1007/JHEP08\(2019\)110](http://dx.doi.org/10.1007/JHEP08(2019)110) (cit. on p. 62).
- 3031
- 3032 [74] ATLAS Collaboration, *Jet reconstruction and performance using particle flow with*
3033 *the ATLAS Detector*, *Eur. Phys. J. C* **77** (2017) 466, arXiv: [1703.10485 \[hep-ex\]](#)
3034 (cit. on pp. 65, 79).
- 3035 [75] ATLAS Collaboration, *Topological cell clustering in the ATLAS calorimeters and*
3036 *its performance in LHC Run 1*, *Eur. Phys. J. C* **77** (2017) 490, arXiv: [1603.02934 \[hep-ex\]](#)
3037 (cit. on p. 65).
- 3038 [76] ATLAS Collaboration, *Variable Radius, Exclusive- k_T , and Center-of-Mass Subjet*
3039 *Reconstruction for Higgs($\rightarrow b\bar{b}$) Tagging in ATLAS*, ATL-PHYS-PUB-2017-010, 2017,
3040 URL: <https://cds.cern.ch/record/2268678> (cit. on pp. 65, 170).
- 3041 [77] M. Cacciari, G. P. Salam, and G. Soyez, *The anti- k_T jet clustering algorithm*, *Journal*
3042 *of High Energy Physics* **2008** (2008) 063, ISSN: 1029-8479, URL: <http://dx.doi.org/10.1088/1126-6708/2008/04/063> (cit. on p. 65).
- 3043

- 3044 [78] G. P. Salam, *Towards jetography*, The European Physical Journal C **67** (2010) 637,
 3045 ISSN: 1434-6052, URL: <http://dx.doi.org/10.1140/epjc/s10052-010-1314-6>
 3046 (cit. on p. 65).
- 3047 [79] A. Collaboration, *Configuration and performance of the ATLAS b-jet triggers in Run*
 3048 *2*, 2021, arXiv: [2106.03584 \[hep-ex\]](https://arxiv.org/abs/2106.03584) (cit. on p. 69).
- 3049 [80] ATLAS Collaboration, *ATLAS b-jet identification performance and efficiency mea-*
 3050 *surement with $t\bar{t}$ events in pp collisions at $\sqrt{s} = 13$ TeV*, Eur. Phys. J. C **79** (2019)
 3051 970, arXiv: [1907.05120 \[hep-ex\]](https://arxiv.org/abs/1907.05120) (cit. on pp. 68, 79, 165).
- 3052 [81] ATLAS Collaboration, *Topological b-hadron decay reconstruction and identification*
 3053 *of b-jets with the JetFitter package in the ATLAS experiment at the LHC*, ATL-
 3054 PHYS-PUB-2018-025, 2018, URL: <https://cds.cern.ch/record/2645405> (cit. on
 3055 p. 71).
- 3056 [82] R. Frühwirth, *Application of Kalman filtering to track and vertex fitting*, Nuclear
 3057 Instruments and Methods in Physics Research Section A: Accelerators, Spectrometers,
 3058 Detectors and Associated Equipment **262** (1987) 444, ISSN: 0168-9002, URL: <https://www.sciencedirect.com/science/article/pii/0168900287908874> (cit. on
 3059 p. 71).
- 3060 [83] ATLAS Collaboration, *Identification of Jets Containing b-Hadrons with Recurrent*
 3061 *Neural Networks at the ATLAS Experiment*, ATL-PHYS-PUB-2017-003, 2017, URL:
 3062 <https://cds.cern.ch/record/2255226> (cit. on p. 72).
- 3063 [84] *Expected performance of the 2019 ATLAS b-taggers*, <http://atlas.web.cern.ch/Atlas/GROUPS/PHYSICS/PLTS/FTAG-2019-005/>, Accessed: 2021-07-14 (cit. on
 3064 p. 74).
- 3065 [85] ATLAS Collaboration, *Search for Higgs boson pair production in the $b\bar{b}WW^*$ decay*
 3066 *mode at $\sqrt{s} = 13$ TeV with the ATLAS detector*, JHEP **04** (2019) 092, arXiv: [1811.04671 \[hep-ex\]](https://arxiv.org/abs/1811.04671) (cit. on p. 78).

- 3070 [86] ATLAS Collaboration, *A search for resonant and non-resonant Higgs boson pair*
 3071 *production in the $b\bar{b}\tau^+\tau^-$ decay channel in pp collisions at $\sqrt{s} = 13 \text{ TeV}$ with the*
 3072 *ATLAS detector*, Phys. Rev. Lett. **121** (2018) 191801, arXiv: [1808.00336 \[hep-ex\]](https://arxiv.org/abs/1808.00336)
 3073 (cit. on p. 78), Erratum: Phys. Rev. Lett. **122** (2019) 089901.
- 3074 [87] ATLAS Collaboration, *Search for Higgs boson pair production in the $WW^{(*)}WW^{(*)}$*
 3075 *decay channel using ATLAS data recorded at $\sqrt{s} = 13 \text{ TeV}$* , JHEP **05** (2019) 124,
 3076 arXiv: [1811.11028 \[hep-ex\]](https://arxiv.org/abs/1811.11028) (cit. on p. 78).
- 3077 [88] ATLAS Collaboration, *Search for Higgs boson pair production in the $\gamma\gamma b\bar{b}$ final state*
 3078 *with 13 TeV pp collision data collected by the ATLAS experiment*, JHEP **11** (2018)
 3079 040, arXiv: [1807.04873 \[hep-ex\]](https://arxiv.org/abs/1807.04873) (cit. on p. 78).
- 3080 [89] ATLAS Collaboration, *Search for Higgs boson pair production in the $\gamma\gamma WW^*$ channel*
 3081 *using pp collision data recorded at $\sqrt{s} = 13 \text{ TeV}$ with the ATLAS detector*, Eur. Phys.
 3082 J. C **78** (2018) 1007, arXiv: [1807.08567 \[hep-ex\]](https://arxiv.org/abs/1807.08567) (cit. on p. 78).
- 3083 [90] ATLAS Collaboration, *Reconstruction and identification of boosted di- τ systems in*
 3084 *a search for Higgs boson pairs using 13 TeV proton–proton collision data in ATLAS*,
 3085 JHEP **11** (2020) 163, arXiv: [2007.14811 \[hep-ex\]](https://arxiv.org/abs/2007.14811) (cit. on p. 78).
- 3086 [91] ATLAS Collaboration, *Search for non-resonant Higgs boson pair production in the*
 3087 *$bb\ell\nu\ell\nu$ final state with the ATLAS detector in pp collisions at $\sqrt{s} = 13 \text{ TeV}$* , Phys.
 3088 Lett. B **801** (2020) 135145, arXiv: [1908.06765 \[hep-ex\]](https://arxiv.org/abs/1908.06765) (cit. on p. 78).
- 3089 [92] ATLAS Collaboration, *Search for Higgs boson pair production in the two bottom quarks*
 3090 *plus two final state with in pp collisions at $\sqrt{s} = 13 \text{ TeV}$ with the ATLAS detector*,
 3091 ATLAS-CONF-2021-016, 2021, URL: <https://cds.cern.ch/record/2759683> (cit. on
 3092 p. 78).
- 3093 [93] CMS Collaboration, *Search for heavy resonances decaying to two Higgs bosons in final*
 3094 *states containing four b quarks*, Eur. Phys. J. C **76** (2016) 371, arXiv: [1602.08762](https://arxiv.org/abs/1602.08762)
 3095 [hep-ex] (cit. on p. 79).

- 3096 [94] CMS Collaboration, *Search for production of Higgs boson pairs in the four b quark*
 3097 *final state using large-area jets in proton–proton collisions at $\sqrt{s} = 13 \text{ TeV}$* , JHEP **01**
 3098 (2019) 040, arXiv: [1808.01473 \[hep-ex\]](https://arxiv.org/abs/1808.01473) (cit. on p. 79).
- 3099 [95] CMS Collaboration, *Combination of Searches for Higgs Boson Pair Production in*
 3100 *Proton–Proton Collisions at $\sqrt{s} = 13 \text{ TeV}$* , Phys. Rev. Lett. **122** (2019) 121803, arXiv:
 3101 [1811.09689 \[hep-ex\]](https://arxiv.org/abs/1811.09689) (cit. on p. 79).
- 3102 [96] G. Bartolini et al., *Performance of the ATLAS b-jet trigger in $p\ p$ collisions at $\sqrt{s} =$*
 3103 *13 TeV* , tech. rep. ATL-COM-DAQ-2019-150, CERN, 2019, URL: <https://cds.cern.ch/record/2688819> (cit. on p. 79).
- 3105 [97] ATLAS Collaboration, *Luminosity determination in pp collisions at $\sqrt{s} = 13 \text{ TeV}$ using the ATLAS detector at the LHC*, ATLAS-CONF-2019-021, 2019, URL: <https://cds.cern.ch/record/2677054> (cit. on pp. 80, 165).
- 3108 [98] J. Butterworth et al., *PDF4LHC recommendations for LHC Run II*, J. Phys. G **43**
 3109 (2016) 023001, arXiv: [1510.03865 \[hep-ph\]](https://arxiv.org/abs/1510.03865) (cit. on pp. 81, 166).
- 3110 [99] M. Bahr et al., *Herwig++ Physics and Manual*, Eur. Phys. J. **C58** (2008) 639, arXiv:
 3111 [0803.0883 \[hep-ph\]](https://arxiv.org/abs/0803.0883) (cit. on p. 81).
- 3112 [100] T. Head et al., *scikit-optimize/scikit-optimize: v0.5.2*, version v0.5.2, 2018, URL: <https://doi.org/10.5281/zenodo.1207017> (cit. on p. 86).
- 3114 [101] A. Carvalho et al., *Higgs pair production: choosing benchmarks with cluster analysis*,
 3115 Journal of High Energy Physics **2016** (2016) 1, ISSN: 1029-8479, URL: [http://dx.doi.org/10.1007/JHEP04\(2016\)126](http://dx.doi.org/10.1007/JHEP04(2016)126) (cit. on p. 95).
- 3117 [102] A. Rogozhnikov, *Reweighting with Boosted Decision Trees*, Journal of Physics: Conference Series **762** (2016) 012036, ISSN: 1742-6596, URL: <http://dx.doi.org/10.1088/1742-6596/762/1/012036> (cit. on p. 97).
- 3120 [103] G. V. Moustakides and K. Basioti, *Training Neural Networks for Likelihood/Density*
 3121 *Ratio Estimation*, 2019, arXiv: [1911.00405 \[eess.SP\]](https://arxiv.org/abs/1911.00405) (cit. on p. 98).

- 3122 [104] T. Kanamori, S. Hido, and M. Sugiyama, *A Least-Squares Approach to Direct Im-*
 3123 *portance Estimation*, J. Mach. Learn. Res. **10** (2009) 1391, ISSN: 1532-4435 (cit. on
 3124 p. 98).
- 3125 [105] A. Andreassen and B. Nachman, *Neural networks for full phase-space reweighting*
 3126 *and parameter tuning*, Physical Review D **101** (2020), ISSN: 2470-0029, URL: <http://dx.doi.org/10.1103/PhysRevD.101.091901> (cit. on p. 99).
- 3128 [106] S. Fort, H. Hu, and B. Lakshminarayanan, *Deep Ensembles: A Loss Landscape Per-*
 3129 *spective*, 2020, arXiv: [1912.02757 \[stat.ML\]](https://arxiv.org/abs/1912.02757) (cit. on p. 100).
- 3130 [107] B. Efron, *Bootstrap Methods: Another Look at the Jackknife*, Ann. Statist. **7** (1979) 1,
 3131 URL: <https://doi.org/10.1214/aos/1176344552> (cit. on p. 157).
- 3132 [108] ATLAS Collaboration, *Jet energy scale and resolution measured in proton–proton*
 3133 *collisions at $\sqrt{s} = 13 \text{ TeV}$ with the ATLAS detector*, (2020), arXiv: [2007 . 02645](https://arxiv.org/abs/2007.02645)
 3134 [[hep-ex](#)] (cit. on p. 165).
- 3135 [109] J. Adelman et al., *Search for Higgs boson pair production in the $b\bar{b}\gamma\gamma$ final state with*
 3136 *the full Run 2 13 TeV pp collision data collected by the ATLAS Experiment Supporting*
 3137 *note.*, tech. rep., CERN, 2020, URL: <https://cds.cern.ch/record/2711865> (cit. on
 3138 p. 165).
- 3139 [110] G. Avoni et al., *The new LUCID-2 detector for luminosity measurement and monitoring*
 3140 *in ATLAS*, JINST **13** (2018) P07017. 33 p, URL: <https://cds.cern.ch/record/2633501> (cit. on p. 165).
- 3142 [111] D. de Florian et al., *Handbook of LHC Higgs Cross Sections: 4. Deciphering the Nature*
 3143 *of the Higgs Sector*, CERN Yellow Reports: Monographs, 869 pages, 295 figures, 248 ta-
 3144 *bles and 1645 citations*. Working Group web page: <https://twiki.cern.ch/twiki/bin/view/LHCPhysics/>
 3145 CERN, 2016, URL: <https://cds.cern.ch/record/2227475> (cit. on p. 166).
- 3146 [112] A. L. Read, *Presentation of search results: the CLs technique*, Journal of Physics G:
 3147 Nuclear and Particle Physics **28** (2002) 2693, ISSN: 0954-3899 (cit. on p. 183).

- 3148 [113] G. Cowan, K. Cranmer, E. Gross, and O. Vitells, *Asymptotic formulae for likelihood-*
 3149 *based tests of new physics*, *The European Physical Journal C* **71** (2011), ISSN: 1434-6052
 3150 (cit. on p. 183).
- 3151 [114] A. Sherstinsky, *Fundamentals of Recurrent Neural Network (RNN) and Long Short-*
 3152 *Term Memory (LSTM) network*, *Physica D: Nonlinear Phenomena* **404** (2020) 132306,
 3153 ISSN: 0167-2789, URL: <http://dx.doi.org/10.1016/j.physd.2019.132306> (cit. on
 3154 p. 190).
- 3155 [115] M. Zaheer et al., *Deep Sets*, 2018, arXiv: [1703.06114 \[cs.LG\]](https://arxiv.org/abs/1703.06114) (cit. on p. 190).
- 3156 [116] J. Zhou et al., *Graph Neural Networks: A Review of Methods and Applications*, 2021,
 3157 arXiv: [1812.08434 \[cs.LG\]](https://arxiv.org/abs/1812.08434) (cit. on p. 190).
- 3158 [117] A. Vaswani et al., *Attention Is All You Need*, 2017, arXiv: [1706.03762 \[cs.CL\]](https://arxiv.org/abs/1706.03762)
 3159 (cit. on p. 190).
- 3160 [118] I. Goodfellow, Y. Bengio, and A. Courville, *Deep Learning*, <http://www.deeplearningbook.org>,
 3161 MIT Press, 2016 (cit. on p. 191).
- 3162 [119] I. Kobyzev, S. Prince, and M. Brubaker, *Normalizing Flows: An Introduction and*
 3163 *Review of Current Methods*, *IEEE Transactions on Pattern Analysis and Machine*
 3164 *Intelligence* (2020) **1**, ISSN: 1939-3539, URL: <http://dx.doi.org/10.1109/TPAMI.2020.2992934> (cit. on p. 196).
- 3166 [120] L. Dinh, J. Sohl-Dickstein, and S. Bengio, *Density estimation using Real NVP*, 2017,
 3167 arXiv: [1605.08803 \[cs.LG\]](https://arxiv.org/abs/1605.08803) (cit. on p. 197).
- 3168 [121] C. Durkan, A. Bekasov, I. Murray, and G. Papamakarios, *Neural Spline Flows*, 2019,
 3169 arXiv: [1906.04032 \[stat.ML\]](https://arxiv.org/abs/1906.04032) (cit. on p. 197).
- 3170 [122] F. Pedregosa et al., *Scikit-learn: Machine Learning in Python*, *Journal of Machine*
 3171 *Learning Research* **12** (2011) 2825 (cit. on p. 199).